



HAL
open science

Nickel-rich NMC materials for lithium-ion batteries : surface reactivity and gas production

Ana Cristina Martinez Maciel

► **To cite this version:**

Ana Cristina Martinez Maciel. Nickel-rich NMC materials for lithium-ion batteries : surface reactivity and gas production. Material chemistry. Université de Picardie Jules Verne, 2021. English. NNT : 2021AMIE0007 . tel-03617814

HAL Id: tel-03617814

<https://theses.hal.science/tel-03617814>

Submitted on 23 Mar 2022

HAL is a multi-disciplinary open access archive for the deposit and dissemination of scientific research documents, whether they are published or not. The documents may come from teaching and research institutions in France or abroad, or from public or private research centers.

L'archive ouverte pluridisciplinaire **HAL**, est destinée au dépôt et à la diffusion de documents scientifiques de niveau recherche, publiés ou non, émanant des établissements d'enseignement et de recherche français ou étrangers, des laboratoires publics ou privés.

Thèse de Doctorat

Mention Chimie

Spécialité Chimie des Solides et Sciences des Matériaux

présentée à l'École Doctorale en Sciences Technologie et Santé (ED 585)

de l'Université de Picardie Jules Verne

par

Ana Cristina MARTINEZ MACIEL

pour obtenir le grade de Docteur de l'Université de Picardie Jules Verne

Nickel-rich NMC materials for lithium-ion batteries: surface reactivity and gas production

Soutenue le 02/02/2021, après avis des rapporteurs, devant le jury d'examen :

Mme Laurence CROGUENNEC, Directrice de Recherche, ICMCB, Bordeaux **Présidente et Rapporteur**

M. Daniel LEMORDANT, Professeur Émérite, Université de Tours **Rapporteur**

M. Michel ARMAND, Directeur de Recherche Émérite CNRS, UPJV Amiens **Examinateur**

Mme Sylvie GRUGEON, Ingénieur de Recherche, UPJV Amiens **Examinatrice**

M. Pierre TRAN-VAN, Docteur Ingénieur, Groupe Renault **Examinateur**

M. Stéphane LARUELLE, Professeur, UPJV Amiens **Directeur de thèse**

Remerciements

First of all, I would like to acknowledge the ANRT for the organization of the CIFRE conventions that allowed me to approach battery materials research from an industrial perspective. Secondly, I would like to thank to all of the people at the LRCS, at the PFA, at the PME of the Université de Picardie Jules Verne, and at Renault that in the last 38 months offered me constantly their help.

In the LRCS I want to acknowledge the permanent people for the fruitful discussions along the corridors, late in the laboratories and in early meetings; and for giving me valuable knowledge for my future career. More personally, I would like to thank Tristan Lombard, François Rabuel, Emiliano Primo, Matthieu Courty, Gregory Gachot, Dominique Larcher, Christine Surcin and Philippe Antitomaso for showing me new techniques, processes and methods. In the PFA, I want to thank Serge Pilard, Sébastien Rigaud, David Mathiron and Dominique Cailleu for their invaluable help with the ESI/HRMS and NMR experiments. In the PME, to Loïc Dupont, Carine Davoisne and Arash Jamali for their help with the SEM and TEM experiments.

I also want to acknowledge the non-permanent people for all the delicious cakes that we got to share before Covid-19, Fridays were awesome just because I knew we would have a cake at 16h30!. Thank you for all of the support and for making the days in the lab nicer, anything became more bearable with your presence! In particular I am very grateful with my office mates #217 Nour Daher and Hélène Tonnoir, cheering each other in bad and good days meant everything to me. Special mention to Laura, Ronan, Caro, Mariem, Mariana, Fenu and Jenny (and for sure many more!) for all of the moments and good memories shared together.

At Renault, I would like to thank Lucas Sannier for trusting in my candidature and to Pierre Tran-Van for taking me as PhD student when Lucas changed position in the company. The knowledge that you, Pierre, gave me is irreplaceable. Presentation after presentation I grew more. Also, thanks to all of the battery innovation team for their constant support and always pertinent comments.

Special mention and infinite thanks to my laboratory advisors Stéphane Laruelle and Sylvie Grugeon, for your patience and constant help all along this work. Today I realize how much

you made me grow. Always in the tough days, always in the good days. Thank you all for all of the support!

Outside of the laboratory, I would like to acknowledge Julio César, Adrián Pérez, Porfirio and Jaime Flores for the wonderful time we spent together visiting Europe. Wendy and Nicolás for the wonderful weekends together and my friends in Mexico Samantha Vázquez, Raquel Valencia, Andy Gómez, Nadia Morales, Lily, Xime, Ady,... for all of the time you have listened to me. For sure this work is also the result of our friend therapy <3.

Finally, this work is dedicated to my family, without them I wouldn't be where I am and what I have become. Mamá, papa, gracias por el esfuerzo e interés que siempre han puesto en mi educación y en mi futuro. Gracias por siempre creer en mí. Diana, gracias por estar conmigo, aunque en la distancia, siempre serás mi querida hermana. A la otra parte de mi familia y amor de mi vida, Alexis Maurel, por tu presencia constante y por siempre motivarme a dar más, a pesar de todo. Tú y tu familia me han dado tanto en estos últimos años, que mi gratitud no cabe en esta página. Esta tesis no hubiera sido lo mismo sin ti, la vida no sería lo mismo sin ti. GRACIAS.

Table of contents

General introduction	1
Chapter I: State of the art and context of the study	5
1. Rechargeable batteries for automotive applications.....	7
1.1. Generalities of batteries.....	7
1.1.1. Description of a battery.....	7
1.1.2. Characteristics to describe batteries.....	8
1.2. History of batteries in electric vehicles.....	9
1.3. Panorama of LIBs in the electric vehicle industry.....	12
2. Components of the lithium-ion batteries.....	16
2.1. Electrolyte.....	16
2.2. Separator.....	19
2.3. Binder, conducting agent and current collectors.....	19
2.4. The negative electrode.....	21
2.5. The positive electrode.....	25
2.5.1. Generalities of layered materials.....	26
2.5.2. Layered LCO, LNO and NCA.....	26
2.5.3. Layered NMC family.....	27
3. Limitations of Ni-rich NMC materials associated with its reactivity.....	31
3.1. Synthesis of stoichiometric NMC materials.....	31
3.2. Structural degradation from environment exposure.....	31
3.3. Structural degradation upon battery functioning.....	32
3.3.1. Oxygen production.....	32
3.3.2. Cation mixing and structural changes.....	34
3.3.3. Cation dissolution.....	35
3.3.4. Particle cracking.....	35
3.4. Electrolyte degradation associated to Ni-rich NMC materials.....	36
3.4.1. Degradation reactions.....	36
3.4.2. Methods for the detection of degradation products.....	38
4. Surface strategies to overcome the limitations of NMC materials.....	39
4.1. Surface coatings.....	39
4.1.1. Classic inorganic coatings.....	39
4.1.2. Coating originated from surface species.....	39
4.2. Electrolyte additives.....	40
5. Chapter conclusion and objectives of this thesis.....	43
6. References.....	45

Chapter II: Identification, quantification and formation mechanism of surface species in Ni-rich NMC materials	55
1. Introduction.....	57
2. Characterization of as-received Ni-rich NMC materials.....	62
2.1. As received Ni-rich NMC materials conditioning.....	62
2.2. As-received Ni-rich NMC materials characterization.....	62
3. Quantification of surface species in as-received NMC materials.....	67
3.1. Quantification of soluble bases through acid-base titration technique.....	67
3.1.1. Optimization of the acid-base titration protocol.....	67
3.1.2. Quantification of soluble bases in as-received materials through acid-base titration.....	74
3.2. Complementary quantification.....	74
3.2.1. Complementary analysis of filtrate solution through AAS.....	75
3.2.2. Complementary analysis of filtrate solution through ICP-AES.....	76
3.2.3. Complementary analysis of NMC materials through FTIR and SEM.....	77
3.3. Conclusion.....	79
4. Characterization of surface species in NMC materials exposed to specific atmospheres.....	81
4.1. Preliminary storage studies under Ar, CO ₂ , dry air and air atmospheres.....	81
4.2. Storage under specific H ₂ O/CO ₂ atmosphere.....	83
4.2.1. Acid-base titration quantification after H ₂ O/CO ₂ storage.....	83
4.2.2. Further investigations through SEM and FTIR.....	85
5. Deciphering the degradation mechanisms through thermal analysis.....	90
5.1. Thermal analysis of as-received NMC materials.....	90
5.2. Thermal analysis of exposed NMC materials.....	91
5.3. Proposed degradation mechanism.....	94
5.4. Attempts to characterize surface species in exposed NMC through Raman and XRD.....	97
6. Conclusion of the chapter.....	100
7. References.....	101

Chapter III: Chemical and electrochemical reactivity of surface species in Ni-rich NMC materials	105
1. Introduction.....	107
2. Reactivity of surface species toward electrolyte.....	108
2.1. Reactivity of reference compounds.....	108
2.2. Reactivity of as-received and exposed NMC materials.....	112
3. Reactivity of surface species under cycling.....	115
3.1. Electrochemical reactivity of powder references.....	115
3.2. Electrochemical reactivity of the Ni-rich NMC materials.....	117
3.2.1. Fabrication of the electrodes.....	117
3.2.2. Galvanostatic profiles of the as-received materials.....	120
3.2.3. Galvanostatic profiles of the exposed NMC 622C.....	123
3.2.4. Evaluation of the Li_2CO_3 consumption in exposed NMC 622C.....	125
3.3. Conclusion.....	126
4. Modification of the surface species by a heat treatment.....	128
4.1. As-received, washed, exposed and their analogs annealed NMC 622C films.....	129
4.2. Impact of heat treatment on as-received NMC 622C.....	131
4.3. Impact of heat treatment on washed NMC 622C.....	132
4.4. Impact of heat treatment on exposed NMC 622C.....	134
4.5. Conclusion.....	137
5. Conclusion of the chapter.....	138
6. References.....	139

Chapter IV: Gas evolution upon storage of batteries containing Ni-rich NMC materials	143
1. Introduction.....	145
1.1. Gas production mechanisms	145
1.1.1. Gas associated with the positive electrode	145
1.1.2. Gas associated with the negative electrode	148
1.2. Gas characterization techniques.....	149
1.3. Conclusion.....	150
2. Optimization of the instrumentation for gas quantification.....	151
2.1. Comparison of the available gas chromatography instruments	151
2.2. Choice of the column	152
2.2.1. Use of a capillary column with the GC/MS-IR equipment	153
2.2.2. Use of a capillary column in the GC/BID equipment.....	154
2.2.3. Use of a micropacked column with the GC/BID equipment.....	156
2.3. Conclusion.....	158
3. Gas evolution associated with the storage of Ni-rich NMC materials.....	159
3.1. Gas production from the storage of NMC with electrolyte	159
3.1.1. Powder storage	159
3.1.2. Film storage.....	163
3.2. Gas production from the storage of NMC/Graphite pouch cells	165
3.2.1. Optimization of the pouch cell format	166
3.2.2. Complete storage protocol of pouch cells	168
3.2.3. Gas production of the formation step.....	169
3.2.4. Gas production of NMC 811 with modified surface composition.....	171
3.2.5. Gas production of different NMC compositions	174
3.2.5.1. Discussion about gas of the formation step.....	176
3.2.5.2. Discussion about gas of the complete storage protocol	177
3.2.6. Impedance evolution after the complete storage protocol.....	181
3.2.6.1. Adaptation of the complete storage protocol.....	181
3.2.6.2. Impedance from pouch cells NMC 622C/Gr and 811/Gr	184
4. Conclusion of the chapter.....	188
5. References.....	189

Chapter V: Study of LiPO₂F₂ as electrolyte additive in batteries containing Ni-rich NMC materials	193
1. Introduction.....	195
2. Impact of LiPO₂F₂ on the electrolyte properties.....	198
3. Impact of LiPO₂F₂ on the electrochemical performance of NMC 622C and 811....	202
3.1. NMC 811 as positive electrode.....	202
3.1.1. Cycling performance of pouch cells NMC 811/Graphite at 25 and 55°C.....	202
3.1.2. Impact of the calendaring process.....	206
3.1.3. Post-mortem analyses.....	208
3.1. NMC 622C as positive electrode.....	211
3.2.1. Cycling performance of pouch cells NMC 622C/Graphite at 55°C.....	211
3.2.2. Post-mortem SEM analysis.....	211
4. Study of the electrolyte degradation products: impact of LiPO₂F₂.....	213
4.1. Study of interphases composition.....	213
4.1.1. Study of SEI composition.....	213
4.1.2. Study of CEI composition.....	216
4.2. Analysis of electrolyte degradation products.....	218
4.2.1. Analysis of electrolytes by “liquid” GC/MS.....	219
4.2.2. Analysis of electrolytes by ESI-HRMS.....	221
4.3. Analysis of gas released.....	224
4.4. Discussion and conclusion.....	228
5. Conclusion of the chapter.....	232
6. References.....	233
General conclusions and perspectives	237
Annexes	I
Table of abbreviations	XV
Résumé développé en Français	XVII

General introduction

Energy is needed in every aspect of daily life. According to an European Environment Agency report, in 2018, energy-related emissions in Europe accounted for nearly 80% of the total greenhouse gas emissions¹. These emissions are a matter of concern because they aggravate global warming.

In France, the transportation sector is the main contributor, out of which road transportation constitutes 27% of the total emissions². To alleviate the negative impact, this sector has intensified the development of greener alternatives, such as electric vehicles (EVs). In this regard, Group Renault has pioneered the manufacture of EVs since the commercialization of the ZOE[®] EV in 2012³. In France, at the beginning of 2020, the sales of EVs represented 8.2% of the market, a huge increase compared to 1.9% of the precedent year in the same period⁴. In parallel, the implementation of sources of renewable energy to power EVs (biofuels, hydraulic power, wind power and others) increased, constituting 17% of the total energy consumption in 2019⁵.

From upcoming EVs, consumers expect quicker charge, lower price and extended driving range. Consequently, improvements in the chemistry of the battery materials are required. To match with the driving range expectation, NMC materials ($\text{LiNi}_{1-x-y}\text{Mn}_x\text{Co}_y\text{O}_2$) of composition 111, 442 and 532, are already being used as active materials for the positive electrode. Nonetheless, the tendency is to achieve the utilization of Ni-rich NMC materials ($\text{Ni} > 0.5$), such as NMC 811, due to the interesting increase in energy density given by the nickel content.

There are significant limitations that impede wider utilization of Ni-rich NMC in batteries for the automotive industry. Indeed, when the NMC materials contain more nickel, they are prone to be more reactive toward the air right after synthesis, resulting in the formation of surface species⁶; and toward the electrolyte, due to the highly-reactive delithiated state of NMC materials⁷. Both result in a negative impact on the electrochemical performances and therefore need to be addressed.

In this context, the main objective of this work, treated throughout five chapters, is the understanding of the surface reactivity of Ni-rich NMC materials, with a focus on the reactions that generate gas upon thermal and cycling processes. In a first approach, an investigation of the composition and the quantification of surface species as function of the

nickel content is performed and followed by a study of their formation mechanism and their reactivity in battery conditions. Afterwards, the gaseous products from electrolyte degradation are investigated as function of the surface species content and of NMC composition. Lastly, a pertinent electrolyte additive is tested for the first time with Ni-rich NMC materials, in the hope of countering the reactivity toward the electrolyte and decrease gas production.

Chapter I: State of the art and context of the study.

This chapter consists of a literature review about rechargeable batteries for automotive applications and the advantages and limitations of Ni-rich NMC positive active materials. The discussed limitations are (i) the difficulty to synthesize stoichiometric materials, (ii) the surface structural degradation from environment exposure and (iii) the NMC materials structural degradation upon battery functioning. Its relationship to the declivity of the electrochemical performances is explained. Additionally, surface coatings and electrolyte additives are described as convenient strategies for the industry to counteract the limitations of these materials.

Chapter II: Identification, quantification and formation mechanism of surface species in Ni-rich NMC materials.

In the first instance, the characterization of five commercial Ni-rich NMC materials with $0.5 \leq \text{Ni} \leq 0.9$ and their native surface species are performed. To ensure the accurate quantification of the totality of surface species, a stepwise optimization of the protocols and methods is undertaken. With the aim of explaining the processes related to the reactivity of Ni-rich NMC materials toward air, the degradation is accelerated in specific controlled atmospheres, as function of nickel content. Interestingly, from the thermal analysis of the resulting surface species, a novel degradation mechanism is proposed.

Chapter III: Chemical and electrochemical reactivity of surface species in Ni-rich NMC materials.

The aim of this chapter is to evaluate the impact of surface species in battery conditions. To achieve this, their degradation products coming from storage at high temperature (chemical reactivity), or from cycling tests (electrochemical reactivity), are analyzed in electrolyte. Moreover, to investigate the role of different surface species contents on the electrochemical performance of a Ni-rich NMC material, modifications to the surface composition by washing, air-exposure and annealing procedures are performed.

Chapter IV: Gas evolution upon storage of batteries containing Ni-rich NMC materials.

In this chapter is studied the surface reactivity of NMC materials toward the electrolyte, through the analysis of gaseous products. First of all, part of this chapter is dedicated to the optimization of the instrumentation and the experimental methods for gas quantification, using two gas chromatography devices. Then, the gas production upon high-temperature storage of Ni-rich NMC materials in electrolyte is studied as function of states of charge and surface compositions. From these analyses, the production and consumption mechanisms of gases inside the battery are explored.

Chapter V: Study of LiPO₂F₂ as electrolyte additive in batteries containing Ni-rich NMC materials.

Being produced in batteries from surface species, in this chapter, lithium difluorophosphate (LiPO₂F₂) is evaluated as electrolyte additive. The literature agrees that it improves the cycling performances and decreases the gas production, although its action mechanism remains a controversial point. Therefore, in this last chapter, the effect of LiPO₂F₂ on physicochemical properties of the electrolyte and on electrochemical performances of complete cells is investigated through thorough analysis of the solid, liquid and gaseous electrolyte degradation products and of the NMC materials texture.

References

1. Total greenhouse gas emission trends and projections in Europe. <https://www.eea.europa.eu/data-and-maps/indicators/greenhouse-gas-emission-trends-6/assessment-3>, **2019**.
2. *Les émissions de gaz à effet de serre des transports*; <https://ree.developpement-durable.gouv.fr/>, **2019**.
3. Renault ZOE: quite simply revolutionary and yet a reality. <https://group.renault.com/en/news-on-air/news/renault-zoe-quietly-revolutionary-and-yet-a-reality/>, **2012**.
4. Peden, J.-P. La part de voitures électriques décolle (enfin) en janvier. <https://www.autoplus.fr/renault/zoe/voiture-electrique-les-ventes-atteignent-8-de-part-de-marche-en-janvier-2020-234029>, **2020**.
5. Chiffres clés des énergies renouvelables - Edition 2020. <https://www.statistiques.developpement-durable.gouv.fr/chiffres-cles-des-energies-renouvelables-edition-2020>.
6. Liu, H. S.; Zhang, Z. R.; Gong, Z. L.; Yang, Y., Origin of deterioration for LiNiO₂ cathode material during storage in air. *Electrochemical and Solid State Letters* **2004**, 7 (7), A190-A193.
7. Schipper, F.; Erickson, E. M.; Erk, C.; Shin, J. Y.; Chesneau, F. F.; Aurbach, D., Review-Recent Advances and Remaining Challenges for Lithium Ion Battery Cathodes. *Journal of the Electrochemical Society* **2017**, 164 (1), A6220-A6228.

CHAPTER I

State of the art and context of the study

1. Rechargeable batteries for automotive applications	7
1.1. Generalities of batteries	7
1.1.1. Description of a battery	7
1.1.2. Characteristics to describe batteries	8
1.2. History of batteries in electric vehicles	9
1.3. Panorama of LIBs in the electric vehicle industry	12
2. Components of the lithium-ion batteries	16
2.1. Electrolyte	16
2.2. Separator	19
2.3. Binder, conducting agent and current collectors	19
2.4. The negative electrode	21
2.5. The positive electrode	25
2.5.1. Generalities of layered materials	26
2.5.2. Layered LCO, LNO and NCA	26
2.5.3. Layered NMC family	27
3. Limitations of Ni-rich NMC materials associated with its reactivity	31
3.1. Synthesis of stoichiometric NMC materials	31
3.2. Structural degradation from environment exposure	31
3.3. Structural degradation upon battery functioning	32
3.3.1. Oxygen production	32
3.3.2. Cation mixing and structural changes	34
3.3.3. Cation dissolution	35
3.3.4. Particle cracking	35
3.4. Electrolyte degradation associated to Ni-rich NMC materials	36
3.4.1. Degradation reactions	36
3.4.2. Methods for the detection of degradation products	38
4. Surface strategies to overcome the limitations of NMC materials	39
4.1. Surface coatings	39
4.1.1. Classic inorganic coatings	39
4.1.2. Coating originated from surface species	39
4.2. Electrolyte additives	40
5. Chapter conclusion and objectives of this thesis	43
6. References	45

1. Rechargeable batteries for automotive applications

1.1. Generalities of batteries

1.1.1. Description of a battery

A battery is a system that converts chemical energy into electricity through electrochemical reactions. It is basically constituted of two electrodes, the energy-providing, an electrolyte, ensuring the ionic conduction within the cell, and a separator, preventing contact between electrodes. Since the discovery of the electrochemical principles by Alessandro Volta in 1799, the functioning principle is the following: during discharge, at the anode occurs an oxidation (or anodic reaction) and at the cathode a reduction (or cathodic reaction), while the charge compensation is achieved by the electron flow through the external circuit¹ (Fig. I.1). During the charge, this process is inverted: the anodic reaction takes place at the positive electrode and the cathodic reaction at the negative electrode. Henceforth, the negative electrode is referred as anode and the positive electrode as cathode in the discharged state.

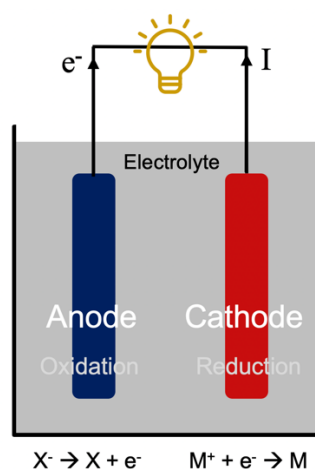


Figure I.1. Scheme of a battery during discharge. Based on Scrosati et al.¹.

Batteries can be classified in primary or secondary. In secondary batteries, the redox reaction is reversible, so the battery is rechargeable; whereas in primary batteries, the redox reaction will solely proceed spontaneously in the forward direction. Precisely the rechargeability of secondary batteries has allowed them to be widely used in numerous applications such as telephones, computers and electric vehicles.

1.1.2. Characteristics to describe batteries

Batteries can be defined by different characteristics¹⁻³, enlisted hereby.

- **Voltage.** In a battery, the nominal voltage (V_O) is the average voltage that the battery outputs during cycling, at the beginning of its cycle life. The open circuit voltage (OCV) corresponds to the voltage between the battery terminals when no load is applied.
- **Current.** The current (i) is the rate of electric charge flow.
- **C-rate.** It refers to the current applied to discharge the battery per unit of time (hours). For instance, a C-rate of $C/2$ means that the total capacity will be delivered in 2 hours.
- **Capacity.** The capacity (Q), measured in ampere-hour (Ah), is the total amount of charge delivered from a battery until it is completely discharged. The **theoretical capacity** of an electrode material, both negative and positive, can be calculated if the quantity (in mol) of exchanged electrons (n) and the molecular weight (M) of the designed materials are known (Eq. I.1). F is the Faraday constant ($96\,485\text{ C}\cdot\text{mol}^{-1}$). In theory, smaller molecular weight and more exchanged electrons in a material deliver higher capacity. It is measured using gravimetric specific capacity ($\text{Ah}\cdot\text{kg}^{-1}$, $\text{mAh}\cdot\text{g}^{-1}$).

$$Q = \frac{nF}{3.6 \cdot M} \quad [\text{I.1}]$$

- **Energy (E).** Energy is the product of the storage capacity by the average potential of the cell.

$$E = Q \cdot V_O \quad [\text{I.2}]$$

Energy density represents the amount of energy stored per unit mass or volume. Similar to battery capacity, it is measured in $\text{Wh}\cdot\text{kg}^{-1}$, $\text{mWh}\cdot\text{g}^{-1}$ or $\text{Wh}\cdot\text{L}^{-1}$, and $\text{mWh}\cdot\text{cm}^{-3}$.

- **Power (P).** The power is the product of current i and potential V_O (Eq. I.3). It measures the amount of current flowing at a given electric potential. Power is measured in Watts (W) and specific power in $\text{W}\cdot\text{kg}^{-1}$, $\text{mW}\cdot\text{g}^{-1}$. The **power density** of a battery refers to the energy that can be delivered per unit of time, measured in $\text{W}\cdot\text{L}^{-1}$ or $\text{mW}\cdot\text{cm}^{-3}$.

$$P = i \cdot V_O \quad [\text{I.3}]$$

- **State of charge (SOC).** The SOC represents the ratio between the available capacity and the total capacity (Eq. I.4). The units of SOC are percentage points.

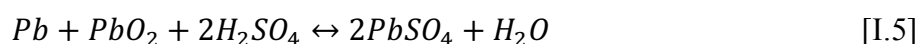
$$\text{SOC} = \left(\frac{Q_{\text{available}}}{Q_{\text{total}}} \right) (100) \quad [\text{I.4}]$$

- **State of health (SoH).** The SoH reflects the condition of a battery (or battery pack), compared to the battery in its original state. The units of SoH are percentage points. A battery's SoH is 100% at the time of manufacture and decreases over time.

- **Coulombic efficiency (CE).** It is the percentage ratio between discharge and charge capacities, given from one complete charge-discharge cycle.
- **Cycle life.** Cycle life corresponds to the number of charge and discharge cycles that a battery can complete before its capacity reaches a threshold that is dependent on the application. It depends on the structural stability of the electrode materials and the stability of the electrolyte and interphases during the charge/discharge process.

1.2. History of batteries in electric vehicles

Electric vehicles are older than we usually think. The concept of electric motor was first introduced by Michael Faraday in 1821 and was perfected from 1830s as a rotating electric motor by the physicists and inventors Ányos Jedlik, Moritz von Jacobi, Thomas Davenport, among others⁴. Initially, these motors were used in small machines but very quickly, they started to be noticeable as alternatives to horse-drawn carriages, thanks to the development of the lead-acid (Pb-acid) secondary battery by Gaston Planté in 1859 and the commercial distribution of electricity from 1880⁵. Around the 1890s, many entrepreneurs started marketing electric cars in major cities around the world, and by 1900, the number of electric cars outnumbered the gasoline cars by almost a factor of two, because they were less polluting, less noisy and did not require the rather dangerous and difficult to use hand crank starter⁶. These cars were powered by a rechargeable Pb-acid battery that exhibited low specific energy of 35–40 Wh.kg⁻¹ and were capable to drive 50–150 km on a single charge, with top speed of 35 km.h⁻¹ ⁶. A Pb-acid battery comprises a spongy lead plate as active material in the negative electrode and lead dioxide (PbO₂) as active material in the positive electrode. These plates are immersed in an electrolyte of sulfuric acid (H₂SO₄) and distilled water, and the energy is obtained from the reaction of H₂SO₄ with Pb and PbO₂ to produce lead sulfate (PbSO₄) and water³ (Eq. I.5):

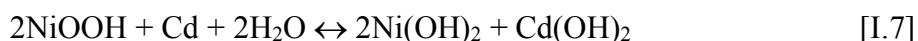


Owing to the limited infrastructure to charge an electric vehicle in comparison to the easy access to fuel containers to refuel ICE vehicles and the decreasing price of gasoline in the following years, ICE vehicles started to regain the market, so that from 1930, the electric vehicles were virtually inexistent. From then, electric vehicles were mainly used in the aeronautic and military fields⁵.

Years later, in the 1990s, concerns about the heavy contribution of the transportation sector to greenhouse emissions, the increasing price of fossil fuels and the commitment in the Kyoto Protocol to reduce CO₂ emissions⁷ intensified again the development of electric vehicles. Companies like Daimler-Chrysler, Ford, and General Motors initially used Pb-acid batteries, while Honda and Toyota used nickel metal-hydride (Ni-MH) batteries and Peugeot, Renault and Citroën nickel-cadmium batteries (Ni-Cd)⁸. A well-known electrified vehicle in the modern history of electric vehicles is the hybrid (HEV) Toyota Prius launched in 1997, powered with a Ni-MH battery pack with a capacity of 6.5 Ah. The Ni-MH battery was used as power source during acceleration and was recharged during the functioning of the vehicle in ICE-mode⁹. It exhibited specific energy between 50–70 Wh.kg⁻¹ and used nickel oxide hydroxide (NiOOH) as positive electrode and a hydrogen-absorbing alloy (MH) as negative electrode (Eq. I.6). The manufacturing, the size, as well as the low power density limited this type of battery for a generalized usage.



The Ni-Cd batteries have the same positive electrode than the Ni-MH battery and metallic cadmium is used as active material in the negative electrode producing cadmium hydroxide (Cd(OH)₂) during its oxidation (Eq. I.7). Through these reactions these batteries exhibited specific energy of around 40–60 Wh.kg⁻¹. Owing to the materials' price higher than Pb-acid and the toxicity and environmental hazard of cadmium, these batteries were not widely used¹⁰.



Around the same years, rechargeable lithium-ion batteries (LIBs) started heavy commercialization by Sony in 1991¹¹. Quickly, most of the companies implemented LIB technology in their electric vehicles¹². The LIBs are rechargeable devices composed of two lithium intercalation electrodes and an ionically conductor, electronically insulator porous separator soaked with non-aqueous electrolyte. The functioning principle is simple, LIBs are based in the lithium intercalation/deintercalation chemistry: during charge, lithium ions deintercalate from the positive electrode (LiMO₂ as example, where M = transition metals) and intercalate into the negative electrode (graphite as example), by migrating through the electrolyte (Eq. I.8 and I.9). Inversely, in the discharge process, lithium ions deintercalate

from the negative electrode and intercalate into the positive electrode. The electron flow through the external circuit between the negative and the positive electrode enables the conversion of chemical to electrochemical energy (Fig. I.2).

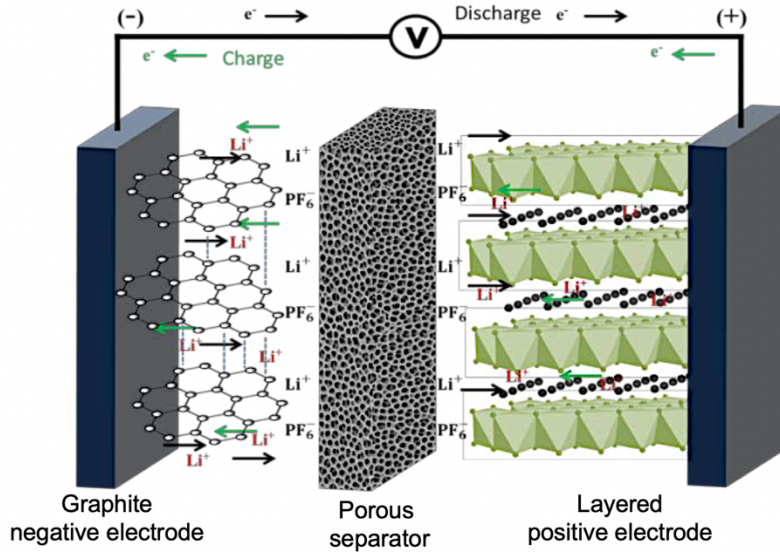
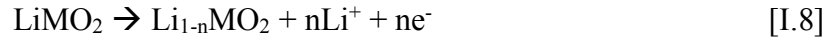


Figure I.2. Scheme of a LIB. Adapted from Abraham et al.¹³.

An alternative to LIBs is the lithium solid polymer batteries commercialized by Bolloré® in Autolib electric vehicles between 2011–2018¹⁴. It consisted in the use of LiFePO₄ at the positive electrode and metallic lithium at the negative electrode. The lithium ions flow through a solid polymer electrolyte (typically polyethylene oxide) in which a lithium salt is dissolved¹⁵. The necessity to keep the battery at high temperature (60–80°C) throughout the usage limits its application in the automotive industry.

With the aim of comparing the battery technologies explored during the development of electric vehicles, Fig. I.3 shows these batteries evaluated by size (volumetric density) and weight (energy density). Heavy and bulky Pb–acid and Ni–Cd are not anymore adapted for the requirements of modern electric vehicles, whereas Ni–MH batteries are still used in some HEV. On the contrary, considering its weight, size occupation and durability, rechargeable LIBs are the best candidates for automotive applications¹⁶.

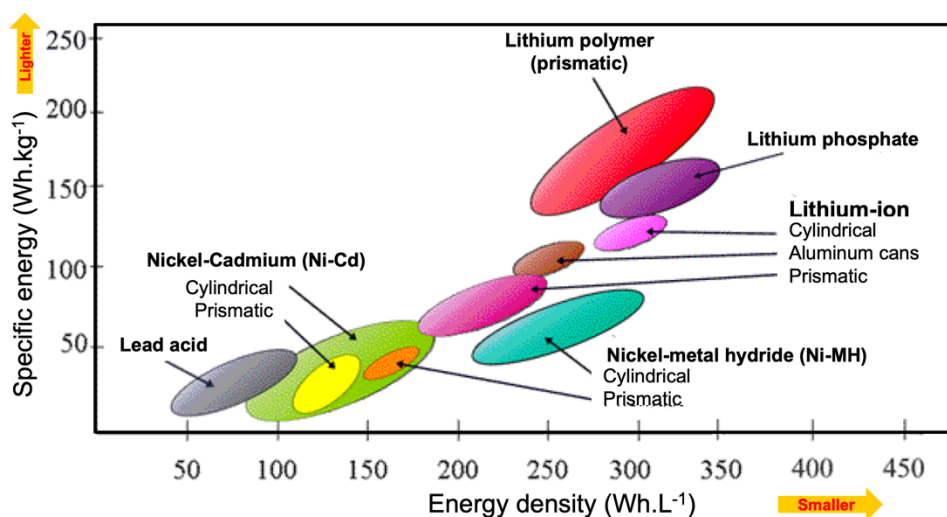


Figure I.3. Specific density vs. energy density in different batteries. Adapted from Scrosati et al.¹ and updated with references 17 and 21.

The commercial electric vehicles containing LIBs are classified in HEVs, plug-in hybrid electric vehicles (PHEVs) and full electric vehicles (EVs). Each one differs in the driving range, the charge manner and the use. In HEVs, the main energy source is gasoline, so low-energy batteries are enough. These vehicles are repeatedly charged and discharged on the road and thus do not need to be separately charged. PHEVs use a small combustion engine and an electric motor, with a small battery similar to the HEVs', although it gets charged externally and more energy density is needed to drive longer distance. Lastly, the EVs operate purely with an electric motor and an outer source of electricity that is stored in a battery pack with variable capacity and energy¹⁷. Their biggest advantage over PHEVs and HEVs is the driving range >100km within a single full charge and the zero-emission while driving.

The focus of this work is the study of LIBs for EVs applications within the framework of Renault's development plan, consequently, the Pb-acid, Ni-Cd and Ni-MH technologies will not be further discussed.

1.3. Panorama of LIBs in the electric vehicle industry

According to the International Energy Agency's (IEA) Global EV Outlook 2019¹⁸ report, in 2018, the EV fleet exceeded 5.1 million globally, from which 45% were in China, 24% in Europe and 22% in the United States; an amazing global increase of 63% in comparison to the previous year¹⁹ (Fig. I.4). In Norway, EVs represent 46% of the vehicles' market share, however globally the market share is still around 2.2%, mostly dominated by ICE vehicles,

number that is expected to grow globally up to 30% by 2030¹⁸. Among the reasons behind the actual low global market share, are the limitations of an EV compared to an ICE vehicle, such as the availability of charging stations, the driving range and the price.

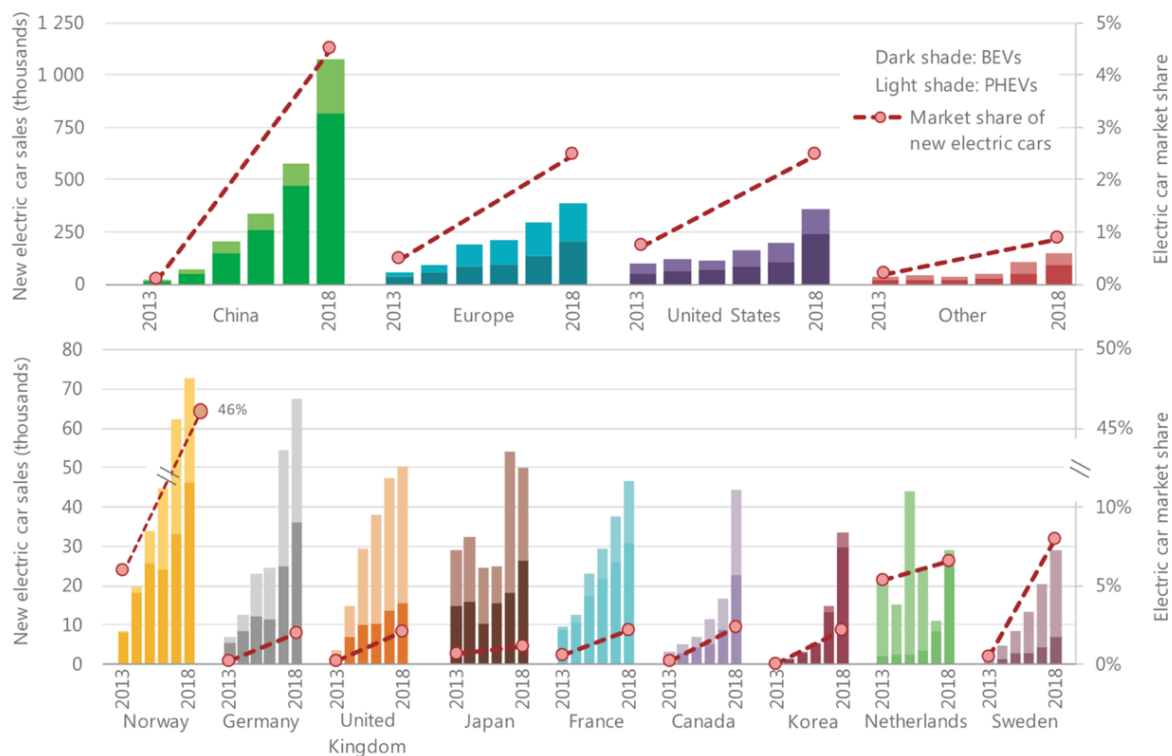


Figure I.4. Global EV market share and sales growth from 2013 to 2018. Taken from the Global EV Outlook 2019 report of the IEA¹⁸.

Concerning the price, Deloitte’s report of 2019 estimates that the market will reach a tipping point in 2022 when the cost to own an EV will be equivalent to an ICE vehicle²⁰. Part of the price drop will be due to the decrease of the battery pack price, the most expensive element in an EV. Two different predictions estimated the price per kWh to drop to \$62¹⁸ and \$95²¹ (Fig. I.5) in 2030, compared to ~\$175 in December 2019, as a result of a decrease of the prices of raw materials and manufacturing.

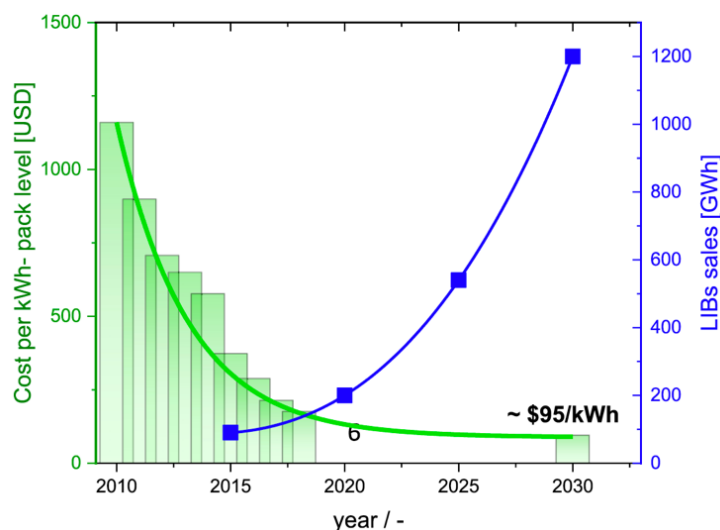


Figure I.5. Prediction of the price drop of LIBs per kWh. Taken from Marinaro et al.²¹.

Commercialization of EVs goes hand in hand with the requirements of the market: efficiency, safety, improved driving range and low-cost. Below, those are addressed, based on several sources^{1, 3, 6, 11, 18}.

- High energy density. In EVs, the energy density is translated as driving range. The existent LIB technologies for city vehicles are limited to a driving range around 400 km p¹², depending on the capacity of their battery, whereas the expectations of the market go above 600 km. For example, the Nissan Leaf[®] can reach 252 km with 40 kWh battery pack, the Volkswagen e-Golf[®] can reach 300 km with 26.5 kWh and the Renault Zoe[®] 400 km with 41 kWh. To achieve longer driving ranges, Andre et al.,²² predicts that the next generations of LIBs (2025) will require positive electrode materials with higher energy densities targeting at least 800 Wh.L⁻¹ and 300 Wh.kg⁻¹ at the cell level.
- Low price. Important characteristic to be competitive against ICE vehicles.
- Size and weight. A battery directed to the electric vehicle market, should be as light and as small as possible.
- Safety. Ensuring safety is particularly important for the constructors of EVs. In the battery, sources for safety concern are: the volatile and flammable solvents in the electrolyte, eventual electrical short circuit between the electrodes and thermal runaway²³⁻²⁵; to mention some.
- Long cycle life. Cycle life is an indicator of how long the battery can be used. The ideal cycle life of the battery for an EV is expected to exceed 15 years, compared to that of current portable devices, which span approximately five years³. Extreme operating conditions such as high/low temperature, deep discharge and repeated fast

charge/discharge, favor early degradation of the battery components and shortens cycle life.

Fig. I.6 summarizes the target values of some of these requirements at the cell level in 2015, and the targets in 2022 and 2025²². In 2025, safety and power are not expected to vary so much, but the cost is expected to significantly decrease. In terms of performance, the energy density, specific energy, power at low temperature are expected to increase, as well as the charging current, as faster charging is needed. Although detailed values vary with the strategies of each EVs constructor, this figure offers a general picture of the complexity associated with future challenges.

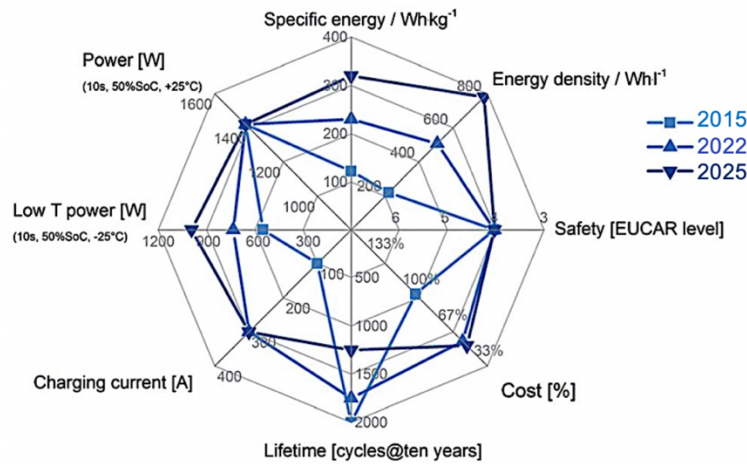


Figure I.6. Targets of LIBs characteristics at the cell level in 2015, 2022 and 2025. Taken from Andre et al.²².

2. Components of the lithium-ion batteries

One of the most crucial challenges for future LIBs is the energy density, which is tightly associated with the choice of electrodes and their compatibility with the rest of the battery components. To understand the synergy between components, each component is thoroughly described below.

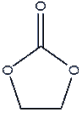
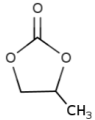
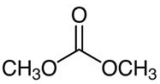
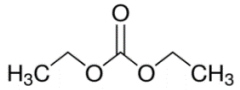
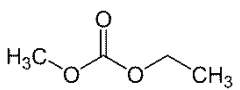
2.1. Electrolyte

The standard commercial non-aqueous electrolyte consists of a lithium salt dissolved in a mix of carbonate solvents and electrolyte additives. The basic requirements are the following^{11, 26, 27}:

- High ionic conductivity in a broad temperature range. The minimum required for lithium ions migration is 10^{-3} S.cm⁻¹ at room temperature.
- Low viscosity. Viscosity, measured in cP or Pascal-second (Pa·s), is inversely related to ionic conductivity, in a sense that high viscosity is translated as low ionic conductivity.
- Safety. Since most of the organic solvents are flammable, in the case of a leakage, solvents with high ignition point and low toxicity are preferred.
- Cost. The price is a key issue to be considered, since depending on the choice of salt, solvent and additives, the price can be very elevated. For a typical liquid electrolyte composition, the price is 6% of the total cost of a battery²⁸.

Regarding the requirements for the solvents, they are expected to present high dielectric constant (ϵ), that is translated in greater ionic dissociation and higher ionic conductivity; and good chemical and electrochemical stability toward the diverse metals and polymers in the system. The physicochemical properties of the most used organic solvents are illustrated in Table I.1. Each solvent presents advantages and disadvantages. For instance, the ϵ values that favor lithium dissociation are >20 , values that only cyclic carbonates EC and PC have. A peculiarity of EC is that it is solid at ambient temperature and requires a liquid solvent to dissolve. On the other hand, linear DMC, DEC and EMC, exhibit viscosity values lower than 1 cP, in comparison to 1.86 (at 40°C) and 2.53 of EC and PC, respectively.

Table I.1. Physicochemical properties of organic solvents for LIBs. Adapted from Park et al.¹¹.

Solvent	Molecular representation	T _m (°C)	T _b (°C)	Dielectric constant ϵ	Viscosity (cP)
Ethylene carbonate (EC)		39	248	89.6	1.86 (at 40°C)
Propylene carbonate (PC)		-49.2	241.7	64.4	2.53
Dimethyl carbonate (DMC)		0.5	90	3.11	0.59
Diethyl carbonate (DEC)		-43	126.8	2.81	0.75
Ethylmethyl carbonate (EMC)		-55	108	2.96	0.65

In order to meet the standards of dielectric constant, chemical/electrochemical stability and safety; in most of the commercial electrolytes a mixture of two or three solvents is used. Despite their high viscosity, cyclic carbonates are a must-have to increase the ionic conductivity. Additionally, EC allows the formation of high-quality solid electrolyte interphase (SEI) layer, required to prevent electrolyte degradation and graphite exfoliation along cycling²⁹. On the contrary, PC is used less often because of its tendency to exfoliate the graphite³⁰. Other important feature of electrolytes is the transference number, which is the fraction of the total electrical current carried in an electrolyte by a given ionic species¹¹. In LIBs, the ideal Li⁺ transference number is 1, however, in a typical LiPF₆-based electrolyte, the Li⁺ transference number is around 0.3.

Other component of the electrolyte is the lithium salt. Lithium salts usually comprise a large anion with delocalized charge to ensure good anion-cation dissociation in the solvents and to limit the ion-pair formation²⁸. The most studied for LIBs are lithium perchlorate (LiClO₄), lithium hexafluoroarsenate (LiAsF₆), lithium tetrafluoroborate (LiBF₄), lithium bis(trifluoromethanesulfonyl)imide (LiTFSI), lithium bis(fluorosulfonyl)imide (LiFSI) and lithium hexafluorophosphate (LiPF₆).

LiPF₆ is the industry's preferred choice owing to its high ionic conductivity in organic solvents (Table I.2), good electrochemical stability and its ability to protect the aluminum current collector from corrosion^{31, 32}. The other salts are not frequently used in EVs for several reasons: LiClO₄ presents safety issues arising from the oxidative environment during charging, however it is used in primary batteries²⁹; LiAsF₆²⁸ is very conductive and as such, does not present any environmental risk as its solvation shell stays intact in biological medium. However, its reduction products, as in SEI, are very toxic; LiBF₄ is not very conductive, and thus, can only be used in low-rate applications³³; LiTFSI allows severe aluminum corrosion near 3.6 V, due to the solubility of Al(TFSI)₃ in alkyl carbonate solvents³⁴; similarly, LiFSI presents aluminum corrosion problems below 4 V vs. Li/Li⁺³⁵, although it can be used in small quantities (< 0.33M) with LiPF₆ without facing corrosion up to 4.3 V vs. Li/Li⁺³⁶.

Table I.2. Ionic conductivity of electrolytes containing 1M LiPF₆. Taken from Park et al.¹¹.

Solvent mixture	Ionic conductivity at 25°C (mS.cm ⁻¹)
EC/DMC (50/50 vol%)	11.6
EC/EMC (50/50 vol%)	9.4
EC/DEC (50/50 vol%)	8.2

Nonetheless, LiPF₆ salt presents two main disadvantages:

(i) poor thermal stability above 55°C, decomposing into lithium fluoride (LiF) and phosphorus pentafluoride (PF₅) (Eq. I.10). Then, PF₅ is capable to react with the solvents to generate highly toxic chemicals³⁷ and promote solvents polymerization³⁸⁻⁴⁰.



(ii) the reaction between PF₅ and water traces produces toxic hydrofluoric acid (HF) and gaseous phosphoryl fluoride (POF₃)^{41, 42} (Eq. I.11):



The last components of the electrolyte are the electrolyte additives that are usually added in small quantities (<10 wt.%). Some additives act on the electrodes' interfaces to improve the quality of the SEI or to extend the electrochemical window²³. There are other additives that

improve electrolyte properties (wettability), stabilize LiPF_6 and enhance safety (overcharge protector, fire retardant) ⁴³.

2.2. Separator

The separator is a microporous membrane placed between the positive and negative electrode to prevent physical contact between the electrodes. The characteristics of a good separator are: electrochemically inactive, microporous enough to let solvated lithium ions flow, possesses good mechanical strength, high wettability and to be chemically stable toward the electrolyte components^{44, 45}. Commercial separators are most of the times made of microporous polyolefins such as polyethylene (PE), polypropylene (PP, Fig. I.7) and polyethylene terephthalate (PET). They exhibit pores of 0.03–1 mm large and 30–50% porosity¹.

The separators can be monolayer, multilayer and ceramic-coated to contribute to the safety of the battery. In the event of high temperatures caused by thermal runaway, the PE in a trilayer PP/PE/PP separator, melts around 140°C, shutting down the pores and interrupting ionic conduction^{46, 47}. Similarly, an alumina-coated separator provides thermal resistance and improves wettability due to the additional high surface area given by the alumina particles⁴⁸.

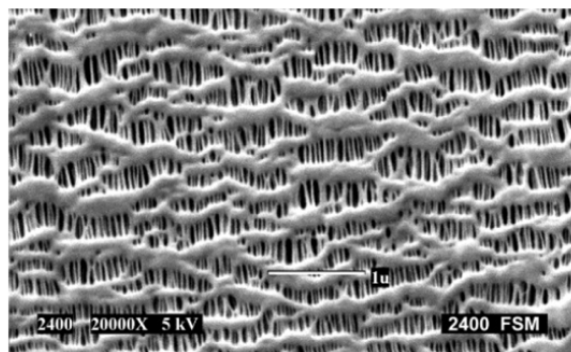


Figure I.7. Scanning electron microscope (SEM) image of a Celgard® PP separator. Taken from Yang et al.⁴⁹.

2.3. Binder, conducting agent and current collectors

In addition to the active materials, the binder, conducting agent and current collectors are the other constituents of the electrodes (Fig I.8). The electrodes are produced from the combination of the binder and conducting agent with the active material in a solvent, usually

N-methyl-2-pyrrolidone (NMP) or water. Then, this slurry is coated onto a foil of current collector that is heated to evaporate the solvent and obtain the finished electrode.

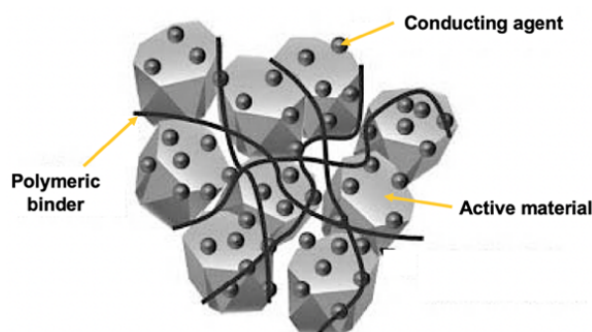


Figure I.8. Representation of electrode composition. Adapted from Park et al.¹¹.

The primary function of the binder is to keep the electrode's mechanical integrity and accommodate the volumetric expansion-contraction of active materials under successive lithium intercalation/deintercalation. In a negative electrode made of graphite, the structural expansion can reach 9.5% along the *c*-axis⁵⁰. Thermal, chemical and electrochemical resistance are the other relevant characteristics. Suitable polymers for binders are polyvinyl difluoride (PVdF), styrene-butadiene rubber (SBR), carboxy methyl cellulose (CMC) and polytetrafluoroethylene (PTFE)⁵¹ (Fig. I.9). For the positive electrode, PVdF remains the best option to maintain mechanical integrity⁵², using NMP as solvent. For the negative electrode a mixture of SBR/CMC is often preferred, using water as solvent. The mass-ratio of active materials and binder is usually in the range of 96:4 – 88:12¹¹.

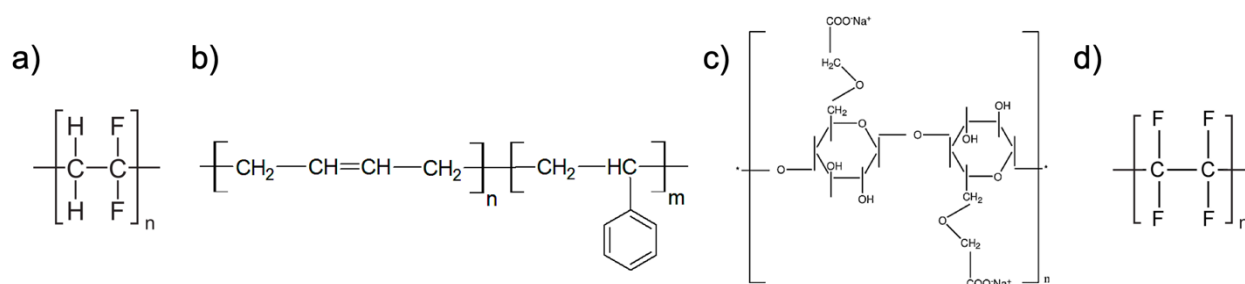


Figure I.9. Molecular representations of **a)** PVdF, **b)** SBR, **c)** CMC and **d)** PTFE.

A conducting agent is desired to help the electronic conduction across the electrodes. The characteristics of an ideal conducting agent are: high dispersibility, high surface area and good electronic conductivity⁵³. Carbon-based materials are the most commonly used, some examples are: carbon black, acetylene black and ketjen black. The difference between them is

the degree of graphitization and porosity, which is highly dependent on the supplier's synthesis, that ultimately defines the microstructure and the surface area¹¹.

Finally, the current collector is the intermediary passage of electrons from the active material to the external circuit, and inversely. The metals used as current collectors are selected as function of their electrochemical stability window and the typical thickness of the foils range between 6–20 μm . For the positive electrode, aluminum foils are used due to its low price, low weight and good electronic conductivity. Additionally, the use of LiPF_6 salt protects aluminum from corrosion, since a passivation layer of AlF_3 is formed from the native Al_2O_3 layer air-formed. If the negative electrode has a low-operating potential, like graphite, the aluminum current collector is not used, due to the Li-Al alloying process at low potentials ($\sim 0.33 \text{ V vs. Li/Li}^+$)⁵⁴. Instead, copper foils are used, since copper does not intercalate or alloy with lithium at low operating potentials, moreover it is a good electronic conductor.

2.4. The negative electrode

An ideal active material for the negative electrode in a LIB displays low operating potential, high specific capacity and presents no significant crystal structure change during lithium intercalation/deintercalation⁵⁵. To fulfill that, many different active materials have been tested in the literature: phosphides, lithium alloys, oxides, silicon-based, titanium-based and carbon-based materials, to mention some. Lithium itself, is very interesting as active material due to its low density of 0.534 g.cm^{-3} , high theoretical specific capacity of 3850 mAh.g^{-1} , and low electrode potential of $-3.04 \text{ V vs. (H}^+/\text{H}_2)$ ⁵⁶. However, lithium metal disadvantages are the price, durability and safety. Durability because it participates in side reactions with the LiPF_6 -based electrolyte that consume lithium ions, form thicker SEI and increase internal resistance; and safety due to dendrites growth and consequent short circuit risk. Alternatives such as lithium alloys with Si, Ge and Sn have been investigated⁵⁷. Despite the high discharge capacities from 500 to 4700 mAh.g^{-1} , they are limited by the large volume expansion–contraction that occurs during cycling, which in turn induces mechanical disintegration and early electrode failure⁵⁸. Similarly, conversion materials made of phosphides, nitrides, sulfides and oxides have been under heavy investigation to reduce the mechanical issues and the inherent poor kinetics of these materials^{59, 60}.

Graphite is generally the preferred choice in almost every LIB application. Graphite is composed of graphene conductive layers with carbon atoms of the sp^2 hybrid orbital layered along a hexagonal plane (Fig. I.10). Amongst its advantages, it presents good electronic conductivity due to the delocalized π electrons in-between graphene layers, the intercalation occurs at potentials below 0.25 V *vs.* Li/Li⁺ and it exhibits a theoretical specific capacity of 372 mAh.g⁻¹, by storing one Li⁺ per six carbon atoms (LiC₆) between its graphene layers¹¹ (Eq. I.12):

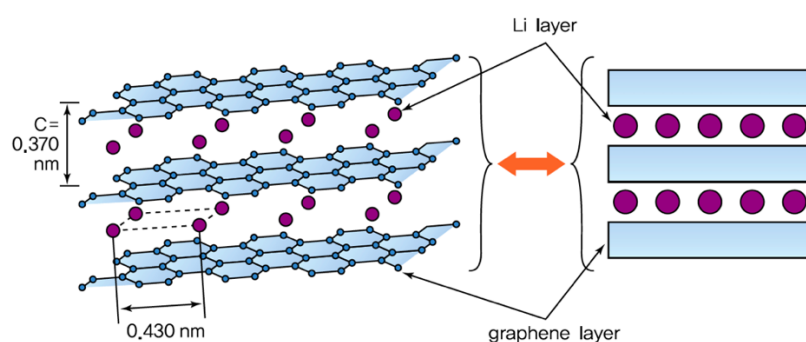


Figure I.10. Side view of lithiated graphene layers. Taken from Park et al.¹¹.

The intercalation of lithium into graphite when using a LiPF₆-based liquid electrolyte is in fact a gradual staging process, schematically represented in Fig. I.11. When there is a low concentration of lithium ions, a single lithium ion layer is randomly formed (stage III at ~210 mV *vs.* Li/Li⁺ sloping down to 150 mV *vs.* Li/Li⁺). Then, the other graphene layers are periodically arranged, and the concentration of lithium ions in graphite increases (stage II at ~140 mV *vs.* Li/Li⁺). In the composition LiC₆, with the highest amount of lithium intercalation, the layers of lithium ions and graphite are arranged one after another (stage I at ~90 mV *vs.* Li/Li⁺).

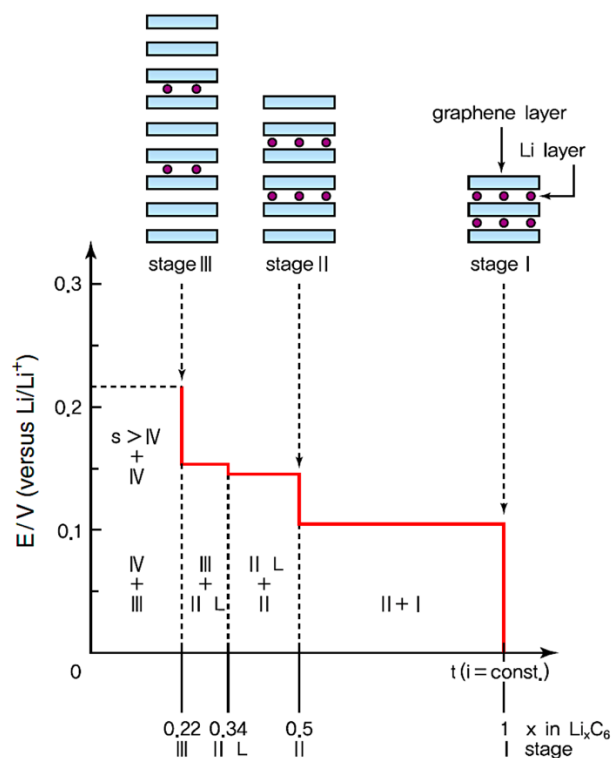


Figure I.11. Schematic galvanostatic curve and staging effects during lithium intercalation between graphene layers. Taken from Park et al.¹¹.

On the other hand, for high-energy applications, silicon can be added to graphite thus resulting in high electrode capacity and superior performance¹¹.

A notable characteristic of the graphite electrodes is the electrochemical decomposition of the alkyl carbonate-based electrolyte, that always occurs during the first charge/discharge cycles (called formation cycles), due to the electrochemical stability limits of the electrolyte. The deposit of solvent reduction products and decomposition products from LiPF_6 lead to the construction of the SEI, as illustrated in Fig. I.12. The SEI formation depends on many variables: the type of graphite, temperature, electrochemical conditions and the electrolyte composition. A good SEI film improves cycle life by preventing further electrolyte decomposition, allowing the facile diffusion of lithium ions, reducing the concentration polarization and preventing graphite exfoliation^{58, 61}. However, the presence of the SEI film increases the internal resistance and consumes part of the available lithium ions, leading to both power and capacity loss.

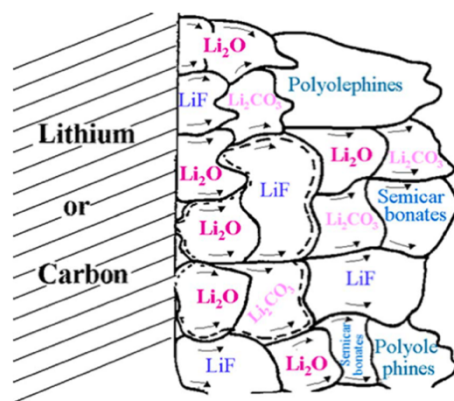


Figure I.12. Peled's schematic representation of the SEI arrangement⁶².

A commercial competitor to graphite is lithium titanium oxide, $\text{Li}_4\text{Ti}_5\text{O}_{12}$ (LTO). During discharge, LTO can intercalate up to three Li^+ in the octahedral vacant sites (Eq. I.13) and achieve 175 mAh.g^{-1} at a mean potential of $1.55 \text{ V vs. Li/Li}^+$ ⁶³.



The advantages of LTO are the negligible structural changes induced by lithium intercalation/deintercalation and the solvents stability at its operating potential. However, the lower electronic conductivity and specific capacity than graphite, in addition to its high operating potential, results in lower available energy for the battery. On the contrary, this material is suitable for power and durability applications⁶⁴⁻⁶⁶.

The above-mentioned negative electrode materials are schematically summarized in Fig. I.13.

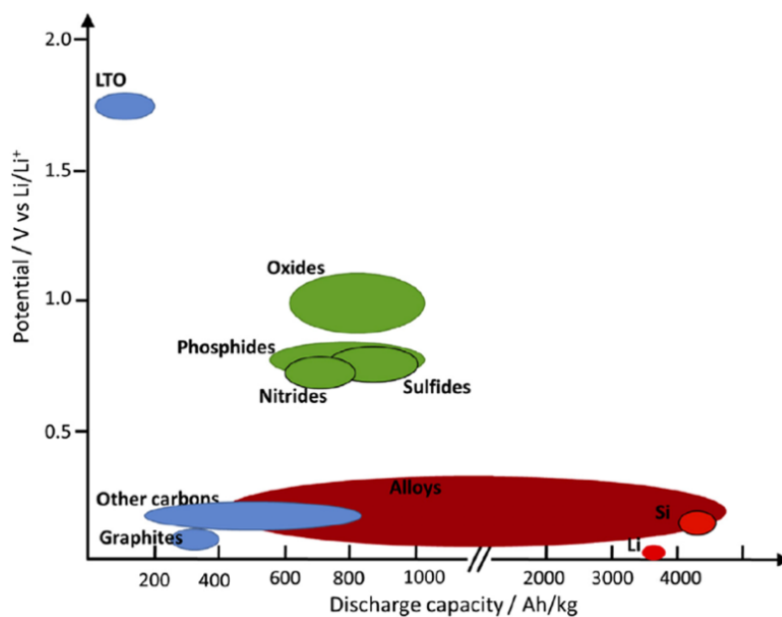


Figure I.13. Approximate range of average discharge capacity and potential of some of the most common active materials for the negative electrode. Taken from Chagnes et al.⁵⁶.

2.5. The positive electrode

Active materials for the positive electrode are commonly made of phosphates, oxides, or complex oxides of transition metals. The transition metals typically display four- or six-fold coordination with oxygen anions, anionic clusters, or ligands; and crystallize into a variety of structural arrangements. Independently of the composition, during discharge, the Li^+ ions intercalate into the material while an equal number of electrons enter the available d orbitals of the transition metal¹¹. Higher potential is expected from compounds with transition metals with more electrons in the d orbital, like nickel or cobalt, because the electrons are more attracted to the core of the atom and more energy is required to extract them⁵⁸.

The electrochemical properties are determined not only by the composition, but also by the structure of the materials, for instance, certain crystallographic orientations facilitate the entry of Li^+ more than others⁶⁷. For a variety of energy and power applications, along the years, many positive electrode materials with crystal structures of spinel⁶⁸, olivine^{69, 70} and layered^{71, 72}, have been proposed. This thesis focuses only the layered materials.

2.5.1. Generalities of layered materials

Layered materials are the most widely used active materials for the positive electrode, because they can meet the high energy density requirements, compared to spinel and olivine structures^{73, 74}. Layered materials present a crystal structure with $R\bar{3}m$ crystal group, where the transition metals occupy the octahedral positions in a face-centered cubic oxygen matrix and the layers of lithium atoms lie between the MO_2 layers ($M = Co, Ni, Mn, Al$), where diffusion of Li^+ ions takes place in two dimensions (Fig. I.14), following Eq. I.14:

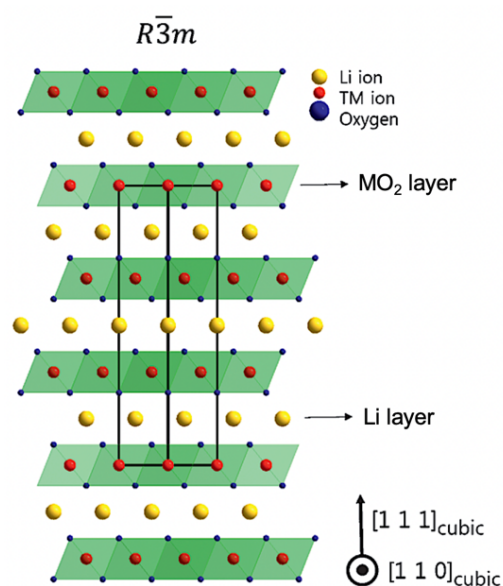
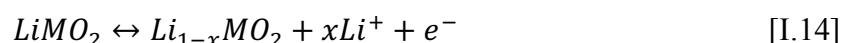


Figure I.14. Crystal structure of layered materials $LiMO_2$. TM stands for metals or transition metals. Adapted from Liu et al.⁷⁵.

Besides high energy density, another characteristic of layered materials is their reactivity at high delithiated states accompanied by oxygen production and the loss of the layered structure⁷⁶. This issue will be further developed in [Section 3.3.1](#).

2.5.2. Layered LCO, LNO and NCA

The oldest layered material still present in the market is the lithium cobalt oxide ($LiCoO_2$ or LCO). It was first introduced in 1976 by Mizushima et al.⁷¹ and heavily commercialized by Sony in the early 1990s¹¹. It presents high energy density, good capacity retention up to 4.3 V

vs. Li/Li^+ , high electric conductivity and good rate capability. Its theoretical capacity can reach 275 mAh.g^{-1} when fully delithiated, however, in practice only 0.5–0.7x in $\text{Li}_{1-x}\text{CoO}_2$ can be extracted, which corresponds to $140\text{--}180 \text{ mAh.g}^{-1}$ ⁷⁶. Due to the insufficient structural properties at high delithiated states⁷⁶, the high price of cobalt in comparison to other transition metals⁷⁷ and its doubtful supply chains^{78, 79}, LCO is not preferred for automotive applications, but is widely used in portable devices.

Alternatives to the use of cobalt emerged since the 90s, amongst them, the lithium nickel oxide (LiNiO_2 or LNO). LNO presents almost the same theoretical specific capacity than LCO, 275 mAh.g^{-1} , and is cheaper due to the natural abundance of nickel in the earth crust⁷⁷. Nonetheless, the synthesis of LNO with R-3m structure is rather difficult due to the non-stoichiometric cation ordering induced by the reduction of Ni^{3+} to Ni^{2+} and consequent migration of Ni^{2+} to Li^+ sites⁷⁴. Furthermore, during cycling, it presents the same structural instability at high delithiation states⁸⁰, phenomenon that is more critical when the nickel content is high^{73, 81}. For that reason, research efforts have been made to substitute part of the nickel by other transition metals, including Mg^{82, 83}, Ti^{84, 85}, Zn^{86, 87}, Fe⁸⁸, Co^{89, 90}, Mn^{91, 92} and Al^{93, 94}. Mn, Co and Al substitutions lead to two very stable layered forms: lithium nickel cobalt aluminum oxide ($\text{LiNi}_{0.8}\text{Co}_{0.15}\text{Al}_{0.05}\text{O}_2$ or NCA) and lithium nickel manganese cobalt oxide ($\text{LiNi}_{1-x-y}\text{Mn}_x\text{Co}_y\text{O}_2$ or NMC).

In NCA, the Al^{3+} atoms are electrochemically inactive but provide thermal stability to the compound, while the Co^{3+} atoms keep high discharge capacity⁹⁰. The NCA material possesses high theoretical capacity of 280 mAh.g^{-1} and in practice, it can reach up to 200 mAh.g^{-1} with cut-off voltage of 4.5 V vs. Li/Li^+ ⁹⁰. NCA material has found automotive application because it shows better thermal stability at high delithiated states than LCO⁹⁴, however the high cobalt price limited its use, so far, only in the Panasonic-based battery pack that powers Tesla[®] models⁹⁵.

2.5.3. Layered NMC family

The NMC materials are a family of lithiated oxides of Ni^{3+} , Ni^{2+} , Mn^{4+} and Co^{3+} . These materials are capable to overcome the thermal stability and cation dissolution issues seen in LCO and LNO, and decrease the price by tuning the cobalt content.

In NMC materials the average valence state of the transition metals is 3+. The electrochemically active redox pairs are Ni^{2+/3+}, Ni^{3+/4+} and Co^{3+/4+}, whereas the manganese atoms remain inactive but its presence improves the structural and thermal properties⁹⁶. The NMC compounds are named by the ratio of each transition metal, for instance, LiNi_{0.4}Mn_{0.3}Co_{0.3}O₂ is named NMC 433. Table I.3 shows a non-exhaustive list of other NMC compounds with their corresponding Ni, Mn and Co fractions.

Table I.3. Composition and name of NMC materials.

Composition	Fractional composition			Abbreviation
	Ni ³⁺	Ni ²⁺ , Mn ⁴⁺	Co ³⁺	
LiNi _{1/3} Mn _{1/3} Co _{1/3} O ₂	0	2/3	1/3	111
LiNi _{0.4} Mn _{0.3} Co _{0.3} O ₂	0.1	0.6	0.3	433
LiNi _{0.4} Mn _{0.4} Co _{0.2} O ₂	0	0.8	0.2	442
LiNi _{0.5} Mn _{0.3} Co _{0.2} O ₂	0.2	0.6	0.2	532
LiNi _{0.6} Mn _{0.2} Co _{0.2} O ₂	0.4	0.4	0.2	622
LiNi _{0.8} Mn _{0.1} Co _{0.1} O ₂	0.7	0.2	0.1	811

Fig. I.15. positions these NMC compositions in the ternary diagram LiCoO₂-LiMnO₂-LiNiO₂ for their facile identification, and mention some of the advantages (in green) and disadvantages (in red) of getting closer to each composition. For EVs applications, it is desired to have as low cobalt as possible due to the high price (34 \$/kg vs. 12-13 \$/kg for nickel and 2-3 \$/kg for manganese⁹⁷). Manganese is required because it retains the crystal structure and improves the thermal stability by minimizing the *c*-axis variation, since it is very stable at octahedral coordination in the MO₂ framework at the expenses, however, of the available energy because the manganese ions are electrochemically inactive⁹⁸. Nickel, meanwhile, is preferred in high amount so more energy density and decreased reversible capacity loss are obtained. Nevertheless, when the Ni³⁺ content is high, production of stoichiometric Li:Ni materials becomes more difficult (see [Section 3.1](#)), the stability in air decreases (see [Section 3.2](#)) and the structural stability is compromised⁹⁹. Considering the above, the nickel content is responsible for both the advantages and disadvantages of the NMC materials.

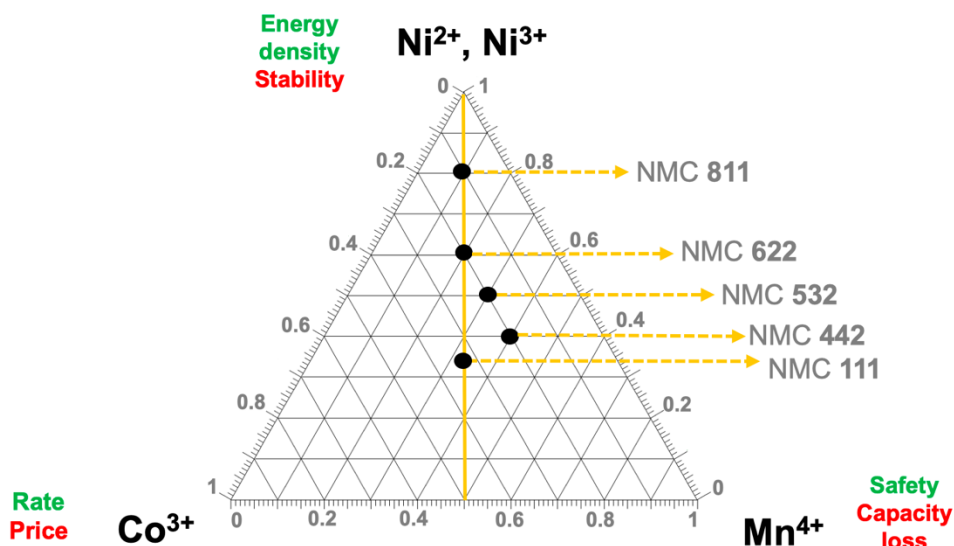


Figure I.15. Ternary phase diagram for the $\text{LiNi}_{1-x-y}\text{Mn}_x\text{Co}_y\text{O}_2$ materials with their main advantages and disadvantages shown in green and red colors, respectively. Adapted from Schipper et al.¹⁰⁰.

The specific discharge capacities of NMC materials range between 150 and 210 $\text{mAh}\cdot\text{g}^{-1}$ in a voltage window of 3–4.3V in half cell¹⁰¹, increasing with the increase of the Ni^{3+} content, although far from the theoretical capacity of 275 $\text{mAh}\cdot\text{g}^{-1}$ due to the reactivity of layered materials at high delithiation states. Fig. I.16 compares the capacity retention and discharge capacity of several NMC materials. It shows that the discharge capacities of NMC materials are improved when the Ni^{3+} content is increased, at the expenses of lower capacity retention. NMC 111, for instance, does not contain Ni^{3+} and presents reversible capacities of 150–160 $\text{mAh}\cdot\text{g}^{-1}$ between 3–4.3 V at 0.1C¹⁰², whilst NMC 811 with 0.7 Ni^{3+} can go as high as 205 $\text{mAh}\cdot\text{g}^{-1}$ in the same voltage window and C-rate¹⁰¹, meaning that more energy can be obtained without increasing the voltage window, just by modifying the content. However, the disadvantage of higher nickel content is a lower capacity retention due to the intrinsic limitations of NMC materials to extract the totality of lithium at high cut-off voltages (see [Section 3.3](#)).

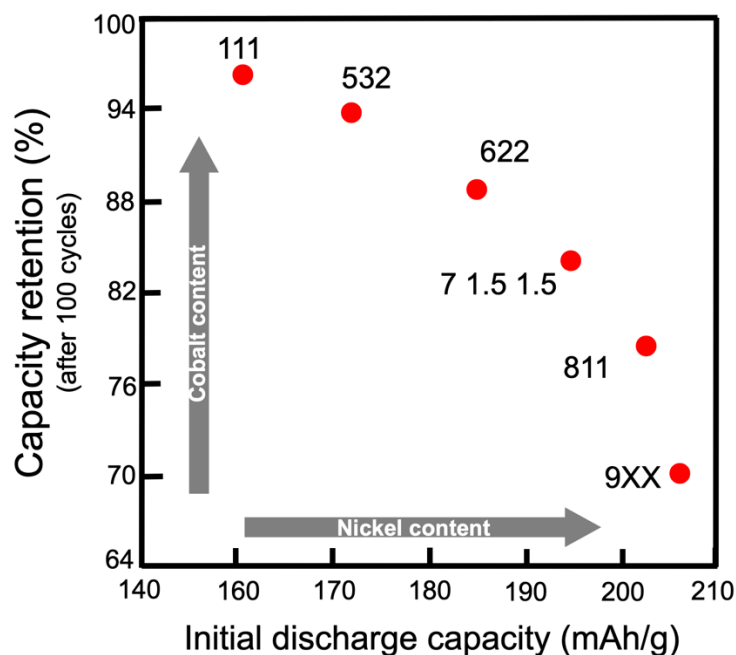


Figure I.16. Comparison of capacity retention and discharge capacity of several NMC materials in the voltage window 3–4.3V and 0.1 C, after 100 cycles. Adapted from Noh et al.¹⁰¹.

In EVs, blends of NMC with spinel LiMn_2O_4 , or layered LCO have already been tested^{22, 103}. They combine the high energy density of NMC with the high power of LiMn_2O_4 and the good capacity retention of LCO.

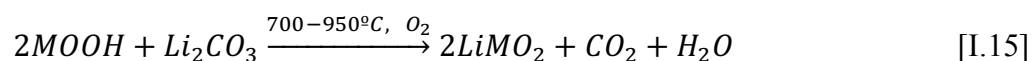
In conclusion, LCO yields good capacity and have good cycling behavior, however, the toxicity and price of cobalt makes it suitable for portable devices, but rather inconvenient for bigger applications. In an attempt to overcome these disadvantages, atomic substitutions in LCO with nickel and manganese lead to the production of LNO, NCA and NMC materials. Even if they are still limited by the reactivity at high delithiation states, NCA and NMC materials present various advantages that makes them suitable for EV applications. Particularly the NMC materials, in which the ratios of transition metals can be tuned to reach desired performances.

3. Limitations of Ni-rich NMC materials associated with its reactivity

3.1. Synthesis of stoichiometric NMC materials

For the synthesis of NMC materials, the lithium source, Li_2CO_3 or LiOH , is reacted with a mixture of transition metals, typically hydroxides ($\text{M}(\text{OH})_2$ or MOOH with $\text{M} = \text{Ni}, \text{Co}$ and Mn) (Eq. I.15 and I.16) ¹⁰⁴. The synthesis then takes place through a two-step heating procedure:

- (i) cooking step between 700–950°C under air or oxygen circulation and
- (ii) sintering step between 850–1000°C ¹⁰⁵.



In the industry, technical grade Li_2CO_3 is mostly the first choice because of its low price and its stability toward air atmosphere¹⁰⁶. An NMC 111, for instance, can be easily prepared under flowing air atmosphere and using Li_2CO_3 as lithium source¹⁰⁶. However, the synthesis of Ni-rich NMC (Nickel > 0.5) is prone to yield non-stoichiometric materials due to the Ni^{3+} reduction into Ni^{2+} and its migration (cation mixing) into the lithium sites¹⁰⁰. To counteract this, the temperature is decreased, pure oxygen atmosphere is employed and, very often, excess of the lithium precursor is used^{104, 107}. The problems is that lithium precursor traces can remain even after the sintering step, which can be very deleterious for the electrochemical performance ^{106, 108} (detailed in the following section).

3.2. Structural degradation from environment exposure

The degradation of NMC materials from environment exposure is rooted in the chemical reactivity toward H_2O and CO_2 , leading to the creation of surface species called soluble surface species^{100, 109} (Fig. I.17). The most reported are the soluble bases lithium carbonate (Li_2CO_3), lithium hydroxide (LiOH) and lithium hydrogenocarbonate (LiHCO_3) ^{97, 110-117}. The growth of soluble bases from environment exposure is not exclusive to NMC materials, but it is intrinsic of layered materials and especially aggravated in Ni-rich NMC due to the presence of Ni^{3+} ^{102, 112}. The consequences of the formation of soluble bases are lithium loss and

increase of the cell impedance due to the obstruction of lithium migration, which leads to early capacity fading^{113, 115, 118}, which will be addressed in [Chapter III](#). In addition, Li_2CO_3 can react chemically and electrochemically inside the battery, which causes battery swelling due to gas production (see [Chapter IV](#)). The elimination of soluble bases is extremely important for the industry, along the years several actions has been taken, for instance washing^{119, 120} and annealing processes prior use^{102, 116}.

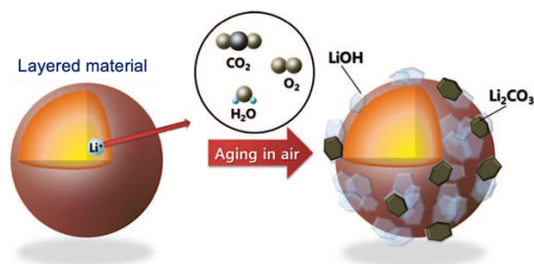


Figure I.17. Schematic representation of the degradation of layered materials in air. Taken from Cho et al.¹¹⁷.

3.3. Structural degradation upon battery functioning

During the operation of the battery, the NMC particles in the electrode are subject to degradation processes, that ultimately cause the deterioration of the electrochemical performance^{109, 121}. The origin is the structural instability and chemical reactivity at high delithiation degrees¹²¹. It consists in the production of oxygen as a consequence of nickel reduction, followed by cation migration of nickel to lithium sites, accompanied by the collapse of the layered structure to spinel and rock salt phases. In the following sections these steps are thoroughly described. At the same time that these surface processes occur, particle cracking may also take place from the surface to the bulk.

3.3.1. Oxygen production

The structural instability of NMC materials at high delithiation states (above 0.6 of extracted lithium) and subsequent oxygen production can be explained with their electronic diagram (Fig. I.18). In the fully lithiated state, the energy bands of the transition metal redox couples, e_g of $\text{Ni}^{3+/4+}$ and t_{2g} of $\text{Co}^{3+/4+}$, are located near the top of the O^{2-} $2p$ band, while $\text{Mn}^{3+/4+}$ lies well above all of them. When the material is delithiated and most of the nickel is Ni^{4+} , the Fermi levels e_g and t_{2g} lowers, overlapping the band $2p$ of oxygen O^{2-} . Consequently, electron transfer occurs from the oxygen to the Ni^{4+} , reducing it to a more stable oxidation state Ni^{3+}

and Ni^{2+} . In regards to the oxygen, due to the deficiency of lithium and the electron transfer to Ni^{4+} , the M-O bond covalency increases, decreasing the O^{2-} charge density and favoring oxidation of the oxygen anions from O^{2-} to a lower charge density. At the same time, the repulsive interactions among the negatively charged oxygen layers, increases the crystallographic parameter c and facilitates the oxygen release ¹²².

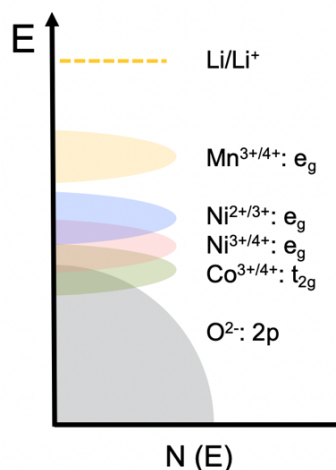


Figure I.18. Schematic illustration of the redox couples positions relative to the top $2p$ band of the oxygen in NMC materials. Adapted from Choi et al.¹²³.

This oxygen is not released as typical ground-state O_2 gas, which does not react with the electrolyte components, but instead, it is produced in a reactive form: the singlet (active) oxygen ($^1\text{O}_2$), a quantum state of oxygen where all electrons are spin paired (Fig. I.19). In terms of chemical reactivity, $^1\text{O}_2$ is far more reactive than triplet ground state O_2 . Interestingly, the production of $^1\text{O}_2$ was found to be related to nickel content in an NMC material, since the onset detection potential for gaseous products was found to be ~ 4.7 V vs. Li/Li^+ in NMC 622 and ~ 4.3 V in NMC 811 ¹²².

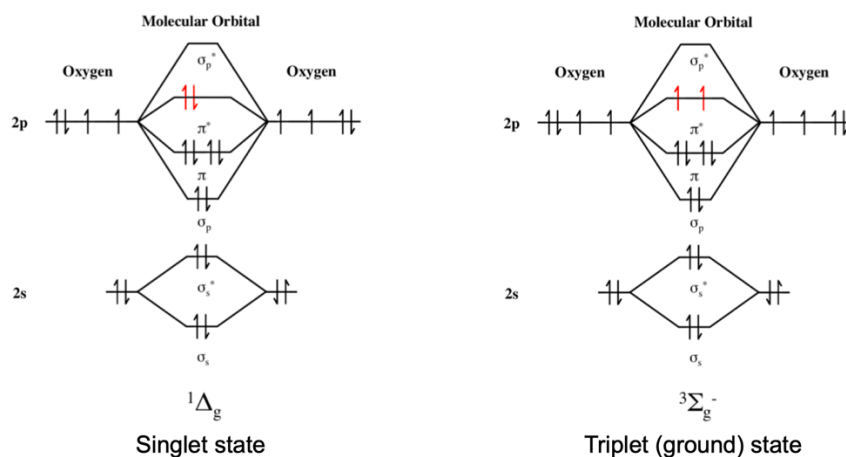


Figure I.19. Lewis representation of the singlet (active) and triplet state of oxygen.

3.3.2. Cation mixing and structural changes

Cation mixing is another consequence of NMC's structural instability, closely related to oxygen evolution. It arises from the migration of the transition metal ions, from the octahedral sites of the transition metal layer, to the octahedral vacant sites of the lithium octahedral layer via a neighboring tetrahedral site. It is facilitated by the increased M–O bond covalency at high delithiation states and the similar radius of Li^+ (0.76 Å) and Ni^{2+} (0.69 Å)^{72, 75, 124}. This cation mixing induces the layered structure collapse. Fig. I.20 represents schematically the phase transition of delithiated layered NMC (LiMO_2 in the figure) to spinel and rock salt phases. First, the nickel cations reduce and migrate to the tetrahedral sites, then, cobalt cations migrate as well, whereas manganese cations remain at its original octahedral sites. The oxygen release and the structural rearrangement caused by cation mixing has been supported in density functional theory (DFT) calculations^{123, 125}.

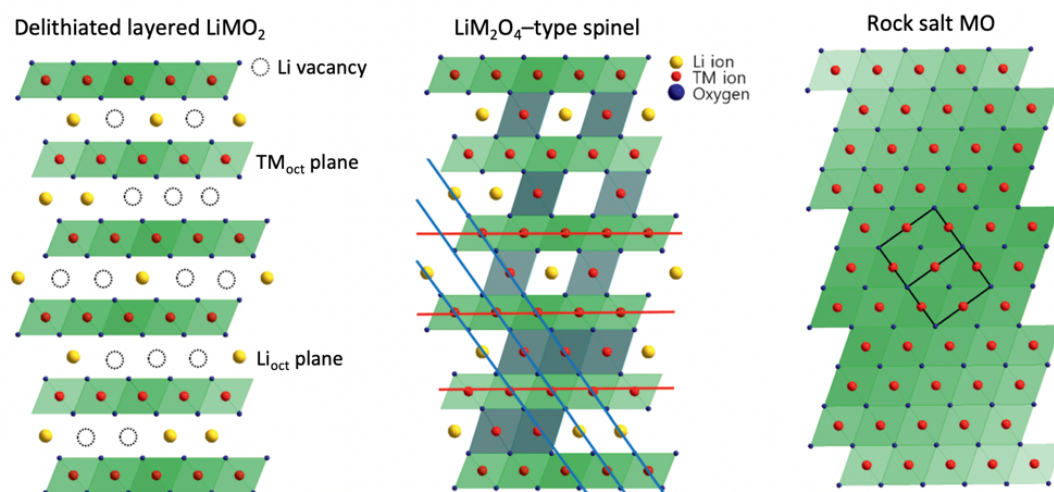


Figure I.20. Schematic representation for the phase transitions driven by cation migration.

Adapted from Liu et al.⁷⁵.

During the collapse of layered NMC to spinel and to rock salt phases, the bulk structure remains intact due to the limited diffusion length of oxygen anions in the primary particle¹²². In order to assess the transformation extent, high-resolution transmission electron microscopy (HRTEM) has been extensively used^{126, 127}. As example, Fig. I.21 shows NMC 532 surfaces cycled with different cut-off voltages, 4.5 V (a) and 4.8 V (b). It can be seen that the rock salt phase is favored when the cut-off voltage is higher and that the structural transformations does not exceed 30 nm¹²⁷.

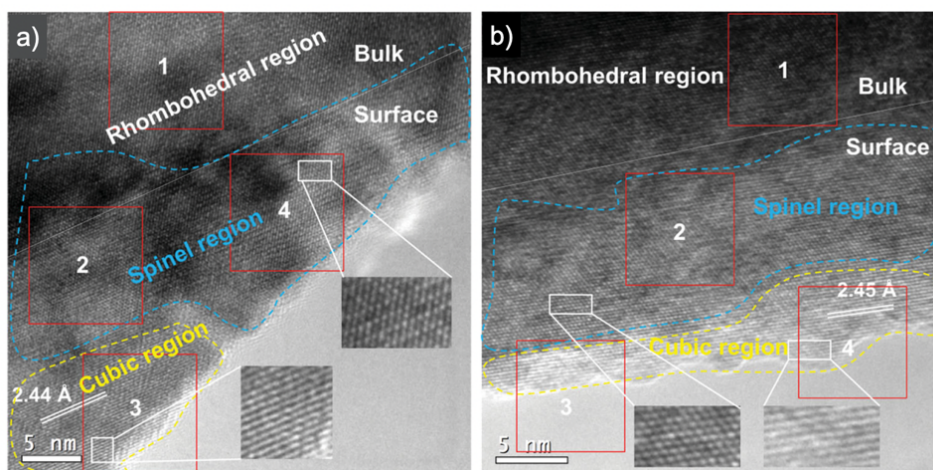


Figure I.21. HRTEM examples of phase transformations in NMC 532 particles after 50 cycles between 3–4.5 V **a)** and 3–4.8 V **b)**. Taken from Jung et al.¹²⁷.

3.3.3. Cation dissolution

Cation dissolution refers to the departure of transition metals from the layered structure. According to Kim et al.¹²⁸, the main cause for cation dissolution in Ni-rich materials is the acidic attack of HF. For Jung et al.¹²⁹, the dissolution is a consequence of aggressive cycling with cut-off voltage above 4.4 V vs. Li/Li⁺. Either way, dissolved metals migrate toward the negative electrode where they reduce and deposit, altering the SEI composition resulting in capacity fade and increase of the cell impedance^{129, 130}. Because the existence of vacancies is not thermodynamically tolerated, the structure collapses into other structural phases¹²⁸.

3.3.4. Particle cracking

Along with the reactivity of NMC at high delithiation degrees, Ni-rich NMC particles often exhibit severe cracking after extended cycling¹²⁸. Cracking results from the severe anisotropic volume changes in the structure of NMC that, in a greater extent, cause cracking of the particles¹³¹. Such morphological changes create fresh available surfaces for further surface degradation processes, thus increasing the chemical reactivity of the NMC materials with the electrolyte. Cracking has been proven to reach the bulk, as shown in Fig. I.22.

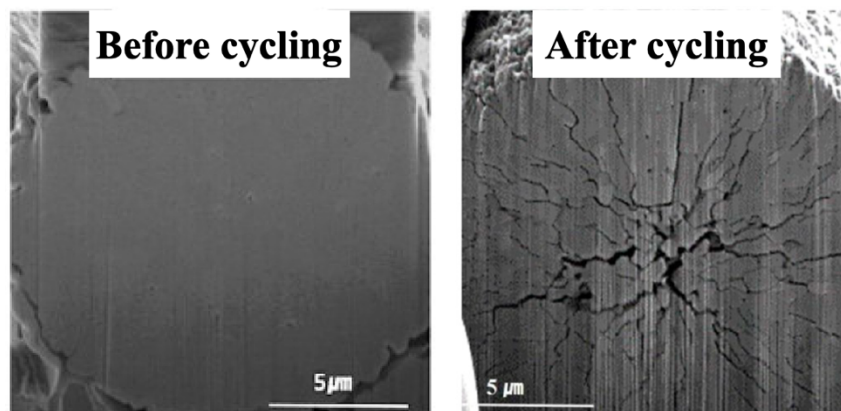


Figure I.22. TEM images of an NMC 622 particle before and after 150 cycles at 60 °C and 0.5C, between 3–4.45V vs. Li/Li⁺. Taken from Kim et al.¹³¹.

3.4. Electrolyte degradation associated with Ni-rich NMC materials

3.4.1. Degradation reactions

The electrolyte decomposition consists in a series of reactions whose products can get dissolved in the electrolyte, deposited in the surface of the electrodes or evolved as gas. This section deals with the degradation reactions linked exclusively to the positive electrode, other degradation reactions associated with the other components of the battery are addressed in [Chapter IV](#) and [V](#).

The electrolyte degradation related to NMC materials can be classified into:

- i. reactions with the surface species (Li₂CO₃ and LiOH),
- ii. reactions with the lattice oxygen and
- iii. potential-dependent reactions.

Regarding the reactions with the surface species, it has been reported that Li₂CO₃ may react with the hydrolysis products of LiPF₆¹³², with pure LiPF₆^{118, 133, 134} or with the carbonate solvents assisted by HF^{135, 136}, to produce a variety of degradation products. Nonetheless, none of these reactions has been proven to occur at the surface of an NMC material. On the other hand, hydroxide compounds have been reported to react with the hydrolysis products of LiPF₆ to produce fluorophosphate species, LiF, H₂O and CO₂^{40, 41} or directly with linear solvents into alkyl carbonates and ROH¹³⁶.

The degradation reactions induced by the oxidation reaction between active oxygen and the electrolyte components are directly related to the nickel content, as discussed before. The more nickel is contained in the material, the more $^1\text{O}_2$ can be produced. Once the reactive oxygen is produced, it either oxidizes the electrolyte solvents to produce gaseous species (CO_2 and CO) and water (see [Chapter IV](#)) or two $^1\text{O}_2$ molecules quench together to form two molecules of O_2 . In addition to reactions with the alkyl carbonate solvents, other reactions between $^1\text{O}_2$ and the electrolyte components have been reported to produce a series of degradation products, such as MF_n , LiF , $\text{Li}_x\text{PO}_y\text{F}_z$ and Li_2CO_3 ^{75, 125, 137}. The precipitation of these products onto the surface of NMC contributes to the formation of a cathode electrolyte interphase (CEI) (Fig. I.23)¹³⁸.

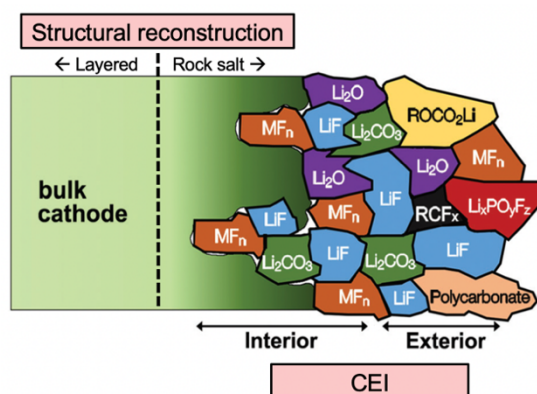


Figure I.23. Schematic representation of the species deposited as CEI and the structural reconstruction in the vicinity. Adapted from Li et al.¹³⁸.

Lastly, there are potential-dependent reactions, for instance, the electrochemical oxidation of surface species and solvents into CO_2 , CO and radical species. This occurs when the potential is increased beyond 4.2 V vs. Li/Li^+ , in order to obtain higher capacity from more extracted lithium.

In short, from the electrolyte degradation, three types of products are generated: gases, products dissolved in the electrolyte and products deposited in the SEI or CEI. Among them, gases are always produced from every degradation reaction; in fact, they are the most deleterious products in LIBs for EV applications because they provoke battery swelling and thus, safety and durability issues²³.

3.4.2. Methods for the detection of degradation products

For gaseous products the simplest method is to measure the expansion of a pouch cell^{139, 140}. It can be done through measuring the thickness increase or in a more accurate way, by immersion of the pouch cell into a viscous liquid and the use of the Archimedes' principle^{141, 142}. Whilst the volume measurement indicates the extent of gas production, this method is not capable to obtain information about composition. For identification and quantification, ex-situ gas chromatography coupled with mass spectrometry¹⁴³⁻¹⁴⁵ (GC/MS) and in-situ on-line electrochemical mass spectrometry^{122, 146-148} (OEMS) have been utilized.

For dissolved products, electrospray ionization-high-resolution mass spectrometry (ESI-HRMS), Raman spectroscopy¹⁴⁹ and liquid nuclear magnetic resonance spectroscopy^{39-41, 150} (NMR) are some of the most common techniques. For deposited products, thermal analysis techniques like differential scanning calorimetry (DSC)^{36, 40} and accelerating rate calorimetry^{76, 151} can be used. To study the interphase composition, Fourier Transform Infrared spectroscopy¹⁵² (FTIR) and X-ray photon spectroscopy (XPS) are commonly employed.

Usually, a combination of many of the aforementioned techniques is necessary to understand and propose a degradation mechanism. In this thesis, special attention is given to gas analysis by GC techniques, although other techniques such as NMR, FTIR and ESI-HRMS are employed.

4. Surface strategies to overcome the limitations of NMC materials

Many strategies have been proposed to overcome the NMC's reactivity issue. For the industry, the selected strategy relies on the easiness, efficacy and cost. The strategies can be classified in **surface or bulk**. **Bulk strategies** such as core-shell or gradient materials are rather complex and more expensive than the traditional synthesis of Ni-rich NMC. Therefore, this thesis focusses only on relevant **surface strategies**.

4.1. Surface coatings

The role of the coatings is to produce a surface passivating film that hinders electrolyte degradation reactions due to HF attack, NMC reactivity or extreme cycling conditions (high potential and low/high temperature), and at the same time, is permeable to lithium ions.

4.1.1. Classic inorganic coatings

Coatings from post-synthesis treatments have proven to be effective to improve the capacity retention, rate capability and reduce particle cracking without sacrificing the initial capacity^{131, 153}. They are constituted by electrochemically inactive materials and in general their formation is easy and cheap. A vast variety of materials have been tested: oxides¹⁵⁴⁻¹⁵⁶, phosphates¹⁵⁷ and fluorides^{158, 159}; to mention some. Among them, oxides have shown promising results to hinder NMC's reactivity. Myung et al.¹⁵⁴ studied the electrochemical performance of NMC 442 coated with several oxides: Al₂O₃, Nb₂O₅, Ta₂O₅, ZrO₂ and ZnO, from which Al₂O₃ (alumina) was found to deliver the best electrochemical performance.

4.1.2. Coating originated from surface species

A relatively simple way to create a coating is to cause the existent soluble bases, Li₂CO₃ and LiOH from synthesis or ambient exposure to react, to generate a surface film. Jo et al.¹⁶⁰ showed that the soluble bases in NMC 622 react in solution with phosphoric acid (H₃PO₄) and after solvent evaporation and annealing at 500°C, a lithium phosphate (Li₃PO₄) layer is produced (Fig. I.24). In addition to reduce the quantity of soluble bases, they claim that the Li₃PO₄ layer scavenges HF and water.

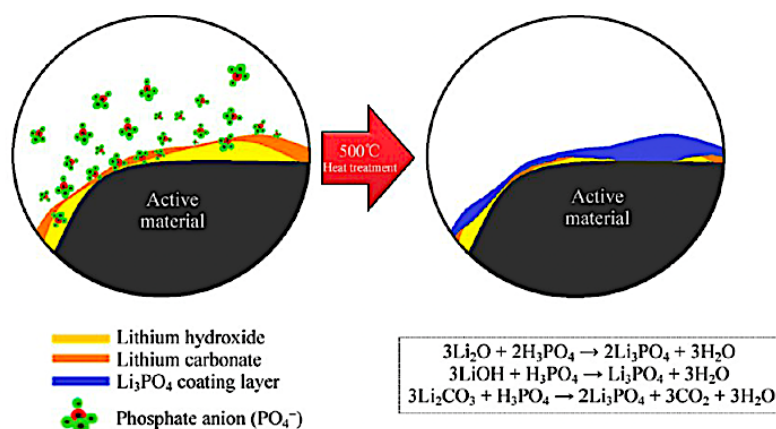


Figure I.24. Illustration of the reaction of SB with H₃PO₄ to form Li₃PO₄. Taken from Jo et al.¹⁶⁰.

Similarly, Kim et al. reacted Li₂CO₃ and LiOH with Co₃(PO₄)₂, at 700°C under air, to form an olivine Li_xCoPO₄ layer on the surface of NCA, and reported that the transition metal dissolution and structural changes were prevented¹⁶¹.

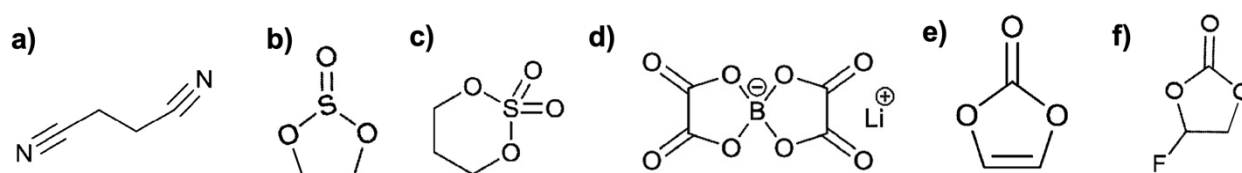
4.2. Electrolyte additives

An easy, relatively cheap and widely used alternative to overcome the reactivity of NMC materials is the incorporation of electrolyte additives²⁹. In the case of additives for the positive electrode, the objective is similar to that of the coatings: to form a CEI surface layer that limits the cation dissolution and the surface reactions at the electrode-electrolyte interface, whilst being permeable to lithium ions and electronically insulating¹⁶². A classical electrolyte additive decompose and precipitate during the formation cycles, forming a CEI of only few nanometers¹⁶³.

Examples of electrolyte additives are compounds that contain nitrile, sulfur or boron groups, and EC-derived. Some are briefly described in Table I.4 and their structures are shown in Fig. I.25.

Table I.4. Examples of electrolyte additives used in LIBs containing NMC as positive electrode.

Additive	Advantages	Disadvantages
Nitriles-containing Succinonitrile (SN)	Exceptional electrochemical and thermal stability due to the -CN group at high potentials ¹⁶⁴	Cell impedance increase ¹⁶⁵
Sulfur-containing Ethylene sulfite (ES). Trimethylene sulfite (TMS)	Increases battery lifetimes ¹⁶⁶ , decrease impedance growth ¹⁶⁷ and suppress gas production ¹⁶⁸	Electrolyte oxidative decomposition ¹⁶⁹
Boron-containing Lithium bis(oxalate)borate (LiBOB)	Formation of protective CEI films in high voltage LIBs ¹⁷⁰ . Stabilizes PF ₆ ⁻ anion and prevent PF ₅ formation ¹⁷¹	
Vinylene carbonate (VC)	Reduces at the surface of the negative electrode during the first charge ⁴³	Poly(VC) formed via oxidative decomposition of VC ¹⁷²
Fluoroethylene carbonate (FEC)	Improves the electrochemical performance of NMC by forming a thin CEI composed mainly of LiF ¹⁶⁹	

**Figure I.25.** Examples of electrolyte additives that have impacted positively the performance of LIBs containing NMC as positive electrode. **a)** SN, **b)** ES, **c)** TMS, **d)** LiBOB **e)** VC and **f)** FEC.

Based on many reports about the synergic effect of mixtures of additives¹⁷³, commercial electrolytes for EVs applications normally use a mixture of electrolyte additives. Regarding binary mixtures, ES and VC have been reported to decrease the cell impedance that ES causes on the positive electrode and VC in the negative electrode¹⁶²; the combination of trimethoxyboroxine (TMOBX) and VC, decreases the cell impedance caused by VC alone¹⁷⁴; and sulfate-containing additives are known to suppress gas production when combined with VC¹⁶⁷. Concerning ternary and quaternary associations, Dahn's group has tested several

additives mixtures, in the search for the best compromise between electrochemical performance and battery swelling^{167, 175, 176}.

Moreover, since traces of water are unavoidable elements of every electrolyte component, it has been proposed by several authors, that the organo-fluorophosphates products from the reaction between water and the electrolyte components can also be used as electrolyte additives^{177, 178}. One example is the lithium difluorophosphate (LiPO_2F_2)⁴¹, which has been used to improve cycling performance by enhancing the CEI layer¹⁷⁹ and decrease cell's impedance^{180, 181}, cation dissolution¹⁸² and structural transformations¹⁷⁹. The advantage is that the CEI is richer in fluorine and phosphorous atoms^{177, 178}.

Up to date, there is no miracle additive or mixture of additives that remedy the limitations of NMC materials, still, they remain as the easiest way to protect the NMC materials from degradation.

5. Chapter conclusion and objectives of this thesis

Due to the increasing concern about the greenhouse gases emitted by ICE cars and the shortage of fossil fuels, in the last years, the market of EVs has been gaining terrain. The constant improvement of the battery components has certainly been a key parameter for their success. Nonetheless, there are still big goals to be met in terms of safety, cycle life and driving range. In this regard, the comparison of several positive electrode materials, in conjunction with the enlisted requirements of the automotive industry, showed the relevance of layered materials for automotive applications, particularly, of the NMC materials.

EVs containing NMC materials are already being commercialized. The next milestone to gain in energy density is to use Ni-rich ($\text{Ni} > 0.5$) NMC materials. Nevertheless, numerous reports have shown that the properties of these materials are compromised due to their reactivity toward air exposure and toward the electrolyte in delithiated state. The former leads to the formation of surface species and the latter to oxygen release and structural transformations, particle cracking, cation dissolution; all linked to the presence of nickel.

Inevitably, at the same time, the electrolyte endures degradation into dissolved, deposited and gaseous species that affect directly the performance of the battery. Considering that gases are almost always produced from the degradation processes, it is particularly relevant for this project to study the degradation mechanisms leading to gaseous products and to look for ways to prevent their formation.

Among the proposed solutions to hinder the reactivity of NMC, the literature shows that surface modifications are effective and cheap strategies. Among them, coating and electrolyte additives stand out. Coatings have been created from surface species LiOH and Li_2CO_3 , however, they include a high-temperature reaction with more chemicals that most probably increases the cost and makes the industrial production harder. An easier option is the inorganic coatings made of oxides. Another approach rather practical is the use of electrolyte additives that promote the formation of a CEI. In this regard, so far, there is no single miraculous additive or mixture that solves the totality of the limitations of Ni-rich NMC materials, but instead, the choice depends on the electrolyte composition, the operating conditions and the nickel content.

In view of the reported limitations and solutions to the reactivity of Ni-rich NMC materials, this thesis intends to:

- Contribute to the understanding of the surface reactivity and degradation processes of Ni-rich NMC materials toward air through a stepwise study of surface species quantification, formation mechanisms and chemical/electrochemical reactivity.
- Understand the reaction mechanisms issued from the reactivity of lithiated or delithiated Ni-rich NMC that lead to gas production upon high-temperature storage.
- Propose solutions to the reactivity of Ni-rich NMC materials in terms of electrolyte additives.

6. References

1. Scrosati, B.; Abraham, K. M. v. S., Walter. Hassoun, Jusef., *Lithium batteries: advanced technologies and applications*. 2013; p 377.
2. Li, J.; Murphy, E.; Winnick, J.; Kohl, P. A., Studies on the cycle life of commercial lithium ion batteries during rapid charge-discharge cycling. *Journal of Power Sources* **2001**, *102* (1-2), 294-301.
3. Larminie, J.; Lowry, J., *Electric Vehicle Technology Explained*. John Wiley & Sons Ltd: 2003.
4. Handy, G. History of Electric Cars. <http://edisontechcenter.org/ElectricCars.html>.
5. U.S. Department Of Energy. Timeline: History of the Electric Car. <https://www.energy.gov/timeline/timeline-history-electric-car>.
6. Dhameja, S., *ELECTRIC VEHICLE BATTERY SYSTEMS*. Reed Elsevier group: 2002.
7. Kyoto Protocol to the United Nations Framework Convention on Climate Change. <http://unfccc.int/resource/docs/convkp/kpeng.html>.
8. Les batteries pour véhicules électriques: Les batteries Ni-Cd (nickel-cadmium). <http://www.avem.fr/?page=batterie&cat=technos&kind=nicd>.
9. History of the Toyota Prius. <https://blog.toyota.co.uk/history-toyota-prius>.
10. Laurent, A. The different types of electric car batteries. <https://easyelectriclife.groupe.renault.com/en/outlook/technology/technology-on-the-market-electric-car-battery/> (accessed May 2020).
11. Park, J.-K., *Principles and Applications of Lithium Secondary Batteries*. WILEY-VCH: 2012.
12. Safari, M., Battery electric vehicles: Looking behind to move forward. *Energy Policy* **2018**, *115*, 54-65.
13. Abraham, K. A. Exploding Hoverboards Explained (and other lithium-ion battery devices). <https://www.electrochem.org/exploding-hoverboards-explained>.
14. All charged up for sharing. <https://www.economist.com/business/2011/09/10/all-charged-up-for-sharing> (accessed May 2020).
15. Murata, K.; Izuchi, S.; Yoshihisa, Y., An overview of the research and development of solid polymer electrolyte batteries. *Electrochimica Acta* **2000**, *45* (8-9), 1501-1508.
16. Konarov, A.; Myung, S. T.; Sun, Y. K., Cathode Materials for Future Electric Vehicles and Energy Storage Systems. *Acs Energy Letters* **2017**, *2* (3), 703-708.
17. Chian, T. Y.; Wei, W. L. J.; Ze, E. L. M.; Ren, L. Z.; Ping, Y. E.; Abu Bakar, N. Z.; Faizal, M.; Sivakumar, S., A Review on Recent Progress of Batteries for Electric Vehicles. *International Journal of Applied Engineering Research*. **2019**, *14*, 4441-4461.
18. *Global EV Outlook 2019*; The International Energy Agency, May 2019.
19. Hertzke, P.; Müller, N.; Schaufuss, P.; Schenk, S.; Wu, T., Expanding electric-vehicle adoption despite early growing pains. August 2019.
20. *New market. New entrants. New challenges. Battery Electric Vehicles*; 2019.
21. Marinaro, M.; Bresser, D.; Beyer, E.; Fagur, P.; Hosoi, K.; Li, H.; Sakovica, J.; Amine, K.; Wohlfahrt-Mehrens, M.; Passerini, S., Bringing forward the development of battery cells for automotive applications: Perspective of R & D activities in China, Japan, the EU and the USA. *Journal of Power Sources*. **2020**, *459*.
22. Andre, D.; Kim, S. J.; Lamp, P.; Lux, S. F.; Maglia, F.; Paschos, O.; Stiaszny, B., Future generations of cathode materials: an automotive industry perspective. *Journal of Materials Chemistry A*. **2015**, *3* (13), 6709-6732.
23. Wen, J. W.; Yu, Y.; Chen, C. H., A Review on Lithium-Ion Batteries Safety Issues: Existing Problems and Possible Solutions. *Materials Express* **2012**, *2* (3), 197-212.
24. Feng, X. N.; Ouyang, M. G.; Liu, X.; Lu, L. G.; Xia, Y.; He, X. M., Thermal runaway mechanism of lithium ion battery for electric vehicles: A review. *Energy Storage Materials* **2018**, *10*, 246-267.
25. Geisbauer, C.; Wohrl, K.; Mittmann, C.; Schweiger, H. G., Review-Review of Safety Aspects of Calendar Aged Lithium Ion Batteries. *Journal of the Electrochemical Society* **2020**, *167* (9).
26. Goodenough, J. B.; Park, K. S., The Li-ion Rechargeable Battery: A Perspective. *Journal of the American Chemical Society* **2013**, *135* (4), 1167-1176.

27. Flamme, B.; Garcia, G. R.; Weil, M.; Haddad, M.; Phansavath, P.; Ratovelomanana-Vidal, V.; Chagnes, A., Guidelines to design organic electrolytes for lithium-ion batteries: environmental impact, physicochemical and electrochemical properties. *Green Chemistry* **2017**, *19* (8), 1828-1849.
28. Mauger, A.; Julien, C. M.; Paoletta, A.; Armand, M.; Zaghbi, K., A comprehensive review of lithium salts and beyond for rechargeable batteries: Progress and perspectives. *Materials Science & Engineering R-Reports* **2018**, *134*, 1-21.
29. Xu, K., Electrolytes and Interphases in Li-Ion Batteries and Beyond. *Chemical Reviews* **2014**, *114* (23), 11503-11618.
30. Chung, G. C.; Kim, H. J.; Yu, S. I.; Jun, S. H.; Choi, J. W.; Kim, M. H., Origin of graphite exfoliation - An investigation of the important role of solvent cointercalation. *Journal of the Electrochemical Society* **2000**, *147* (12), 4391-4398.
31. Stewart, S.; Newman, J., Measuring the salt activity coefficient in lithium-battery electrolytes. *Journal of the Electrochemical Society* **2008**, *155* (6), A458-A463.
32. Yang, H.; Zhuang, G. V.; Ross, P. N., Thermal stability of LiPF₆ salt and Li-ion battery electrolytes containing LiPF₆. *Journal of Power Sources* **2006**, *161* (1), 573-579.
33. Zhang, S. S.; Xu, K.; Jow, T. R., Study of LiBF₄ as an electrolyte salt for a Li-ion battery. *Journal of the Electrochemical Society* **2002**, *149* (5), A586-A590.
34. Krause, L. J.; Lamanna, W.; Summerfield, J.; Engle, M.; Korba, G.; Loch, R.; Atanasoski, R., Corrosion of aluminum at high voltages in non-aqueous electrolytes containing perfluoroalkylsulfonamide imides; new lithium salts for lithium-ion cells. *Journal of Power Sources* **1997**, *68* (2), 320-325.
35. Han, H. B.; Zhou, S. S.; Zhang, D. J.; Feng, S. W.; Li, L. F.; Liu, K.; Feng, W. F.; Nie, J.; Li, H.; Huang, X. J.; Armand, M.; Zhou, Z. B., Lithium bis(fluorosulfonyl)imide (LiFSI) as conducting salt for nonaqueous liquid electrolytes for lithium-ion batteries: Physicochemical and electrochemical properties. *Journal of Power Sources* **2011**, *196* (7), 3623-3632.
36. Forestier, C.; Grugeon, S.; Davoisne, C.; Lecocq, A.; Marlair, G.; Armand, M.; Sannier, L.; Laruelle, S., Graphite electrode thermal behavior and solid electrolyte interphase investigations: Role of state-of-the-art binders, carbonate additives and lithium bis(fluorosulfonyl)imide salt. *Journal of Power Sources* **2016**, *330*, 186-194.
37. Campion, C. L.; Li, W. T.; Euler, W. B.; Lucht, B. L.; Ravdel, B.; DiCarlo, J. F.; Gitzendanner, R.; Abraham, K. M., Suppression of toxic compounds produced in the decomposition of lithium-ion battery electrolytes. *Electrochemical and Solid State Letters* **2004**, *7* (7), A194-A197.
38. Tasaki, K.; Kanda, K.; Nakamura, S.; Ue, M., Decomposition of LiPF₆ and stability of PF₅ in Li-ion battery electrolytes - Density functional theory and molecular dynamics studies. *Journal of the Electrochemical Society* **2003**, *150* (12), A1628-A1636.
39. Campion, C. L.; Li, W. T.; Lucht, B. L., Thermal decomposition of LiPF₆-based electrolytes for lithium-ion batteries. *Journal of the Electrochemical Society* **2005**, *152* (12), A2327-A2334.
40. Ravdel, B.; Abraham, K. M.; Gitzendanner, R.; DiCarlo, J.; Lucht, B.; Campion, C., Thermal stability of lithium-ion battery electrolytes. *Journal of Power Sources* **2003**, *119*, 805-810.
41. Plakhotnyk, A. V.; Ernst, L.; Schmutzler, R., Hydrolysis in the system LiPF₆-propylene carbonate-dimethyl carbonate-H₂O. *Journal of Fluorine Chemistry* **2005**, *126* (1), 27-31.
42. Lux, S. F.; Lucas, I. T.; Pollak, E.; Passerini, S.; Winter, M.; Kostecki, R., The mechanism of HF formation in LiPF₆ based organic carbonate electrolytes. *Electrochemistry Communications* **2012**, *14* (1), 47-50.
43. Zhang, S. S., A review on electrolyte additives for lithium-ion batteries. *Journal of Power Sources* **2006**, *162* (2), 1379-1394.
44. Zhang, H.; Zhou, M. Y.; Lin, C. E.; Zhu, B. K., Progress in polymeric separators for lithium ion batteries. *Rsc Advances* **2015**, *5* (109), 89848-89860.
45. Deimede, V.; Elmasides, C., Separators for Lithium-Ion Batteries: A Review on the Production Processes and Recent Developments. *Energy Technology* **2015**, *3* (5), 453-468.
46. Venugopal, G.; Moore, J.; Howard, J.; Pendalwar, S., Characterization of microporous separators for lithium-ion batteries. *Journal of Power Sources* **1999**, *77* (1), 34-41.
47. Orendorff, C. J., The Role of Separators in Lithium-Ion Cell Safety. *Electrochem. Soc. Interface* **2012**, *21*, 61-65.

48. Choi, J. A.; Kim, S. H.; Kim, D. W., Enhancement of thermal stability and cycling performance in lithium-ion cells through the use of ceramic-coated separators. *Journal of Power Sources* **2010**, *195* (18), 6192-6196.
49. Yang, M.; Hou, J., Membranes in Lithium Ion Batteries. *Membranes* **2012**, (2), 367-383.
50. Li, Y.; Lu, Y. X.; Adelhelm, P.; Titirici, M. M.; Hu, Y. S., Intercalation chemistry of graphite: alkali metal ions and beyond. *Chemical Society Reviews* **2019**, *48* (17), 4655-4687.
51. Ji-Yong, E.; Lei, C., Effect of anode binders on low-temperature performance of automotive lithium-ion batteries. *Journal of Power Sources* **2019**, *441*.
52. Wang, M.; Hu, J. Z.; Wang, Y. K.; Cheng, Y. T., The Influence of Polyvinylidene Fluoride (PVDF) Binder Properties on $\text{LiNi}_{0.33}\text{Co}_{0.33}\text{Mn}_{0.33}\text{O}_2$ (NMC) Electrodes Made by a Dry-Powder-Coating Process. *Journal of the Electrochemical Society* **2019**, *166* (10), A2151-A2157.
53. Zhang, X. B.; Ma, J.; Chen, K. Z., Impact of Morphology of Conductive Agent and Anode Material on Lithium Storage Properties. *Nano-Micro Letters* **2015**, *7* (4), 360-367.
54. Myung, S. T.; Hitoshi, Y.; Sun, Y. K., Electrochemical behavior and passivation of current collectors in lithium-ion batteries. *Journal of Materials Chemistry* **2011**, *21* (27), 9891-9911.
55. Yoo, H. D.; Markevich, E.; Salitra, G.; Sharon, D.; Aurbach, D., On the challenge of developing advanced technologies for electrochemical energy storage and conversion. *Materials Today* **2014**, *17* (3), 110-121.
56. Chagnes, A.; Swiatowska, J., Lithium Process Chemistry. Resources, Extraction, Batteries, and Recycling. Elsevier Inc: 2015.
57. Zhang, W. J., A review of the electrochemical performance of alloy anodes for lithium-ion batteries. *Journal of Power Sources* **2011**, *196* (1), 13-24.
58. Liu, C. F.; Neale, Z. G.; Cao, G. Z., Understanding electrochemical potentials of cathode materials in rechargeable batteries. *Materials Today* **2016**, *19* (2), 109-123.
59. Poizot, P.; Laruelle, S.; Grugeon, S.; Dupont, L.; Tarascon, J. M., Nano-sized transition-metaloxides as negative-electrode materials for lithium-ion batteries. *Nature* **2000**, *407* (6803), 496-499.
60. Cabana, J.; Monconduit, L.; Larcher, D.; Palacin, M. R., Beyond Intercalation-Based Li-Ion Batteries: The State of the Art and Challenges of Electrode Materials Reacting Through Conversion Reactions. *Advanced Materials* **2010**, *22* (35), E170-E192.
61. An, S. J.; Li, J. L.; Daniel, C.; Mohanty, D.; Nagpure, S.; Wood, D. L., The state of understanding of the lithium-ion-battery graphite solid electrolyte interphase (SEI) and its relationship to formation cycling. *Carbon* **2016**, *105*, 52-76.
62. Peled, E.; Menkin, S., Review-SEI: Past, Present and Future. *Journal of the Electrochemical Society* **2017**, *164* (7), A1703-A1719.
63. Ohzuku, T.; Ueda, A.; Yamamoto, N., Zero-strain Insertion Material of $\text{Li}(\text{Li}_{1/3}\text{Ti}_{5/3})\text{O}_4$ for Rechargeable Lithium Cells. *Journal of the Electrochemical Society* **1995**, *142* (5), 1431-1435.
64. Takami, N.; Inagaki, H.; Tatebayashi, Y.; Saruwatari, H.; Honda, K.; Egusa, S., High-power and long-life lithium-ion batteries using lithium titanium oxide anode for automotive and stationary power applications. *Journal of Power Sources* **2013**, *244*, 469-475.
65. Wu, K.; Yang, J.; Zhang, Y.; Wang, C. Y.; Wang, D. Y., Investigation on $\text{Li}_4\text{Ti}_5\text{O}_{12}$ batteries developed for hybrid electric vehicle. *Journal of Applied Electrochemistry* **2012**, *42* (12), 989-995.
66. Yan, D. X.; Lu, L. G.; Li, Z.; Feng, X. N.; Ouyang, M. G.; Jiang, F. C., Durability comparison of four different types of high-power batteries in HEV and their degradation mechanism analysis. *Applied Energy* **2016**, *179*, 1123-1130.
67. Nitta, N.; Wu, F. X.; Lee, J. T.; Yushin, G., Li-ion battery materials: present and future. *Materials Today* **2015**, *18* (5), 252-264.
68. Toprakci, O.; Toprakci, H. A. K.; Ji, L. W.; Zhang, X. W., Fabrication and Electrochemical Characteristics of LiFePO_4 Powders for Lithium-Ion Batteries. *Kona Powder and Particle Journal* **2010**, (28), 50-73.
69. Padhi, A. K.; Nanjundaswamy, K. S.; Goodenough, J. B., Phospho-olivines as positive-electrode materials for rechargeable lithium batteries. *Journal of the Electrochemical Society* **1997**, *144*, 1188-1194.
70. Lindsay, D., Buses and batteries: a rising sector. In *Power Technology*, 2016.

71. Mizushima, K.; Jones, P. C.; Wiseman, P. J.; Goodenough, J. B., Li_xCoO_2 ($0 < x < 1$): A New Cathode Material For Batteries of High-Energy Density. *Materials Research Bulletin* **1980**, *15*, 783-789.
72. Dahn, J. R.; Vonsacken, U.; Juzkow, M. W.; Aljanaby, H., Rechargeable LiNiO_2 Carbon Cells. *Journal of the Electrochemical Society* **1991**, *138* (8), 2207-2211.
73. Myung, S. T.; Maglia, F.; Park, K. J.; Yoon, C. S.; Lamp, P.; Kim, S. J.; Sun, Y. K., Nickel-Rich Layered Cathode Materials for Automotive Lithium-Ion Batteries: Achievements and Perspectives. *Acs Energy Letters* **2017**, *2* (1), 196-223.
74. Daniel, C.; Mohanty, D.; Li, J. L.; Wood, D. L. In *Cathode Materials Review*, 1st International Freiberg Conference on Electrochemical Storage Materials, TU Bergakademie Freiberg, Freiberg, Germany, Jun 03-04; TU Bergakademie Freiberg, Freiberg, Germany, 2013; pp 26-43.
75. Liu, W.; Oh, P.; Liu, X.; Lee, M. J.; Cho, W.; Chae, S.; Kim, Y.; Cho, J., Nickel-Rich Layered Lithium Transition-Metal Oxide for High-Energy Lithium-Ion Batteries. *Angewandte Chemie-International Edition* **2015**, *54* (15), 4440-4457.
76. MacNeil, D. D.; Dahn, J. R., The reaction of charged cathodes with nonaqueous solvents and electrolytes - I. $\text{Li}_{0.5}\text{CoO}_2$. *Journal of the Electrochemical Society* **2001**, *148* (11), A1205-A1210.
77. Schmuck, R.; Wagner, R.; Horpel, G.; Placke, T.; Winter, M., Performance and cost of materials for lithium-based rechargeable automotive batteries. *Nature Energy* **2018**, *3* (4), 267-278.
78. Nkulu, C. B. L.; Casas, L.; Haufroid, V.; Saenen, N. D.; Kayembe-Kitenge, T.; Obadia, P. M.; Mukoma, D. K. W.; Ilunga, J. M. L.; Nawrot, T. S.; Numbi, O. L.; Smolders, E.; Nemery, B., Sustainability of artisanal mining of cobalt in DR Congo. *Nature Sustainability* **2018**, *1* (9), 495-504.
79. Olivetti, E. A.; Ceder, G.; Gaustad, G. G.; Fu, X. K., Lithium-Ion Battery Supply Chain Considerations: Analysis of Potential Bottlenecks in Critical Metals. *Joule* **2017**, *1* (2), 229-243.
80. Arai, H.; Okada, S.; Sakurai, Y.; Yamaki, J., Thermal behavior of $\text{Li}_{1-y}\text{NiO}_2$ and the decomposition mechanism. *Solid State Ionics* **1998**, *109* (3-4), 295-302.
81. Bianchini, M.; Roca-Ayats, M.; Hartmann, P.; Brezesinski, T.; Janek, J., There and Back Again-The Journey of LiNiO_2 as a Cathode Active Material. *Angewandte Chemie-International Edition* **2019**, *58* (31), 10434-10458.
82. Chowdari, B. V. R.; Rao, G. V. S.; Chow, S. Y., Cathodic behavior of (Co, Ti, Mg)-doped LiNiO_2 . *Solid State Ionics* **2001**, *140* (1-2), 55-62.
83. Kim, J.; Kim, B. H.; Baik, Y. H.; Chang, P. K.; Park, H. S.; Amine, K., Effect of (Al, Mg) substitution in LiNiO_2 electrode for lithium batteries. *Journal of Power Sources* **2006**, *158* (1), 641-645.
84. Kim, J.; Amine, K., The effect of tetravalent titanium substitution in $\text{LiNi}_{1-x}\text{Ti}_x\text{O}_2$ ($0.025 \leq x \leq 0.2$) system. *Electrochemistry Communications* **2001**, *3* (2), 52-55.
85. Ha, H. W.; Jeong, K. H.; Kim, K., Effect of titanium substitution in layered LiNiO_2 cathode material prepared by molten-salt synthesis. *Journal of Power Sources* **2006**, *161* (1), 606-611.
86. Kim, H. U.; Song, J. H.; Mumm, D. R.; Song, M. Y., Effects of Zn or Ti substitution for Ni on the electrochemical properties of LiNiO_2 . *Ceramics International* **2011**, *37* (3), 779-782.
87. Kwon, I. H.; Park, H. R.; Song, Y. Y., Effects of Zn, Al and Ti substitution on the electrochemical properties of LiNiO_2 synthesized by the combustion method. *Russian Journal of Electrochemistry* **2013**, *49* (3), 221-227.
88. Guo, X.; Greenbaum, S.; Ronci, F.; Scrosati, B., X-ray diffraction and Li-7 nuclear magnetic resonance studies of iron- and cobalt-substituted LiNiO_2 prepared from inorganic transition metal nitrates. *Solid State Ionics* **2004**, *168* (1-2), 37-49.
89. Chen, H. R.; Dawson, J. A.; Harding, J. H., Effects of cationic substitution on structural defects in layered cathode materials LiNiO_2 . *Journal of Materials Chemistry A* **2014**, *2* (21), 7988-7996.
90. Zhecheva, E.; Stoyanova, R., Stabilization of the Layered Crystal Structure of LiNiO_2 by Co-substitution. *Solid State Ionics* **1993**, *66* (1-2), 143-149.
91. Guilmard, M.; Croguennec, L.; Delmas, C., Effects of manganese substitution for nickel on the structural and electrochemical properties of LiNiO_2 . *Journal of the Electrochemical Society* **2003**, *150* (10), A1287-A1293.
92. Stoyanova, R.; Zhecheva, E.; Zarkova, L., Effect of Mn-Substitution for Co on the Crystal Structure and Acid Delithiation of $\text{LiMn}_y\text{Co}_{1-y}\text{O}_2$ Solid-Solutions. *Solid State Ionics* **1994**, *73* (3-4), 233-240.

93. Madhavi, S.; Rao, G. V. S.; Chowdari, B. V. R.; Li, S. F. Y., Effect of aluminium doping on cathodic behaviour of $\text{LiNi}_{0.7}\text{Co}_{0.3}\text{O}_2$. *Journal of Power Sources* **2001**, 93 (1-2), 156-162.
94. Lee, K. K.; Yoon, W. S.; Kim, K. B.; Lee, K. Y.; Hong, S. T., Characterization of $\text{LiNi}_{0.85}\text{Co}_{0.10}\text{M}_{0.05}\text{O}_2$ (M = Al, Fe) as a cathode material for lithium secondary batteries. *Journal of Power Sources* **2001**, 97-8, 308-312.
95. Panasonic and Tesla Reach Agreement to Expand Supply of Automotive-Grade Battery Cells. 2013.
96. Lu, Z. H.; MacNeil, D. D.; Dahn, J. R., Layered $\text{LiNi}_x\text{Co}_{1-2x}\text{Mn}_x\text{O}_2$ cathode materials for lithium-ion batteries. *Electrochemical and Solid State Letters* **2001**, 4 (12), A200-A203.
97. Paulsen, J. M.; Park, H. K.; Kwon, Y. H., Ni-based lithium transition metal oxide. Google Patents: 2010. US7648693 B2.
98. Ohzuku, T.; Makimura, Y., Layered lithium insertion material of $\text{LiNi}_{1/2}\text{Mn}_{1/2}\text{O}_2$: A possible alternative to LiCoO_2 for advanced lithium-ion batteries. *Chemistry Letters* **2001**, (8), 744-745.
99. Paulsen, J. M.; Park, H. K.; Kwon, Y. H. Process of making cathode material containing Ni-based lithium transition metal oxide. 2011. US 2009/0224201 A1.
100. Schipper, F.; Erickson, E. M.; Erk, C.; Shin, J. Y.; Chesneau, F. F.; Aurbach, D., Review-Recent Advances and Remaining Challenges for Lithium Ion Battery Cathodes. *Journal of the Electrochemical Society* **2017**, 164 (1), A6220-A6228.
101. Noh, H. J.; Youn, S.; Yoon, C. S.; Sun, Y. K., Comparison of the structural and electrochemical properties of layered $\text{LiNi}_x\text{Co}_y\text{Mn}_z\text{O}_2$ (x=1/3, 0.5, 0.6, 0.7, 0.8 and 0.85) cathode material for lithium-ion batteries. *Journal of Power Sources* **2013**, 233, 121-130.
102. Mijung, N.; Lee, Y.; Cho, J., Water adsorption and storage characteristics of optimized LiCoO_2 and $\text{LiNi}_{1/3}\text{Co}_{1/3}\text{Mn}_{1/3}\text{O}_2$ composite cathode material for Li-ion cells. *Journal of the Electrochemical Society* **2006**, 153 (5), A935-A940.
103. Croy, J. R.; Abouimrane, A.; Zhang, Z. C., Next-generation lithium-ion batteries: The promise of near-term advancements. *Mrs Bulletin* **2014**, 39 (5), 407-415.
104. Lee, K. K.; Kim, K. B., Electrochemical and structural characterization of $\text{LiNi}_{1-y}\text{Co}_y\text{O}_2$ (0 ≤ y ≤ 0.2) positive electrodes during initial cycling. *Journal of the Electrochemical Society* **2000**, 147 (5), 1709-1717.
105. Park, H.-K.; Shin, S. S.; Park, S. Y.; Shin, H. S.; Paulsen, J. M. Material for lithium secondary battery of high performance. 2010. WO/2007/129860.
106. Paulsen, J.; Kim, J. High nickel cathode material having low soluble base content. 2012. WO 2012/107313 A1.
107. Paulsen, J. K., Dae-Hyun. Sulfate containing rechargeable battery cathode with oxidized surface. 2015. WO 2015/128722 A1.
108. Ohzuku, T.; Ueda, A.; Nagayama, M., Electrochemistry and Structural Chemistry of LiNiO_2 (R-3m) for 4 Volt Secondary Lithium Cells. *Journal of the Electrochemical Society* **1993**, 140 (7), 1862-1870.
109. Lu, L. G.; Han, X. B.; Li, J. Q.; Hua, J. F.; Ouyang, M. G., A review on the key issues for lithium-ion battery management in electric vehicles. *Journal of Power Sources* **2013**, 226, 272-288.
110. Liu, H. S.; Zhang, Z. R.; Gong, Z. L.; Yang, Y., Origin of deterioration for LiNiO_2 cathode material during storage in air. *Electrochemical and Solid State Letters* **2004**, 7 (7), A190-A193.
111. Matsumoto, K.; Kuzuo, R.; Takeya, K.; Yamanaka, A., Effects of CO_2 in air on Li deintercalation from $\text{LiNi}_{1-x-y}\text{Co}_x\text{Al}_y\text{O}_2$. *Journal of Power Sources* **1999**, 81, 558-561.
112. Shizuka, K.; Kiyohara, C.; Shima, K.; Takeda, Y., Effect of CO_2 on layered $\text{Li}_{1+z}\text{Ni}_{1-x-y}\text{Co}_x\text{Mn}_y\text{O}_2$ (M = Al, Mn) cathode materials for lithium ion batteries. *Journal of Power Sources* **2007**, 166 (1), 233-238.
113. Zhuang, G. V.; Chen, G. Y.; Shim, J.; Song, X. Y.; Ross, P. N.; Richardson, T. J., Li_2CO_3 in $\text{LiNi}_{0.8}\text{Co}_{0.15}\text{Al}_{0.05}\text{O}_2$ cathodes and its effects on capacity and power. *Journal of Power Sources* **2004**, 134 (2), 293-297.
114. Li, J.; Zheng, J. M.; Yang, Y., Studies on storage characteristics of $\text{LiNi}_{0.4}\text{Co}_{0.2}\text{Mn}_{0.4}\text{O}_2$ as cathode materials in lithium-ion batteries. *Journal of the Electrochemical Society* **2007**, 154 (5), A427-A432.
115. Liu, H. S.; Yang, Y.; Zhang, J. J., Investigation and improvement on the storage property of $\text{LiNi}_{0.8}\text{Co}_{0.2}\text{O}_2$ as a cathode material for lithium-ion batteries. *Journal of Power Sources* **2006**, 162, 644-650.

116. Faenza, N. V.; Bruce, L.; Lebens-Higgins, Z. W.; Plitz, I.; Pereira, N.; Piper, L. F. J.; Amatucci, G. G., Growth of Ambient Induced Surface Impurity Species on Layered Positive Electrode Materials and Impact on Electrochemical Performance. *Journal of the Electrochemical Society* **2018**, *164* (14), A3727-A3741.
117. Cho, D. H.; Jo, C. H.; Cho, W.; Kim, Y. J.; Yashiro, H.; Sun, Y. K.; Myung, S. T., Effect of Residual Lithium Compounds on Layer Ni-Rich $\text{LiNi}_{0.7}\text{Mn}_{0.3}\text{O}_2$. *Journal of the Electrochemical Society* **2014**, *161* (6), A920-A926.
118. Bi, Y. J.; Wang, T.; Liu, M.; Du, R.; Yang, W. C.; Liu, Z. X.; Peng, Z.; Liu, Y.; Wang, D. Y.; Sun, X. L., Stability of Li_2CO_3 in cathode of lithium ion battery and its influence on electrochemical performance. *Rsc Advances* **2016**, *6* (23), 19233-19237.
119. Xu, S. G.; Wang, X. N.; Zhang, W. Y.; Xu, K. H.; Zhou, X. Y.; Zhang, Y. J.; Wang, H. B.; Zhao, J. Q., The effects of washing on $\text{LiNi}_{0.83}\text{Co}_{0.13}\text{Mn}_{0.04}\text{O}_2$ cathode materials. *Solid State Ionics* **2019**, *334*, 105-110.
120. Liu, W. M.; Qin, M. L.; Xu, L.; Yi, S.; Deng, J. Y.; Huang, Z. H., Washing effect on properties of $\text{LiNi}_{0.8}\text{Co}_{0.15}\text{Al}_{0.05}\text{O}_2$ cathode material by ethanol solvent. *Transactions of Nonferrous Metals Society of China* **2018**, *28* (8), 1626-1631.
121. Waldmann, T.; Iturrondobeitia, A.; Kasper, M.; Ghanbari, N.; Aguesse, F.; Bekaert, E.; Daniel, L.; Genies, S.; Gordon, I. J.; Loble, M. W.; De Vito, E.; Wohlfahrt-Mehrens, M., Review-Post-Mortem Analysis of Aged Lithium-Ion Batteries: Disassembly Methodology and Physico-Chemical Analysis Techniques. *Journal of the Electrochemical Society* **2016**, *163* (10), A2149-A2164.
122. Jung, R.; Metzger, M.; Maglia, F.; Stinner, C.; Gasteiger, H. A., Oxygen Release and Its Effect on the Cycling Stability of $\text{LiNi}_x\text{Mn}_y\text{Co}_z\text{O}_2$ (NMC) Cathode Materials for Li-Ion Batteries. *Journal of the Electrochemical Society* **2017**, *164* (7), A1361-A1377.
123. Choi, J.; Manthiram, A., Role of chemical and structural stabilities on the electrochemical properties of layered $\text{LiNi}_{1/3}\text{Mn}_{1/3}\text{Co}_{1/3}\text{O}_2$ cathodes. *Journal of the Electrochemical Society* **2005**, *152* (9), A1714-A1718.
124. Chebiam, R. V.; Prado, F.; Manthiram, A., Structural instability of delithiated $\text{Li}_{1-x}\text{Ni}_{1-y}\text{Co}_y\text{O}_2$ cathodes. *Journal of the Electrochemical Society* **2001**, *148* (1), A49-A53.
125. Yu, Y.; Karayaylali, P.; Katayama, Y.; Giordano, L.; Gauthier, M.; Maglia, F.; Jung, R.; Lund, I.; Shao-Horn, Y., Coupled LiPF_6 Decomposition and Carbonate Dehydrogenation Enhanced by Highly Covalent Metal Oxides in High-Energy Li-Ion Batteries. *Journal of Physical Chemistry C* **2018**, *122* (48), 27368-27382.
126. Lin, F.; Markus, I. M.; Nordlund, D.; Weng, T. C.; Asta, M. D.; Xin, H. L. L.; Doeff, M. M., Surface reconstruction and chemical evolution of stoichiometric layered cathode materials for lithium-ion batteries. *Nature Communications* **2014**, *5*.
127. Jung, S. K.; Gwon, H.; Hong, J.; Park, K. Y.; Seo, D. H.; Kim, H.; Hyun, J.; Yang, W.; Kang, K., Understanding the Degradation Mechanisms of $\text{LiNi}_{0.5}\text{Co}_{0.2}\text{Mn}_{0.3}\text{O}_2$ Cathode Material in Lithium Ion Batteries. *Advanced Energy Materials* **2014**, *4* (1).
128. Kim, J.; Cha, H.; Lee, H.; Oh, P.; Cho, J., Surface and Interfacial Chemistry in the Nickel-Rich Cathode Materials. *Batteries & Supercaps* **2020**, *3* (4), 309-322.
129. Jung, R.; Linsenmann, F.; Thomas, R.; Wandt, J.; Solchenbach, S.; Maglia, F.; Stinner, C.; Tromp, M.; Gasteiger, H. A., Nickel, Manganese, and Cobalt Dissolution from Ni-Rich NMC and Their Effects on NMC622-Graphite Cell. *Journal of the Electrochemical Society* **2019**, *166* (2), A378-A389.
130. Jimenez-Gordon, I. A.; Grugeon, S.; Takenouti, H.; Tribollet, B.; Armand, M.; Davoisne, C.; Debart, A.; Laruelle, S., Electrochemical Impedance Spectroscopy response study of a commercial graphite-based negative electrode for Li-ion batteries as function of the cell state of charge and ageing. *Electrochimica Acta* **2017**, *223*, 63-73.
131. Kim, H.; Kim, M. G.; Jeong, H. Y.; Nam, H.; Cho, J., A New Coating Method for Alleviating Surface Degradation of $\text{LiNi}_{0.6}\text{Co}_{0.2}\text{Mn}_{0.2}\text{O}_2$. Cathode Material: Nanoscale Surface Treatment of Primary Particles. *Nano Letters* **2015**, *15* (3), 2111-2119.
132. Park, J. H.; Choi, B.; Kang, Y. S.; Park, S. Y.; Yun, D. J.; Park, I.; Ha Shim, J.; Han, H. N.; Park, K., Effect of Residual Lithium Rearrangement on Ni-rich Layered Oxide Cathodes for Lithium-Ion Batteries. *Energy Technology* **2018**, *6* (7), 1361-1369.

133. Ellis, L. D.; Allen, J. P.; Thompson, L. M.; Harlow, J. E.; Stone, W. J.; Hill, I. G.; Dahn, J. R., Quantifying, Understanding and Evaluating the Effects of Gas Consumption in Lithium-Ion Cells. *Journal of the Electrochemical Society* **2017**, *164* (14), A3518-A3528.
134. Parimalam, B. S.; MacIntosh, A. D.; Kadam, R.; Lucht, B. L., Decomposition Reactions of Anode Solid Electrolyte Interphase (SEI) Components with LiPF₆. *Journal of Physical Chemistry C* **2017**, *121* (41), 22733-22738.
135. Kim, Y., Encapsulation of LiNi_{0.5}Co_{0.2}Mn_{0.3}O₂ with a thin inorganic electrolyte film to reduce gas evolution in the application of lithium ion batteries. *Physical Chemistry Chemical Physics* **2013**, *15* (17), 6400-6405.
136. Kim, Y., Mechanism of gas evolution from the cathode of lithium-ion batteries at the initial stage of high-temperature storage. *Journal of Materials Science* **2013**, *48* (24), 8547-8551.
137. Gauthier, M.; Carney, T. J.; Grimaud, A.; Giordano, L.; Pour, N.; Chang, H. H.; Fenning, D. P.; Lux, S. F.; Paschos, O.; Bauer, C.; Magia, F.; Lupart, S.; Lamp, P.; Shao-Horn, Y., Electrode-Electrolyte Interface in Li-Ion Batteries: Current Understanding and New Insights. *Journal of Physical Chemistry Letters* **2015**, *6* (22), 4653-4672.
138. Li, W. D.; Dolocan, A.; Oh, P.; Celio, H.; Park, S.; Cho, J.; Manthiram, A., Dynamic behaviour of interphases and its implication on high-energy-density cathode materials in lithium-ion batteries. *Nature Communications* **2017**, *8*.
139. Lee, K. H.; Song, E. H.; Lee, J. Y.; Jung, B. H.; Lim, H. S., Mechanism of gas build-up in a Li-ion cell at elevated temperature. *Journal of Power Sources* **2004**, *132* (1-2), 201-205.
140. Xiong, D. J.; Petibon, R.; Nie, M.; Ma, L.; Xia, J.; Dahn, J. R., Interactions between Positive and Negative Electrodes in Li-Ion Cells Operated at High Temperature and High Voltage. *Journal of the Electrochemical Society* **2016**, *163* (3), A546-A551.
141. Aiken, C. P.; Xia, J.; Wang, D. Y. H.; Stevens, D. A.; Trussler, S.; Dahn, J. R., An Apparatus for the Study of In Situ Gas Evolution in Li-Ion Pouch Cells. *Journal of the Electrochemical Society* **2014**, *161* (10), A1548-A1554.
142. Aiken, C. P.; Self, J.; Petibon, R.; Xia, X.; Paulsen, J. M.; Dahn, J. R., A Survey of In Situ Gas Evolution during High Voltage Formation in Li-Ion Pouch Cells. *Journal of the Electrochemical Society* **2015**, *162* (4), A760-A767.
143. Gachot, G.; Grugeon, S.; Armand, M.; Pilard, S.; Guenot, P.; Tarascon, J. M.; Laruelle, S., Deciphering the multi-step degradation mechanisms of carbonate-based electrolyte in Li batteries. *Journal of Power Sources* **2008**, *178* (1), 409-421.
144. Petibon, R.; Rotermund, L.; Nelson, K. J.; Gozdz, A. S.; Xia, J.; Dahn, J. R., Study of Electrolyte Components in Li Ion Cells Using Liquid-Liquid Extraction and Gas Chromatography Coupled with Mass Spectrometry. *Journal of the Electrochemical Society* **2014**, *161* (6), A1167-A1172.
145. Gachot, G.; Ribiere, P.; Mathiron, D.; Grugeon, S.; Armand, M.; Leriche, J. B.; Pilard, S.; Laruelle, S., Gas Chromatography/Mass Spectrometry As a Suitable Tool for the Li-Ion Battery Electrolyte Degradation Mechanisms Study. *Analytical Chemistry* **2011**, *83* (2), 478-485.
146. Hahn, H.; Wagner, R.; Schappacher, F.; Winter, M.; Nowak, S., In operando X-shaped cell online electrochemical mass spectrometry (OEMS): New online analysis enables insight into lab scale lithium ion batteries during operation. *Journal of Electroanalytical Chemistry* **2016**, *772*, 52-57.
147. Gueguen, A.; Streich, D.; He, M. L.; Mendez, M.; Chesneau, F. F.; Novak, P.; Berg, E. J., Decomposition of LiPF₆ in High Energy Lithium-Ion Batteries Studied with Online Electrochemical Mass Spectrometry. *Journal of the Electrochemical Society* **2016**, *163* (6), A1095-A1100.
148. Metzger, M.; Strehle, B.; Solchenbach, S.; Gasteiger, H. A., Origin of H₂ Evolution in LIBs: H₂O Reduction vs. Electrolyte Oxidation. *Journal of the Electrochemical Society* **2016**, *163*, A798-A809.
149. Wilken, S.; Treskow, M.; Scheers, J.; Johansson, P.; Jacobsson, P., Initial stages of thermal decomposition of LiPF₆-based lithium ion battery electrolytes by detailed Raman and NMR spectroscopy. *Rsc Advances* **2013**, *3* (37), 16359-16364.
150. Wiemers-Meyer, S.; Winter, M.; Nowak, S., Mechanistic insights into lithium ion battery electrolyte degradation - a quantitative NMR study. *Physical Chemistry Chemical Physics* **2016**, *18* (38), 26595-26601.

151. Richard, M. N.; Dahn, J. R., Accelerating rate calorimetry study on the thermal stability of lithium intercalated graphite in electrolyte II. Modeling the results and predicting differential scanning calorimeter curves. *Journal of the Electrochemical Society* **1999**, *146* (6), 2078-2084.
152. Gireaud, L.; Grugeon, S.; Laruelle, S.; Pilard, S.; Tarascon, J. M., Identification of Li battery electrolyte degradation products through direct synthesis and characterization of alkyl carbonate salts. *Journal of the Electrochemical Society* **2005**, *152* (5), A850-A857.
153. Rozier, P.; Tarascon, J. M., Review-Li-Rich Layered Oxide Cathodes for Next-Generation Li-Ion Batteries: Chances and Challenges. *Journal of the Electrochemical Society* **2015**, *162* (14), A2490-A2499.
154. Myung, S. T.; Izumi, K.; Komaba, S.; Yashiro, H.; Bang, H. J.; Sun, Y. K.; Kumagai, N., Functionality of oxide coating for $\text{Li}(\text{Li}_{0.05}\text{Ni}_{0.4}\text{Co}_{0.15}\text{Mn}_{0.4})\text{O}_2$ as positive electrode materials for lithium-ion secondary batteries. *Journal of Physical Chemistry C* **2007**, *111* (10), 4061-4067.
155. Yoon, C. S.; Kim, U. H.; Park, G. T.; Kim, S. J.; Kim, K. H.; Sun, Y. K., Self-Passivation of a LiNiO_2 Cathode for a Lithium-Ion Battery through Zr Doping. *Acs Energy Letters* **2018**, *3* (7), 1634-1639.
156. Myung, S. T.; Izumi, K.; Komaba, S.; Sun, Y. K.; Yashiro, H.; Kumagai, N., Role of alumina coating on Li-Ni-Co-Mn-O particles as positive electrode material for lithium-ion batteries. *Chemistry of Materials* **2005**, *17* (14), 3695-3704.
157. Yao, C.; Mo, Y.; Jia, X. B.; Chen, X. L.; Xia, J. S.; Chen, Y., LiMnPO_4 surface coating on $\text{LiNi}_{0.5}\text{Co}_{0.2}\text{Mn}_{0.3}\text{O}_2$ by a simple sol-gel method and improving electrochemical properties. *Solid State Ionics* **2018**, *317*, 156-163.
158. Sun, Y. K.; Han, J. M.; Myung, S. T.; Lee, S. W.; Amine, K., Significant improvement of high voltage cycling behavior AlF_3 -coated LiCoO_2 cathode. *Electrochemistry Communications* **2006**, *8*, 821-826.
159. Julien, C. M.; Mauger, A., Functional behavior of AlF_3 coatings for high-performance cathode materials for lithium-ion batteries. *Aims Materials Science* **2019**, *6* (3), 406-440.
160. Jo, C. H.; Cho, D. H.; Noh, H. J.; Yashiro, H.; Sun, Y. K.; Myung, S. T., An effective method to reduce residual lithium compounds on Ni-rich $\text{LiNi}_{0.6}\text{Co}_{0.2}\text{Mn}_{0.2}\text{O}_2$ active material using a phosphoric acid derived Li_3PO_4 nanolayer. *Nano Research* **2015**, *8* (5), 1464-1479.
161. Kim, Y.; Cho, J., Lithium-reactive $\text{Co}_3(\text{PO}_4)_2$ nanoparticle coating on high-capacity $\text{LiNi}_{0.8}\text{Co}_{0.16}\text{Al}_{0.04}\text{O}_2$ cathode material for lithium rechargeable batteries. *Journal of the Electrochemical Society* **2007**, *154* (6), A495-A499.
162. Haregewoin, A. M.; Wotango, A. S.; Hwang, B. J., Electrolyte additives for lithium ion battery electrodes: progress and perspectives. *Energy & Environmental Science* **2016**, *9* (6), 1955-1988.
163. Manthiram, A., An Outlook on Lithium Ion Battery Technology. *Acs Central Science* **2017**, *3* (10), 1063-1069.
164. Wang, X. S.; Zheng, X. W.; Liao, Y. H.; Huang, Q. M.; Xing, L. D.; Xu, M. Q.; Li, W. S., Maintaining structural integrity of 4.5 V Lithium cobalt oxide cathode with fumaronitrile as a novel electrolyte additive. *Journal of Power Sources* **2017**, *338*, 108-116.
165. Kim, G. Y.; Dahn, J. R., The Effect of Some Nitriles as Electrolyte Additives in Li-Ion Batteries. *Journal of the Electrochemical Society* **2015**, *162* (3), A437-A447.
166. Chae, B. J.; Yim, T., Sulfonate-immobilized artificial cathode electrolyte interphases layer on Ni-rich cathode. *Journal of Power Sources* **2017**, *360*, 480-487.
167. Xia, J.; Sinha, N. N.; Chen, L. P.; Dahn, J. R., A Comparative Study of a Family of Sulfate Electrolyte Additives. *Journal of the Electrochemical Society* **2014**, *161* (3), A264-A274.
168. Hekmatfar, M.; Hasa, I.; Eghbal, R.; Carvalho, D. V.; Moretti, A.; Passerini, S., Effect of Electrolyte Additives on the $\text{LiNi}_{0.5}\text{Mn}_{0.3}\text{Co}_{0.2}\text{O}_2$ Surface Film Formation with Lithium and Graphite Negative Electrodes. *Advanced Materials Interfaces* **2020**, *7* (1).
169. Qian, Y. X.; Niehoff, P.; Borner, M.; Grutzke, M.; Monnighoff, X.; Behrends, P.; Nowak, S.; Winter, M.; Schappacher, F. M., Influence of electrolyte additives on the cathode electrolyte interphase (CEI) formation on $\text{LiNi}_{1/3}\text{Mn}_{1/3}\text{Co}_{1/3}\text{O}_2$ in half cells with Li metal counter electrode. *Journal of Power Sources* **2016**, *329*, 31-40.
170. Charton, C. Thèse de doctorat "Étude des interfaces électrode/électrolyte de batteries lithium-ion 5 V de type graphite/ $\text{LiNi}_{0.5}\text{Mn}_{1.5}\text{O}_4$ ". Soutenue le 13 décembre 2017. Université François - Rabelais de Tours.

171. Wang, X. S.; Xing, L. D.; Liao, X. L.; Chen, X. F.; Huang, W. N.; Yu, Q. P.; Xu, M. Q.; Huang, Q. M.; Li, W. S., Improving cyclic stability of lithium cobalt oxide based lithium ion battery at high voltage by using trimethylboroxine as an electrolyte additive. *Electrochimica Acta* **2015**, *173*, 804-811.
172. El Ouatani, L.; Dedryvere, R.; Siret, C.; Biensan, P.; Reynaud, S.; Iratcabal, P.; Gonbeau, D., The Effect of Vinylene Carbonate Additive on Surface Film Formation on Both Electrodes in Li-Ion Batteries. *Journal of the Electrochemical Society* **2009**, *156* (2), A103-A113.
173. Cekic-Laskovic, I.; von Aspern, N.; Imholt, L.; Kaymaksiz, S.; Oldiges, K.; Rad, B. R.; Winter, M., Synergistic Effect of Blended Components in Nonaqueous Electrolytes for Lithium Ion Batteries. *Topics in Current Chemistry* **2017**, *375* (2).
174. Burns, J. C.; Sinha, N. N.; Jain, G.; Ye, H.; VanElzen, C. M.; Lamanna, W. M.; Xiao, A.; Scott, E.; Choi, J.; Dahn, J. R., Impedance Reducing Additives and Their Effect on Cell Performance I. $\text{LiN}(\text{CF}_3\text{SO}_2)_2$. *Journal of the Electrochemical Society* **2012**, *159* (7), A1095-A1104.
175. Madec, L.; Xia, J.; Petibon, R.; Nelson, K. J.; Sun, J. P.; Hill, I. G.; Dahn, J. R., Effect of Sulfate Electrolyte Additives on $\text{LiNi}_{1/3}\text{Mn}_{1/3}\text{Co}_{1/3}\text{O}_2$ /Graphite Pouch Cell Lifetime: Correlation between XPS Surface Studies and Electrochemical Test Results. *Journal of Physical Chemistry C* **2014**, *118* (51), 29608-29622.
176. Wang, D. Y.; Xia, J.; Ma, L.; Nelson, K. J.; Harlow, J. E.; Xiong, D. J.; Downie, L. E.; Petibon, R.; Burns, J. C.; Xiao, A.; Lamanna, W. M.; Dahn, J. R., A Systematic Study of Electrolyte Additives in $\text{LiNi}_{1/3}\text{Mn}_{1/3}\text{Co}_{1/3}\text{O}_2$ (NMC)/Graphite Pouch Cells. *Journal of the Electrochemical Society* **2014**, *161* (12), A1818-A1827.
177. Wagner, R.; Korth, M.; Streipert, B.; Kasnatscheew, J.; Gallus, D. R.; Brox, S.; Arnereller, M.; Cekic-Laskovic, I.; Winter, M., Impact of Selected LiPF_6 Hydrolysis Products on the High Voltage Stability of Lithium-Ion Battery Cells. *Acs Applied Materials & Interfaces* **2016**, *8* (45), 30871-30878.
178. Chen, J. W.; Xing, L. D.; Yang, X. R.; Liu, X.; Li, T. J.; Li, W. S., Outstanding electrochemical performance of high-voltage $\text{LiNi}_{1/3}\text{Co}_{1/3}\text{Mn}_{1/3}\text{O}_2$ cathode achieved by application of LiPO_2F_2 electrolyte additive. *Electrochimica Acta* **2018**, *290*, 568-576.
179. Seok, J. W.; Lee, J.; Rodgers, T.; Ko, D. H.; Shim, J. H., Effect of LiPO_2F_2 Electrolyte Additive on Surface Electrical Properties of $\text{LiNi}_{0.6}\text{Co}_{0.2}\text{Mn}_{0.2}\text{O}_2$ Cathode. *Transactions on Electrical and Electronic Materials* **2019**, *20* (6), 548-553.
180. Ma, L.; Ellis, L.; Glazier, S. L.; Ma, X. W.; Liu, Q. Q.; Li, J.; Dahn, J. R., LiPO_2F_2 as an Electrolyte Additive in $\text{LiNi}_{0.5}\text{Mn}_{0.3}\text{Co}_{0.2}\text{O}_2$ /Graphite Pouch Cells. *Journal of the Electrochemical Society* **2018**, *165* (5), A891-A899.
181. Wang, C. Y.; Yu, L.; Fan, W. Z.; Liu, R.; Liu, J. W.; Ouyang, L. Z.; Yang, L. C.; Zhu, M., Enhanced high-voltage cyclability of $\text{LiNi}_{0.5}\text{Co}_{0.2}\text{Mn}_{0.3}\text{O}_2$ -based pouch cells via lithium difluorophosphate introducing as electrolyte additive. *Journal of Alloys and Compounds* **2018**, *755*, 1-9.
182. Lei, Q. F.; Yang, T. X.; Zhao, X. Y.; Fan, W. Z.; Wang, W. L.; Yu, L.; Guo, S. B.; Zuo, X. X.; Zeng, R. H.; Nan, J. M., Lithium difluorophosphate as a multi-functional electrolyte additive for 4.4 V $\text{LiNi}_{0.5}\text{Co}_{0.2}\text{Mn}_{0.3}\text{O}_2$ /graphite lithium ion batteries. *Journal of Electroanalytical Chemistry* **2019**, 846.

Chapter II

Identification, quantification and formation mechanism of surface species in Ni-rich NMC materials

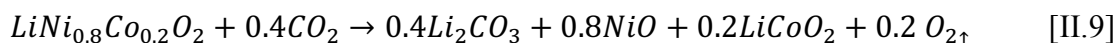
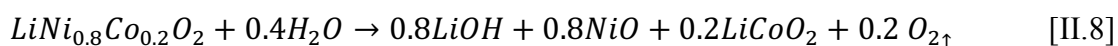
1. Introduction	57
2. Characterization of as-received Ni-rich NMC materials	62
2.1. As received Ni-rich NMC materials conditioning.....	62
2.2. As-received Ni-rich NMC materials characterization	62
3. Quantification of surface species in as-received NMC materials	67
3.1. Quantification of soluble bases through acid-base titration technique	67
3.1.1. Optimization of the acid-base titration protocol	67
3.1.2. Quantification of soluble bases in as-received materials through acid-base titration ...	74
3.2. Complementary quantification.....	74
3.2.1. Complementary analysis of filtrate solution through AAS	75
3.2.2. Complementary analysis of filtrate solution through ICP-AES	76
3.2.3. Complementary analysis of NMC materials through FTIR and SEM	77
3.3. Conclusion	79
4. Characterization of surface species in NMC materials exposed to specific atmospheres	81
4.1. Preliminary storage studies under Ar, CO ₂ , dry air and air atmospheres	81
4.2. Storage under specific H ₂ O/CO ₂ atmosphere.....	83
4.2.1. Acid-base titration quantification after H ₂ O/CO ₂ storage	83
4.2.2. Further investigations through SEM and FTIR	85
5. Deciphering the degradation mechanisms through thermal analysis	90
5.1. Thermal analysis of as-received NMC materials	90
5.2. Thermal analysis of exposed NMC materials	91
5.3. Proposed degradation mechanism.....	94
5.4. Attempts to characterize surface species in exposed NMC through Raman and XRD	97
6. Conclusion of the chapter	100
7. References	101

1. Introduction

Throughout the industrial production of layered materials, precursors residues can be left from the synthesis and constitute what are called the soluble bases: Li_2CO_3 and LiOH ^{1,2} (Eqs. II.1 – 3 in Table II.1). In addition, during the handling of the materials, they may be exposed to air, also creating Li_2CO_3 and LiOH ^{3,4}, and supposedly LiHCO_3 as well^{5,6}, through the reaction of H_2O and CO_2 with the outermost surface of NMC particles. Among layered materials, the promising Ni-rich NMCs ($\text{Ni} > 0.5$ in $\text{LiNi}_{1-x-y}\text{Mn}_x\text{Co}_y\text{O}_2$) are known to be highly reactive to H_2O and CO_2 , thus stunting their utilization as positive electrode materials in LIBs for EVs⁷. As a matter of fact, the presence of OH^- groups induces slurry gelation by reacting with the PVDF binder during the preparation of electrodes⁸, the insulative nature of the soluble bases increases cell impedance⁴, capacity fade is often observed with air-exposed materials^{5,9} and more gas is produced during battery operation¹⁰⁻¹³.

The formation of soluble bases from air is not exclusive to NMC materials, but is characteristic of layered materials. Despite having been identified for a long time, the formation mechanisms are still source of debate. Table II.1 summarizes all of the proposed mechanisms.

Goodenough's group¹⁴⁻¹⁶ reported, very early, the migration of lithium ions to the surface of layered materials LiVO_2 and LCO upon air exposure, to form Li_2CO_3 , but did not show any mechanism. Years later, Matsumoto et al.¹⁷ proposed a redox reaction to explain how layered materials LiMO_2 ($\text{M} = \text{Ni}, \text{Co}, \text{Mn}, \text{Al}$) react with O_2 and CO_2 from air to form Li_2CO_3 (Eq. II.4 in Table II.1). Based on this study, and on XPS and XRD analysis of an as-received and a 1 year air-exposed LNO material, Liu et al.^{3,5} suggested another redox mechanism where Ni^{3+} reduces to Ni^{2+} (Eq. II.5 in Table II.1), followed by production of O_2 and active oxygen ($\text{O}^{2-}_{(\text{active})}$) (Eq. II.6 in Table II.1), the latter reacting with H_2O and CO_2 from air to form LiOH and Li_2CO_3 (Eq. II.7 in Table II.1). Following this theory, degradation reactions taking place in layered $\text{LiNi}_{0.8}\text{Co}_{0.2}\text{O}_2$ (NMC 820) would be Eq. II.8 and II.9. The problem with the redox mechanism is that it does not explain how soluble bases are formed in materials without Ni^{3+} like NMC 111 or 442.



To explain soluble bases formation in NMC 111, Mijung et al.¹⁸ and Huang et al.¹⁹, proposed that H₂O get adsorbed on the particles' surface, followed by the adsorption of CO₂ that form slightly acidic surface with H₂CO₃ (Eq. II.10). Then, Li₂CO₃ is formed from the reaction of H₂CO₃ with LiMO₂, while the O²⁻ lattice ions combine with H⁺ to produce LiOH and keep charge balance. LiOH can further react with CO₂ to form Li₂CO₃ (Eqs. II.11 and II.12). Moreover, works by Schkrob et al.²⁰ and Faenza et al.⁶, also supported the absence of a redox processes by proposing that in NMC 532 (Ni³⁺_{0.2}Ni²⁺_{0.3}) and NCA (Ni³⁺_{0.8}), LiOH originates first from an ion-exchange process involving partial Li⁺ substitution by H⁺, when the OH⁻ from water strongly adsorbs via coordination with lithium or with the transition metals (Eq. II.13). After LiOH is formed, it would react with CO₂ to form LiHCO₃ (Eq. II.14) or Li₂CO₃.

For years, only these lithium surface species have been considered to originate from the degradation of layered materials after air exposure, even if it was recognized very early, that there might exist other non-identified surface species⁵. In this respect, very recently, new evidence has been published regarding the existence of nickel-based surface species. From the same group, Sicklinger et al.²¹ and Jung et al.²² suggested, through Raman spectroscopy and thermogravimetric/mass spectrometry (TG-MS) results interpretation, that nickel-hydroxycarbonate (NiCO₃.2Ni(OH)₂.xH₂O) is the major degradation product on NMC 111 and 811 upon air exposure. Despite the experimental support, neither of them presented mechanisms that explained the degradation of NMC to nickel-based species.

Table II.1. Summary of the surface species proposed to exist in layered materials along with their origin, formation mechanisms and credibility

Origin	Surface specie	Reaction mechanisms	[#]	Credibility	Refs
Synthesis	Li ₂ CO ₃	Residual from: $2MOOH + Li_2CO_3 \xrightarrow{700-950^\circ C, O_2} 2LiMO_2 + CO_2 + H_2O$	[II.1]	High	1, 2, 7, 23
	LiOH	Residual from: $MOOH + LiOH.H_2O \xrightarrow{700-950^\circ C, O_2} LiMO_2 + 2H_2O$	[II.2]	High	
	Li ₂ O	Calcination reaction: $2LiOH \xrightarrow{\Delta} Li_2O + H_2O$	[II.3]	High but almost never detected	24
Air-grown	Li ₂ CO ₃	Redox reaction (1): $LiMO_2 + \frac{z}{4}O_2 + \frac{z}{2}CO_2 \rightarrow Li_{1-z}MO_2 + \frac{z}{2}Li_2CO_3$	[II.4]	Low, today it is known O ₂ does not intervene	17
		Redox reaction (2): $Ni^{3+} + O^{2-}_{(lattice)} \rightarrow Ni^{2+} + O^-$	[II.5]	Low, does not consider NMC without Ni ³⁺	3, 5
		$O^- + O^- \rightarrow O^{2-}_{(active)} + \frac{1}{2}O_2$	[II.6]		
	LiOH	$2Li^+ + O^{2-}_{(active)} + CO_2/H_2O \rightarrow Li_2CO_3/2LiOH$	[II.7]		
		Acid-base reaction: $CO_2 + H_2O \rightarrow H_2CO_3$	[II.10]	Medium, not enough support LiOH+CO ₂ : High	18, 19
	$LiMO_2 + \frac{x}{4}H_2CO_3 \rightarrow Li_{1-x}MO_{2-x/2} + \frac{x}{2}LiOH + \frac{x}{4}Li_2CO_3$	[II.11]			
		$2LiOH + CO_2 \rightarrow Li_2CO_3 + H_2O$	[II.12]		
	Ion exchange: $Li^+_{(surface\ lattice)} + H_2O \rightarrow LiOH + H^+$	[II.13]	Medium, not enough support	6, 20	
	LiHCO ₃	$LiOH + CO_2 \rightarrow LiHCO_3$	[II.14]	Low, solid LiHCO ₃ cannot exist	3
	NiCO ₃ .2Ni(OH) ₂ .xH ₂ O	Deduced experimentally through Raman and TGA but reaction mechanism is absent		Medium, unclear formation	21, 22

In the literature, direct identification and quantification techniques of soluble bases in powder materials have been reported (Table II.2). For example, XRD has been used to identify Li_2CO_3 as a secondary phase when the ratio toward the bulk is high^{4, 5, 18, 25, 26}, and in few cases, the Rietveld refinement of the XRD data allowed to quantify it. Liu et al.³ showed that in a 1-year air-exposed LNO material, the amount of Li_2CO_3 was 13.3 wt.%. Matsumoto et al.¹⁷ quantified 8 wt.% of Li_2CO_3 in exposed $\text{LiNi}_{0.81}\text{Co}_{0.16}\text{Al}_{0.03}\text{O}_2$ and Zhuang et al.⁴ 6 wt.% in exposed NCA. Conversely, when the ratio of soluble bases toward the bulk mass is small and does not constitute a secondary phase (below ~3 wt.%), the carbonate and hydroxide groups have been identified by Fourier-transform infrared (FTIR)^{4, 6, 25, 27, 28}, Raman^{22, 25, 29} and XPS spectroscopy^{3, 9, 26, 30}. Only Faenza et al.⁶ and Zhuang et al.⁴ reported the quantification of $\text{LiOH}\cdot\text{H}_2\text{O}$ and Li_2CO_3 by FTIR using a standard.

One less common and indirect technique that has been used to quantify Li_2CO_3 is the gas chromatography-mass spectrometry (GC/MS). In this respect, Jung et al.²² quantified the CO_2 produced from the chemical reaction of Li_2CO_3 and HCl (Eq. II.15). Through this method, they reported high experimental error between 12 – 29% and ignored that CO_2 can remain dissolved in the slurry. Hence, this method is not preferred.

Currently, the most reliable and widespread of these techniques to quantify CO_3^{2-} and OH^- , is the Warder’s method³¹, also called acid-base titration. This technique thus emerged as the technique of choice for quantifying the soluble bases present in the as-received and exposed NMC materials.

Table II.2. Methods for the identification and quantification of soluble bases.

Identification technique		Characteristics
Bulk (> 6 wt.%)	XRD	Li_2CO_3 phase identification, if it exceeds 6 wt.% quantification is possible through Rietveld refinement ^{3, 4, 17}
Surface (< 3 wt.%)	FTIR	Mostly qualitative of CO_3^{2-} and OH^- ^{4, 6, 25, 27, 28} Quantification is possible with internal reference ^{4, 6}
	Raman	Qualitative identification of Li_2CO_3 and LiOH ^{22, 25, 29}
	XPS	Qualitative identification of Li_2CO_3 and LiOH ^{3, 9, 26, 30}
Indirect	GC/MS	Quantification through CO_2 detection in: $\text{Li}_2\text{CO}_3 + 2\text{HCl} \rightarrow 2\text{LiCl} + \text{CO}_2 + \text{H}_2\text{O} \quad [\text{II.15}]$
	Warder’s titration	Identification and quantification of CO_3^{2-} and OH^- in a precise way ³¹

Overall, these studies revealed that determining the precise surface composition in Ni-rich NMC materials is still challenging. As it is a prerequisite to further understand the whole processes occurring upon NMC storage under air and subsequent reactivity upon cycling, we undertook a quantitative study on different Ni-rich NMC materials. Beforehand, a deep characterization of the materials followed by a stepwise optimization work on the entire procedure (solubilization and titration) was required to get high measurement accuracy. Complementary techniques as FTIR, AAS, ICP-AES and TGA-MS were, in turn, indispensable to identify other surface species and to highlight a novel formation mechanism.

2. Characterization of as-received Ni-rich NMC materials

In addition to perform several analyses by using surface characterization and/or analytical tools, the difficulty of achieving the entire identification and accurate quantification of surface species may also rely on the precise knowledge of the post-synthesis conditioning and storage conditions of the materials as well as their physical-chemical characteristics.

2.1. As received Ni-rich NMC materials conditioning

The five studied Ni-rich NMC materials $\text{LiNi}_{0.5}\text{Mn}_{0.3}\text{Co}_{0.2}\text{O}_2$ (532), $\text{LiNi}_{0.6}\text{Mn}_{0.2}\text{Co}_{0.2}\text{O}_2$ (622), $\text{LiNi}_{0.8}\text{Mn}_{0.1}\text{Co}_{0.1}\text{O}_2$ (811), $\text{LiNi}_{0.9}\text{Co}_{0.1}\text{O}_2$ (901), and alumina-coated $\text{LiNi}_{0.6}\text{Mn}_{0.2}\text{Co}_{0.2}\text{O}_2$ (622C) were received in individual tight-closed 1 kg bags originally sealed in a dry atmosphere, from Umicore® Korea.

Considering the air-sensitivity of Ni-rich NMC materials and the importance to maintain a clean surface state, the bags were transferred to a dry room with dew point between -58 and -63°C (~ 5 - 10 ppm of H_2O). In there, the powders were reconditioned in PTFE flasks of 25 cm^3 that were filled and tapped to ensure that the least amount of dry air remains inside. Then, the closed flasks were put inside aluminum laminated bags and sealed under vacuum without further treatment. Throughout the duration of this project, flasks were transferred, one by one, when needed, from the dry room to an argon-filled glovebox (< 0.1 ppm O_2 and H_2O , MBraun) without air exposure. Henceforward, the powders coming from the glovebox are called **as-received NMC**.

2.2. As-received Ni-rich NMC materials characterization

The molar composition of each transition metal (Table II.3) of the five NMC materials and of aluminum in NMC 622C were determined at the Technocentre–Renault, after dissolution in *aqua regia* (protocol in Annex I) and through inductively coupled plasma atomic emission spectroscopy (ICP-AES). The transition metal molar percentages compare very well ($\leq 1.8\%$ of error) with the terminology given by the Umicore. Based on the quantity of aluminum found, the coating of Al_2O_3 was determined to constitute $18.5\ \mu\text{mol.g}_{\text{NMC622C}}^{-1}$.

Particle sizes and BET surface areas were obtained from the data sheet supplied with the materials. The particle size distribution (PSD) values, classified in D10, D50 and D90, are equivalent to what has been reported in the literature for Ni-rich NMC materials³²⁻³⁴.

Table II.3. Physicochemical characteristics of the Ni-rich NMC materials. The error bars of the element composition represent the standard deviation from three repetitions.

Material	PSD (μm)	Element composition (mol%)	BET ($\text{m}^2\cdot\text{g}^{-1}$)
532	D10: 5.6 D50: 9.8 D90: 16.8	Ni: 51.2 ± 0.008 Co: 28.2 ± 0.003 Mn: 20.6 ± 0.004	0.27
622C	D10: 6.5 D50: 11.8 D90: 20.8	Ni: 60.6 ± 0.011 Co: 20.3 ± 0.004 Mn: 19.1 ± 0.004	0.27
622	D10: 6.5 D50: 11.8 D90: 20.8	Ni: 60.5 ± 0.004 Co: 20.4 ± 0.009 Mn: 19.1 ± 0.01	0.27
811	D10: 8.1 D50: 11.7 D90: 15.7	Ni: 80.6 ± 1.8 Co: 9.9 ± 0.4 Mn: 9.4 ± 0.2	0.24
901	D10: 5.8 D50: 11.7 D90: 21.1	Ni: 90.4 ± 1.7 Co: 0 Mn: 9.6 ± 0.2	0.20

Observed by scanning electron microscopy (SEM), the five Ni-rich NMC materials present spherical particles with diameters between 10–20 μm (Fig. II.1a–e). The granular morphology is given by the arrangement of primary particles ($\leq 1\mu\text{m}$). Upon increase of the nickel content, the surface of the particles becomes smoother and BET surface areas decrease, which is supposed to be due to the adaptation of the annealing temperature of precursors between 750 – 950 $^{\circ}\text{C}$, to limit cation disordering between Ni^{2+} and Li^{+} sites and yield highly crystalline materials^{35, 36}. Noh et al.³⁵, for instance, annealed during 15h at 950 $^{\circ}\text{C}$ to yield NMC 111 and 532, at 900 $^{\circ}\text{C}$ for 622 and at 780 $^{\circ}\text{C}$ for 811.

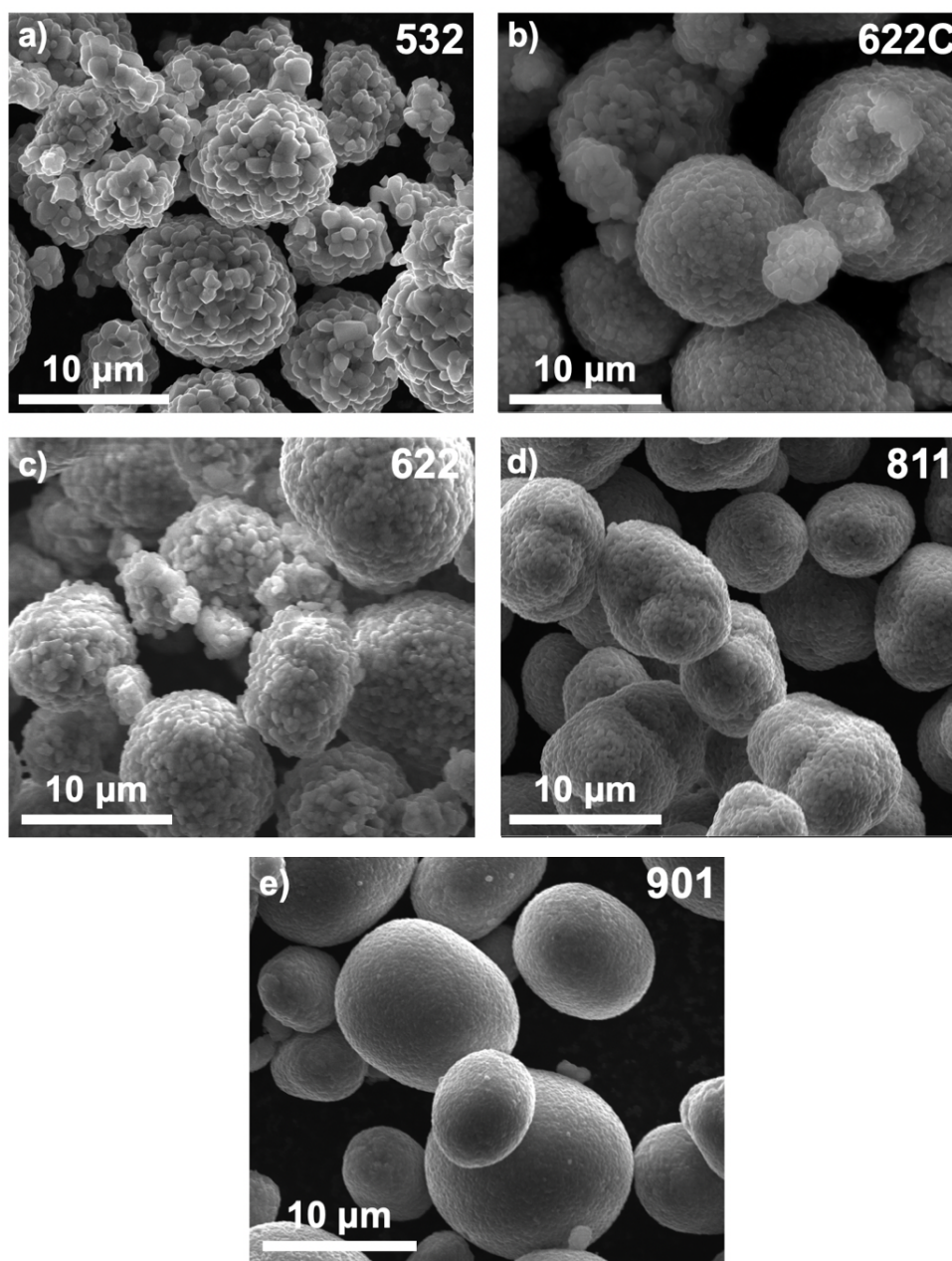


Figure II.1. Representative SEM pictures of Ni-rich NMC materials: **a)** 532, **b)** 622C, **c)** 622, **d)** 811 and **e)** 901.

Closer SEM pictures (Fig. II.2a, b) were obtained to portray the alumina coating on NMC 622C particles. As confirmed through electron dispersive X-ray (EDX) analysis (Fig. II.2c), the coating is in the form of well distinguished small particles of less than 50 nm, covering unevenly the surface.

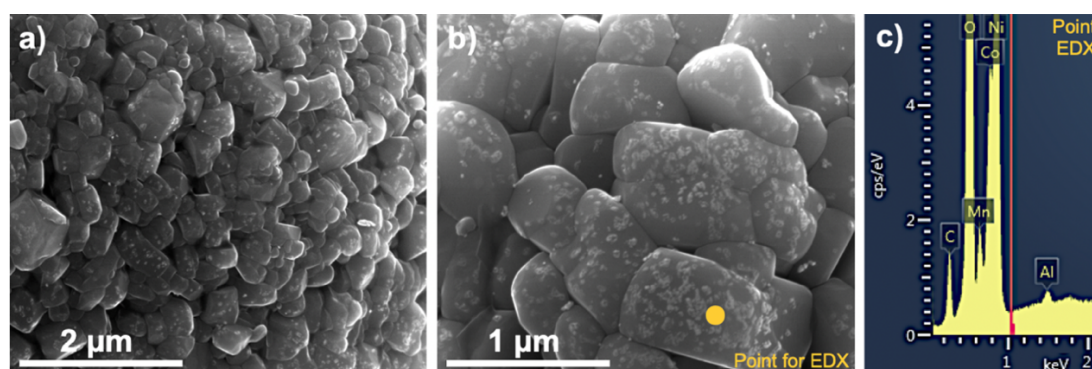


Figure II.2. SEM pictures of the alumina coating in NMC 622C, at **a)** 25000X and **b)** 50000X magnification. **c)** EDX point analysis showing aluminum presence.

Structural characterization was performed by means of powder X-Ray diffraction (XRD) and FullProf refinement. Every material exhibits a well-defined layered structure based on a hexagonal α -NaFeO₂ structure with the R-3m crystal group, typical for the layered NMC materials^{35,37,38}. The XRD patterns are shown in Fig. II.3, the split into doublets of the reflections (006)–(102) and (108)–(110) have been reported to be a sign of good crystallinity^{3,25}.

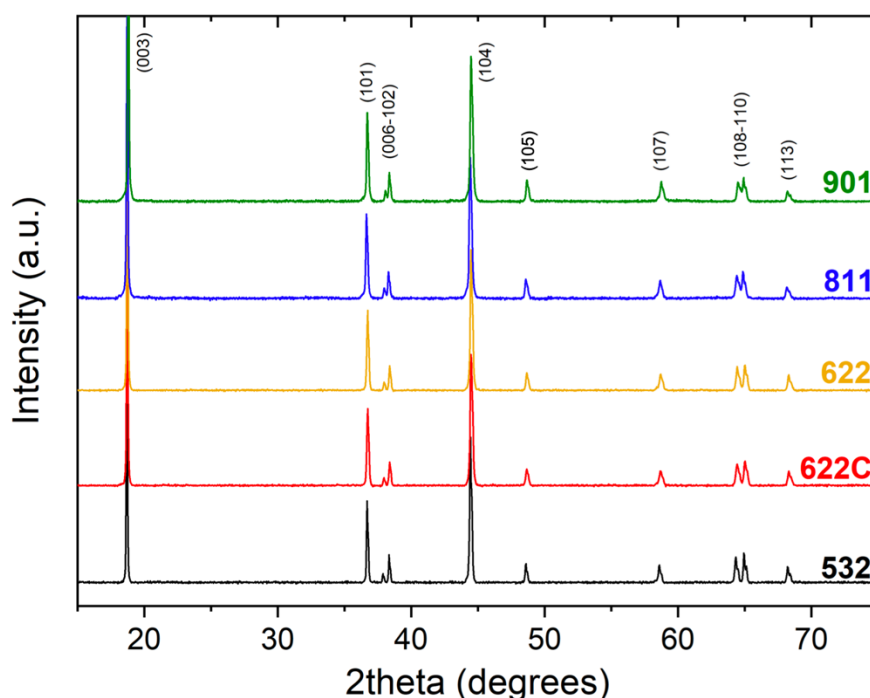


Figure II.3. Powder XRD patterns of the five Ni-rich NMC materials.

The five NMC materials were all issued from the same supplier that controlled the synthesis conditions to the highest standard. They present close structural and global morphological features, except the surface microstructure evolving from granular to relatively smooth with increase of Ni³⁺ amount from NMC 532 to 901. These high-grade materials were thus considered

as suitable samples for the comparative study of their reactivity toward different atmospheres exposure.

3. Quantification of surface species in as-received NMC materials

Inherently, as-received NMC materials contain soluble bases that originate either from the synthesis, since excess lithium precursors (LiOH or Li₂CO₃) are utilized to avoid getting non-stoichiometric NMC after synthesis^{1, 23} and may be left after reaction; or from air exposure as a consequence of NMC's structural instability^{7, 39}. The first part of this section is devoted to their quantification through acid-base titration after experimental conditions optimization. In the second part are implemented complementary techniques, with the aim of achieving the complete characterization of the soluble surface species.

3.1. Quantification of soluble bases through acid-base titration technique

3.1.1. Optimization of the acid-base titration protocol

The protocol for the titration of soluble bases includes a solubilization step (NMC washing) which consists in stirring the powder material for a certain time in water, followed by vacuum filtration in order to recover separately the washed powder and the solution containing the soluble bases (Fig. II.4). Then, the filtrate solution containing the soluble bases is titrated with a strong acid.

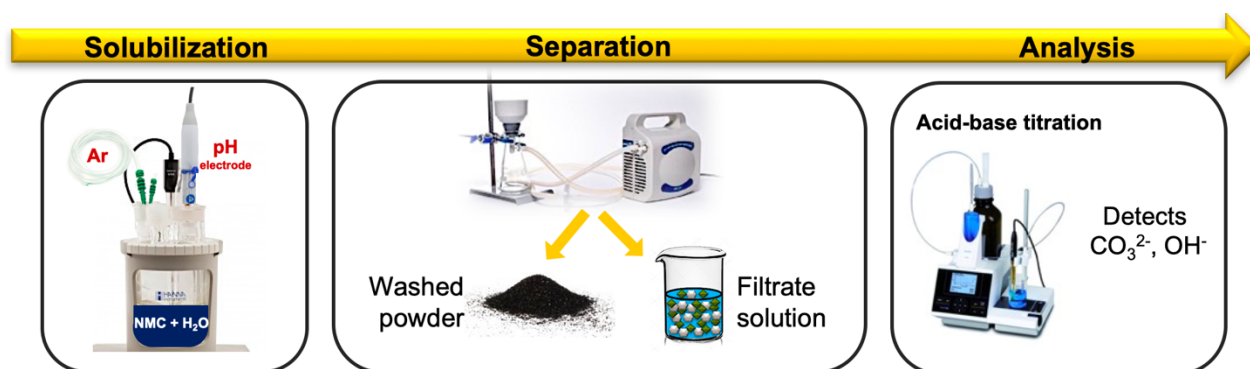


Figure II.4. Schematic diagram of the protocol for the soluble bases solubilization and analysis

Based on the likelihood that the accurate quantification of soluble bases is affected by the NMC's instability in water^{24, 40} and the atmosphere CO₂ solubilization⁴¹, the impact of the agitation time upon NMC washing and the atmosphere composition was evaluated.

3.1.1.1. Impact of the atmosphere composition

It is known that the filtrated solution of CO_3^{2-} and OH^- resulting from the washing procedure can be acidified with CO_2 from the atmosphere⁴¹. The following experiments show the range in which the pH of an aqueous solution containing dissolved Li_2CO_3 varies while being stirred under argon or air atmosphere. For this, 0.18 mmol of Li_2CO_3 (Sigma-Aldrich, purity > 99%) were added to 100 ml of bi-distilled water under air or under inert atmosphere (argon), and the pH was immediately recorded as function of time by means of an automatic titrimeter equipped with a pH electrode (TitroLine 7000, SI Analytics GmbH) (Fig. II.5).

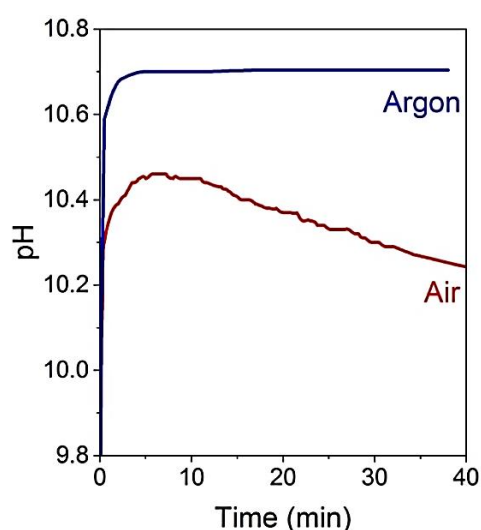
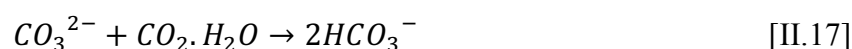


Figure II.5. Impact of air (red curve) or argon (blue curve) atmosphere on pH variation as function of time of a solution of Li_2CO_3 dissolved in bi-distilled water.

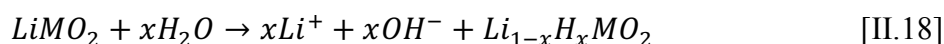
From the gradual but fast increase of pH when the Li_2CO_3 is added, it can be deduced that Li_2CO_3 in both solutions takes around five minutes to be solubilized. Under argon bubbling (blue curve), the pH levels off at a value of 10.7 for at least 40 min. On the other hand, the pH of the solution stirred under air (red curve) reaches only 10.45. This is explained by the simultaneous solubilization of Li_2CO_3 and CO_2 from air which entails a pH decrease with time, according to the following reactions (Eq. II.16 and 17):



These experiments prove the necessity of performing the solubilization and titration steps under inert atmosphere, to avoid quantification errors given by CO_2 solubilization.

3.1.1.2. Impact of the stirring time upon NMC washing procedure

After soluble bases solubilization from NMC surface, the pH of the aqueous solution increases due to an ion-exchange phenomenon that takes place when a lithium ion in the material is substituted by a proton in solution^{24, 40} (Eq. II.18). Furthermore, this process can result in structural defects initiated by cation mixing^{42, 43}.



The actual effect of stirring time on the pH evolution during the NMC's washing procedure was thus investigated. To this end, 5 g of each as-received material were weighed inside the glove box and taken out without air exposure. They were then transferred to an adapted flask for the washing step and magnetically stirred with 100 ml of bi-distilled water (mass ratio 1:20) for up to 30 minutes under argon atmosphere. The pH was recorded as a function of time, immediately after the introduction of the NMC powder in water (Fig. II.6).

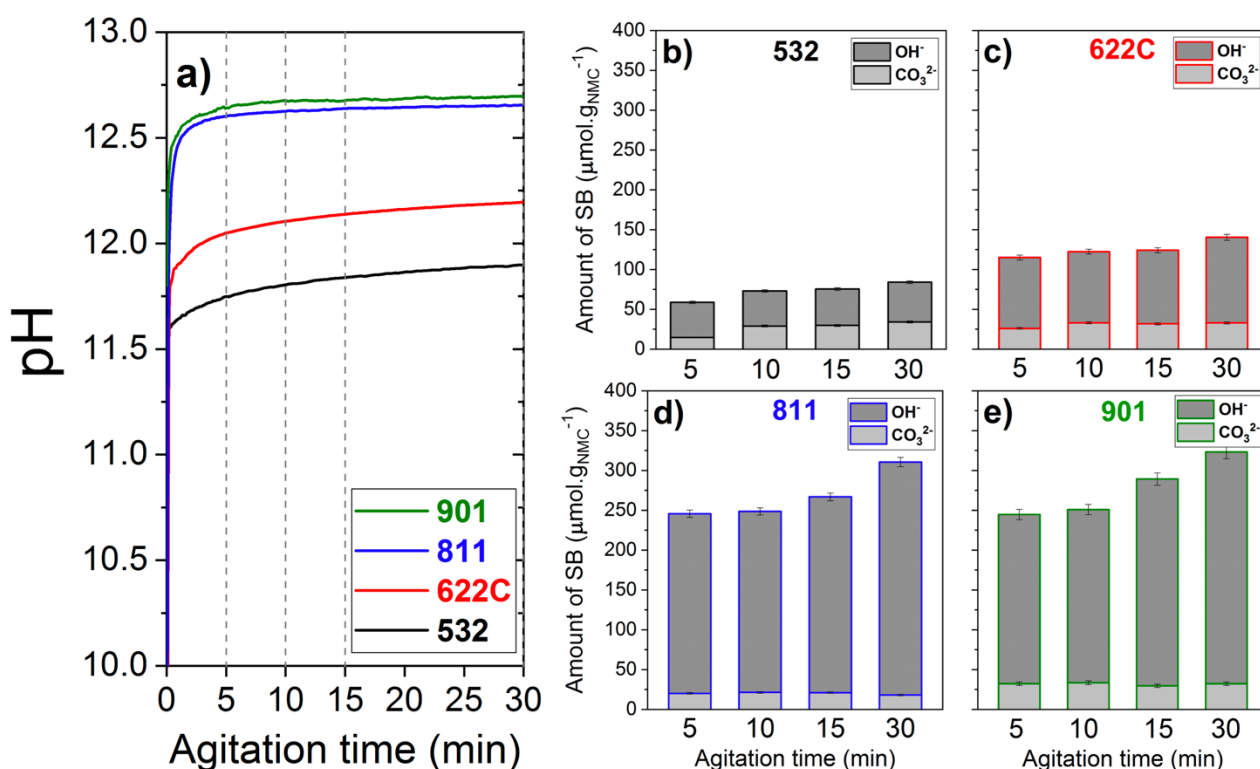


Figure II.6. a) Variation of pH values over time for a suspension of 5 g in 100 ml of bi-distilled water for NMC 532, 622C, 811 and 901. Amounts of OH⁻ and CO₃²⁻ determined by acid-base titration of filtrate solutions at different stirring times for b) 532, c) 622C, d) 811 and e) 901.

As shown in Fig.II.6, the pH increases rapidly up to values of 11.2, 11.8, 12.15 and 12.20 for 532, 622C, 811 and 901, respectively; which denotes the different concentration of soluble bases in each NMC material surface. Subsequently, the pH tends to stabilize between 5 and 15 minutes of stirring, depending on the nickel content. From there, a slow but constant pH increase explained by the Li^+/H^+ exchange phenomenon is depicted. These observations demonstrate the need to reach a compromise on the stirring time enabling complete soluble bases solubilization while avoiding, as much as possible, the Li^+/H^+ exchange phenomenon, for each NMC composition. Hence, in order to define the optimal stirring time required for each material, the solution was filtered and titrated with a 0.05 M HCl solution under argon atmosphere after 5, 10, 15 and 30 minutes of stirring time, denoted by the dotted lines in Fig. II.6a. The individual acid-base titration results are depicted in Fig. II.6b–e. In there, the error bars correspond to the standard deviation from three repetitions of the solubilization and titration procedure. Their small values corroborate the reproducibility of this method.

As a reminder of the experimental determination of dissolved carbonate and hydroxide species through the acid-base titration, Fig. II.7 shows a representative pH curve with two equivalence points. Up to the first equivalence point, V_1 , all OH^- and CO_3^{2-} are dosed. Then, HCO_3^- are dosed up to the second equivalence point, V_2 . From the values of added volume at the equivalence points, it is possible to calculate accurately the quantity of soluble bases with the following equations (Eqs. II.19 and II.20):

$$\text{Li}_2\text{CO}_3 \text{ amount (mmol)} = \frac{(V_2 - V_1)(M_{\text{acid}})}{\frac{m_{\text{H}_2\text{O final}}}{m_{\text{H}_2\text{O initial}}}} * 1000 \quad [\text{II.19}]$$

$$\text{LiOH amount (mmol)} = \frac{(2 * V_1 - V_2)(M_{\text{acid}})}{\frac{m_{\text{H}_2\text{O final}}}{m_{\text{H}_2\text{O initial}}}} * 1000 \quad [\text{II.20}]$$

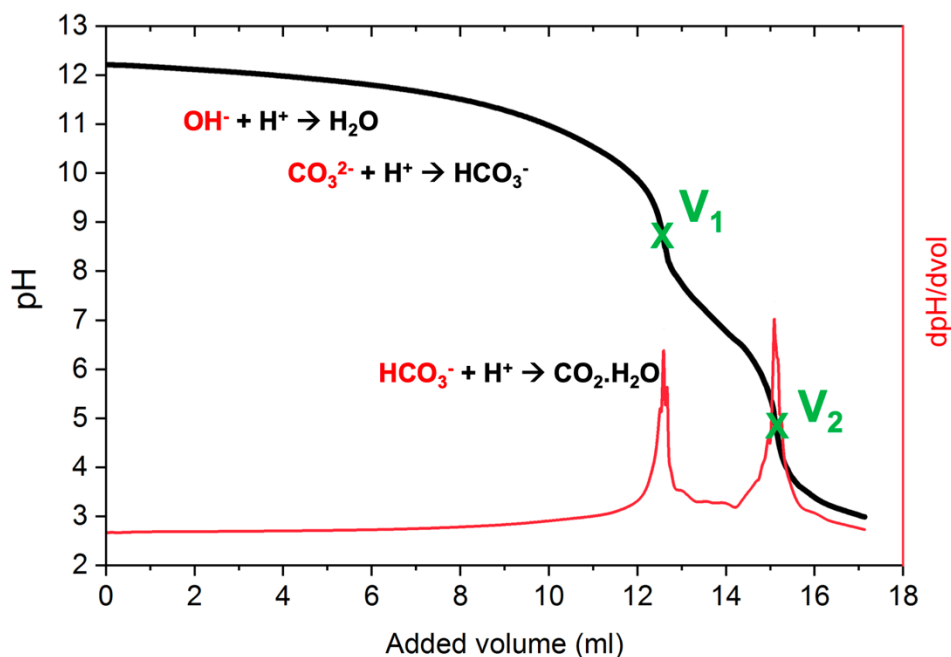


Figure II.7. Acid-base titration curve (black) with two equivalence points evidenced by the derivative curve (red), including dosing reactions.

The CO_3^{2-} concentrations (Fig. II.6b–e), calculated from the hereabove reminded calculation method, reach a maximum value at 10 minutes for NMC 532 and 622C and at 5 minutes of stirring time for 811 and 901 NMC materials. As for OH^- concentration, they remain constant around 10 to 15 minutes for NMC 532 and 622C and 5 to 10 minutes of stirring time for 811 and 901; they increase right after, as a result of the Li^+/H^+ exchange dominating process. Assuming that Li_2CO_3 needs at least 5 minutes to completely dissolve, as determined in [Section 3.1.1.1](#), and that Fig. II.7. shows that the solubilization time above 15 minutes for 532 and 622 and above 10 minutes for 811 and 901 induces Li^+/H^+ exchange reactions, the stirring time was set at 15 minutes for 532, 622 and 622C, and 8 minutes for 811 and 901. In the literature, surface transformations have been detected as a consequence of a prolonged water washing procedure, up to 20 minutes for NMC 811²⁸ and 1 hour for NMC 532³⁴.

In order to ensure that the NMC's texture and bulk structure were not affected by the washing step, SEM and XRD analyses were performed. Through SEM, it was proven that the granular morphology of every NMC material is kept and the distribution of the coating particles (Fig. II.8a) remains unchanged. Moreover, through XRD, it was confirmed that the layered $F-3m$ bulk structure (Fig. II.8b) was not affected. To be concise, only the results from NMC 622C are shown.

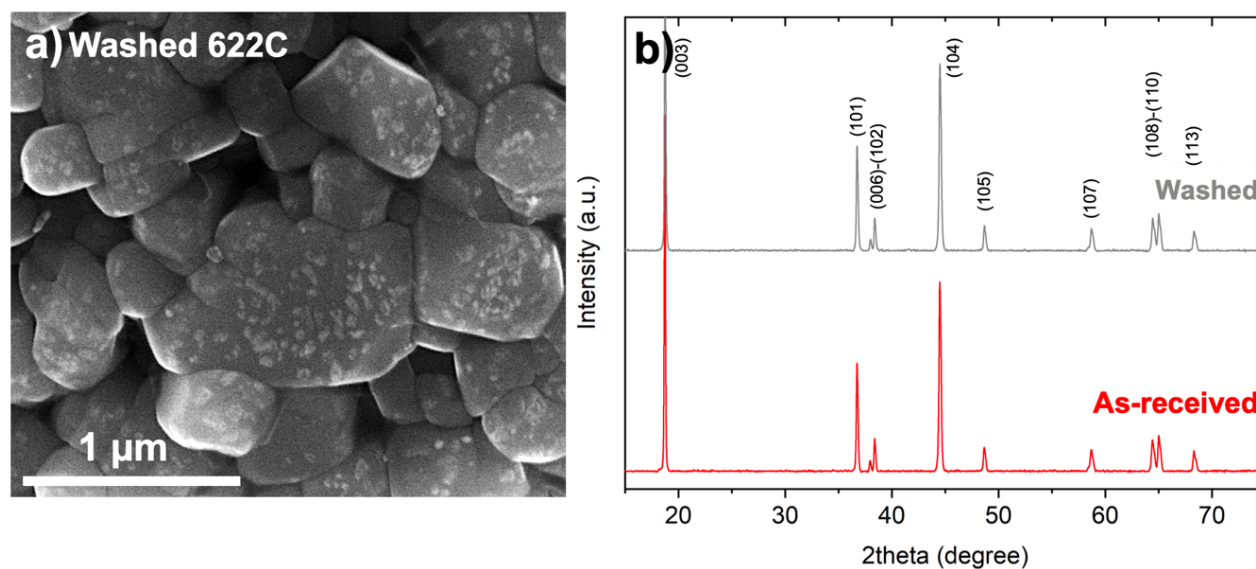


Figure II.8. a) Representative SEM picture of the alumina coating on the as-received NMC 622C and b) powder XRD patterns of as-received and washed 622C.

3.1.1.3. Impact of the powder-to-water mass ratio

Driven by the patents of Paulsen et al.^{1, 2, 24}, the NMC powder-to-water mass ratio of 1:20 was previously used for the solubilization procedure. Although the results unveiled complete soluble bases solubilization, this parameter was considered relevant to investigate with the aim of guaranteeing reliable measurements with, potentially, higher degrees of accuracy.

In the literature, Park et al.⁴⁴ stated that a mass ratio 1:1 of NMC 8 1.5 0.5/water and a washing time of 10 minutes is not enough to dissolve entirely the soluble bases, therefore proving that a bigger ratio is needed. On their side, Xiong et al.²⁸, performed the solubilization step for 20 minutes with a 1:2 and a 1:10 mass ratio, but only showed quantification from the 1:10 mass ratio, probably due to the inconvenience to obtain the filtrate solution from the 1:2 mass ratio solution. In light of these works, a compromise has to be found between the complete solubilization of Li_2CO_3 , a sufficient volume of water to be filtered, not wasting too much NMC powder and enough concentration of soluble bases to be titrated with accuracy.

For the sake of comparison with the previous 1:20 mass ratio (5 g in 100 ml), lower masses of 1, 2, 3 and 4 g of each NMC, corresponding to 1:100, 1:50, 1:33, 1:25 mass ratios, were stirred in an equivalent 100 ml volume of bi-distilled water. Fig. II.9a and b show the titrated amount of OH^- and CO_3^{2-} as a function of the powder-to-water mass ratio. The error bars were constructed from the standard deviation from three repetitions of each mass ratio and each material. The linear fit

of every material data indicates that all of tested mass ratios would be adequate in terms of soluble bases solubilization. However, for the mass ratios of 1:100 and 1:50, bigger standard deviations are found, so they must to be avoided to ensure reproducibility.

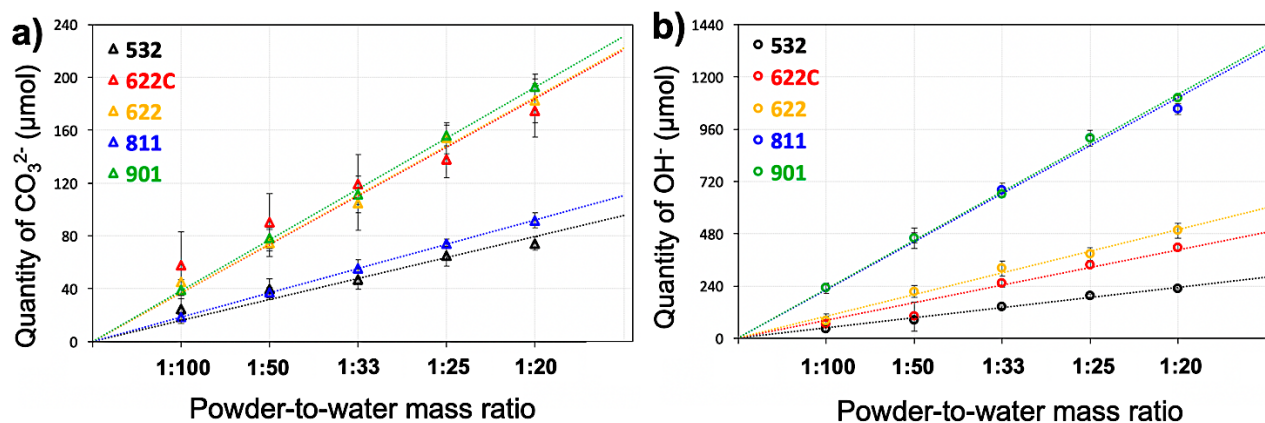


Figure II.9. a) OH^- and b) CO_3^{2-} amount in different powder-to-water mass ratios.

3.1.1.4. Optimized protocol for the solubilization and acid-base titration of soluble bases

All the experimental parameters hereabove optimized for the protocol of solubilization and quantification of soluble bases contained in as-received and exposed NMC materials are gathered in Table II.4. The whole protocol is detailed hereafter.

Table II.4. Protocol parameters for the solubilization and titration of soluble bases

	Chemicals		Duration		Atmosphere
Solubilization	NMC 3-5 g	bidist. H_2O 100 ml	532,622,622C 15 min.	811,901 8 min.	Ar bubbling
Filtration			5 min.		Ar flowing
Titration	Filtrate 50 ml	HCl 0.05 M			Ar bubbling

3 to 5 grams of the Ni-rich NMC material are weighed inside the argon-filled glove box and then taken out in a closed flask. Afterwards, the powder is put with 100 ml of bi-distilled water in a custom closed flask with an entrance and exit for argon gas. Immediately, the solution is magnetically stirred, for 8 or 15 minutes, depending on the nickel content.

Thereafter, the powder and the solution are recovered through vacuum filtering for five minutes maximum. A flux of argon is implemented around the system, to minimize air exposure. The recovered powder is vacuum-dried for 12h at 120°C, in a Büchi oven for future characterizations.

50 ml of the filtrate solution are weighed inside the customized closed flask of the automatic titrimeter, with three entrances for the pH electrode, the titrant solution of HCl 0.05 M and the argon bubbling. The acid-base titration analyses performed in dynamic titration mode ends when the pH reaches 3. The amount of CO_3^{2-} and OH^- is calculated from Eqs. II.19 and II.20.

3.1.2. Quantification of soluble bases in as-received materials through acid-base titration

After solubilization, the soluble bases contained in the filtrate solutions obtained from each as-received NMC material were titrated. As shown in Table II.5, The OH^- concentration varies between 40 and 214 $\mu\text{mol.g}_{\text{NMC}}^{-1}$, increasing with the nickel content from 532 to 901. The CO_3^{2-} quantity does not vary much and reaches a maximal value of 40 $\mu\text{mol.g}_{\text{NMC}}^{-1}$ in every NMC. It is worth noting that there is no significant difference between coated and uncoated 622 materials, which means that this type of alumina coating does not interfere with soluble bases solubilization, most probably because the particles' surface is unevenly covered, as shown by SEM previously.

Table II.5. Acid-base titration results of CO_3^{2-} and OH^- in the as-received materials. Error bars correspond to the standard deviation from three repetitions.

$\mu\text{mol.g}_{\text{NMC}}^{-1}$	532	622C	622	811	901
OH^-	40 ± 1	90 ± 2	103 ± 3	214 ± 5	214 ± 5
CO_3^{2-}	18 ± 1	37 ± 2	40 ± 2	19 ± 1	39 ± 2

3.2. Complementary quantification

The acid-base titration technique has proven to be a powerful technique for the accurate quantification of OH^- and CO_3^{2-} basic species. AAS and ICP-AES analysis of the filtrate solutions were required as complementary techniques to correlate the amount of CO_3^{2-} and OH^- with the Li^+ amount in the filtrate solution and to unveil the possible presence of other soluble salts. These elemental analyses were carried out on the remaining half of the filtrate solution.

3.2.1. Complementary analysis of filtrate solution through AAS

The AAS analysis of the filtrate solution is based on the energy absorption at a specific wavelength of an atom in the ground state. For each diluted sample, the concentrations were determined through comparison of the amount of absorbed light, to the calibration curves constructed with the standards of known concentration (protocol in Annex I).

Typically, the atomization of a lithium-containing solution into the AAS blue flame turns to yellow. However, upon atomization of the diluted filtrate solution, the flame turned to orange color, indicating that other dissolved metals co-exist with lithium. Indeed, sodium was also detected in noticeable concentrations. The synthesis of the transition metal precursors of NMC materials ($M(OH)_2$ and $MOOH$) requires the precipitation of MSO_4 ($M= Ni, Mn$ and Co) by $NaOH$ in the presence of ammonia solution as complexing agent^{2, 24}, consequently, sodium-based species might remain in the surface of the final materials.

For the sake of comparison, Fig. II.10 shows the quantification of lithium and sodium obtained by AAS and acid-base titration. Assuming that all soluble bases detected by acid-base titration were lithium salts, their concentrations were converted into lithium concentrations with the respective molar equivalences of 2 and 1 for Li_2CO_3 and $LiOH$.

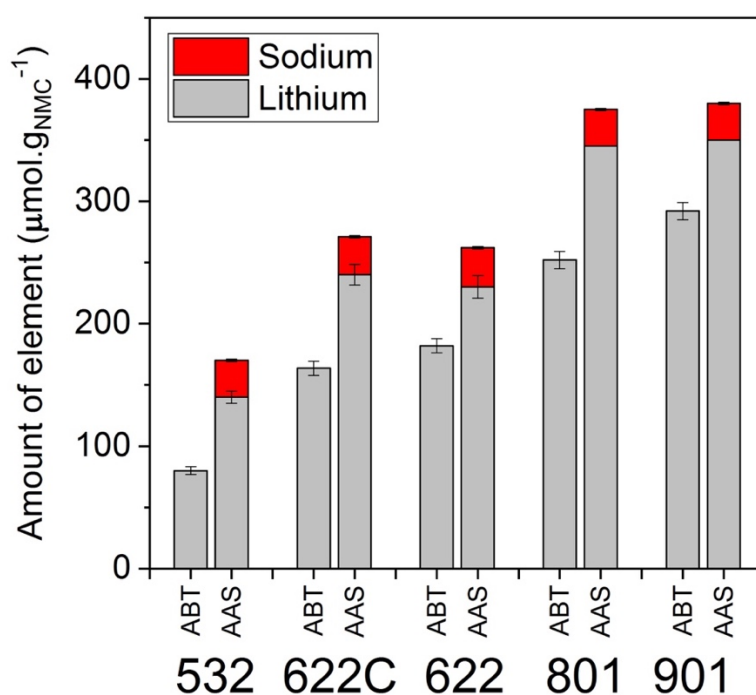


Figure II.10. Acid-base titration and AAS results comparison of lithium and sodium elements contained in the filtrate solutions.

Three main observations stand out from the AAS results:

- i. The lithium concentration increases with the Ni amount from 532 to 901 materials. These results are in line with those reported by Noh et al.³⁵, who quantified by titration 84, 171 and 806 $\mu\text{mol.g}_{\text{NMC}}^{-1}$ for NMC 532, 622 and 811, respectively; assuming, as above-reported, that all detected hydroxide and carbonate were lithium salts.
- ii. The lithium concentration values in each material are higher than those obtained from acid-base titration. This leads to the conclusion that some soluble lithium salts are not titrated due to a weak or a non-acid-base property.
- iii. Constant values of sodium are found for each NMC, in concentrations equal to $31 \pm 2 \mu\text{mol.g}_{\text{NMC}}^{-1}$, meaning that sodium does not depend on the NMC composition, but it remained from the synthesis in the same quantity, in each material.

Even though AAS is a powerful technique for elementary analysis, the temperature of the flame limits the detection of elements other than metals and over-estimation of Na^+ in the presence of Li^+ is possible, since both are easily ionizable elements that enrich the flame in electrons.

3.2.2. Complementary analysis of filtrate solution through ICP-AES

The ICP-AES equipment is capable to atomize a wider range of elements than AAS, since it does not require lamps to be changed. Only elements with significant concentrations were compared to calibration curves constructed with the intensities emitted by standards (protocol in Annex I).

For the sake of comparison, Fig. II.11 shows the acid-base titration, AAS and ICP-AES results obtained from the filtrate solutions of each NMC composition. ICP-AES analyses unveil noticeable concentrations of lithium, sodium and sulfur elements. The lithium concentrations determined by ICP-AES, are ranged within the standard deviation of the AAS data, corroborating that the lithium quantification by AAS was accurate. However, the sodium concentrations obtained by ICP-AES were found to be lower ($14 \pm 3 \mu\text{mol.g}_{\text{NMC}}^{-1}$) than by AAS ($31 \pm 2 \mu\text{mol.g}_{\text{NMC}}^{-1}$), confirming an over-estimation in the order of two and a half times. Moreover, the detection of sulfur suggests that some sulfur-based salts remain after synthesis at the surface of the material, in concentrations equal to $40 \pm 2 \mu\text{mol.g}_{\text{NMC}}^{-1}$. Assuming that the sulfur element detected by ICP-AES originates from sulfate(s) and considering the additional lithium, sodium

and sulfur concentrations detected by ICP-AES, it can be inferred that these elements are stemming from Li_2SO_4 and Na_2SO_4 compounds.

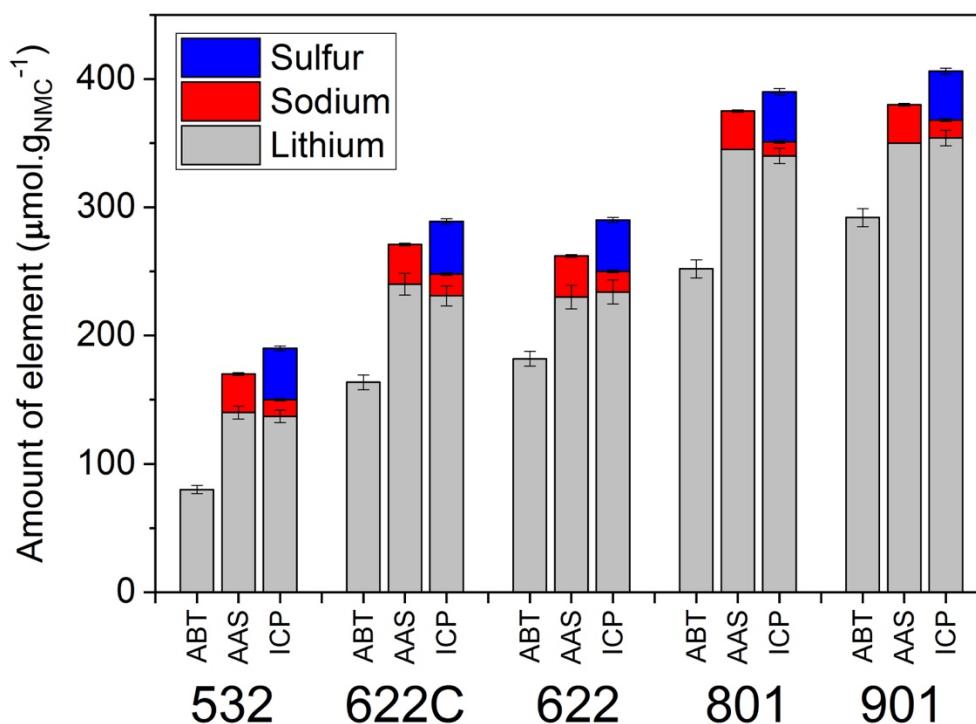


Figure II.11. Acid-base titration (ABT), AAS and ICP-AES results comparison of lithium (gray bars), sodium (red bars) and sulfur (blue bars) contained in the filtrate solutions.

These techniques allowed the identification of all soluble bases in the five types of NMC materials and gave reliable quantification results. It is worth noting that the implementation of both the titration and ICP techniques would have been sufficient for those studies; compared to AAS, sodium concentrations with higher accuracy and sulfur quantification can be achieved through ICP. We found that Li_2CO_3 and LiOH concentration values increase from 18 to 40 and from 40 to $214 \mu\text{mol.g}_{\text{NMC}}^{-1}$, respectively, with the nickel content in the different NMC materials. Furthermore, evidence was given that Li_2CO_3 and LiOH are not the only soluble species in as-received materials; M_2SO_4 ($\text{M} = \text{Li}, \text{Na}$) is present in all samples with an equal concentration of $40 \mu\text{mol.g}_{\text{NMC}}^{-1}$. This is the first time that lithium, sodium and sulfur-based salts have been identified and quantified thoroughly in a variety of NMC materials.

3.2.3. Complementary analysis of NMC materials through FTIR and SEM

FTIR analysis (protocol in Annex I) was performed on each as-received NMC material to evidence the presence of sulfate along with carbonate and hydroxide ions. FTIR spectra of

Li_2SO_4 , Li_2CO_3 and LiOH compounds are included as references with colored bands pertaining to the most prominent peaks (Fig. II.12).

The presence of sulfate species was confirmed in each as-received NMC spectrum through the ν S–O band of SO_4^{2-} (orange) centered at *ca.* 1125 cm^{-1} , confirmed by the Li_2SO_4 reference. Over the last two years, You et al.⁴⁵ showed a spectrum recorded on a freshly-synthesized $\text{LiNi}_{0.939}\text{Co}_{0.061}\text{O}_2$, in which a non-assigned band emerged in the same wavenumber range; thereafter, Sicklinger et al.²¹ attributed a peak in the same position in NCA to SO_4^{2-} species. As expected from acid-base titration results, all NMC materials revealed bands (blue) at 878 , 1425 and 1500 cm^{-1} assigned to the bending mode and the asymmetric and symmetric C–O stretching modes in CO_3^{2-} .^{4, 27} Intriguingly, there is no sign of the ν O–H band (green) near 3675 cm^{-1} of LiOH .^{6, 21} This raises questions about its presence in our materials, which will be further discussed in Chapter III.

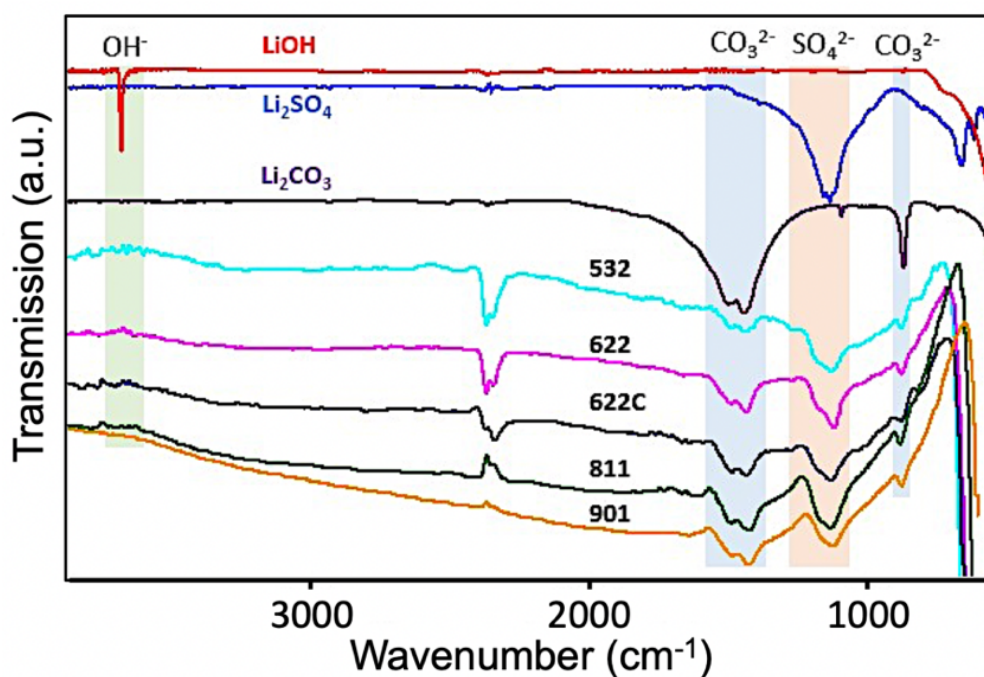


Figure II.12. FTIR-ATR (Ge crystal) spectra of as-received 532, 622, 622C, 811, 901 NMC; and Li_2SO_4 , Li_2CO_3 and LiOH reference compounds.

After confirmation of the presence of sulfate species (most probably Na_2SO_4 and Li_2SO_4) through ICP-AES and FTIR, the question arose as to whether they are well distributed in the material. In this regard, the SEM-EDX analysis of the as-received NMC materials disclosed the presence of micrometric particles not bigger than $10\mu\text{m}$ (ellipses in Fig. II.13a and e), whose shapes do not correspond to the granular morphology of NMC 532. The EDX analysis unveils both sodium and

sulfur elements on one spot (Fig. II.13a, b, c) and sulfur only on the other (Fig. II.13e, f, g); which suggests the existence of Na_2SO_4 and Li_2SO_4 , respectively, since lithium is too light to be detected by EDX.

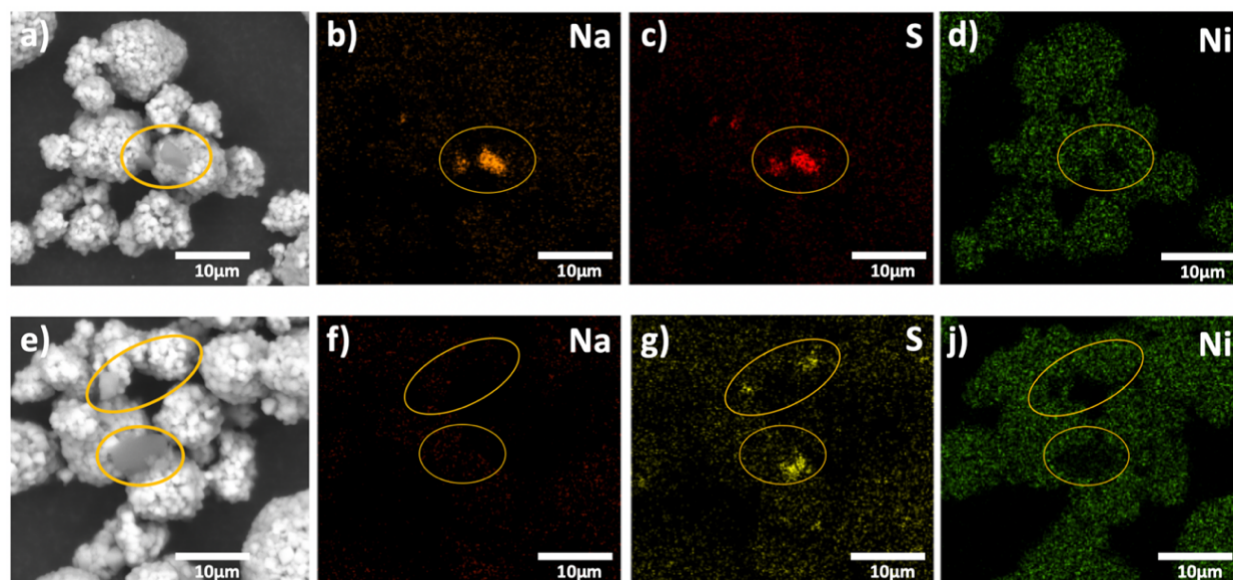


Figure II.13. a) and e) SEM images in backscattered (BSE) mode of the as-received NMC 532 material and their corresponding Na (b and f), S (c and g) and Ni (d and j) EDX mappings.

3.3. Conclusion

Thanks to a stepwise optimization of the washing and titration parameters (atmosphere composition, duration of the solubilization step and powder-to-water ratio), the soluble bases contained on the surfaces of NMC materials from synthesis or reactivity toward air atmosphere have been accurately quantified through acid-base titration. As compared to literature, their amounts were found to be relatively low with an OH^- concentration between 40 and 214 $\mu\text{mol.g}_{\text{NMC}}^{-1}$, increasing with the nickel content and a maximal CO_3^{2-} concentration value of 40 $\mu\text{mol.g}_{\text{NMC}}^{-1}$. The complementary techniques ICP-AES, FTIR and SEM/EDX evidenced the presence of Na_2SO_4 and Li_2SO_4 in similar concentrations ($40 \pm 2 \mu\text{mol.g}_{\text{NMC}}^{-1}$) as leftovers from the synthesis, whatever the material. Only the presence of LiOH was not confirmed through FTIR in the as-received materials, which leads to the hypothesis that it might originate from a hydrolysis reaction upon washing procedure. This assumption will be confirmed later while studying their reactivity in [Chapter III](#). This in-depth characterization of the surface species contained in the as-received materials provide us sound background data that will be meaningful

for deciphering the global formation mechanism of components grown upon exposure of NMC materials to a specific H₂O/CO₂ atmosphere.

4. Characterization of surface species in NMC materials exposed to specific atmospheres

As reported in [Chapter I](#), since the early 2000's, several investigations have been devoted to defining the impact of air exposure on NMC particles^{3, 5, 10-13, 17-19, 29, 30}. However, despite these very interesting works, reaction mechanisms regarding surface species formation still lack of clarification. Therefore, to gain insight into the composition of the surface species grown in air and their formation mechanisms, storage experiments under specific conditions were carried out.

4.1. Preliminary storage studies under Ar, CO₂, dry air and air atmospheres

10g of the five Ni-rich NMC materials were stored in open Petri dishes, for two weeks under four different atmospheres:

- **argon**, in the glove box (< 0.1 ppm O₂ and H₂O),
- **CO₂/Ar**, in an 8/92 molar ratio inside a closed desiccator,
- **dry air**, in the dry room (5 – 10 ppm of H₂O) and
- **air**, under a fume hood.

At the end of the storage time, the Petri dishes in the desiccator and dry room were closed and transferred without air exposure, to the glove box; whereas the powder stored in air was vacuum-dried in a Büchi oven for 24h at 120°C prior to being transferred to the glove box. Each powder was gently milled in a mortar inside the glove box to homogenize the sample, then weighed for the soluble bases quantification by acid-base titration (Fig. II.14a–e), following the optimized conditions reported in [Section 3.1.1.4](#).

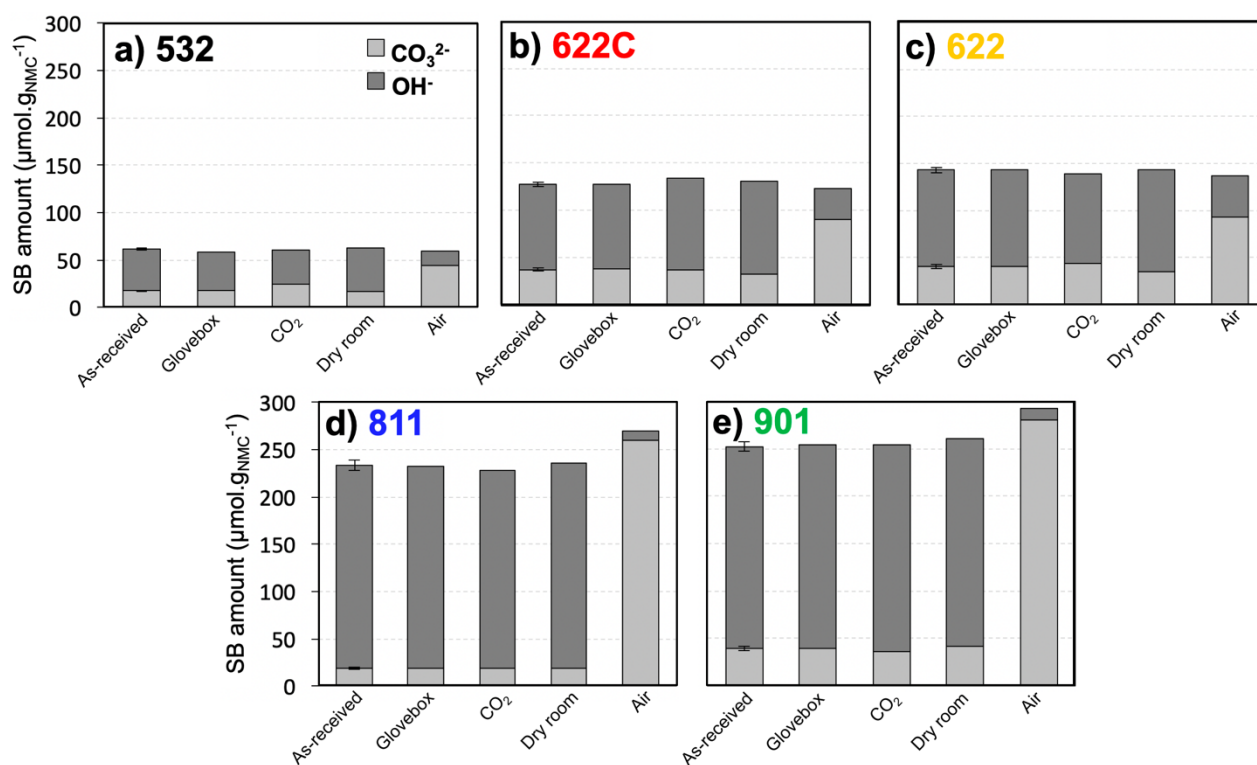
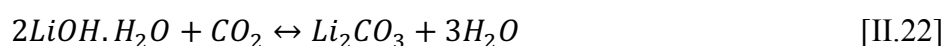


Figure II.14. Acid-base titration results of NMC materials **a) 532**, **b) 622C**, **c) 622**, **d) 811** and **e) 901**; in the as-received form and after storage in different atmospheres for two weeks.

As was foreseeable, the powders stored under argon do not present any soluble bases content change, as observed by other authors before^{30, 46} and the storage under CO_2/Ar and dry air entails very little variation, compared to the as-received materials. As a matter of fact, in these two atmospheres where CO_2 is available, no significant additional Li_2CO_3 is produced. This observation had also been featured by Matsumoto et al.¹⁷ and Faenza et al.⁶. The latter stored NCA powder in a bag containing only dry CO_2 gas (<10 ppm), and noticed that Li_2CO_3 was not produced. On the contrary, when stored under flowing air, Li_2CO_3 grew fast due to the presence of H_2O , which was already evidenced in Williams et al.'s work⁴⁷. A two-step reaction with hydrated lithium hydroxide as intermediary species (Eqs. II.21 and II.22) was proposed:



The NMC materials stored under air reveal a large amount of CO_3^{2-} , a part of which originates from the H_2O -assisted consumption of OH^- . The other part implies the formation of Li_2CO_3 through a delithiation process occurring at the NMC's surface, as suggested, very early, by

Goodenough's group¹⁴⁻¹⁶ in other type of layered materials. However, as reported in [Section 1](#) by several authors^{3, 5, 18, 20}, the degradation mechanism is a matter of controversy.

Therefore, clarifying this point was envisaged through promoting the NMC surface species growth under a controlled atmosphere of H₂O/CO₂/Ar (hereby simply called H₂O/CO₂); thus, satisfying the required simultaneous presence of CO₂ and H₂O.

4.2. Storage under specific H₂O/CO₂ atmosphere

10g of each NMC material were stored during **six days at 35°C**, inside a desiccator with a controlled atmosphere of 8/92 molar ratio of CO₂/Ar and with 90% of relative humidity. After exposure, the samples were vacuum-dried in a Büchi oven for 24h at 120°C, prior to being transferred to the argon-filled glove box. These materials stored in the atmosphere H₂O/CO₂ are called **exposed NMC** materials.

4.2.1. Acid-base titration quantification after H₂O/CO₂ storage

The amounts of soluble bases detected by acid-base titration in the exposed NMC materials are compared to the as-received and displayed in Fig. II.15a and b. In the as-received materials, mainly OH⁻ species are detected. After exposure, OH⁻ is detected only in the case of the NMC materials containing highest Ni contents, 811 and 901, and its concentration does not exceed 30 μmol.g_{NMC}⁻¹. It is worth noting that the 811 values are close to the ones reported in literature for a 811 material (diameter ~25μm) exposed for 7 days in air, as being 82 and 257 μmol.g_{NMC}⁻¹ for LiOH and Li₂CO₃, respectively²¹. Note that the amount of soluble bases increases with the Ni³⁺ concentration in both as-received and exposed materials, which was also previously observed by You et al.⁴⁵.

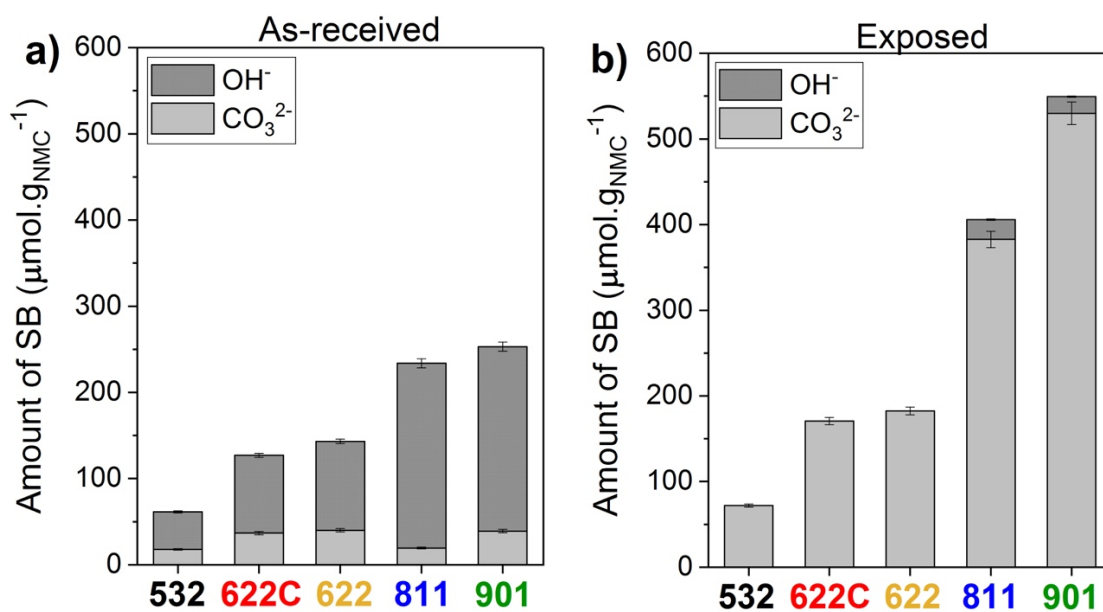


Figure II.15. Amounts of OH^- and CO_3^{2-} determined by the analysis of the filtrate solution from the **a)** as-received and **b)** exposed ($\text{H}_2\text{O}/\text{CO}_2$ atmosphere for 6 days) NMC materials.

Concerning Li_2SO_4 and Na_2SO_4 , a question may arise on their chemical behavior toward the $\text{H}_2\text{O}/\text{CO}_2$ exposure atmosphere. In fact, they are chemically inert toward CO_2 gas, but would hydrate in presence of the humid atmosphere into lithium sulfate monohydrate ($\text{Li}_2\text{SO}_4 \cdot \text{H}_2\text{O}$) and sodium sulfate decahydrate ($\text{Na}_2\text{SO}_4 \cdot 10\text{H}_2\text{O}$). On the basis of the ICP-AES results (Section 3.2.2), a maximum H_2O concentration of $150 \mu\text{mol.g}_{\text{NMC}}^{-1}$ could be uptaken. Since $\text{Na}_2\text{SO}_4 \cdot 10\text{H}_2\text{O}$ decompose peritectically at 32.4°C to yield anhydrous Na_2SO_4 ⁴⁸ and $\text{Li}_2\text{SO}_4 \cdot \text{H}_2\text{O}$ dehydrate around $100\text{--}120^\circ\text{C}$ ⁴⁹, the water removal is expected to occur after the exposure, upon the drying process at 120°C .

Furthermore, from the acid-base titration results, the reacted lithium quantity was calculated (Eq. II.23), assuming that all of the carbonate and hydroxide salts are lithium salts. The results are shown in Table II.6. Lithium quantity was found to increase with the amount of nickel in NMC. For the exposed 532, 622 and 622C materials, the molar percentage of extracted lithium does not exceed 2 mol%. Likewise, exposed NMC 622C and 622 display very close values of 1.72 and 1.77 mol%, respectively, demonstrating that the alumina coating does not prevent soluble bases formation upon $\text{H}_2\text{O}/\text{CO}_2$ exposure. More substantially, values as high as 5 and 8 mol% were reached for 811 and 901 materials, respectively, in only six days of exposure. These elevated values were expected as a higher reactivity toward CO_2 was reported in literature to depend on Ni^{3+} content²⁶. For the sake of comparison, from titration analysis, Bichon et al.³⁴ reported 0.3 mol% of extracted lithium from a 532 material exposed in air for one year and Matsumoto et

al.¹⁷, a value of 8 mol% for a NCA material exposed for 500 hours to air. Owing to the prominent extraction of lattice lithium, these materials are expected to experience cation mixing and structural transformations in the near-surface region^{3, 5, 46}.

$$Reacted Li = \frac{n_{Li_{exposed}} - n_{Li_{as-received}}}{n_{NMC}} * 100 \quad [II.23]$$

Table II.6. Lithium content and reacted percentage in as-received and exposed (H₂O/CO₂ for 6 days) NMC materials.

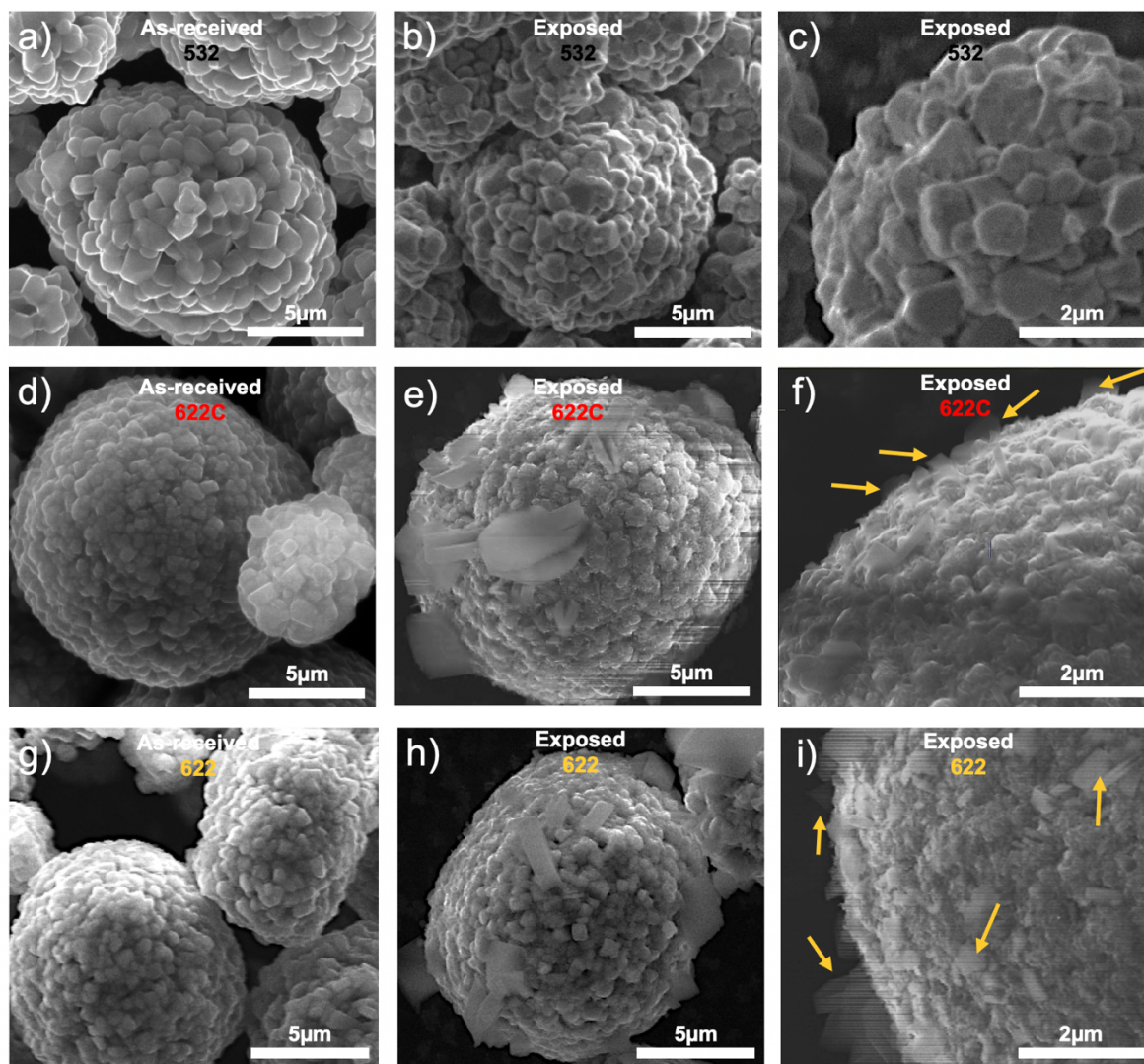
Lithium quantity	532	622C	622	811	901
as-received ($\mu\text{mol.g}_{\text{NMC}}^{-1}$)	80 ± 3	164 ± 6	182 ± 6	252 ± 7	292 ± 7
exposed ($\mu\text{mol.g}_{\text{NMC}}^{-1}$)	143 ± 4	341 ± 8	365 ± 9	788 ± 20	1079 ± 27
reacted (mol %)	0.63 ± 0.01	1.72 ± 0.01	1.77 ± 0.02	5.40 ± 0.03	7.90 ± 0.03

4.2.2. Further investigations through SEM and FTIR

The prominent delithiation process that happened upon H₂O/CO₂ storage, certainly induces surface textural modification, clearly observed through SEM analysis (Fig. II.16a-o). In the exposed NMC 532 (Fig. II.16b, c), almost no noticeable soluble bases growth took place, in comparison to the as-received material (Fig. II.16a). This result agrees with the acid-base titration results of the exposed NMC 532, that showed only 0.63 mol% of reacted lithium. In the exposed NMC 622C and 622, where heavier delithiation occurs, the growth of flakes (up to 4 μm) can be observed at the outermost surface of the materials (Fig. II.16e, f, h, i). Astonishingly, exposed NMC 811 and 901 present substantial surface textural modifications. The flakes form a shell-like layer that covers, almost completely, the granular morphology (Fig. II.16k, l, n, o). Some particles depict a non-uniform shell (denoted with ellipses) which we suppose is the result of an uneven exposure to H₂O/CO₂.

This SEM investigation visually shows the extent to which the surface is affected by the H₂O/CO₂ exposure, with a clear dependence on the Ni content. It is supposed that the degradation reactions start at the surface of the material and form a thin film, as it has been observed before^{25, 28, 44}, then, once the products are crystallized enough, flakes become visible. When these reactions

are favored due to the high reactivity of the material, the flakes form a thick layer that tends to detach from the NMC surface, as in the case of NMC 811 and 901. Interestingly, Cho et al.⁵⁰ performed time-of-flight secondary ion mass spectroscopy (ToF-SIMS) analysis in an air-exposed NMC 730, and revealed that the Li_2CO_3 layer lies above the LiOH layer and both of them are situated above the granular morphology of NMC 730.



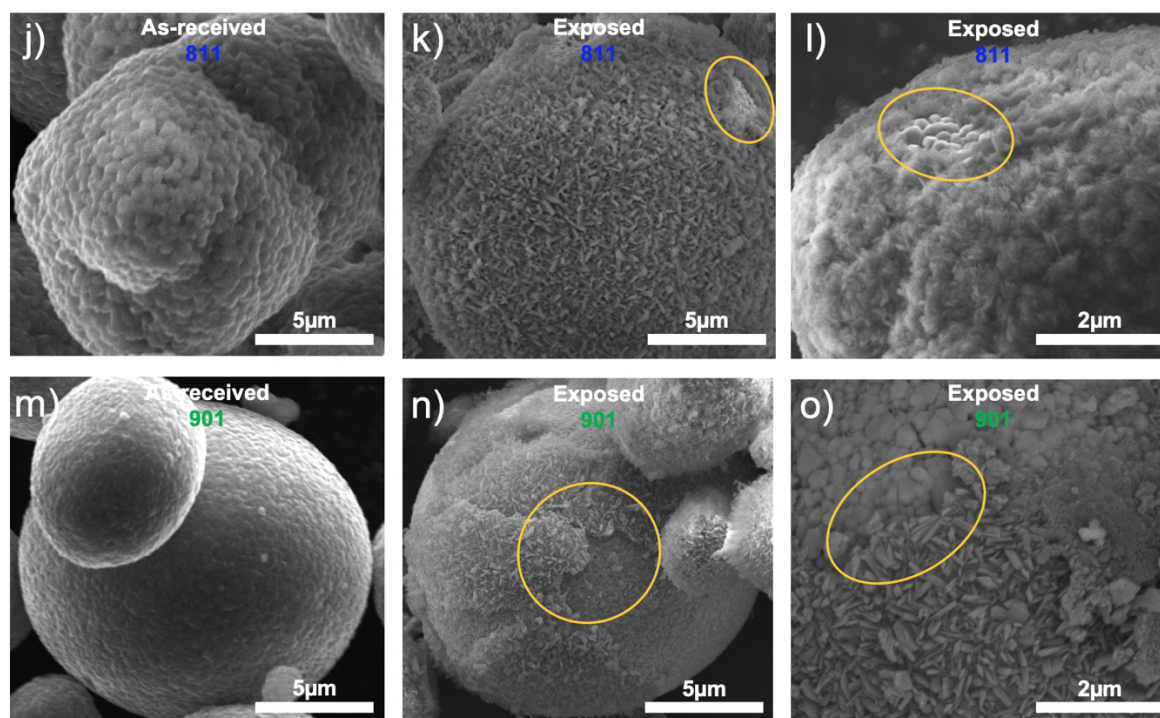


Figure II.16. Representative SEM images of as-received and exposed 532, 622C, 622, 811 and 901 materials for 6 days under $\text{H}_2\text{O}/\text{CO}_2$ atmosphere. Arrows point Li_2CO_3 flakes growth.

In the literature, estimates of the layer thickness through high-resolution transmission electron microscopy (HRTEM) have been reported. For the sake of comparison, a layer of ~ 6 nm thick and 3.5–5 nm thick was depicted at the surface, respectively, of an exposed NMC 622 (28 days in at 55°C and 80% RH)²⁵ and NMC 811 (30 days in air)²⁸. The growth of Li_2CO_3 with average crystallite size of 50 nm into a layer of around 75 nm thick, was found in an exposed NMC 8-0.5-1.5 (2 years in air)⁴. When compared, for instance, with the layer thickness of the exposed 811, estimated to <150 nm from Fig. II.16l, it can be inferred that the specific atmosphere chosen in this study is very efficient in promoting fast degradation.

In order to assess the surface degradation state over an extended time, NMC 622C was stored under similar conditions, during 6, 10, 20, 36 and 120 days and the resulting soluble bases were quantified by acid-base titration. Fig. II.17 shows the evolution of Li^+ amount as function of the square root of the storage time. It can be observed that the production of soluble bases follows a linear relationship up to 36 days of storage, confirming the kinetics observed by Chen et al.²⁵, who stored an NMC 622 up to 42 days in air at 55°C and 80% RH. However, from there, the linear relationship is lost and the degradation rate decreases owing to the difficulty to extract deeper lithium. At 120 days of 622C exposure, the reacted lithium amount reaches an astonishing percentage of 7.2 mol%.

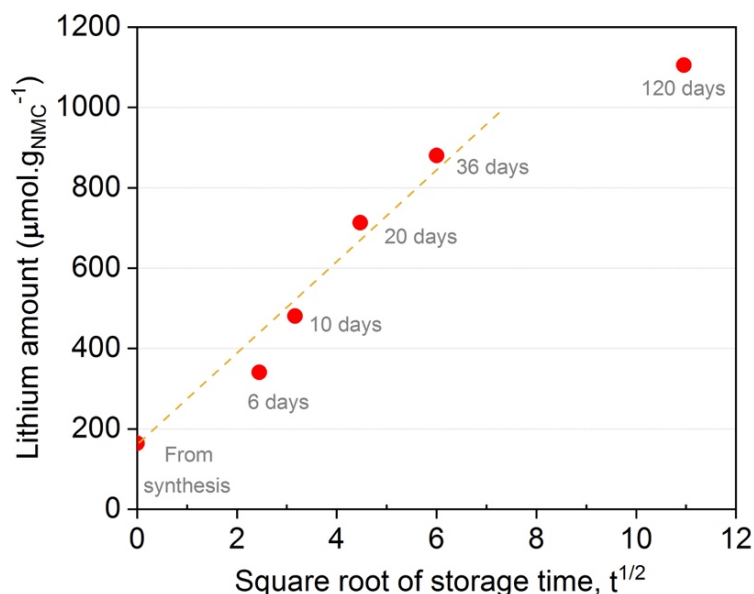


Figure II.17. Delithiation evolution determined by acid-base titration vs. the square root of the storage time in $\text{H}_2\text{O}/\text{CO}_2$ atmosphere.

Thanks to sulfate species acting as internal standard, evidence to the relationship between the nickel content and the Li_2CO_3 growth can be provided by the FTIR-ATR analysis of the powders exposed for 6 days to $\text{H}_2\text{O}/\text{CO}_2$ atmosphere (Fig. II.18). Since it was determined previously by ICP-AES that all of the as-received materials contain the same sulfate quantity and that it does not react toward the $\text{H}_2\text{O}/\text{CO}_2$ atmosphere, the spectra were normalized by the sulfate band, clearly visible after exposure. The intensity of the Li_2CO_3 bands around 875 , 1320 and 1490 cm^{-1} agrees well with the amount of Li_2CO_3 found by acid-base titration, in the sense that NMC 532 is the material with the lower amount and 901 has the highest, whereas 622C and 622 have pretty close amount. Hence, this FTIR analysis turns out to be a convenient and fast way to evaluate the degradation state of sulfate species-containing NMC surface upon air exposure. Moreover, if the normalized integrated area of the $1300 - 1600\text{ cm}^{-1}$ peaks of NMC 532 is defined as x , the other compositions are $2.4x$, $3.1x$, $6.2x$ and $10.5x$, in ascendant nickel content, respectively. If the same reasoning is applied to the titration results ($x = [\text{CO}_3^{2-}]_{532}$), we found $2.4x$, $2.5x$, $5.3x$ and $7.4x$. Owing to the proximity of the values, we can consider FTIR peak integration, through a sulfate peak normalization, as a semi-quantitative method.

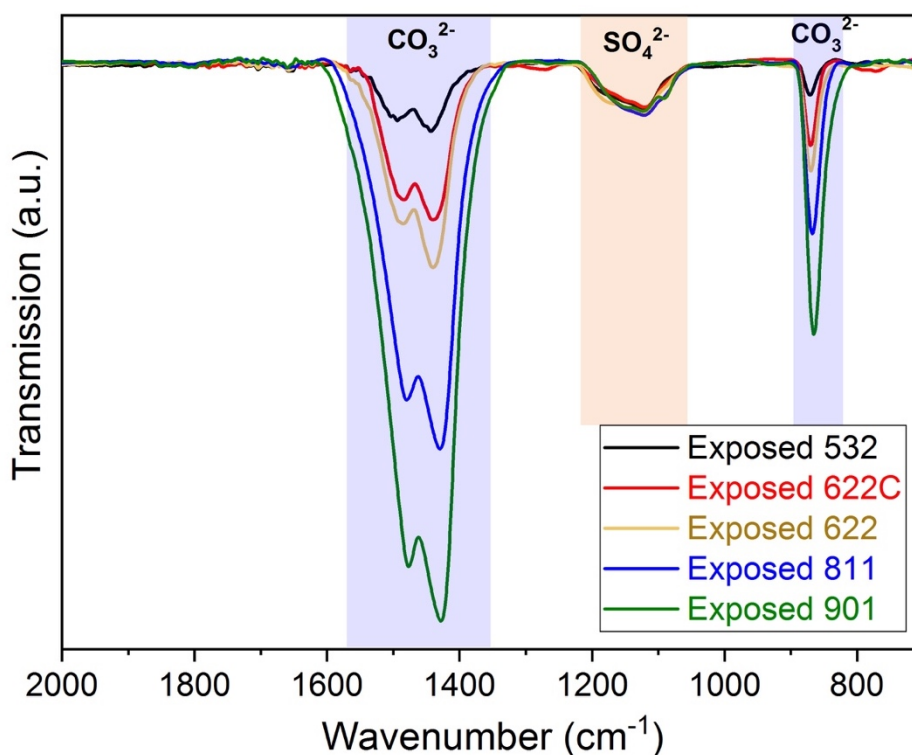


Figure II.18. FTIR-ATR spectra of the exposed NMC materials stored for 6 days in H₂O/CO₂ atmosphere.

Overall, quantifying soluble bases after exposure to the H₂O/CO₂ atmosphere helped estimate the incremental reactivity of Ni-rich NMC materials as a function of the nickel content. Such exposure enlightens the transformation of LiOH into Li₂CO₃ along with the delithiation of the materials to produce more soluble bases. As unveiled in literature, other metal-based surface species may also form, which prompted us to pursue investigations through thermal analysis.

5. Deciphering the degradation mechanisms through thermal analysis

The soluble bases, LiOH and Li₂CO₃, decompose respectively above 400°C into Li₂O and H₂O⁵¹, and above 700°C into Li₂O and CO₂⁵² (Eqs. II.24 and II.25). Therefore, from the thermogravimetric analysis coupled with mass spectrometry (TGA-MS) of the exposed materials, only CO₂ and H₂O are potentially detected at those temperatures.



5.1. Thermal analysis of as-received NMC materials

All the NMC materials were analyzed in a TGA-MS instrument placed inside an argon-filled glove box, the experimental conditions can be found in Annex I. Fig. II.19a–d display the TG and CO₂ (m/z 44), O₂ (m/z 32) and H₂O (m/z 18) MS curves for each as-received material.

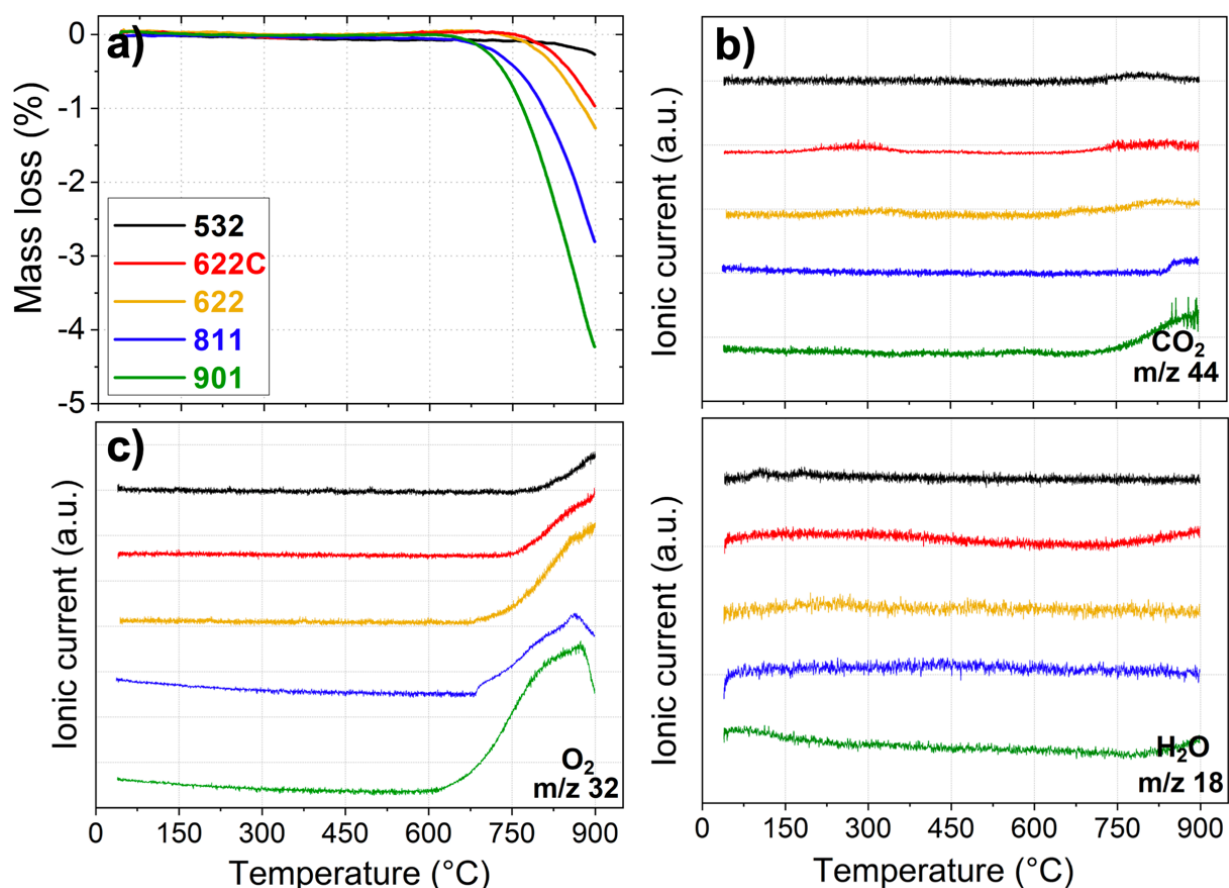
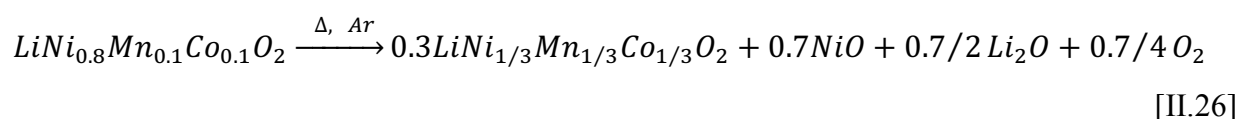


Figure II.19. a) TGA curves of as-received NMC materials and mass traces of b) CO₂ (m/z 44), c) O₂ (m/z 32) and d) H₂O (m/z 18).

TGA curves do not present noticeable weight losses between 40 – 600°C, until the characteristic thermal decomposition of NMC above 600°C, associated with O₂ evolution. The figures clearly demonstrate the influence of the increasing Ni³⁺ content, as 532 and 901 materials start decomposition at 800 and 625°C, respectively. Since these experiments were performed under argon flow (O₂ < 2ppm), the oxygen partial pressure was not sufficiently elevated to stabilize the Ni³⁺ oxidation state at these high temperatures, leading to its reduction through the following structural transformation, exemplified for NMC 811 (Eq. II.26):



Noteworthy that H₂O (m/z 18) evolution profile does not depict any noticeable weight loss around the temperature where the thermal degradation of LiOH should take place, here again suggesting that LiOH is not contained in as-received NMC. On the other hand, the CO₂ (m/z 44) profile presents a minimal increase above 700°C resulting from the low amount of Li₂CO₃. Note that, SO₂ could not be detected as Li₂SO₄ and Na₂SO₄ decompose above 900°C⁵³.

5.2. Thermal analysis of exposed NMC materials

The H₂O/CO₂ exposed materials present two main weight loss regions between 150–450°C and above 650°C (Fig. II.20a).

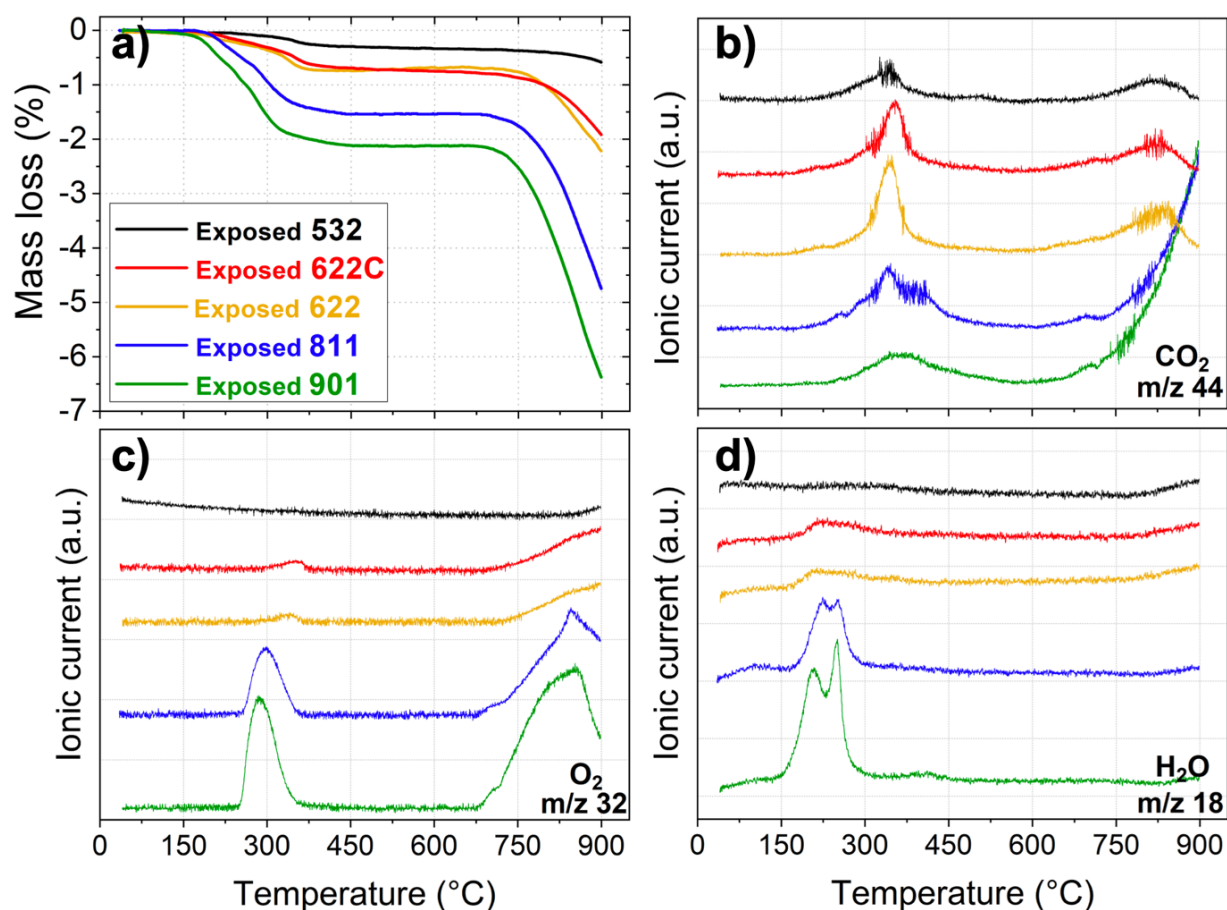


Figure II.20. a) TGA curves of exposed (H₂O/CO₂ for 6 days) materials and mass traces of b) CO₂ (m/z 44), c) O₂ (m/z 32) and d) H₂O (m/z 18).

In the region above 650°C, the evolution of O₂ (Fig. II.20c) is coherent with regard to the material bulk decomposition, as above-mentioned. The exposed materials display higher Li₂CO₃ concentration than the as-received, therefore, in the same temperature region, heavier CO₂ (m/z 44) production is observed (Fig. II.20b).

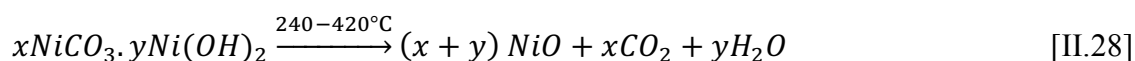
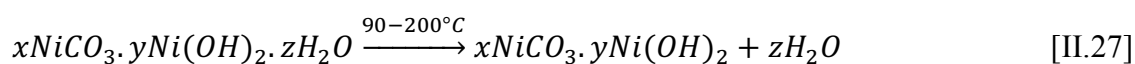
The weight loss in the 150–450°C region, pertaining to the decomposition of the surface species formed during the H₂O/CO₂ exposure, increases from 0.4 to 2.13 wt.% with the increasing Ni³⁺ amount in the materials. Note that maximum values of 3.7–4 wt.% have been reported^{5, 25} in the literature.

The gases detected in this region (Fig. II.20b–d) are H₂O (m/z 18), CO₂ (m/z 44) and O₂ (m/z 32). First, H₂O evolves from each material between 150 to 300°C, displaying an almost undetectable to a clear two-step signal from NMC 532 until 901. CO₂, on the other hand, is detected between 200–550°C, far below the Li₂CO₃ decomposition temperature range, and the peak broadens with the Ni³⁺ content. Lastly, O₂ is also produced between 250–370°C.

In the literature, CO₂ produced at low temperature is believed to originate from the decomposition of adsorbed carbonate-containing species. Comforted by the fact that H₂O and CO₂ peaks evolved simultaneously around 270°C, Liu et al.⁵ proposed the decomposition of LiHCO₃ into Li₂O, H₂O and CO₂. However, the existence of LiHCO₃ as a solid compound can be thermodynamically ruled out. The other reported explanation for H₂O and CO₂ evolution at low temperature, is the decomposition of cobalt (+II) and manganese (+II) carbonate hydrate (CoCO₃·H₂O and MnCO₃·H₂O) and of NiCO₃·Ni(OH)₂·xH₂O, proposed by Gasteiger's group^{21, 22}. However, they do not provide a mechanism that considers the release of O₂ between 250–370°C or that explain the reduction of Co³⁺ and Mn⁴⁺ to divalent metals.

So as to ascertain the existence of NiCO₃·2Ni(OH)₂·xH₂O in the exposed materials, a commercial reference powder of NiCO₃·2Ni(OH)₂·1H₂O (Alfa Aesar, >99% purity) was analyzed by TGA-MS (Fig. II.21), under the same conditions. Its thermal decomposition took place in two steps^{54, 55}:

- i. the dehydration between 90–200°C (Eq. II.27), at a lower temperature range than what was detected in the exposed materials (150–300°C); and
- ii. the decomposition of the hydroxycarbonate between 240–420°C (Eq. II.28) with simultaneous production of CO₂ and H₂O, contrary to the exposed materials where the H₂O preceded CO₂.



Furthermore, the O₂ produced around 300°C from exposed NMC materials is neither predicted in the hereabove decomposition reactions nor detected in the TGA-MS. In short, since the weight losses and onset temperatures do not match with what has been found in any of the exposed NMC materials, the existence of NiCO₃·2Ni(OH)₂·1H₂O is questionable.

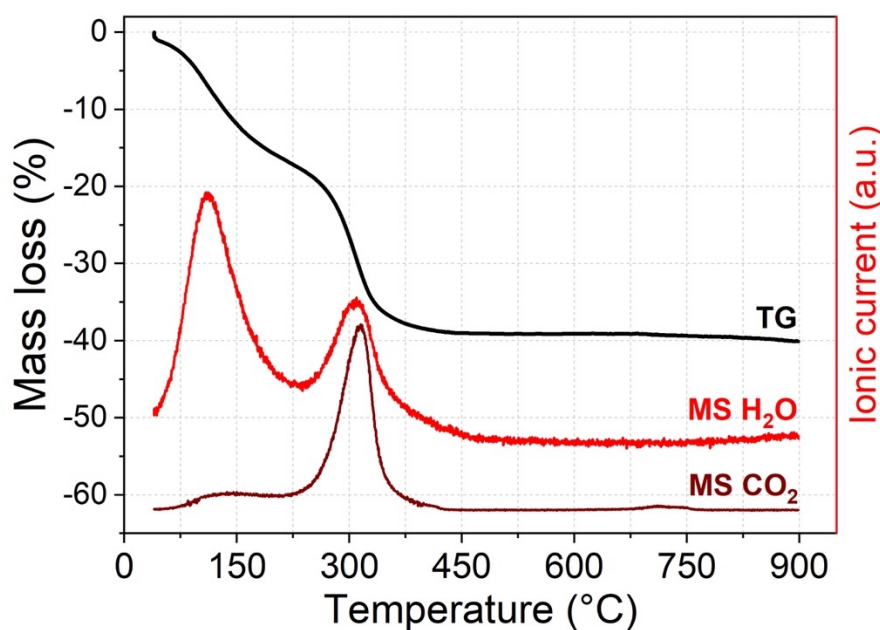
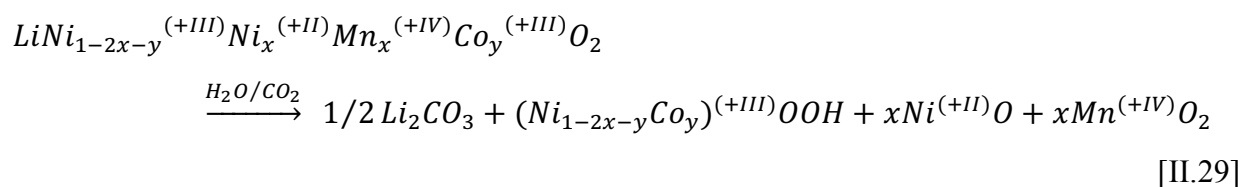


Figure II.21. TGA-MS curves of $\text{NiCO}_3 \cdot 2\text{Ni}(\text{OH})_2 \cdot \text{H}_2\text{O}$ reference.

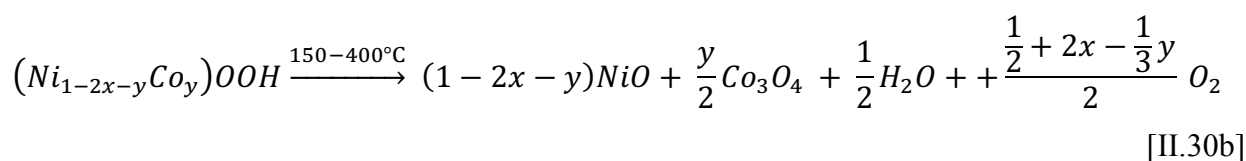
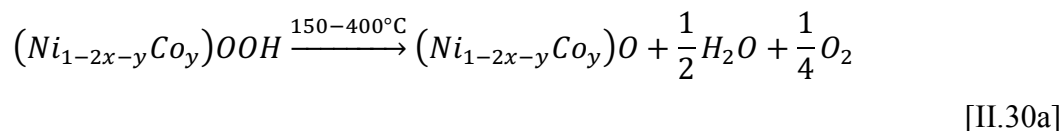
5.3. Proposed degradation mechanism

In light of the TGA-MS results and the quantification of soluble bases in the exposed materials, a novel degradation mechanism is proposed. Upon $\text{H}_2\text{O}/\text{CO}_2$ exposure, LiOH turns into Li_2CO_3 , and the production of more Li_2CO_3 is accompanied by lithium extraction reactions, this process increasing with the Ni^{3+} content. Considering that the soluble bases formation takes place in every NMC, regardless of the presence of Ni^{3+} to be reduced^{3, 29, 30}, it is plausible to consider that no redox process takes place during exposure and that the metallic elements maintain their oxidation state. As a consequence, the Li_2CO_3 production can be explained by the transformation of the NMC materials into nickel or cobalt oxyhydroxide $(\text{Ni}_{1-2x-y}\text{Co}_y)\text{OOH}$; NiO and MnO_2 ; in accordance with the proposed following reaction (Eq. II.29):



As cobalt presents an oxidation state of Co^{3+} , it is highly probable that it forms also an oxyhydroxide compound. Following this proposition, NMC 901 is more prone to degrade in $\text{H}_2\text{O}/\text{CO}_2$ atmosphere than NMC 532, because it possess higher content of Ni^{3+} , whose bonding energy to oxygen in the octahedral MO_2 structure is smaller than for Co^{3+} or Mn^{4+} ⁵⁶.

Furthermore, the presence of oxyhydroxides is supported by the fact that NiOOH decomposes between 150–400°C, into NiO along with H₂O and O₂ release⁵⁷; precisely in the temperature range where O₂ and H₂O were detected in the TGA-MS experiments of the exposed materials. In this case, the reaction would be (Eq. II.30a and b):



Nonetheless, the formation of oxyhydroxide compounds does not explain the CO₂ production in the 250–450°C range, far from the decomposition temperature of Li₂CO₃. An alternative explanation is the CO₂ production from the consumption of Li₂CO₃ by a re-lithiation solid-state reaction occurring at low temperature^{58, 59}. In this regard, a reaction of this type is likely to occur in the exposed materials with the oxyhydroxide decomposition products and Li₂CO₃. To validate this theory and acquire more insight into the thermal decomposition process, an exposed NMC 811 sample was subjected to water washing procedure, to solubilize all Li₂CO₃. Afterwards, the sample was analyzed by TGA-MS.

Fig. II.22 shows the comparison of the 6-days exposed NMC 811 before and after washing. Up to 300°C, the weight loss profile is identical for both samples and H₂O and O₂ gas evolve in a similar way. This result supports the proposed mechanism (Eq. II.29) involving the formation of oxyhydroxides; these compounds present a low solubility in water^{60, 61} and thus remain at the surface of the particles after the solubilization procedure.

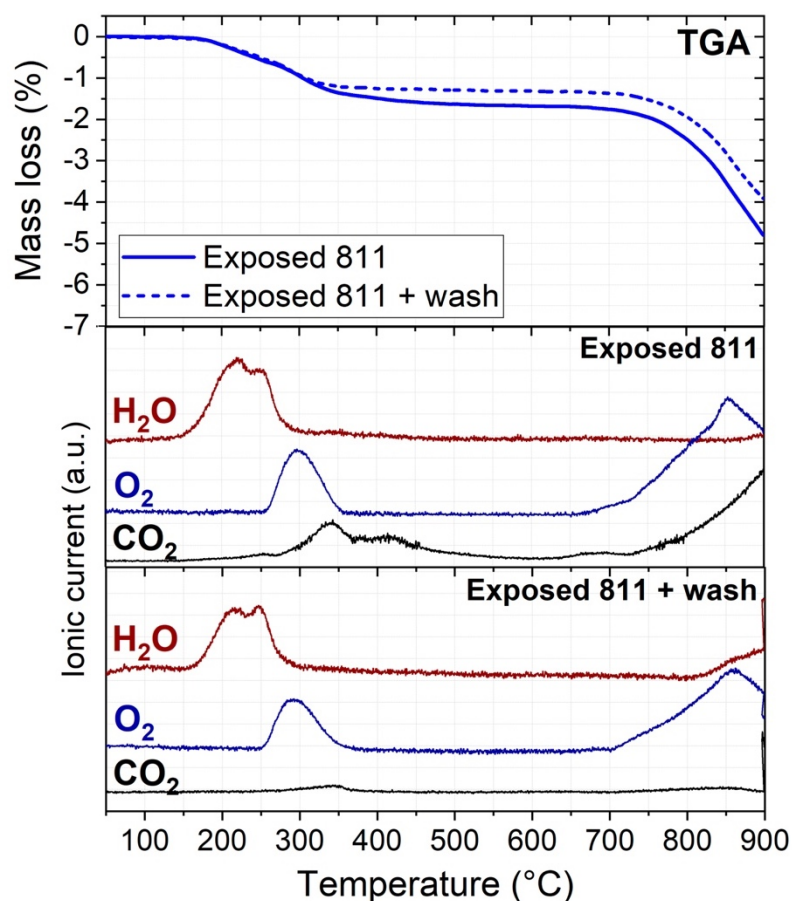
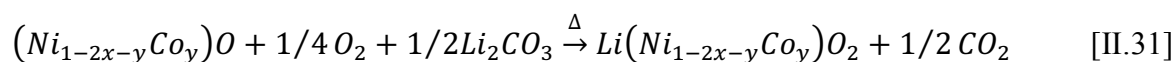


Figure II.22. TGA curves along with mass traces of H₂O (m/z 18), O₂ (m/z 32) and CO₂ (m/z 44) of an NMC 811 exposed (H₂O/CO₂ for 6 days) and exposed + washed.

Beyond 300°C, the weight loss depicted for the exposed + washed material is less important (of 0.35 wt.%) than for the exposed sample. The CO₂ gas is almost undetectable along the complete temperature range, indicating that nearly all Li₂CO₃ was removed from the surface. Considering these results, we propose the following reaction to explain the CO₂ evolution below 500°C from an exposed material; the metal oxides produced by the thermal decomposition of (Ni_{1-2x-y}Co_y)OOH (Eq. II.30) reacts in-situ, upon the thermal analysis, with O₂ and Li₂CO₃, to form layered oxides and gaseous CO₂, following the chemical reaction exemplified for the mixed oxide (Eq. II.31):



Remarkably, the shell-like degradation layer in the exposed NMC 811 (Fig. II.23a) disappears after washing (Fig. II.23b). This means that this layer is composed mainly of Li₂CO₃ and that insoluble (Ni_{1-2x-y}Co_y)OOH, NiO and MnO₂ species are located into the surface degradation

layers at the extreme surface of NMC particles. This is in accordance with the presence of NiO of rock-salt structure and other crystalline structures detected at the surface of air-exposed materials by HRTEM^{20,25,28}, that were wrongly attributed by Xiong et al.²⁸ and Chen et al.²⁵ as the result of processes involving the reduction of Ni³⁺ to Ni²⁺.

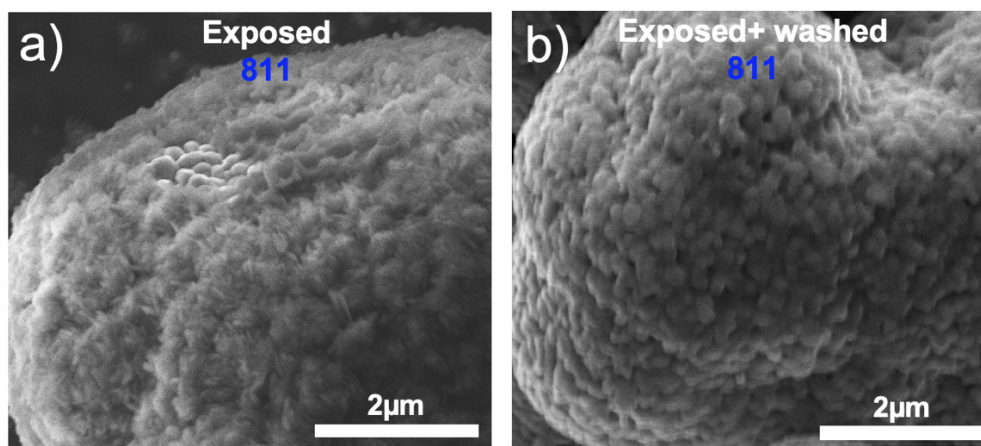
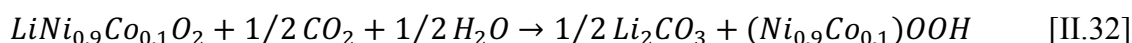


Figure 2.23. Representative SEM images of a) exposed (H₂O/CO₂ for 6 days) and b) exposed 811 after washing.

Only last year, during the course of this thesis, Jeong et al.⁶² and Pritzl et al.⁴⁰ also insinuated the formation of CoOOH and NiOOH compounds at the surface of LiCoO₂ and Ni-rich NMC materials, respectively, due to Li⁺/H⁺ exchange upon washing procedure. Interestingly, same O₂ and H₂O TGA-MS profiles were obtained from the water-exposed LiNi_{0.85}Co_{0.10}Mn_{0.05}O₂ between 120 and 450°C, without CO₂ evolution⁴⁰, which supports our hypothesis of the in-situ reaction of Li₂CO₃ consumption (Eq. II.31). Unfortunately, they not propose any formation mechanism.

5.4. Attempts to characterize surface species in exposed NMC through Raman and XRD

According to the assumption that nickel hydroxycarbonate (NiCO₃.2Ni(OH)₂.xH₂O) as a surface specie can be detected on NMC through Raman spectroscopy²², supplementary investigation was conducted (protocol in Annex I) to characterize the surface species that grew in the exposed 901 material. Owing to the absence of Ni²⁺, its decomposition reaction during exposure would not yield NiO and MnO₂, but only (Ni,Co)OOH (Eq. II.32):



Reference spectra of NiCO_3 , CoCO_3 , MnCO_3 , $\text{NiCO}_3 \cdot 2\text{Ni}(\text{OH})_2 \cdot \text{H}_2\text{O}$, $\text{Ni}(\text{OH})_2$, $\text{LiOH} \cdot \text{H}_2\text{O}$ and Li_2CO_3 were also recorded for comparison purposes. As shown in Fig. II.24, the exposed NMC 901 exhibits the characteristic metal oxide broad Raman signal between $250 - 650 \text{ cm}^{-1}$, attributed to the combination of the M–O symmetrical stretch and O–M–O bending vibration modes²⁵, and bands at 1080, 1010, 200 and 160 cm^{-1} pertaining to the surface species. The peaks at 1080, 200 and 160 cm^{-1} are characteristic bands of Li_2CO_3 (yellow arrows)^{25, 29}. Unfortunately, the small peak at 1010 cm^{-1} remains unidentified.

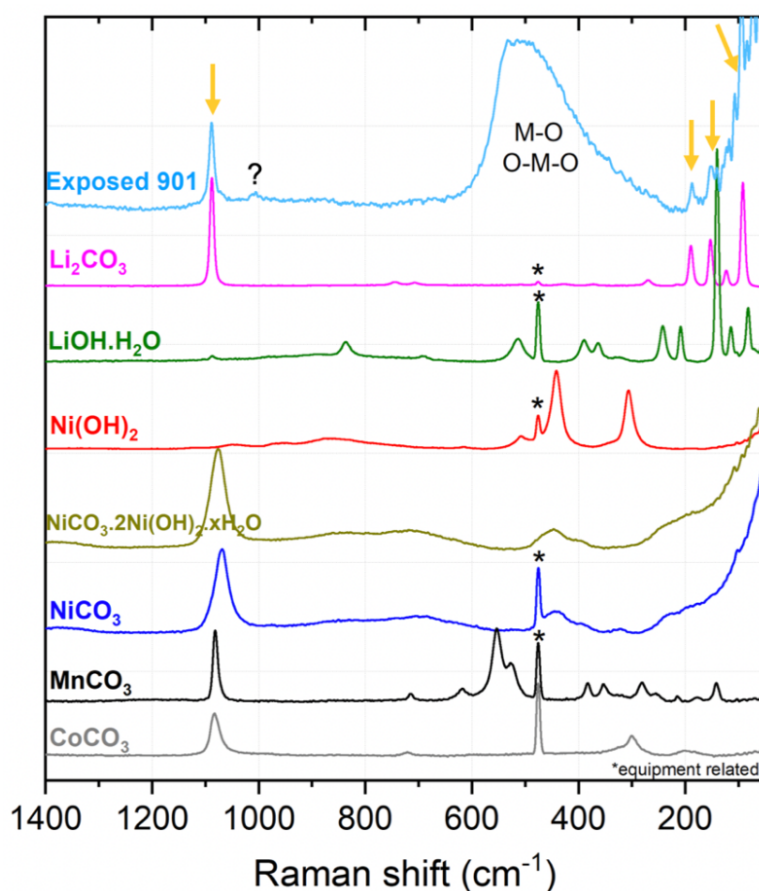


Figure II.24. Raman spectra of the exposed NMC 901 ($\text{H}_2\text{O}/\text{CO}_2$ for 6 days) and several references.

Contrary to the work by Jung et al.²² performed on a 1-year air exposed NMC 811, any of the peaks at $\sim 615 \text{ cm}^{-1}$ and $\sim 1050 \text{ cm}^{-1}$, characteristic of the $(\text{NiCO}_3)_2 \cdot (\text{Ni}(\text{OH})_2)_3 \cdot 4\text{H}_2\text{O}$ reference compound have been detected. Undoubtedly, the peaks of $(\text{Ni}_{0.9}\text{Co}_{0.1})\text{OOH}$ are contained into the M–O broad signal. Concisely, through Raman analysis alone, the presence of hydroxycarbonates cannot be completely excluded.

Afterwards, XRD analysis was performed on the exposed NMC 901 to detect secondary crystalline phases. Fig. II.25 compares the XRD patterns of the exposed NMC 901 to the as-received and Li_2CO_3 reference. It can be seen that the Li_2CO_3 secondary phase is barely visible (yellow arrows), whereas any other phase is distinguishable. The absence of peaks corresponding to nickel-based species, can be explained by the lack of crystallinity or because their concentration is too low to constitute a secondary phase.

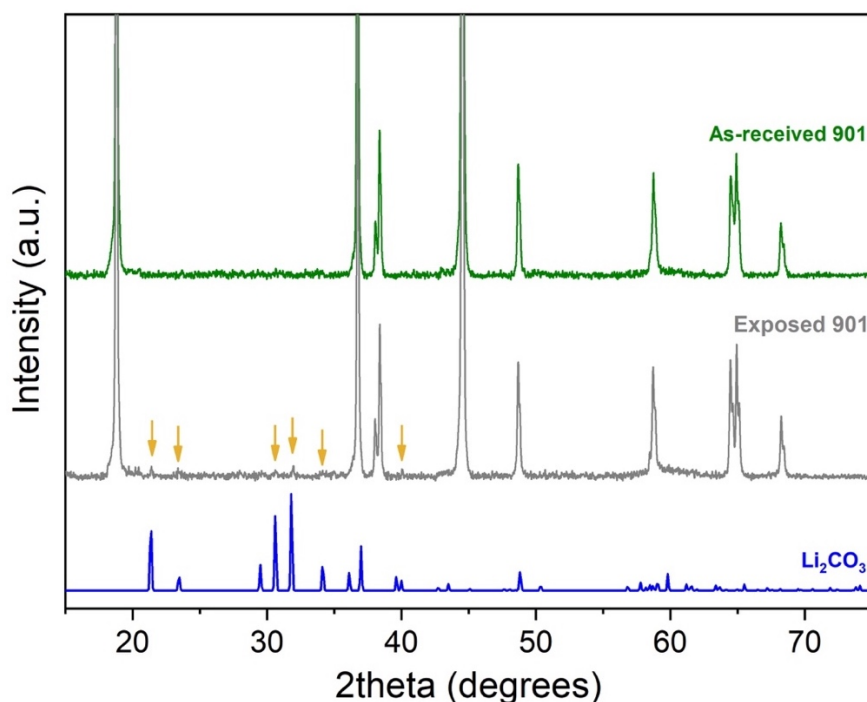


Figure II.25. Powder XRD patterns of the as-received, exposed 901, and the Li_2CO_3 reference.

To summarize, coupled TGA/MS experiments allowed for the proposition of a degradation mechanism that accounts for the formation of Li_2CO_3 detected through titration, Raman and XRD techniques and the gaseous compounds H_2O , CO_2 and O_2 released upon heating.

6. Conclusion of the chapter

Residual lithium salts in Ni-rich NMC materials left from the synthesis, or formed as a consequence of NMC's high reactivity toward air atmosphere, are well-identified issues with respect to the performance of Li-ion batteries in terms of gas release, interfacial resistance and decreased capacity. Given the abundant literature on this topic, first conclusion drawn was that degradation mechanisms involving a nickel reduction process and the formation of nickel hydroxycarbonate were approved by the battery community. However, after a deeper analysis of results, no tangible proof could have been brought to light. This incited us to undertake a stepwise work aiming at achieving the complete identification of surface species. Provided by a single supplier, different compositions of Ni-rich NMC with controlled morphology and structure helped assess the increasing reactivity associated with the presence of Ni^{3+} . Before and after exposure to a specific and rather effective $\text{H}_2\text{O}/\text{CO}_2$ atmosphere, soluble species were accurately quantified through acid-base titration, AAS and ICP-AES techniques; Li_2CO_3 is the main soluble compound formed upon exposure. It is formed either from LiOH through a water-requiring two-step reaction or from a newly proposed degradation reaction enlightened through TGA-MS analysis. Contrary to all expectations, the proposed mechanism does not involve either reduction processes or the formation of a metal hydroxycarbonate, but instead, metal oxyhydroxide, and potentially oxides NiO and MnO_2 if NMC contains Ni^{2+} and Mn^{4+} . Other outstanding observations from this chapter are:

- Li and Na sulfates have been quantified in a constant amount in all Ni-rich NMC materials, and were not affected by the exposure procedure. These compounds could act as internal standard for analyzing the degradation upon exposure to air through facile FTIR-ATR measurements.
- FTIR and TG-MS results suggest LiOH is not present at the surface of as-received NMC materials. It may arise from a hydrolysis reaction with lithium oxide, which will be confirmed in the next chapter.
- The thermal analysis revealed an in-situ re-lithiation process of metal oxide in presence of Li_2CO_3 to form a layered metal oxide LiMO_2 , which can explain some positive effects of heating a Ni-rich NMC material on the electrochemical performances, as already reported in literature.

7. References

1. Paulsen, J.; Kim, J. High nickel cathode material having low soluble base content. 2012. WO 2012/107313 A1.
2. Park, H.-K.; Shin, S. S.; Park, S. Y.; Shin, H. S.; Paulsen, J. M. Material for lithium secondary battery of high performance. 2010. WO/2007/129860.
3. Liu, H. S.; Zhang, Z. R.; Gong, Z. L.; Yang, Y., Origin of deterioration for LiNiO₂ cathode material during storage in air. *Electrochemical and Solid State Letters* **2004**, *7* (7), A190-A193.
4. Zhuang, G. V.; Chen, G. Y.; Shim, J.; Song, X. Y.; Ross, P. N.; Richardson, T. J., Li₂CO₃ in LiNi_{0.8}Co_{0.15}Al_{0.05}O₂ cathodes and its effects on capacity and power. *Journal of Power Sources* **2004**, *134* (2), 293-297.
5. Liu, H. S.; Yang, Y.; Zhang, J. J., Investigation and improvement on the storage property of LiNi_{0.8}Co_{0.2}O₂ as a cathode material for lithium-ion batteries. *Journal of Power Sources* **2006**, *162* (1), 644-650.
6. Faenza, N. V.; Bruce, L.; Lebens-Higgins, Z. W.; Plitz, I.; Pereira, N.; Piper, L. F. J.; Amatucci, G. G., Growth of Ambient Induced Surface Impurity Species on Layered Positive Electrode Materials and Impact on Electrochemical Performance. *Journal of the Electrochemical Society* **2018**, *164* (14), A3727-A3741.
7. Schipper, F.; Erickson, E. M.; Erk, C.; Shin, J. Y.; Chesneau, F. F.; Aurbach, D., Review-Recent Advances and Remaining Challenges for Lithium Ion Battery Cathodes. *Journal of the Electrochemical Society* **2017**, *164* (1), A6220-A6228.
8. Kim, D.; Cha, J.; Kim, H. Positive electrode slurry composition for lithium secondary battery, lithium secondary battery comprising the same and method of making the lithium secondary battery. 2012. US 2013/0309570 A1.
9. Bi, Y. J.; Wang, T.; Liu, M.; Du, R.; Yang, W. C.; Liu, Z. X.; Peng, Z.; Liu, Y.; Wang, D. Y.; Sun, X. L., Stability of Li₂CO₃ in cathode of lithium ion battery and its influence on electrochemical performance. *Rsc Advances* **2016**, *6* (23), 19233-19237.
10. Renfrew, S. E.; McCloskey, B. D., Residual Lithium Carbonate Predominantly Accounts for First Cycle CO₂ and CO Outgassing of Li-Stoichiometric and Li-Rich Layered Transition-Metal Oxides. *Journal of the American Chemical Society* **2017**, *139* (49), 17853-17860.
11. Mahne, N.; Renfrew, S. E.; McCloskey, B. D.; Freunberger, S. A., Electrochemical Oxidation of Lithium Carbonate Generates Singlet Oxygen. *Angewandte Chemie-International Edition* **2018**, *57* (19), 5529-5533.
12. Kim, Y., Mechanism of gas evolution from the cathode of lithium-ion batteries at the initial stage of high-temperature storage. *Journal of Materials Science* **2013**, *48* (24), 8547-8551.
13. Metzger, M.; Strehle, B.; Solchenbach, S.; Gasteiger, H. A., Origin of H₂ Evolution in LIBs: H₂O Reduction vs. Electrolyte Oxidation. *Journal of the Electrochemical Society* **2016**, *163* (5), A798-A809.
14. Manthiram, A.; Goodenough, J. B., Refinement of the Critical V-V Separation for Spontaneous Magnetism in Oxides. *Canadian Journal of Physics* **1987**, *65* (10), 1309-1317.
15. Mizushima, K.; Jones, P. C.; Wiseman, P. J.; Goodenough, J. B., Li_xCoO₂ (0<x<1) - A new cathode material for batteries of high-energy density. *Materials Research Bulletin* **1980**, *15* (6), 783-789.
16. Thomas, M.; Bruce, P. G.; Goodenough, J. B., Lithium Mobility in the Layered Oxide Li_{1-x}CoO₂. *Solid State Ionics* **1985**, *17* (1), 13-19.
17. Matsumoto, K.; Kuzuo, R.; Takeya, K.; Yamanaka, A., Effects of CO₂ in air on Li deintercalation from LiNi_{1-x-y}Co_xAl_yO₂. *Journal of Power Sources* **1999**, *81*, 558-561.
18. Mijung, N.; Lee, Y.; Cho, J., Water adsorption and storage characteristics of optimized LiCoO₂ and LiNi_{1/3}Co_{1/3}Mn_{1/3}O₂ composite cathode material for Li-ion cells. *Journal of the Electrochemical Society* **2006**, *153* (5), A935-A940.
19. Huang, B. H.; Qian, K.; Liu, Y. X.; Liu, D. Q.; Zhou, K.; Kong, F. Y.; Li, B. H., Investigations on the Surface Degradation of LiNi_{1/3}Co_{1/3}Mn_{1/3}O₂ after Storage. *Acs Sustainable Chemistry & Engineering* **2019**, *7* (7), 7378-7385.
20. Shkrob, I. A.; Gilbert, J. A.; Phillips, P. J.; Klie, R.; Haasch, R. T.; Baren, J.; Abraham, D. P., Chemical Weathering of Layered Ni-Rich Oxide Electrode Materials: Evidence for Cation Exchange. *Journal of the Electrochemical Society* **2017**, *164* (7), A1489-A1498.
21. Sicklinger, J.; Metzger, M.; Beyer, H.; Pritzl, D.; Gasteiger, H. A., Ambient Storage Derived Surface Contamination of NCM811 and NCM111: Performance Implications and Mitigation Strategies. *Journal of the Electrochemical Society* **2019**, *166* (12), A2322-A2335.
22. Jung, R.; Morasch, R.; Karayalali, P.; Phillips, K.; Maglia, F.; Stinner, C.; Shao-Horn, Y.; Gasteiger, H. A., Effect of Ambient Storage on the Degradation of Ni-Rich Positive Electrode Materials (NMC811) for Li-Ion Batteries. *Journal of the Electrochemical Society* **2018**, *165* (2), A132-A141.

23. Ohzuku, T.; Ueda, A.; Nagayama, M., Electrochemistry and Structural Chemistry of LiNiO₂ (R-3m) for 4 Volt Secondary Lithium Cells. *Journal of the Electrochemical Society* **1993**, *140* (7), 1862-1870.
24. Paulsen, J. M.; Park, H. K.; Kwon, Y. H. Process of making cathode material containing Ni-based lithium transition metal oxide. 2011. US 2009/0224201 A1.
25. Chen, Z. Q.; Wang, J.; Huang, J. X.; Fu, T.; Sun, G. Y.; Lai, S. B.; Zhou, R.; Li, K.; Zhao, J. B., The high-temperature and high-humidity storage behaviors and electrochemical degradation mechanism of LiNi_{0.6}Co_{0.2}Mn_{0.2}O₂ cathode material for lithium ion batteries. *Journal of Power Sources* **2017**, 168-176.
26. Shizuka, K.; Kiyohara, C.; Shima, K.; Takeda, Y., Effect of CO₂ on layered Li_{1+z}Ni_{1-x-y}Co_xMn_yO₂ (M = Al, Mn) cathode materials for lithium ion batteries. *Journal of Power Sources* **2007**, *166* (1), 233-238.
27. Kim, J.; Hong, Y. S.; Ryu, K. S.; Kim, M. G.; Cho, J., Washing effect of a LiNi_{0.83}Co_{0.15}Al_{0.02}O₂ cathode in water. *Electrochemical and Solid State Letters* **2006**, *9* (1), A19-A23.
28. Xiong, X. H.; Wang, Z. X.; Yue, P.; Guo, H. J.; Wu, F. X.; Wang, J. X.; Li, X. H., Washing effects on electrochemical performance and storage characteristics of LiNi_{0.8}Co_{0.1}Mn_{0.1}O₂ as cathode material for lithium-ion batteries. *Journal of Power Sources* **2013**, *222*, 318-325.
29. Zhang, X. Y.; Jiang, W. J.; Zhu, X. P.; Mauger, A.; Qilu, Julien, C. M., Aging of LiNi_{1/3}Mn_{1/3}Co_{1/3}O₂ cathode material upon exposure to H₂O. *Journal of Power Sources* **2011**, *196* (11), 5102-5108.
30. Li, J.; Zheng, J. M.; Yang, Y., Studies on storage characteristics of LiNi_{0.4}Co_{0.2}Mn_{0.4}O₂ as cathode materials in lithium-ion batteries. *Journal of the Electrochemical Society* **2007**, *154* (5), A427-A432.
31. Benedetti-Pichler, A. A.; Cefola, M.; Waldman, B.; Warder's method for the titration of carbonates. *Industrial and Engineering Chemistry-Analytical Edition* **1939**, *11*, 0327-0332.
32. Voronov, V. A. S., A. O. Gubin, S. P. Cheglakov, A. V.; Kornilov, D. Y.; Karaseva, E. S.; Krasnova, A. S.; Tkachev, S. V., Comparison of the Basic Physical and Chemical Properties of Complex Oxides LiNi_xMn_yCo_{1-x-y}O₂ (0.3 ≤ x ≤ 0.6; 0.2 ≤ y ≤ 0.4) Obtained by Different Methods *Materials for electronics technology* **2016**, *8*, 229-237.
33. Ren, D.; Shen, Y.; Yang, Y.; Shen, L. X.; Levin, B. D. A.; Yu, Y. C.; Muller, D. A.; Abruna, H. D., Systematic Optimization of Battery Materials: Key Parameter Optimization for the Scalable Synthesis of Uniform, High-Energy, and High Stability LiNi_{0.6}Mn_{0.2}Co_{0.2}O₂ Cathode Material for Lithium-Ion Batteries. *Acs Applied Materials & Interfaces* **2017**, *9* (41), 35811-35819.
34. Bichon, M.; Sotta, D.; Dupre, N.; De Vito, E.; Boulineau, A.; Porcher, W.; Lestriez, B., Study of Immersion of LiNi_{0.5}Mn_{0.3}Co_{0.2}O₂ Material in Water for Aqueous Processing of Positive Electrode for Li-Ion Batteries. *Acs Applied Materials & Interfaces* **2019**, *11* (20), 18331-18341.
35. Noh, H. J.; Yoon, S.; Yoon, C. S.; Sun, Y. K., Comparison of the structural and electrochemical properties of layered LiNi_xCo_yMn_zO₂ (x=1/3, 0.5, 0.6, 0.7, 0.8 and 0.85) cathode material for lithium-ion batteries. *Journal of Power Sources* **2013**, *233*, 121-130.
36. Sa, Q. N.; Gratz, E.; Heelan, J. A.; Ma, S. J.; Apelian, D.; Wang, Y., Synthesis of Diverse LiNi_xMn_yCo_zO₂ Cathode Materials from Lithium Ion Battery Recovery Stream. *Journal of Sustainable Metallurgy* **2016**, *2* (3), 248-256.
37. Bak, S. M.; Nam, K. W.; Chang, W.; Yu, X. Q.; Hu, E. Y.; Hwang, S.; Stach, E. A.; Kim, K. B.; Chung, K. Y.; Yang, X. Q., Correlating Structural Changes and Gas Evolution during the Thermal Decomposition of Charged Li_xNi_{0.8}Co_{0.15}Al_{0.05}O₂ Cathode Materials. *Chemistry of Materials* **2013**, *25* (3), 337-351.
38. Bak, S. M.; Hu, E. Y.; Zhou, Y. N.; Yu, X. Q.; Senanayake, S. D.; Cho, S. J.; Kim, K. B.; Chung, K. Y.; Yang, X. Q.; Nam, K. W., Structural Changes and Thermal Stability of Charged LiNi_xMn_yCo_zO₂ Cathode Materials Studied by Combined In Situ Time-Resolved XRD and Mass Spectroscopy. *Acs Applied Materials & Interfaces* **2014**, *6* (24), 22594-22601.
39. Lu, L. G.; Han, X. B.; Li, J. Q.; Hua, J. F.; Ouyang, M. G., A review on the key issues for lithium-ion battery management in electric vehicles. *Journal of Power Sources* **2013**, *226*, 272-288.
40. Pritzl, D.; Teufl, T.; Freiberg, A. T. S.; Strehle, B.; Sicklinger, J.; Sommer, H.; Hartmann, P.; Gasteiger, H. A., Washing of Nickel-Rich Cathode Materials for Lithium-Ion Batteries: Towards a Mechanistic Understanding. *Journal of the Electrochemical Society* **2019**, *166* (16), A4056-A4066.
41. Smit, B.; Reimer, J. A.; Oldenburg, C. M.; Bourg, I. C., Introduction To Carbon Capture And Sequestration. Imperial College Press: 2014; Vol. 1.
42. Liu, W.; Oh, P.; Liu, X.; Lee, M. J.; Cho, W.; Chae, S.; Kim, Y.; Cho, J., Nickel-Rich Layered Lithium Transition-Metal Oxide for High-Energy Lithium-Ion Batteries. *Angewandte Chemie-International Edition* **2015**, *54* (15), 4440-4457.
43. Myung, S. T.; Maglia, F.; Park, K. J.; Yoon, C. S.; Lamp, P.; Kim, S. J.; Sun, Y. K., Nickel-Rich Layered Cathode Materials for Automotive Lithium-Ion Batteries: Achievements and Perspectives. *Acs Energy Letters* **2017**, *2* (1), 196-223.

44. Park, J. H.; Choi, B.; Kang, Y. S.; Park, S. Y.; Yun, D. J.; Park, I.; Ha Shim, J.; Han, H. N.; Park, K., Effect of Residual Lithium Rearrangement on Ni-rich Layered Oxide Cathodes for Lithium-Ion Batteries. *Energy Technology* **2018**, *6* (7), 1361-1369.
45. You, Y.; Celio, H.; Li, J. Y.; Dolocan, A.; Manthiram, A., Modified High-Nickel Cathodes with Stable Surface Chemistry Against Ambient Air for Lithium-Ion Batteries. *Angewandte Chemie-International Edition* **2018**, *57* (22), 6480-6485.
46. Park, J. H.; Park, J. K.; Lee, J. W., Stability of $\text{LiNi}_{0.6}\text{Mn}_{0.2}\text{Co}_{0.2}\text{O}_2$ as a Cathode Material for Lithium-Ion Batteries against Air and Moisture. *Bulletin of the Korean Chemical Society* **2016**, *37* (3), 344-348.
47. Williams, D. D.; Miller, R. R., Effect of Water Vapor on the LiOH-CO_2 Reaction. Dynamic Isothermal System. *Industrial & Engineering Chemistry Fundamentals* **1970**, *9* (3), 454-457.
48. Biswas, D. R., Thermal-Energy Storage Using Sodium-sulfate Decahydrate and Water. *Solar Energy* **1977**, *19* (1), 99-100.
49. Koga, N.; Tanaka, H., Kinetics and mechanisms of the thermal dehydration of dilithium sulfate monohydrate. *The Journal of Physical Chemistry* **1989**, *93* (23), 7793-7798.
50. Cho, D. H.; Jo, C. H.; Cho, W.; Kim, Y. J.; Yashiro, H.; Sun, Y. K.; Myung, S. T., Effect of Residual Lithium Compounds on Layer Ni-Rich $\text{Li Ni}_{0.7}\text{Mn}_{0.3}\text{O}_2$. *Journal of the Electrochemical Society* **2014**, *161* (6), A920-A926.
51. Kiat, J. M.; Boemare, G.; Rieu, B.; Aymes, D., Structural evolution of LiOH : Evidence of a solid-solid transformation toward Li_2O close to the melting temperature. *Solid State Communications* **1998**, *108*, 241-245.
52. Gruver, R. M., Differential Thermal-Analysis Studies of Ceramic Materials: I, Characteristic Heat Effects of Some Carbonates. *Journal of The American Ceramic Society* **1950**, *33* (3), 96-101.
53. Halle, J. C.; Stern, K. H., Vaporization and Decomposition of Na_2SO_4 . Thermodynamics and Kinetics. *The Journal of Physical Chemistry* **1980**, *84*, 1699-1704.
54. Henmi, H.; Mori, M.; Hirayama, T.; Mizutani, N.; Kato, M., Influence of the Self-generated and Controlled-Atmosphere on the Thermal-Decomposition of Basic Nickel Carbonate, $\text{NiCO}_3 \cdot 2\text{Ni}(\text{OH})_2 \cdot 4\text{H}_2\text{O}$. *Thermochimica Acta* **1986**, *104*, 101-109.
55. Rhamdhani, M. A.; Jak, E.; Hayes, P. C., Basic nickel carbonate: Part I. Microstructure and phase changes during oxidation and reduction processes. *Metallurgical and Materials Transactions B-Process Metallurgy and Materials Processing Science* **2008**, *39* (2), 218-233.
56. Moltved, K. A.; Kepp, K. P., The Chemical Bond between Transition Metals and Oxygen: Electronegativity, d-Orbital Effects, and Oxophilicity as Descriptors of Metal-Oxygen Interactions. *Journal of Physical Chemistry C* **2019**, *123* (30), 18432-18444.
57. Horanyi, T. S., The thermal stability of the $\beta\text{-Ni}(\text{OH})_2\text{-}\beta\text{-NiOOH}$ system. *Thermochimica Acta* **1989**, *137*, 247-253.
58. Shao-Horn, Y.; Hackney, S. A.; Kahaian, A. J.; Thackeray, M. M., Structural stability of LiCoO_2 at 400 degrees C. *Journal of Solid State Chemistry* **2002**, *168* (1), 60-68.
59. Jo, J. H.; Jo, C. H.; Yashiro, H.; Kim, S. J.; Myung, S. T., Re-heating effect of Ni-rich cathode material on structure and electrochemical properties. *Journal of Power Sources* **2016**, *313*, 1-8.
60. Kim, J. H.; Gibb, H. J.; How, P., *Cobalt and Inorganic Cobalt Compounds*. WHO Library: 2006.
61. Morrow, G. W., Nickel(II) Peroxide. In *Encyclopedia of reagents for organic synthesis*, John Wiley & Sons, Ltd.: 2001.
62. Jeong, S.; Kim, J.; Mun, J., Self-Generated Coating of LiCoO_2 by Washing and Heat Treatment without Coating Precursors. *Journal of the Electrochemical Society* **2019**, *166* (3).

Chapter III

Chemical and electrochemical reactivity of surface species in Ni-rich NMC materials

1. Introduction	107
2. Reactivity of surface species toward electrolyte	108
2.1. Reactivity of reference compounds.....	108
2.2. Reactivity of as-received and exposed NMC materials.....	112
3. Reactivity of surface species under cycling	115
3.1. Electrochemical reactivity of powder references.....	115
3.2. Electrochemical reactivity of the Ni-rich NMC materials.....	117
3.2.1. Fabrication of the electrodes.....	117
3.2.2. Galvanostatic profiles of the as-received materials.....	120
3.2.3. Galvanostatic profiles of the exposed NMC 622C.....	123
3.2.4. Evaluation of the Li ₂ CO ₃ consumption in exposed NMC 622C.....	125
3.3. Conclusion.....	126
4. Modification of the surface species by a heat treatment	128
4.1. As-received, washed, exposed and their analogs annealed NMC 622C films.....	129
4.2. Impact of heat treatment on as-received NMC 622C.....	131
4.3. Impact of heat treatment on washed NMC 622C.....	132
4.4. Impact of heat treatment on exposed NMC 622C.....	134
4.5. Conclusion.....	137
5. Conclusion of the chapter	138
6. References	139

1. Introduction

Li_2CO_3 , LiOH , Li_2SO_4 and Na_2SO_4 soluble surface species were identified and quantified through titration, AAS and ICP after aqueous washing of five as-received Ni-rich NMC materials and it was determined that upon $\text{H}_2\text{O}/\text{CO}_2$ exposure, the uppermost surface material reacts into Li_2CO_3 , $(\text{Ni},\text{Co})\text{OOH}$, NiO and MnO_2 .

It is well-known that the presence of surface species from synthesis or grown from air exposure alter the surface state and the electrochemical performance of layered materials^{1, 2}. Reasonably, the most reported are Li_2CO_3 and LiOH , since, for years, they were the only identified surface species. They have been reported to be electronic insulators, in addition to being capable to react chemically and electrochemically with the battery components³⁻⁷. However, a better analysis of these processes would certainly contribute to the understanding and prevention. For this reason, in a first instance, this chapter elucidates the chemical reactivity of relevant surface species in contact with a LiPF_6 -based electrolyte, as well as an as-received and an exposed NMC 811, focusing on the analysis by liquid NMR of the degradation products in the electrolyte. Then, as Li_2CO_3 can be electrochemically oxidized and produce gases^{8, 9}, the electrochemical consumption of surface species in as-received and exposed materials was evaluated. Finally, based on the evidence of the thermal consumption of $(\text{Ni},\text{Co})\text{OOH}$ presented in [Chapter II](#), a heat treatment was performed to as-received, washed and exposed NMC 622C and their electrochemical performance was examined.

2. Reactivity of surface species toward electrolyte

The chemical reactivity of surface species with the LiPF₆-based electrolyte was studied through storage experiments at 25 and 55°C. First, the reactivity of reference compounds Li₂CO₃, LiOH, NiO and Li₂SO₄ was evaluated. As its presence on NMC surface was suggested by Paulsen et al.¹⁰, the reactivity of Li₂O was also investigated. Then, the chemical reactivity of surface species on as-received and exposed NMC 811 was assessed under similar storage conditions.

2.1. Reactivity of reference compounds

Reference materials were added to 1 ml of electrolyte (1M LiPF₆ in EC/DEC/EMC 1:1:1 vol.) inside an aluminum laminated bag for four days of storage at 25 or 55°C. The chemical inertness of the inner component (polyethylene) of the bag toward the electrolyte was verified prior to the experiments. After storage, 0.5 ml of the electrolyte were recovered in the glove box by centrifugation and transferred into an NMR tube for liquid ¹⁹F NMR analysis (all experimental conditions can be found in Annex II).

Fig. III.1 shows the ¹⁹F NMR spectrum of Li₂CO₃, Li₂O and Li₂SO₄ at 25 and 55°C. In all cases, the doublet signal corresponding to LiPF₆ is centered at $\delta_F = -74.2$ ppm ($J(P,F) = 709$ Hz). In some cases (Fig. III.1a, b, d and e), another doublet centered at a lower chemical shift ($\delta_F = -84.6$ ppm, $J(P,F) = 929.4$ Hz) can be attributed to LiPO₂F₂ (LDFP)¹¹. For simplicity, the spectra were cut at 95 ppm, but upon enlarging to 160 ppm, the peak of LiF is also clearly observed at $\delta_F = -155.8$ ppm (exemplary shown for Li₂CO₃ at 55°C in Fig. III.2). Note that, unlike Li₂CO₃, Li₂O, LiOH and Li₂SO₄ reference compounds, NiO did not reveal any reactivity toward the electrolyte, whatever the temperature.

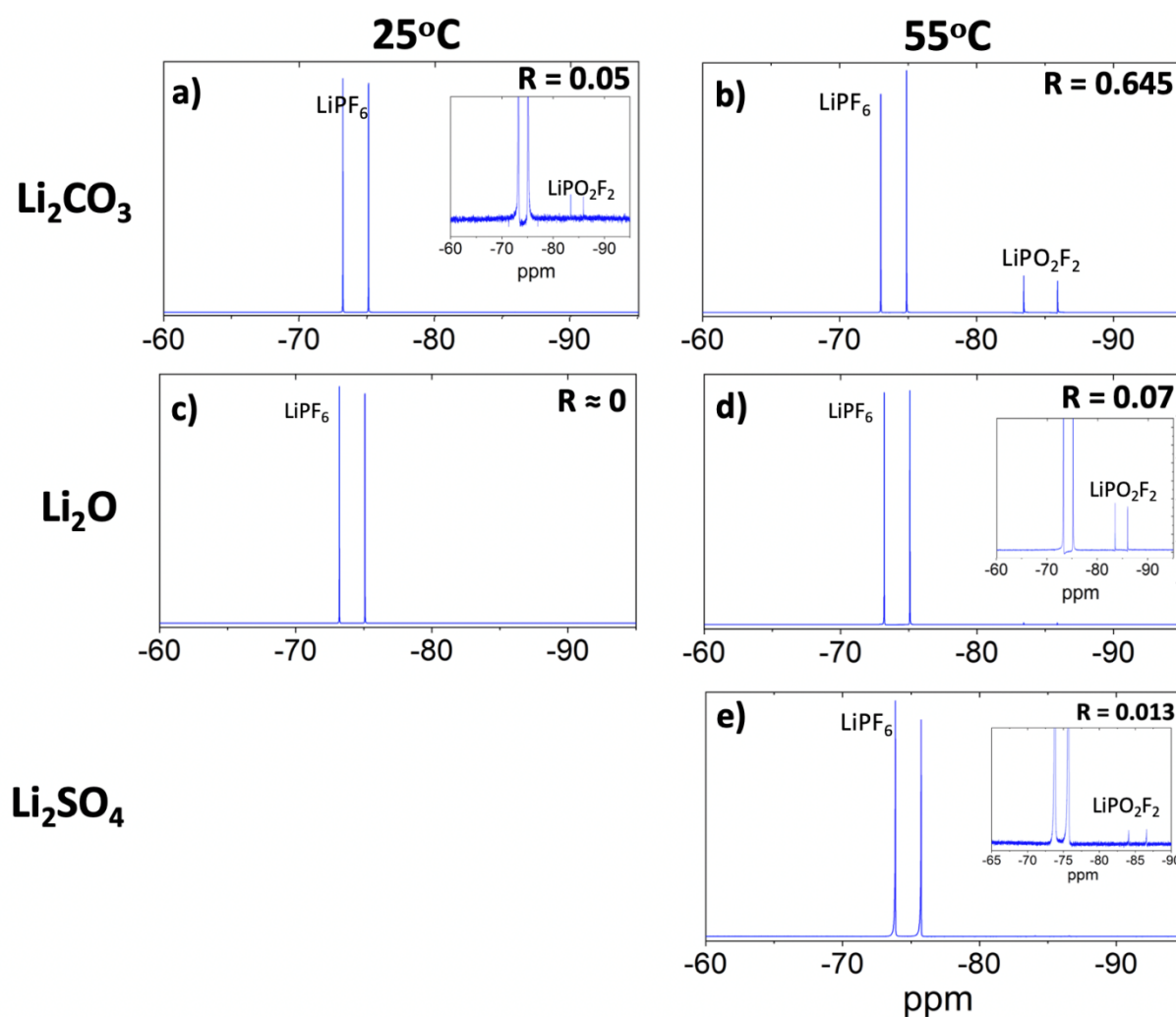


Figure III.1. Liquid ^{19}F NMR spectra of the electrolyte recovered after storage, for 4 days at 25 and 55°C, in presence of **a, b)** Li_2CO_3 , **c, d)** Li_2O and **e)** Li_2SO_4 at 55°C; with $\text{LiPO}_2\text{F}_2/\text{LiPF}_6$ molar ratio (R) determined from the integration of the peaks.

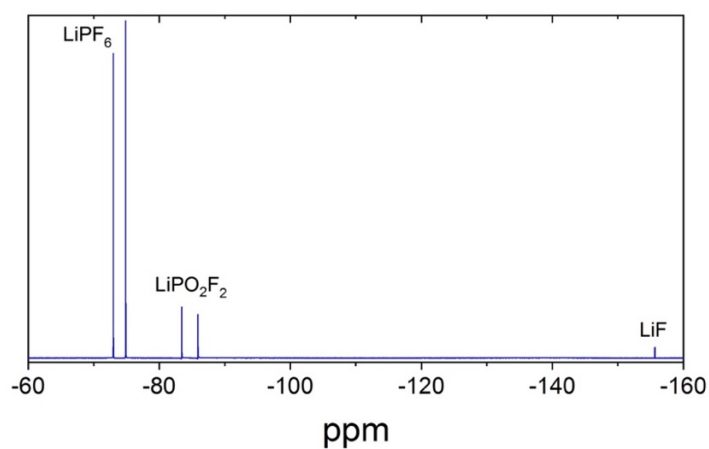
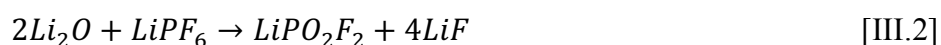


Figure III.2. Liquid ^{19}F NMR complete spectrum of the electrolyte recovered after the storage of Li_2CO_3 and electrolyte for 4 days at 55°C.

The corresponding reaction mechanisms leading to LDFP production with LiPF_6 from the electrolyte can be proposed for the three reactants as following (Eqs. III.1–3). The first reaction (Eq. III.1) has been already proposed by Parimalam et al.¹² during the study of the solid electrolyte interphase (SEI) generated at the negative electrode surface, but has never been reported to occur with Li_2CO_3 contained on the positive electrode.



The $\text{LiPO}_2\text{F}_2/\text{LiPF}_6$ molar ratios R calculated from the NMR peaks integration, ranges from almost zero, when the reaction temperature is 25°C , to 0.645 in presence of Li_2CO_3 at 55°C . Considering the reaction stoichiometry and the starting molar ratio M/LiPF_6 ($M=\text{Li}_2\text{CO}_3$, Li_2O , Li_2SO_4) of 1.35, a maximum value of $R = 2.08$ can be expected. Note that this value could not be reached at 25°C as the LDFP solubility in carbonate solvents is less than 0.5 M¹³.

The FTIR analysis of the white precipitate recovered after the Li_2CO_3 storage test at 55°C did not reveal any Li_2CO_3 but only LDFP and LiPF_6 , thus, revealing that Eq. III.1 is complete with this reactant at this temperature.

Regarding the storage tests with Li_2O , the R value reaches only 0.07 at 55°C . Hence, the Li_2CO_3 turns out to be much more reactive toward LiPF_6 to produce LDFP, than Li_2O . Li_2SO_4 is even less reactive as the test at 25°C revealed no reaction and a low R value of 0.013 is obtained at 55°C .

Concerning LiOH , Fig. III.3 shows the ^{19}F NMR results of its storage with electrolyte at 25 (a) and 55°C (b). It can be observed that LiOH is extremely reactive, even at 25°C . Based on previous studies¹⁴⁻¹⁷, most of the peaks can be ascribed to fluorophosphates such as:

- $\text{OPF}(\text{OH})_2$ with a doublet centered at $\delta_{\text{F}} = -77.3$ ppm ($J(\text{P},\text{F}) = 927$ Hz), labelled as **1** in Fig. III.1a, b
- $\text{OPF}(\text{OR})(\text{OR}')$ with $\text{R} = \text{CH}_3$ or C_2H_5 and $\text{R}' = \text{H}$, CH_3 or C_2H_5
 - a doublet centered at $\delta_{\text{F}} = -81$ ppm ($J(\text{P},\text{F}) = 944$ Hz), labelled as **2**
 - a doublet centered at $\delta_{\text{F}} = -81.3$ ppm ($J(\text{P},\text{F}) = 943$ Hz), labelled as **3**
- $\text{OPF}_2(\text{OH})$ with a doublet centered at $\delta_{\text{F}} = -85.2$ ppm ($J(\text{P},\text{F}) = 950$ Hz), labelled as **4**.

Interestingly, storage at 55°C leads to the consumption of difluorophosphate (labelled as **4**) and the formation of fluoroalkane denoted by the RF peak. Moreover, LiF is also clearly detected at -155.8 ppm (Fig. III.4).

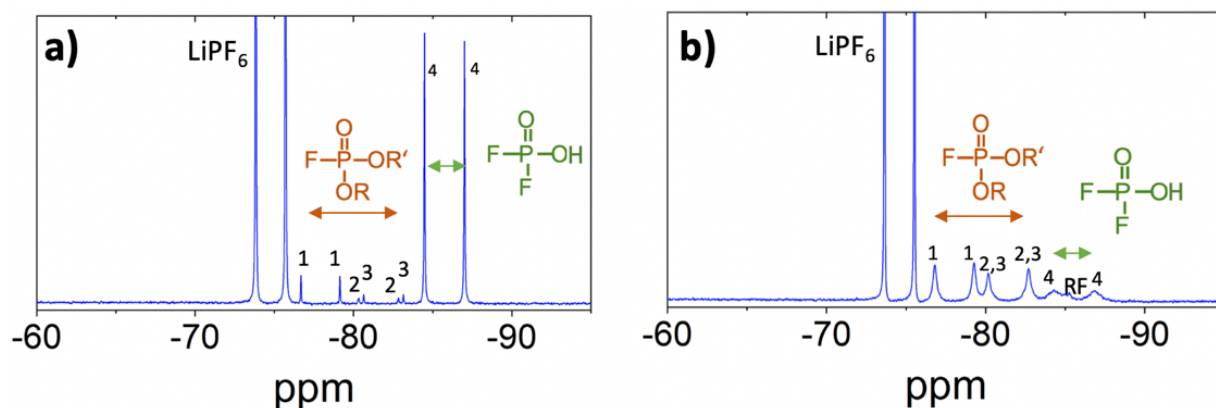


Figure III.3. Liquid ^{19}F NMR spectra of the electrolyte recovered after storage for 4 days in presence LiOH at **a)** 25 and **b)** 55°C. Label 1, 2, 3 and 4 stands for the doublets **1)** $\text{OPF}(\text{OH})_2$; **2** and **3)** $\text{OPF}(\text{OR})(\text{OR}')$ with $\text{R} = \text{CH}_3$ or C_2H_5 and $\text{R}' = \text{H}$ or CH_3 or C_2H_5 and **4)** $\text{OPF}_2(\text{OH})$, respectively.

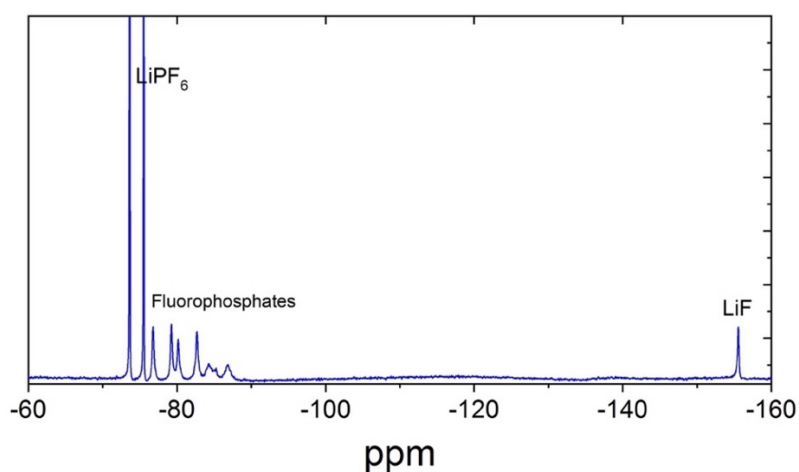
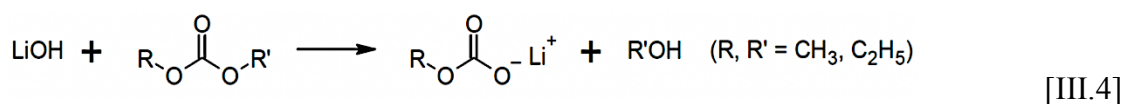


Figure III.4. ^{19}F NMR spectrum of electrolyte after storage with LiOH at 55°C for 4 days.

As observed, the reaction with LiOH did not produce the difluorophosphate LDFP, as Li_2CO_3 , Li_2O and Li_2SO_4 do, on the contrary, it forms fluorophosphates substituted with OH, CH_3 or C_2H_5 . The fact that lithium-based species react and form non-lithium salt indicates a more complex formation pathway. To account for this, a two-step mechanism is proposed:

- i. Lithium alkyl carbonates form from the reaction of LiOH with linear carbonates (Eq. III.4), whose feasibility was proven by FTIR analysis of the solid product from the reaction of EMC with LiOH during 4 days at 55°C (Fig. III.5).



- ii. These lithium alkyl carbonates react with LiPF_6 to form substituted fluorophosphates (Eqs. III.5-7) as demonstrated by Parimalam et al.¹²:

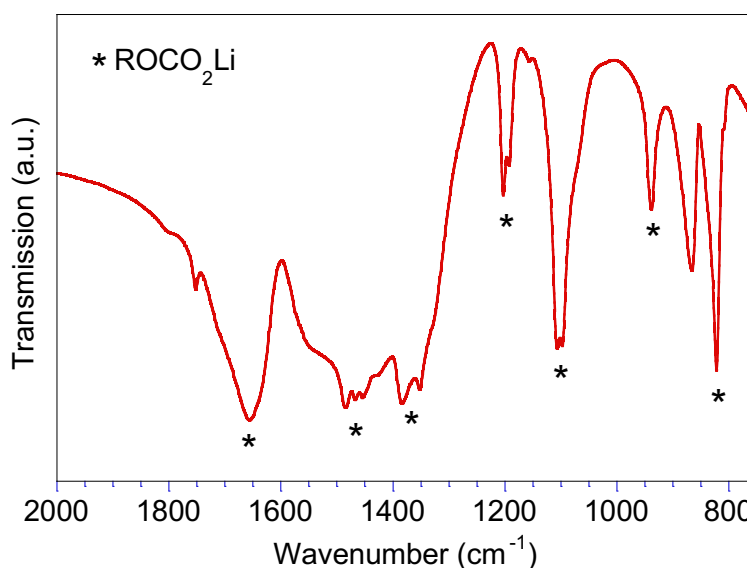
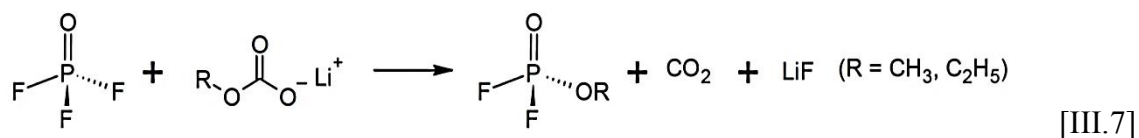
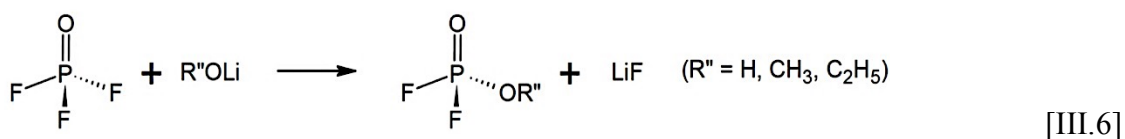
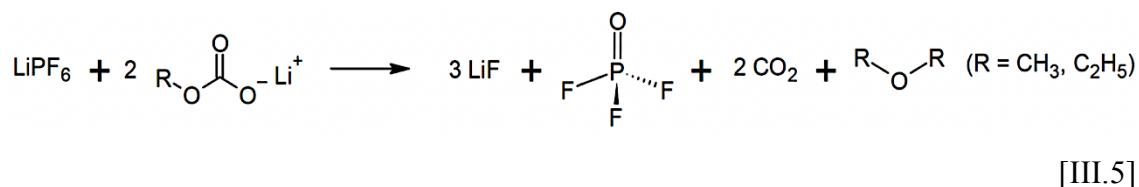


Figure III.5. FTIR spectrum of the precipitate recovered after the storage of EMC and LiOH during 4 days at 55°C. *Bands ascribed to lithium alkyl carbonate according to Gireaud et al.¹⁸

2.2. Reactivity of as-received and exposed NMC materials

In a similar way, reactivity tests were performed with the as-received and exposed NMC 811 materials. In this case, 100 mg of as-received or exposed NMC 811 powder were added to 1 ml of LiPF_6 -based electrolyte and subjected to the same storage conditions and NMR analysis.

From the ^{19}F RMN analysis, LiPF_6 , LDFP and LiF were detected in both materials and at both temperatures. However, the absence of fluorophosphates is intriguing, as they were found to be easily produced from hydroxide species. As already mentioned in Chapter II, most probably, Li_2O instead of LiOH is present at the NMC surface. Hydroxide ions analyzed by acid-base titration would be the reaction products of Li_2O hydrolysis that takes place upon NMC washing procedure (Eq. III.8):



This result explains the absence of the LiOH band in FTIR spectra (Fig. II.12, Chapter II) and the absence of H_2O release around 500°C in TGA/MS profile (Fig. II.19 a and d, Chapter II). It is noteworthy that for the exposed NMC 811 material, the oxyhydroxides species did not generate fluorophosphates when in contact with electrolyte.

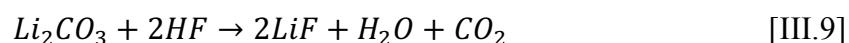
The $\text{LiPO}_2\text{F}_2/\text{LiPF}_6$ molar ratios R deduced from the different NMR analyses are reported in Table III.1. For both as-received and exposed materials, the LDFP formation was facilitated by the temperature augmentation, as it was found for the reference compounds. From these R values, the LDFP moles quantity in 1 ml of electrolyte was calculated and compared to the one expected from the complete reaction of Li_2CO_3 , Li_2O and M_2SO_4 ($\text{M} = \text{Li}, \text{Na}$) with the electrolyte, considering Li_2O instead of LiOH from acid-base titration results (Eqs. III.1–3). As each material contains $40 \pm 2 \mu\text{mol.g}_{\text{NMC}}^{-1}$ of M_2SO_4 , an expected LDFP value of $2 \pm 0.1 \mu\text{mol}$ per 100 mg of NMC can be calculated from sulphate reactants.

Table III.1. Comparison of expected and experimental LDFP moles in 1 ml of LiPF_6 -based electrolyte after storage with as-received and exposed NMC 811.

Material	Soluble bases from ABT ($\mu\text{mol.g}_{\text{NMC}}^{-1}$)		Expected n LiPO_2F_2 from Li_2CO_3 , Li_2O and M_2SO_4 for 100 mg of NMC in 1 ml (μmol)	NMR experiments		
	Li_2CO_3	LiOH from Li_2O		Storage temperature ($^\circ\text{C}$)	R	n LiPO_2F_2 in 1 ml (μmol)
NMC 811 as-received	19 ± 1	205 ± 14	8.1 ± 0.9	25	0.006	6
				55	0.007	7
NM 811 exposed	370 ± 10	17 ± 5	20.9 ± 1.3	25	0.003	3
				55	0.013	13

Note that, in the as-received 811 material, a large quantity of the reactants has reacted to form LiPO_2F_2 , whatever the temperature, which may be explained by the very thin layer. For the exposed NMC 811, higher quantity of LiPO_2F_2 was expected (20.9 vs. 8.1 μmol in as-received), but the layer is thicker and consequently, as in case of the reference compound, the transformation process is slowed down; only a R value of 13 is attained at 55°C. The reaction yield may also be affected by the complexity of the exposed surface layer made of oxyhydroxides, oxides and soluble bases, which makes it difficult for the LiPF_6 to react with the soluble bases and sulphates.

Furthermore, it is possible that other chemical reactions inside the battery with the electrolyte constituents and at any temperature can take place. For instance, it has been reported that Li_2CO_3 reacts with HF to produce LiF, H_2O and CO_2 (Eq. III.9, the production of HF is shown in Eqs. I.10 and 11)^{4, 5, 21, 22}. Hence, the content of Li_2CO_3 associated with moisture, including chemically adsorbed moisture in the NMC powder is highly undesirable.



To summarize, a stepwise investigation of the chemical reactivity of the surface species toward LiPF_6 -based electrolyte was carried out through ^{19}F NMR measurements, and following the observation that fluorophosphate-type compounds were not produced from the storage of as-received NMC 811 with LiPF_6 -based electrolyte, it was revealed that Li_2O is present in NMC. Furthermore, it was clearly demonstrated that the NMC surface species, Li_2CO_3 , Li_2O and Li_2SO_4 , produce LDFP upon storage with the electrolyte, even at room temperature for the first two.

Since it has been reported that LDFP is an efficient electrolyte additive, notably to decrease the impedance of the electrodes and to improve the capacity retention of batteries²³⁻²⁵, it is suggested that soluble bases and sulfates may benefit the battery's electrochemical performance. However, gas can be formed from Li_2CO_3 , and the surface contains also insoluble bases $(\text{Ni},\text{Co})\text{OOH}$, MnO_2 and NiO , which may impact negatively the electrochemical performance.

3. Reactivity of surface species under cycling

The above-results evidenced that, without specific Li-ion batteries formation conditions, the NMC surface species as Li_2CO_3 , Li_2O and Li_2SO_4 might never fully chemically react with LiPF_6 before their first charge. Hence, Li_2CO_3 would be prone to electrochemical oxidation.

3.1. Electrochemical reactivity of powder references

Among the mentioned surface species, Li_2CO_3 has been reported to electrochemically oxidize in the first cycles^{8, 26} and also to induce charge transfer resistance increase^{3, 27}, decrease the rate capability and impact negatively the capacity retention^{2-4, 6, 7}. However, there are some discrepancies regarding the oxidation potential of Li_2CO_3 . Meini et al.²⁸, for instance, calculated that pure Li_2CO_3 on a carbon electrode would oxidize at 3.82 V vs. Li/Li^+ and Bi et al.⁴, determined through linear sweep voltammetry that the oxidation of Li_2CO_3 on a carbon electrode starts at 4.4 V vs. Li/Li^+ . Regarding Li_2CO_3 on NMC materials, through online electrochemical mass spectrometry (OEMS), Metzger et al.²⁹ found that oxidation starts at 4.1 V vs. Li/Li^+ , based on the CO_2 evolution seen in the first cycle of NMC 111/Graphite full cells. Also by OEMS, Renfrew et al.⁸ stated that the oxidation starts at 3.8 V vs. Li/Li^+ in a NMC 622/Li half-cell.

Given the wide potential range upon which Li_2CO_3 can oxidize, a decision was made to make our own assessment of its oxidation capability as pure compound before examining the electrochemical behavior of as-received and exposed NMC electrode films in half-cells.

With the aim of exploring the electrochemistry of Li_2CO_3 as close to the conditions on the surface of NMC as possible, Li_2CO_3 powder was mechanically ball-milled for 30 minutes (experimental details in Annex II). The particle size of pristine Li_2CO_3 was effectively reduced from $10 \pm 3 \mu\text{m}$ to $7 \pm 5 \mu\text{m}$ (Fig. III.6a and b).

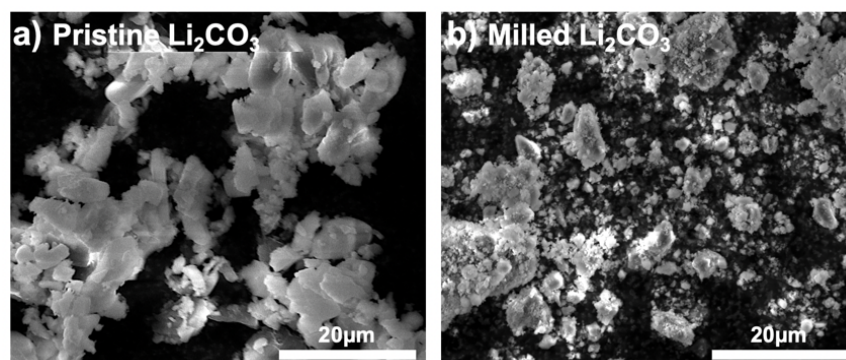


Figure III.6. SEM images of **a)** pristine and **b)** ball-milled Li_2CO_3 .

Afterwards, both Li_2CO_3 powders and a reference powder of Li_2SO_4 (as a blank compound) were intimately mixed, in a mortar with 10 wt.% of C45 conductive carbon before assessing their electrochemical activity in half-cell, with lithium as counter electrode. The cells were cycled at 25°C , in a potential window of 2.8–4.5 V vs. Li/Li^+ , and at a C-rate of C/40. Fig. III.7a shows the incremental capacity curve of the first galvanostatic charge of Li_2SO_4 and pristine and milled Li_2CO_3 . Fig. III.7b shows the consecutive six charges of milled Li_2CO_3 .

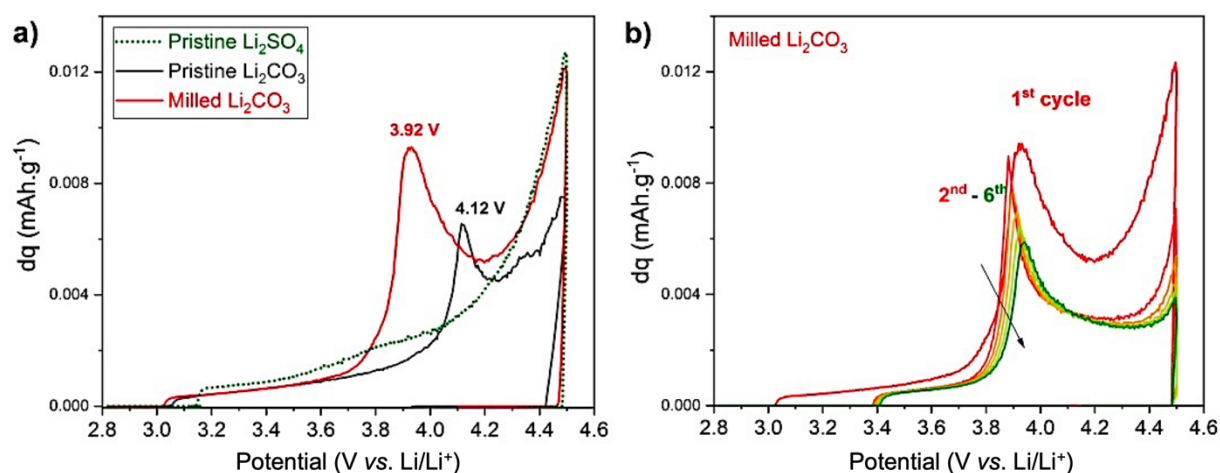
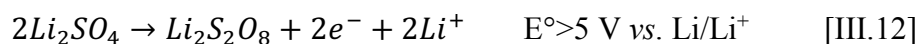
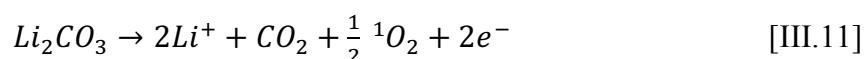
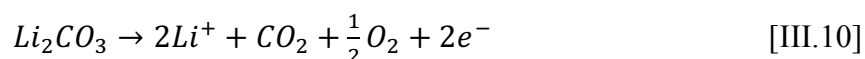


Figure III.7. Incremental capacity curves (5 mV increment) of **a)** the first galvanostatic charge of Li_2SO_4 and pristine and milled Li_2CO_3 and **b)** first six cycles of the milled Li_2CO_3 , all measured in half cells Li_2CO_3 - or Li_2SO_4 -C45/Li at C/40 and 25°C .

As expected, Li_2SO_4 does not show any additional oxidation peak upon charge as the calculated potential at which the electrochemical oxidation of Li_2SO_4 , to produce lithium persulfate ($\text{Li}_2\text{S}_2\text{O}_8$, Eq. III.12) would occur is above the working potential window of NMC (above 5 V vs. Li/Li^+ according to Ghauch et al.³⁰). The solvents oxidation occurs at high potential and would explain the increasing potential up to 4.5 V.



The pristine Li_2CO_3 incremental capacity curve depicts an oxidation peak starting around 4 V (max. intensity at 4.12 V vs. Li/Li^+) while the milled powder starts oxidizing earlier, around 3.6 V vs. Li/Li^+ . Because of the poor electrical conductivity of this compound, it remains difficult, even for milled particles and a low rate to efficiently oxidize (less than 1% was calculated in this case). The oxidation proceeds upon the subsequent cycles (Fig. III.7b) revealing a smaller oxidation peak. The electrochemical oxidation of Li_2CO_3 produces CO_2 and O_2 (Eq. III.10). Recently, it has been proposed through well-founded results, that this oxygen is produced as active oxygen⁸ (1O_2 , Eq. III.11) that rapidly oxidizes the electrolyte components, since O_2 has not been identified by classical spectrometric methods^{8, 9}. Further discussion about the fate of 1O_2 is detailed in [Chapter IV](#).



Through the analysis of the milled powder, it is clearly demonstrated that the oxidation potential is size-dependent, ranging within the working potential window of NMC materials.

3.2. Electrochemical reactivity of the Ni-rich NMC materials

The electrochemical performance of the five electrode films containing as-received NMC 532, 622, 622C, 811, 901; and exposed 622C was studied in half-cell configuration.

3.2.1. Fabrication of the electrodes

Electrodes of each NMC composition were fabricated in a dry room (5–10 ppm of H_2O) following three main steps (details can be found in Annex II):

- i.** Slurry preparation with 90 wt.% active material, 6 wt.% conductive carbon black C45 (BET = $45 \text{ m}^2 \cdot \text{g}^{-1}$, 20 nm particle size, Sigma Aldrich) and 4 wt.% of PVDF binder (Sigma Aldrich).
- ii.** Slurry coating onto an aluminum foil with a target loading of 11-12 $\text{mg} \cdot \text{cm}^{-2}$ and overnight drying at 60°C open in the dry room.

- iii. Calendering of the electrodes to fix porosity at 35%, except for NMC 811 and 901, for the reasons mentioned hereafter.

At this point, it is necessary to evoke the increased reactivity of Ni-rich NMC materials toward H₂O/CO₂ that was studied in [Chapter II](#). The NMC 811 and 901 electrode films were not calendered because the calendering machine is located in a room without controlled humidity. Theoretical porosity values of 48 and 52% were calculated for 811 and 901, respectively.

In order to assess the extent of the degradation that such films would have endured during the calendering process in air, non-calendered as-received NMC 811 and 901 films were exposed 15 minutes to air, the typical duration of the calendering step, followed by electrochemical tests.

First, the growth of carbonates was evidenced by FTIR-ATR analysis of the pristine and air-exposed NMC 811 and 901 films (Fig. III.9). The spectra were normalized by the SO₄²⁻ band centered at 1170 cm⁻¹, similar to what has been done in [Section 4.2.2](#) of [Chapter II](#). The enlargement of the CO₃²⁻ peak located at 878 cm⁻¹ denotes the increase of carbonate content, and thus, confirms the surface degradation of NMC materials after only 15 minutes in air.

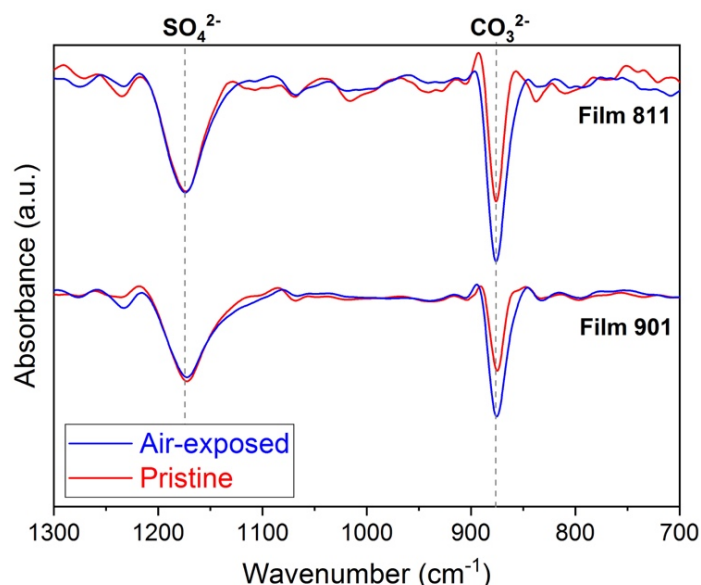


Figure III.9. FTIR-ATR spectra of the pristine and air-exposed film of NMC a) 811 and b) 901.

Afterwards, pristine and air-exposed NMC 811 and 901 films were subjected to galvanostatic cycling in half-cell between 2.8 – 4.3 V vs. Li/Li⁺ at a rate of C/10 (Fig. III.10b and c). For comparison, the electrochemical performance of non-calendered NMC 622C (45% porosity), a

composition less reactive toward air, is also included (Fig. III.10a). Importantly, the applied current density was calculated with the mass of the positive electrode active material, assuming total delithiation; even if, as function of their nickel content, the delithiation varies between 0.6 for NMC 532 to 0.75 for NMC 901 in this potential window. Therefore, a rate of C/10 corresponds experimentally to C/6 – C/7.5, low enough rates to allow the comparison of the different materials.

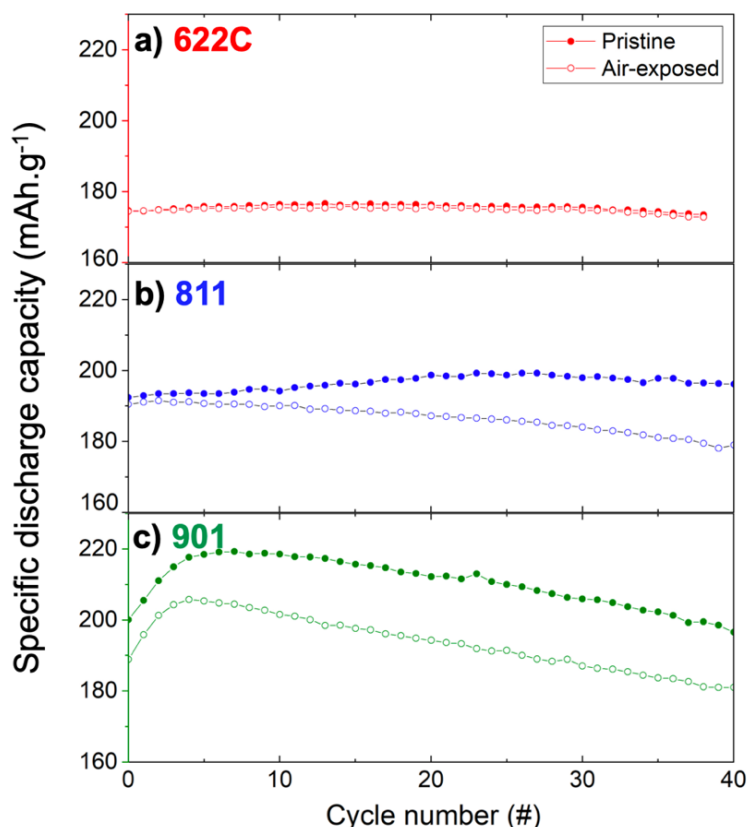


Figure III.10. Cycling performance of as-received and 15 min air-exposed non-calendered films of NMC **a)** 622C, **b)** 811 and **c)** 901; between 2.8–4.3V vs. Li/Li⁺ at C/10 (rate considering a total delithiation) and 25°C.

The 15 minutes exposure of the NMC 811 and 901 films to air has a deleterious effect on the specific capacity and capacity retention values. For instance, air-exposed NMC 811 film decreased its specific capacity after 40 cycles from 190 to 178 mAh.g⁻¹ (-6.3%) and NMC 901 film from 189 to 180 mAh.g⁻¹ (-4.8%), while the unexposed films kept around the same value of the starting specific capacity of 192 mAh.g⁻¹ and 198 mAh.g⁻¹, respectively. In contrast, the NMC 622C film depicts an almost constant capacity of ~175 mAh.g⁻¹ over the 40 cycles. Surprisingly, 811 and 901 NMC materials present an unusual increase in specific capacity from cycle #10 for pristine NMC 811 (up to 200 mAh.g⁻¹) and in the first 8 cycles for pristine

and air-exposed NMC 901 (up to 220 mAh.g⁻¹). This can be explained by the increase of electronic conductivity after partial or complete Li₂CO₃ electrochemical/chemical consumption and/or an improved electrolyte impregnation across the outermost NMC layer. Calculations regarding the electrochemical consumption of Li₂CO₃ are shown later.

Since the electrochemical performance of NMC 622C was very slightly affected by air exposure, it is safe to assume that NMC 532, 622C and 622 can be calendered in air. To date, only Renfrew et al.⁸ evaluated the impact of exposing a Ni-rich NMC material to air. It consisted in air-exposing the NMC 622C during the electrode preparation (step i and ii) that lasts ~30 min. According to their results, the exposure time did not modify the Li₂CO₃ content, corroborating what was observed in our experiments. To the best of the author's knowledge, no other studies of this type have been carried out.

To conclude, the calendaring procedure is meant to fix equal porosity of the electrodes, but doing it in air is very damaging for NMC 811 and 901, since it induces bad capacity retention and reduced specific capacity. Therefore, in the following section, the non-calendered NMC 811 and 901 (48 and 52% porosity) are tested together with calendered 532, 622 and 622C (35% of porosity), in order to evaluate impact of soluble bases on the five as-received NMC.

3.2.2. Galvanostatic profiles of the as-received materials

Figs. III.11a and b. show the first and second galvanostatic cycle of the five as-received materials.

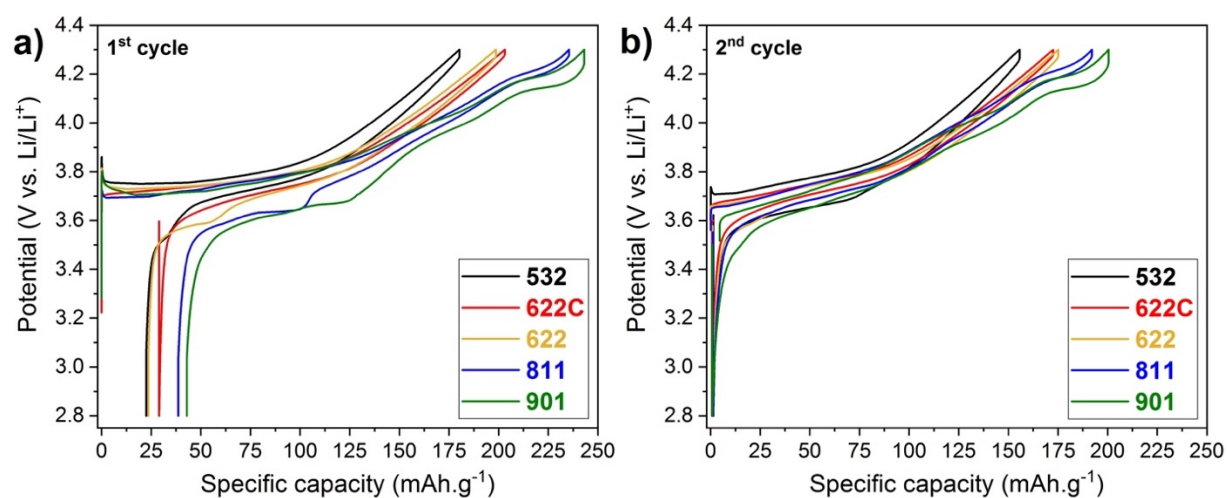


Figure III.11. a) First and b) second charge-discharge cycle of each Ni-rich NMC material, between 2.8–4.3V vs. Li/Li⁺ at C/10 (rate considering total delithiation) and 25°C.

Intriguingly, the NMC 532, 622, 811 and 901 materials present an overpotential (“coup de fouet”) at the beginning of the first charge in half-cell from about 50 to 110 mV (Fig. III.11a). Furthermore, a potential bump is observed in the first discharge at around 65-75 % of extracted lithium from the lithium electrode (between 35 – 150 mAh.g⁻¹ in the x-axis, depending on the NMC composition). However, as it will be shown in [Chapter V](#), these phenomena are not observed when the NMC materials are cycled in full cell with graphite as negative electrode, which discards any contribution from the NMC film. They are most probably linked to the resistive solid electrolyte interphase of the lithium counter electrode. The overpotential is explained by the difficult access of Li⁺ across the SEI to allow lithium plating. As part of the plated lithium is lost in solvents reduction, native lithium must be oxidized to achieve the complete discharge. This stripping process implies that the lithium cations cross the resistive SEI or break it, hence explaining the bump. The occurrence and the magnitude of these phenomena are unpredictable as they depend on the surface state of the lithium; the latter being scratched just before cell assembling. During the second discharge, the SEI of the native lithium is already broken hence both processes tend to disappear, as shown in Fig. III.11b.

Table III.2 shows a summary of some electrochemical performance data from the first two cycles. The 2nd cycle discharge capacity values are in good agreement with previously reported data for these compositions³¹, except for NMC 901, for which there is no published data. Irreversible capacities range between 11.6 to 18.2 % without following a trend with the nickel content. The theoretical capacity delivered by the complete electrochemical oxidation of Li₂CO₃ contained in these NMC materials, represents only 0.5 to 1.2% of the first charge capacity. These values are not necessarily increasing with the nickel content and cannot explain the values of irreversible capacity among the different compositions. Therefore, it seems that the oxidation of Li₂CO₃ does not contribute significantly either to the irreversible or to the reversible capacity.

Table III.2. Summary of the electrochemical performances of the five Ni-rich NMC materials.

Material	Reversible disch. capacity 2 nd cycle (mAh.g _{NMC} ⁻¹)	Irreversible capacity	Theoretical capacity from Li ₂ CO ₃ (mAh.g _{NMC} ⁻¹)
532	158 (0.57 Li)	12.7 %	0.96 (0.6%)
622C	170 (0.61 Li)	14.2 %	1.98 (1.1%)
622	175 (0.63 Li)	11.6 %	2.14 (1.2%)
811	192 (0.70 Li)	18.2 %	1.02 (0.5%)
901	200 (0.72 Li)	17.1 %	2.10 (1.0%)

Although we can make suppositions about the higher irreversibility in NMC 811 and 901, at this point we cannot attribute it to with full certainty to any process. In the literature, the irreversible capacity of the first cycle in NMC-containing batteries has been attributed to³²⁻³⁴:

- Slow lithium kinetics above 0.7 Li inserted in the first discharge proved through GITT measurements of the lithium diffusion coefficient. Increasing the temperature to at least 45 °C decreases this kinetic limitation.
- Absence of calendaring that prevents proper ion transport between the particles.
- The surface area of the particles. According to Choi et al.³⁵, the irreversible capacity increases with the surface area of NMC 111, following a linear relationship. However, this is not our case, since, among the different compositions, NMC 532 has a higher BET surface area (0.27 m².g⁻¹) than NMC 901 (0.20 m².g⁻¹) and their irreversible capacities are 12.7 and 17.1%, respectively.

More information about the nature of the structural changes of as-received NMC materials can be obtained from the incremental charge capacity profile (Fig. III.12). After the overpotential observed at the beginning of the first charge, the NMC materials exhibit a reversible redox process starting at 3.75, 3.76, 3.73, 3.71 and 3.70 V vs. Li/Li⁺ (ordered from highest to lowest nickel content) and lasting until 3.77 V. This potential region corresponds to the structural transition from 1st hexagonal to monoclinic phase (H1→M) upon lithium deintercalation³⁶. Consecutive to the sharp peaks, small ones can be observed and are associated with transitions between states where lithium is ordered and disordered depending on the available octahedral or tetrahedral vacant sites in the crystal structure³¹. Then, above 3.9 V, NMC 811 and 901 present two additional peaks. The first, starting at 3.95 V, corresponds to the monoclinic to 2nd

hexagonal phase transition ($M \rightarrow H_2$) and the second, starting at 4.12 V, corresponds to the 2nd hexagonal to 3rd hexagonal phase transition ($H_2 \rightarrow H_3$).

As afore-mentioned, the oxidation of Li_2CO_3 would represent less than 1% of the total capacity, thus, it could not be visible in the incremental capacity profiles.

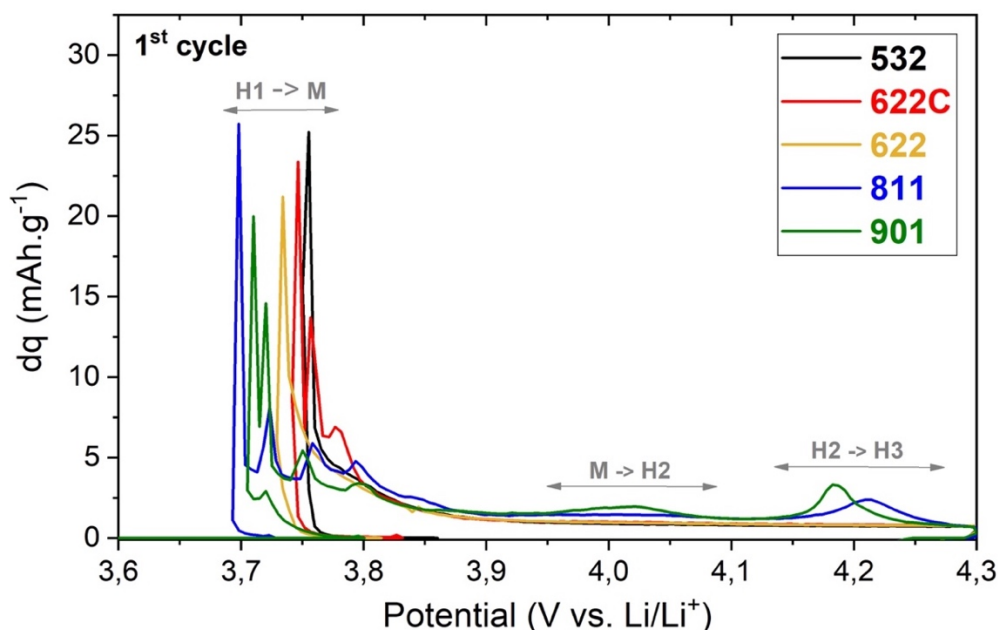


Figure III.12. Incremental capacity profile of the first charge of each material.

In conclusion, the oxidation of the Li_2CO_3 left from synthesis in the as-received materials is not detectable from the electrochemical tests and does not seem to affect the discharge capacity of the materials in the first two cycles.

3.2.3. Galvanostatic profiles of the exposed NMC 622C

In this section the electrochemical evaluation of the surface species contained on exposed NMC 622C is presented. Electrode films were made out of a **20-day exposed NMC 622C powder**, containing no LiOH , $356 \mu\text{mol.g}_{\text{NMC}}^{-1}$ of Li_2CO_3 (instead of $175 \mu\text{mol.g}_{\text{NMC}}^{-1}$ for the 6-day exposed) and insoluble surface species ($(\text{Ni},\text{Co})\text{OOH}$, MnO_2 and NiO). The electrodes were calendered to 35% of porosity and evaluated in half-cell.

Fig. III.13a shows the potential profile versus capacity curves for the first cycle of the exposed NMC 622C. For comparison purposes, the as-received material is also shown.

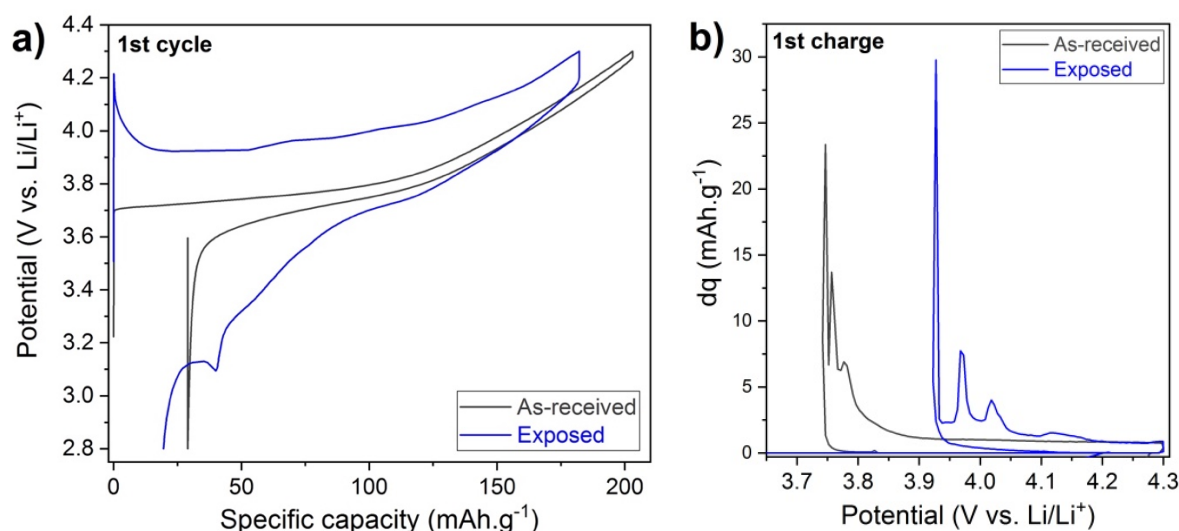


Figure III.13. a) Potential profile in half-cell of the first galvanostatic cycle of the as-received and exposed NMC 622C materials. b) Corresponding incremental capacity profiles.

In the exposed material, the initial overpotential has substantially increased, this time caused by the film resistance across both the lithium SEI and the insulative surface species layer of NMC. The potential bump linked to the lithium stripping process is seen around 40 mAh.g⁻¹ during discharge. Moreover, the initial cell polarization accounts for ~200 mV (Fig. III.13), which limits the available capacity compared to the as-received material. It is highly possible that this large polarization is the combination of multiple processes provoked by the presence of surface species, such as:

- the inter-particles electronic disconnection,
- the blocking of lithium ions migration by the low ionic conductivity of the surface species interphase and
- the obstruction of electrolyte transport in pores (by surface species themselves, or by the decomposition products).

Concomitantly, Li₂CO₃ oxidation may consume current upon charging. Far above to what was predicted in case of the as-received materials, the electrochemical consumption of this amount of Li₂CO₃ would deliver a maximum value of ~19 mAh.g_{NMC}⁻¹, counting for ~11% of the second charge capacity of the exposed NMC 622C. It is possible that it takes place at 4.12 V, where a tiny bump is barely visible (Fig. III.13), since normally NMC 622C has no electrochemical activity at this potential.

3.2.4. Evaluation of the Li_2CO_3 consumption in exposed NMC 622C

With the aim of assessing the extent of Li_2CO_3 consumption during the first electrochemical charge, a composite powder of **20-day exposed NMC 622C** (containing $356 \pm 8 \mu\text{mol.g}_{\text{NMC}}^{-1}$ of Li_2CO_3) and conductive carbon was subjected to **a resting period in OCV** (called 622C(exp.)/Li rest in OCV) or to **a single delithiation** (called 622C(exp.)/Li first delithiation). Initially, both powders rested at OCV during 5 hours to allow complete impregnation of the electrolyte. Then, a current density of 0.416 mA (C/10 calculated for a total delithiation) was applied to the “622C(exp.)/Li first delithiation” powder, whereas the “622C(exp.)/Li rest in OCV” powder only stayed in contact with the electrolyte during the same time in the cell (5.8 h). After, the powders were washed with DMC and vacuum-dried for FTIR analysis (experimental details are in Annex II). Note that this analysis was performed on powder instead of film to avoid the presence of PVDF peaks in the spectra.

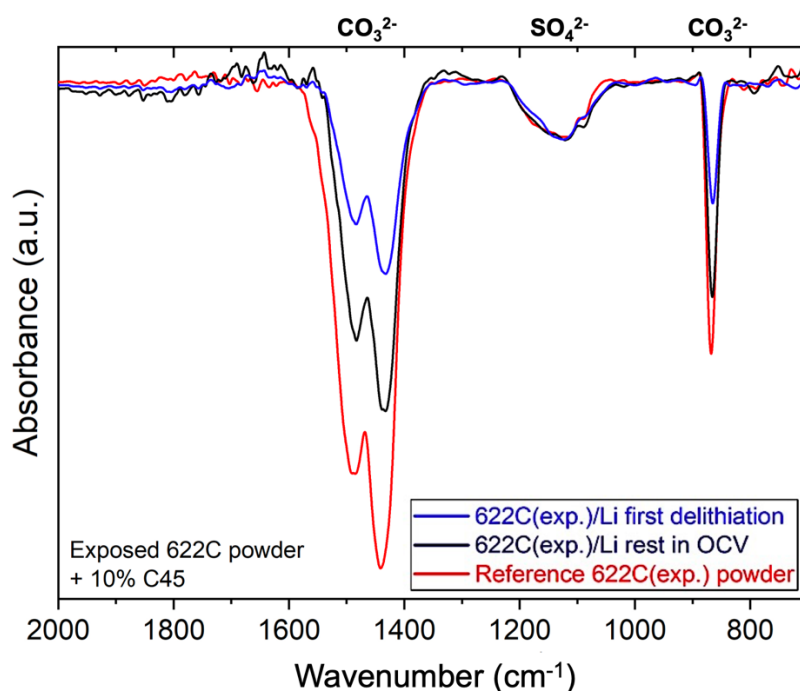


Figure III.14. FTIR-ATR spectra of the exposed NMC 622C powders.

For comparison, powder of exposed NMC 622C without any treatment or exposure to electrolyte was used as IR reference (called Reference 622C(exp.) powder). The obtained FTIR spectra in Fig. III.14 exhibit carbonate bands situated at 875, 1430 and 1490 cm^{-1} and the sulfate band centered at 1125 cm^{-1} . Both powders that were contained in the cells consumed partially Li_2CO_3 , as evidenced by the peak area decrease of carbonate bands, compared to those of the Reference 622C(exp.) powder.

Given that the sulfate band is constant at 25°C, it was possible to get a rough evaluation of the percentage of Li₂CO₃ consumed, through the integration of peak areas. Taking the peak between 1350-1600 cm⁻¹ of the reference material as 100% of Li₂CO₃, it can be calculated that “622C(exp.)/Li rest in OCV” material consumed ~27% of Li₂CO₃, which corresponds to 96.1 μmol.g_{NMC}⁻¹ of Li₂CO₃ chemically consumed (Eq. III.1); and the charged material ~59%, which corresponds to 210 μmol.g_{NMC}⁻¹ of Li₂CO₃ chemically and electrochemically consumed (Eq. III.1 and III.11). Obviously, it is necessary to consider that the consumption yield in the first charge may change from powder to film.

Through OEMS, Metzger et al.²⁹ attributed 0.24 μmol of CO₂ in the first charge of NMC 111/Graphite cell cycled at C/10, exclusively to the electrochemical oxidation of Li₂CO₃, representing 88.9% of the theoretical quantity. Strangely, ~0.20 μmol of CO₂ at the same onset potential were evolved during the second cycle. Even if no explanation was given, most probably, there was a significant contribution from other degradation processes, such as solvent oxidation, that were ignored. Similarly, Renfrew et al.⁸ determined in a NMC 622/Li half-cell cycled at C/10, that 0.81 μmol of CO₂ were produced, 86.2% of the total Li₂CO₃. These studies corroborate that Li₂CO₃ is not entirely consumed during the first cycle, but is likely to be consumed in the consecutive cycles by electrochemical and/or chemical pathways.

3.3. Conclusion

The high reactivity of Ni-rich NMC 811 and 901 materials compels to store and handle these powders under moisture-free environment. This was practically ascertained through exposure of electrode films under air for 15 min. As such a short exposure time leads to decreased electrochemical performances, the decision was made not to calender them; the calendering machine being located in the prototyping room under air environment. Hence, this step, though crucial to confer suitable electrical conductivity to films, was performed only with the less reactive 532, 622 and 622C materials, for incoming electrochemical tests.

Through the electrochemical reactivity experiments, it was determined that the decomposition of Li₂CO₃ during the first cycle of exposed NMC 622C at ambient temperature, is the result of chemical and electrochemical contributions. More specifically, it was found that pure Li₂CO₃ is decomposed from an onset of 3.6 V vs. Li/Li⁺, although the potential is strongly influenced by the size of the Li₂CO₃ particles. Because the layer of Li₂CO₃ grown after exposure is thin

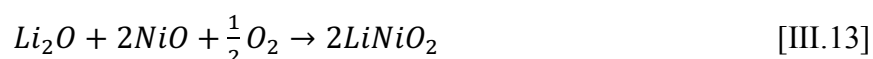
(<150 nm), it can oxidize at any potential within the functioning potential range of NMC materials.

Through FTIR analyses, it was determined that more than half of the Li_2CO_3 contained in the exposed NMC 622C can be eliminated during the first charge. Its chemical and electrochemical consumption may improve the electronic conduction, but at the same time, produce detrimental gases CO_2 and $^1\text{O}_2$. As example, the as-received and 20-day exposed NMC 622C powders contain 37 ± 2 and 356 ± 8 μmol of Li_2CO_3 per gram., respectively, which would convert, at 20 °C under 1 atm., into 0.89 ± 0.05 mL and 8.6 ± 0.2 mL of CO_2 , considering CO_2 as an ideal gas ($24.055 \text{ L}\cdot\text{mol}^{-1}$).

Unlike the electrochemical oxidation, the chemical reaction of Li_2CO_3 with LiPF_6 is supposed to reduce gas production within the cell as no reactive oxygen species are released, thus avoiding reactions with carbonate solvents. Besides, the sub-product LDFP is likely to improve performances (see [Chapter V](#)). Therefore, upon the industrial formation step, leaving the cell after partial charge (to avoid copper oxidation³⁷), under high temperature should be favorable to hinder as much as possible subsequent electrochemical oxidation of Li_2CO_3 .

4. Modification of the surface species by a heat treatment

Annealing NMC materials has proven to be an efficient way to improve the electrochemical performances of air-exposed NMC materials. It is widely accepted that annealing above 400 °C eliminates LiOH and LiHCO₃^{2, 7, 26, 38}, and Li₂CO₃ above 700 °C^{2, 39, 40}. Because LiHCO₃ does not exist, it is unlikely that this is the only explanation to the improved performances. In this sense, during the study of the elimination of soluble bases from synthesis, Park et al.⁴¹, proposed that the surface species (according to them, Li₂CO₃ and LiOH) in their as-received NMC 8-0.5-1.5 can be “re-sintered” into a layered phase at 700°C under O₂ atmosphere, in a procedure analogous to the synthesis in oxidizing atmosphere^{42, 43}. This is done through the reaction of O₂, NiO (a rock salt phase that exists from synthesis) and Li₂O (stemming from the decomposition of LiOH contained in their materials) (Eq. III.13):



However, according to this reaction, O₂ would be necessarily required, which is not the case for other authors that have observed that annealing under argon atmosphere also improved the electrochemical performances⁷. In this sense, in [Chapter II](#), it was demonstrated that between 150–400°C under Ar atmosphere, the re-formation of a layered material occurs through the thermal decomposition of MOOH species and, at the same time, the in-situ reaction between the formed (Ni,Co)O, O₂ and Li₂CO₃. This layered phase is thus suspected to improve the electrochemical performance of exposed materials.

In an attempt to get further insight about the impact of the annealing procedure, the following section is devoted to the study of three surface states of the NMC 622C: as-received, washed and 20-day exposed, and their counterparts annealed in argon atmosphere. All of the annealing experiments were performed at 500 °C, right after the decomposition of MOOH species and reformation of a layered phase (experimental conditions can be found in [Annex II](#)). The electrochemical performances of all these powders have been assessed in half cell after the elaboration of films, following the same procedure of [Section 3.2.1](#).

4.1. As-received, washed, exposed and their analogs annealed NMC 622C films

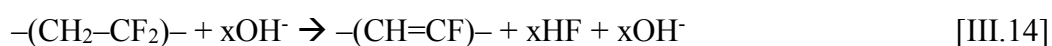
Loadings have been estimated from the weighing of several electrodes at different places in the film.

Table III.3. CO₃²⁻ and OH⁻ amounts quantified through titration in each untreated and annealed NMC 622C and loadings of each corresponding film.

Material NMC 622C	Abbrev.	CO ₃ ²⁻ (μmol.g _{NMC} ⁻¹)	OH ⁻ (from Li ₂ O) (μmol.g _{NMC} ⁻¹)	Loading (mg.cm ⁻²)
As-received	R	37	90	11.4 ± 0.5
As-received + Annealed	R-A	36	130	11 ± 0.3
Washed	W	5	26	11.1 ± 0.4
Washed + Annealed	W-A	17	68	12.5 ± 0.5
Exposed (20 days)	E	356	0	14.2 ± 0.6
Exposed + Annealed	E-A	196	146	14.4 ± 0.6

As shown in Table III.3, as-received, washed and corresponding annealed NMC films depict almost the same loadings between 11 and 12.5 mg.cm⁻² whereas both exposed NMC films present higher values of 14.2 and 14.3 mg.cm⁻². This seems to be related to the viscosity of the slurries, therefore, we undertook preliminary tests on as-received and exposed materials.

According to the literature, during the electrode films fabrication with PVDF binder, the viscosity of the slurry can increase owing to the presence of LiOH^{44, 45}. This behavior, known as slurry gelation, is due to the double bond formation after HF release (Eq. III.14) that renders the polymer more rigid. It is possible that PVDF also reacts with Li₂O. Even if it is less soluble in NMP than LiOH, trace of water in NMP would turn it into LiOH.



Given this reaction, a decision was made to adapt the choice of the material tested to evaluate the role of this potential surface species. Hence, NMC 811 was chosen as LiOH was detected after H₂O/CO₂ exposure in an amount of 25 μmol.g_{NMC}⁻¹. Its potential impact on the rheological properties of slurries was studied at 25°C with a rotational rheometer Kinexus Lab+ (Malvern) employing planar plate geometry. For comparison purposes, Fig. III.15 shows the viscosity versus shear rate plot of both as-received and 6-day exposed NMC 811. Both slurries behave similarly at high shear rates, however, at low shear rates, close to the stationary state, the differences are more pronounced. Our hypothesis is that the surface deterioration

caused by H₂O/CO₂ exposure, influences the interaction between these particles and the polymer-carbon matrix during slurry preparation. These differences could not be explained by the afore-mentioned slurry gelation process as it would bring about a decrease of the viscosity at any shear rate.

Moreover, the shear rate value of 34 s⁻¹ (calculation in Annex II) that the slurry endures when cast onto the aluminum foil can be used as a reference point to compare both slurries property more accurately. At this shear rate, viscosity values of 6.4 and 6.0 Pa.s were found for as-received and exposed NMC 811 slurries, respectively. From this little difference, it can be ascertained that slurry gelation did not take place in any of them. According to Paulsen et al.⁴⁴, above around 46 μmol.g_{NMC}⁻¹ of LiOH, the slurry is “unstable”, which means that its viscosity increases and may cause gelation or flocculation. In the 6-day exposed NMC 811, only 25 μmol.g_{NMC}⁻¹ of OH⁻ were quantified; a too low amount to induce gelation. In the as-received material, 214 μmol.g_{NMC}⁻¹ of OH⁻ were found, a sufficient amount for visible viscosity increase at every shear rate, which is not observed in Fig. III.15. This result confirms the existence of Li₂O instead of LiOH, as proposed in [Chapter II](#).

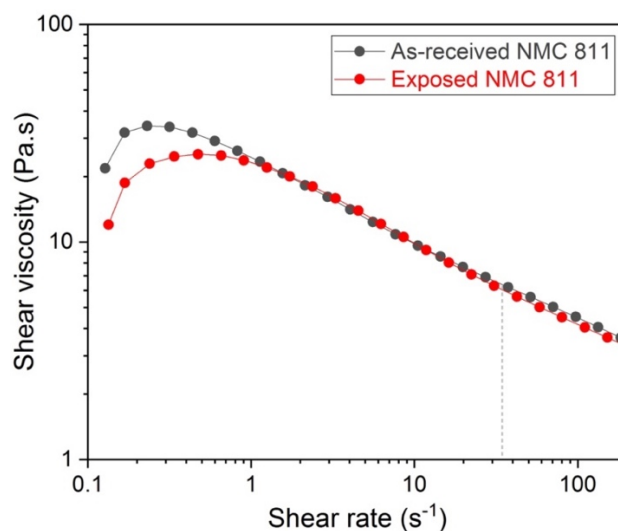


Figure III.15. Viscosity versus shear rate plot of two slurries. The dashed gray line signals the shear rate of 34 s⁻¹ corresponding to that induced by the coating of the slurries onto an Al foil.

In NMC 622C, LiOH detected in as-received powder was suggested to be originated from Li₂O and the exposed powder does not contain any, which suggest similar viscosity results would be obtained. Therefore, loading differences do not seem to be caused by the viscosity change. Further in-depth investigations are required for the complete understanding, but are beyond the scope of this study.

4.2. Impact of heat treatment on as-received NMC 622C

The capacity retention obtained for the R and R–A NMC 622C films in half-cell are shown in Fig. III.16 and the quantities of CO_3^{2-} and OH^- from Li_2O are written on the inset table.

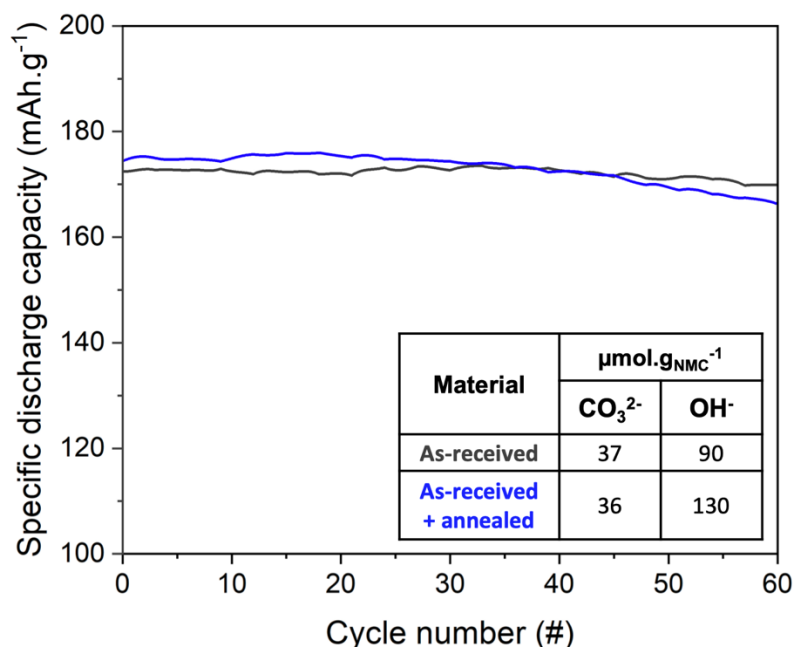


Figure III.16. Discharge capacity retention curves of the R and A–R NMC 622C/Li half-cell at C/10 between 2.8–4.3 V. **Inset:** table with the quantities of soluble bases obtained from acid-base titration.

Annealing an as-received NMC 622C at 500°C under Ar flow brings about no change in the CO_3^{2-} content and slight increase of OH^- which will be explained hereafter (inset Fig. III.16). According to the assumption that Li_2CO_3 can react in situ with O_2 , from MOOH decomposition (Eq. II.31), no variation of the content after annealing supposes that the soluble bases are mainly originating from synthesis. This result was expected as all necessary precautions were taken to keep the as-received NMC materials under moisture-free environment. On the other hand, Park et al.²² showed that the quantity of Li_2CO_3 in their as-received NMC 80.5-1.5 decreased from 99 to 62 $\mu\text{mol.g}_{\text{NMC}}^{-1}$ when heated at 720°C under O_2 atmosphere, the temperature at which Li_2CO_3 starts melting and thus could easily react.

The electrochemical performance of both films presents no conclusive change over 60 cycles, apart from the small difference in the initial discharge capacity (174 mAh.g^{-1} , compared to 172 mAh.g^{-1} of the as-received material) and a lower capacity retention after 40 cycles (95.4 %, 170 mAh.g^{-1} of the as-received material).

compared to 98.5 % for the as-received material after 60 cycles). Larger-scale tests could confirm a real impact of the annealing process on as-received NMC.

4.3. Impact of heat treatment on washed NMC 622C

This section aims at defining the influence of an aqueous washing procedure on the electrochemical performances of NMC 622C. The washing procedure is similar to that optimized for acid-base titration analysis described in [Chapter II](#) (15 minutes of stirring time in argon atmosphere). It has been reported that poor performances are achieved from washed NMC 811 material⁴⁶. As a matter of fact, SBs are not necessarily considered as impurities but rather as “surface properties”. Hence, in Paulsen’s patent⁴⁴, it is proposed a threshold value of soluble base content, found experimentally, referred to as “equilibrium value”. For instance, equilibrium values given for commercial NMC 111, 532 and 622 with about the same morphology (spherical dense particles with D50 of about 8-10 μm , with crystallite size of 500 nm) increases from 15-20 to 50-70 to 100-150 $\mu\text{mol.g}_{\text{NMC}}^{-1}$, respectively. Later, Park et al.²² determined that leaving 163 $\mu\text{mol.g}_{\text{NMC}}^{-1}$ of soluble bases improved the capacity retention. It has to be emphasized that these contents were obtained by acid-base titration without mentioning the origin of LiOH as potentially coming from Li_2O .

Interestingly, the as-received NMC 622C values (145 and 166 $\mu\text{mol.g}_{\text{NMC}}^{-1}$ for R and R–A samples) are in the given equilibrium content range. As expected, washed samples depict lower values (31 and 85 $\mu\text{mol.g}_{\text{NMC}}^{-1}$ for W and W–A samples, respectively) and exposed samples depict higher values (356 and 342 $\mu\text{mol.g}_{\text{NMC}}^{-1}$ for E and E–A samples, respectively). With the equilibrium value as reference, it is thus predicted that either washed or exposed materials will not deliver good performances as compared with as-received ones.

Noteworthy, the washing procedure decreased almost to zero the quantity of CO_3^{2-} , and decreased the OH^- by five. These values are not zero due to two possible reasons, (i) the presence of CO_2 and H_2O traces that may exist in the argon (99.999% purity); and (ii) a brief exposure to air during the transfer to and from the furnace used for the annealing treatment; in addition to the severe sensibility of washed materials toward air²².

The capacity retention obtained for the W and W–A NMC 622C are shown in Fig. III.17. For comparison, the as-received material is also displayed. The almost entire elimination of the soluble bases in W material did not improve the capacity retention, but slightly improved the initial discharge capacity from 172 to 176 mAh.g^{-1} . Unfortunately, the gain is rapidly lost,

since at 20 cycles the capacity reaches the same value as the as-received material and continues to decrease until 157 mAh.g⁻¹ at 60 cycles (red curve), compared to 170 mAh.g⁻¹ from the as-received material (grey curve).

The W-A material presents 17 and 68 μmol/g_{AM powder} of CO₃²⁻ and OH⁻, respectively. The reason for the increase of SB content compared to the W material (5 and 26 μmol/g_{AM powder}, respectively) is believed to be the transfer to and from the furnace used for the annealing treatment. Concerning the electrochemical effect, annealing the washed material makes it perform slightly better but still lower than the as-received material. In spite of the initial lower discharge capacity (172 compared to 177 mAh.g⁻¹), after 60 cycles the washed + annealed retained 91 % of the original capacity, compared to 88 % of the washed material.

Up to this point, neither the washing nor the annealing procedures seem to improve the capacity retention of as-received NMC 622C.

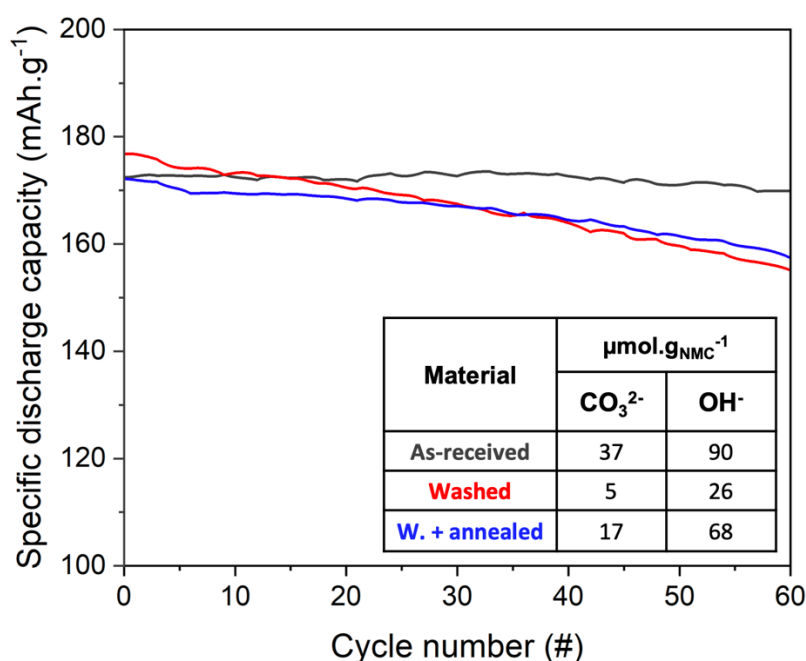
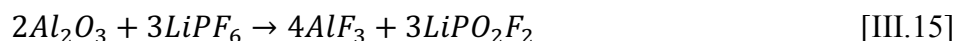


Figure III.17. Discharge capacity retention curves of the as-received and as-received + annealed NMC 622C/Li half-cell at C/10 between 2.8–4.3 V. **Inset:** table with the quantity of soluble bases obtained from acid-base titration.

While in literature, surface species are considered in general terms as “surface property”, it is reasonable to assume, in light of earlier results, that the capacity fade could be partly due to the absence of enough surface species (Li₂CO₃, Li₂O, Li₂SO₄) to react with LiPF₆ into LDFP

and LiF acting, respectively, as electrolyte additive and passivating layer. Note that the role of the coating on the particles is not well defined; it has been proved experimentally that pure Al_2O_3 is prone to react with LiPF_6 in a similar way to produce AlF_3 and LiPO_2F_2 (Eq. III.15)⁴⁷, but may also hydrate at room temperature to give $\text{Al}(\text{OH})_3$ ⁴⁸.



4.4. Impact of heat treatment on exposed NMC 622C

Upon **20-day exposure** to specific $\text{H}_2\text{O}/\text{CO}_2$ (Chapter II), the totality of Li_2O contained in as-received NMC 622C transformed into Li_2CO_3 and through further degradation, almost ten times more Li_2CO_3 than in the as-received material was created (inset in Fig. III.18), equivalent to an astonishing value of 5.3 mol% of reacted lithium. Due to this heavy degradation, the initial discharge capacity of exposed NMC is considerably lower, 145mAh.g^{-1} (-16 %), compared to the as-received material of 172mAh.g^{-1} . From there, the regular increase of capacity seen during the first 20 cycles can be explained by the gradual chemical and electrochemical consumption of surface species. Given that the capacity was neither recuperated nor improved after 60 cycles, after Li_2CO_3 has been chemically or electrochemically consumed, it is reasonable to assume that the oxides and oxyhydroxides are responsible for the ceaseless low capacity. Thus, the bad electrochemical performance cannot be only attributed to the Li_2CO_3 presence, as has been proposed in the literature.

The surface layer in the exposed NMC 622C was expected to heavily evolve after annealing. Indeed, the content of CO_3^{2-} decreased by $160\ \mu\text{mol.g}_{\text{NMC}}^{-1}$ after annealing. Since this temperature is too low to decompose thermally Li_2CO_3 , it underwent the in-situ reaction with O_2 and Ni and Co oxides products from the decomposition of MOOH, according to previous TGA-MS findings. Since from 1 mole of Li_2CO_3 , 2 moles of $\text{Li}(\text{Ni}_{1-2x-y}\text{Co}_y)\text{O}_2$ are produced (Eq. II.31), the quantity of $\text{Li}(\text{Ni}_{1-2x-y}\text{Co}_y)\text{O}_2$ formed would be $320\ \mu\text{mol.g}_{\text{NMC}}^{-1}$. The presence of this newly formed layered phase along with the disappearance of part of Li_2CO_3 and metal oxides/hydroxides upon heating should lead to improved electrochemical performances. On the other hand, similarly as the other annealed materials, a relatively high amount of OH^- ($146\ \mu\text{mol.g}_{\text{NMC}}^{-1}$) was detected after annealing, which could not be explained only by the presence of impurities in argon, but mostly due to rapid degradation during the transfers.

Regarding the electrochemical performance of the corresponding films, initial discharge capacity is around 164 mAh.g^{-1} (+12 % compared to the exposed) which accounts for 95 % of the as-received material discharge capacity of 172 mAh.g^{-1} . Therefore, the annealing process at 500°C under argon allowed $\text{H}_2\text{O}/\text{CO}_2$ exposed NMC 622C materials to recover part of their capacity due to layered oxides reformation and decomposition products vanishing. Nevertheless, the poor retention capacity of the exposed material is not improved after annealing, which may limit the applicability of this process as a long-term solution.

Correspondingly, Oh et al.⁴⁹ reported that annealing a 3-month exposed NMC 7-1.5-1.5 at 600°C under O_2 atmosphere gave the biggest improvement among the annealing temperatures of 100, 400 and 600°C . Similarly, Liu et al.² reported that 98.8% of the original discharge capacity of a 6-month exposed NMC 802 can be recovered by annealing at 725°C under flowing O_2 . These two works attributed the capacity improvements to the reconstruction of a layered phase because of the use of O_2 and the high annealing temperature. Based on the findings of this work, we think that the reconstruction is in reality due to the reaction of the MOOH species with O_2 and Li_2CO_3 .

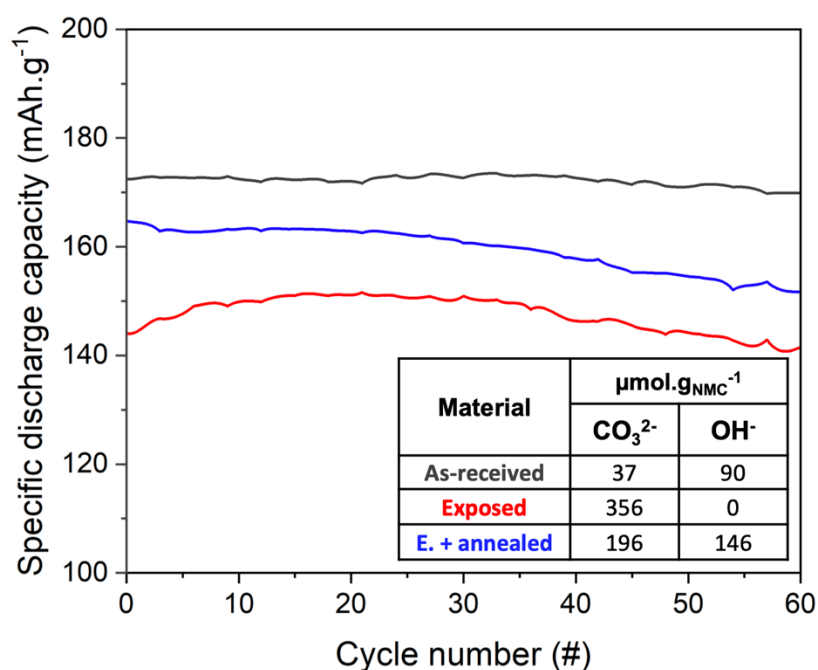


Figure III.18. Discharge capacity retention curves of the R, E and E–A NMC 622C/Li half-cell at C/10 between 2.8–4.3 V. **Inset:** table with the quantity of soluble bases obtained from acid-base titration.

To further investigate the beneficial effect of annealing on exposed NMC materials, the first galvanostatic cycle potential profile of the E–A material was compared to those of the as-received and exposed materials, as shown in Fig. III.19. It can be appreciated that the large polarization in the exposed material is significantly reduced by annealing at 500°C, almost to the point of recuperating the low polarization of the as-received material. As aforementioned, the original capacity was not totally recuperated, certainly due to the surface species that were not consumed at 500°C, like MnO₂ and the remaining Li₂CO₃. These experiments point out that both (Ni,Co)OOH and Li₂CO₃ account for the large polarization of the untreated electrode, but the remaining oxides and carbonates in annealed electrodes account for the persistent low capacity.

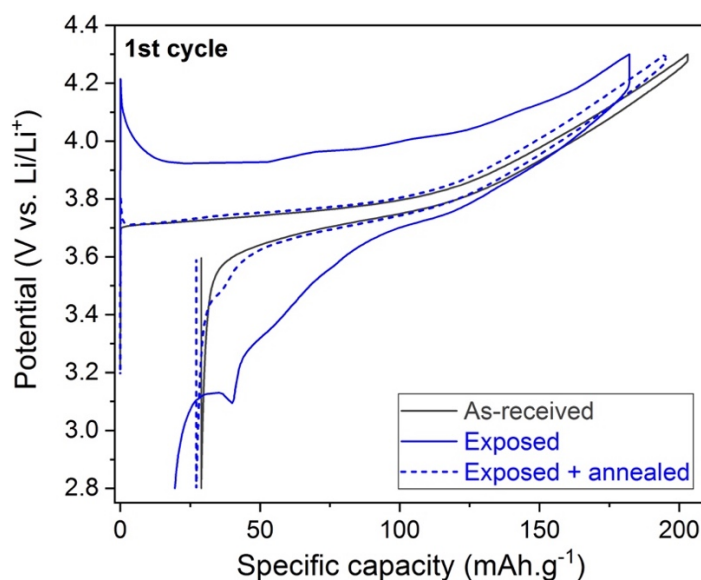


Figure III.19. Voltage profiles vs. capacity for half-cells at a rate of C/10 between 2.8–4.3 V for the as-received, exposed and exposed + annealed materials.

Moreover, the decomposition of oxyhydroxide species was confirmed by TGA-MS analysis (Fig. III.20), following the conditions mentioned in Annex I. The exposed material presents the expected weight loss and the associated production of H₂O, O₂ and CO₂ between 150–450°C. Interestingly, the exposed + annealed material does not present any weight loss in this region and H₂O, O₂ or CO₂ were not detected, suggesting that all of the (Ni,Co)OOH species were eliminated during the annealing at 500°C. The weight loss detected from 750°C corresponds to Li₂CO₃ and the NMC thermal decomposition.

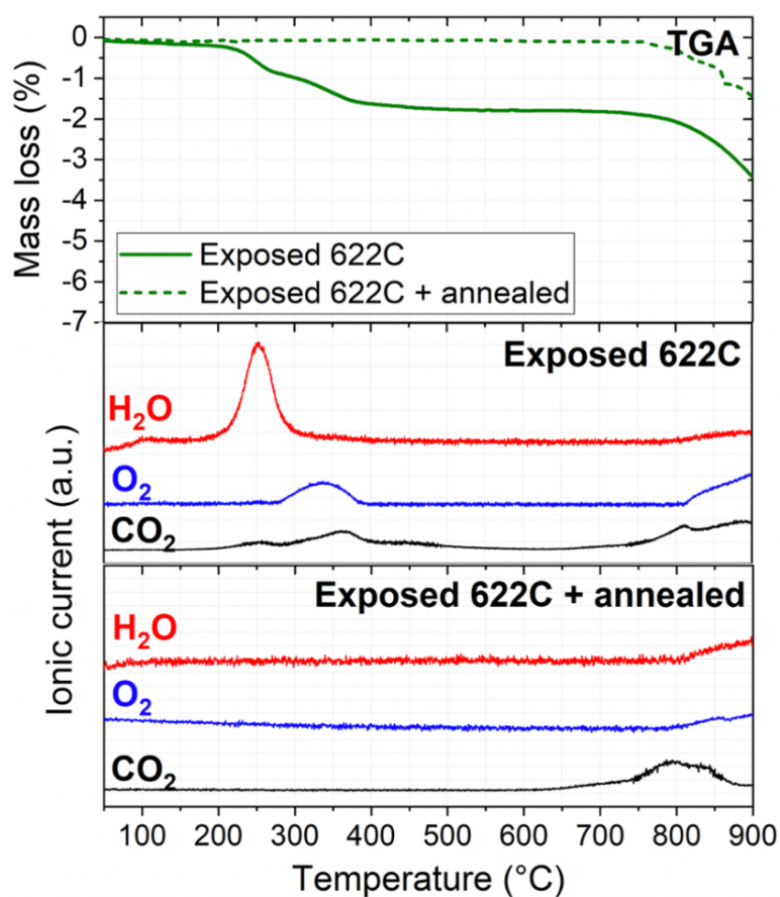


Figure III.20. TGA curves along with mass traces of H₂O (m/z 18), O₂ (m/z 32) and CO₂ (m/z 44) of an E and E–A NMC 622C.

4.5. Conclusion

With the objective to evaluate the role of surface species on cycling, as-received, washed and H₂O/CO₂ exposed NMC 622C were studied with and without annealing treatment at 500°C under flowing argon. The electrochemical performances of the electrode films made of non-annealed powders were predicted by comparing the values of soluble base content with the equilibrium value given in literature. It is suggested that these surface species could benefit the performance through reaction with acidic species (HF...) or LiPF₆ in the electrolyte.

In addition, it was found that a too large amount of electronically insulating surface species formed upon excessive H₂O/CO₂ exposure leads to a large polarization and lower capacities. In this case, the annealing treatment enables the recovering of the original polarization and a part of the capacity due to the decomposition of oxyhydroxides MOOH along with the in-situ reaction of Li₂CO₃ with O₂ and metal oxides to reform active layered oxides (Eqs. II.29 – 31 of [Chapter II](#)). Overall, this section helped clarify the relation between the decomposition of surface species and the electrochemical performance of Ni-rich NMC materials.

5. Conclusion of the chapter

The chapter was devoted to getting further insight into the fate of surface species in Ni-rich NMC materials when used as Li-ion battery positive active material, as well as their influence on the electrochemical performances. Therefore, a stepwise investigation of their chemical reactivity toward a classical electrolyte was first undertaken. It was proven that the soluble bases Li_2CO_3 , Li_2O , Li_2SO_4 react with LiPF_6 , especially at 55°C , to produce LDFP, LiF . On the other hand, the high reactivity of LiOH with carbonate solvents produces fluorophosphates along with LiF . This allowed to ascertain, through the absence of fluorophosphates and LiF in ^{19}F NMR spectra, that LiOH detected from acid-base titration in as-received NMC powders, was coming from Li_2O . This result can be of paramount importance when considering the responsibility of LiOH in the PVDF-based slurry gelation process.

If the totality of Li_2CO_3 is not chemically consumed in contact with LiPF_6 , it may oxidize upon charge at a potential value that is strongly influenced by the particle size of Li_2CO_3 . As a sacrificial salt, it leads to the production of additional Li^+ but also CO_2 and $^1\text{O}_2$ species. Given the high reactivity of the latter toward carbonate solvents, producing further gas, it is assumed that the chemical consumption of Li_2CO_3 with LiPF_6 is preferable over electrochemical oxidation. Moreover, it favors the production of LDFP, an electrolyte additive known to improve electrochemical performances and LiF , a stable passivating compound.

The removal of the surface species through a washing procedure was demonstrated to be detrimental to the capacity retention which steadily decreases from the first cycles whereas forming soluble bases in a too large amount through NMC exposure under $\text{H}_2\text{O}/\text{CO}_2$ atmosphere leads to polarization enlargement and limited delivered capacities. These results seem to corroborate the existence of an equilibrium value corresponding to an ideal amount of surface species that acts positively on the electrochemical stability of NMC materials. The annealing treatment at 500°C under argon of exposed materials helped to recover some capacity and reduce polarization owing to the decomposition of MOOH species that made it possible to reform electrochemically-active layered oxides.

6. References

1. Liu, H. S.; Zhang, Z. R.; Gong, Z. L.; Yang, Y., Origin of deterioration for LiNiO₂ cathode material during storage in air. *Electrochemical and Solid State Letters* **2004**, 7 (7), A190-A193.
2. Liu, H. S.; Yang, Y.; Zhang, J. J., Investigation and improvement on the storage property of LiNi_{0.8}Co_{0.2}O₂ as a cathode material for lithium-ion batteries. *Journal of Power Sources* **2006**, 162 (1), 644-650.
3. Zhuang, G. V.; Chen, G. Y.; Shim, J.; Song, X. Y.; Ross, P. N.; Richardson, T. J., Li₂CO₃ in LiNi_{0.8}Co_{0.15}Al_{0.05}O₂ cathodes and its effects on capacity and power. *Journal of Power Sources* **2004**, 134 (2), 293-297.
4. Bi, Y. J.; Wang, T.; Liu, M.; Du, R.; Yang, W. C.; Liu, Z. X.; Peng, Z.; Liu, Y.; Wang, D. Y.; Sun, X. L., Stability of Li₂CO₃ in cathode of lithium ion battery and its influence on electrochemical performance. *Rsc Advances* **2016**, 6 (23), 19233-19237.
5. Kim, Y., Mechanism of gas evolution from the cathode of lithium-ion batteries at the initial stage of high-temperature storage. *Journal of Materials Science* **2013**, 48 (24), 8547-8551.
6. Zhang, X. Y.; Jiang, W. J.; Zhu, X. P.; Mauger, A.; Qilu; Julien, C. M., Aging of LiNi_{1/3}Mn_{1/3}Co_{1/3}O₂ cathode material upon exposure to H₂O. *Journal of Power Sources* **2011**, 196 (11), 5102-5108.
7. Chen, Z. Q.; Wang, J.; Huang, J. X.; Fu, T.; Sun, G. Y.; Lai, S. B.; Zhou, R.; Li, K.; Zhao, J. B., The high-temperature and high-humidity storage behaviors and electrochemical degradation mechanism of LiNi_{0.6}Co_{0.2}Mn_{0.2}O₂ cathode material for lithium ion batteries. *Journal of Power Sources* **2017**, 363, 168-176.
8. Renfrew, S. E.; McCloskey, B. D., Residual Lithium Carbonate Predominantly Accounts for First Cycle CO₂ and CO Outgassing of Li-Stoichiometric and Li-Rich Layered Transition-Metal Oxides. *Journal of the American Chemical Society* **2017**, 139 (49), 17853-17860.
9. Mahne, N.; Renfrew, S. E.; McCloskey, B. D.; Freunberger, S. A., Electrochemical Oxidation of Lithium Carbonate Generates Singlet Oxygen. *Angewandte Chemie-International Edition* **2018**, 57 (19), 5529-5533.
10. Paulsen, J. M.; Park, H. K.; Kwon, Y. H. Process of making cathode material containing Ni-based lithium transition metal oxide. US7943111. 2011.
11. Tasaki, K.; Goldberg, A.; Lian, J. J.; Walker, M.; Timmons, A.; Harris, S. J., Solubility of Lithium Salts Formed on the Lithium-Ion Battery Negative Electrode Surface in Organic Solvents. *Journal of the Electrochemical Society* **2009**, 156 (12), A1019-A1027.
12. Parimalam, B. S.; MacIntosh, A. D.; Kadam, R.; Lucht, B. L., Decomposition Reactions of Anode Solid Electrolyte Interphase (SEI) Components with LiPF₆. *Journal of Physical Chemistry C* **2017**, 121 (41), 22733-22738.
13. Garcia-Juan, P.; Shultz, A., Manufacture of mixtures comprising LiPO₂F₂ and LiPF₆. WO 2013/023902. 2013.
14. Campion, C. L.; Li, W. T.; Lucht, B. L., Thermal decomposition of LiPF₆-based electrolytes for lithium-ion batteries. *Journal of the Electrochemical Society* **2005**, 152 (12), A2327-A2334.
15. Plakhotnyk, A. V.; Ernst, L.; Schmutzler, R., Hydrolysis in the system LiPF₆-propylene carbonate-dimethyl carbonate-H₂O. *Journal of Fluorine Chemistry* **2005**, 126 (1), 27-31.
16. Ravdel, B.; Abraham, K. M.; Gitzendanner, R.; DiCarlo, J.; Lucht, B.; Campion, C., Thermal stability of lithium-ion battery electrolytes. *Journal of Power Sources* **2003**, 119, 805-810.
17. Wilken, S.; Treskow, M.; Scheers, J.; Johansson, P.; Jacobsson, P., Initial stages of thermal decomposition of LiPF₆-based lithium ion battery electrolytes by detailed Raman and NMR spectroscopy. *Rsc Advances* **2013**, 3 (37), 16359-16364.
18. Gireaud, L.; Grugeon, S.; Laruelle, S.; Pilard, S.; Tarascon, J. M., Identification of Li battery electrolyte degradation products through direct synthesis and characterization of alkyl carbonate salts. *Journal of the Electrochemical Society* **2005**, 152 (5), A850-A857.
19. Zhao, D. N.; Song, S. N.; Ye, X. S.; Wang, P.; Wang, J.; Wei, Y.; Li, C. L.; Mao, L. P.; Zhang, H. M.; Li, S. Y., New insight into the mechanism of LiPO₂F₂ on the interface of high-voltage cathode LiNi_{0.5}Mn_{1.5}O₄ with truncated octahedral structure. *Applied Surface Science* **2019**, 491, 595-606.

20. Wang, C. Y.; Yu, L.; Fan, W. Z.; Liu, J. W.; Ouyang, L. Z.; Yang, L. C.; Zhu, M., Lithium Difluorophosphate As a Promising Electrolyte Lithium Additive for High-Voltage Lithium-Ion Batteries. *Acs Applied Energy Materials* **2018**, *1* (6), 2647-2656.
21. Andersson, A. M.; Abraham, D. P.; Haasch, R.; MacLaren, S.; Liu, J.; Amine, K., Surface characterization of electrodes from high power lithium-ion batteries. *Journal of the Electrochemical Society* **2002**, *149* (10), A1358-A1369.
22. Park, J. H.; Choi, B.; Kang, Y. S.; Park, S. Y.; Yun, D. J.; Park, I.; Ha Shim, J.; Han, H. N.; Park, K., Effect of Residual Lithium Rearrangement on Ni-rich Layered Oxide Cathodes for Lithium-Ion Batteries. *Energy Technology* **2018**, *6* (7), 1361-1369.
23. Yang, G. H.; Shi, J. L.; Shen, C.; Wang, S. W.; Xia, L.; Hu, H. S.; Luo, H.; Xia, Y. G.; Liu, Z. P., Improving the cyclability performance of lithium-ion batteries by introducing lithium difluorophosphate (LiPO₂F₂) additive. *Rsc Advances* **2017**, *7* (42), 26052-26059.
24. Wang, C. Y.; Yu, L.; Fan, W. Z.; Liu, R.; Liu, J. W.; Ouyang, L. Z.; Yang, L. C.; Zhu, M., Enhanced high-voltage cyclability of LiNi_{0.5}Co_{0.2}Mn_{0.3}O₂-based pouch cells via lithium difluorophosphate introducing as electrolyte additive. *Journal of Alloys and Compounds* **2018**, *755*, 1-9.
25. Lei, Q. F.; Yang, T. X.; Zhao, X. Y.; Fan, W. Z.; Wang, W. L.; Yu, L.; Guo, S. B.; Zuo, X. X.; Zeng, R. H.; Nan, J. M., Lithium difluorophosphate as a multi-functional electrolyte additive for 4.4 V LiNi_{0.5}Co_{0.2}Mn_{0.3}O₂/graphite lithium ion batteries. *Journal of Electroanalytical Chemistry* **2019**, *846*.
26. Faenza, N. V.; Bruce, L.; Lebens-Higgins, Z. W.; Plitz, I.; Pereira, N.; Piper, L. F. J.; Amatucci, G. G., Growth of Ambient Induced Surface Impurity Species on Layered Positive Electrode Materials and Impact on Electrochemical Performance. *Journal of the Electrochemical Society* **2018**, *164* (14), A3727-A3741.
27. Chen, Z. Q.; Liu, C. Y.; Sun, G. Y.; Kong, X. B.; Lai, S. B.; Li, J. Y.; Zhou, R.; Wang, J.; Zhao, J. B., Electrochemical Degradation Mechanism and Thermal Behaviors of the Stored LiNi_{0.5}Co_{0.2}Mn_{0.3}O₂ Cathode Materials. *Acs Applied Materials & Interfaces* **2018**, *10* (30), 25454-25464.
28. Meini, S.; Tsiouvaras, N.; Schwenke, K. U.; Piana, M.; Beyer, H.; Lange, L.; Gasteiger, H. A., Rechargeability of Li-air cathodes pre-filled with discharge products using an ether-based electrolyte solution: implications for cycle-life of Li-air cells. *Physical Chemistry Chemical Physics* **2013**, *15* (27), 11478-11493.
29. Metzger, M.; Strehle, B.; Solchenbach, S.; Gasteiger, H. A., Origin of H₂ Evolution in LIBs: H₂O Reduction vs. Electrolyte Oxidation. *Journal of the Electrochemical Society* **2016**, *163* (5), A798-A809.
30. Ghauch, A.; Tuqan, A., Oxidation of bisoprolol in heated persulfate/H₂O systems: Kinetics and products. *Chemical Engineering Journal* **2012**, *183*, 162-171.
31. Noh, H. J.; Youn, S.; Yoon, C. S.; Sun, Y. K., Comparison of the structural and electrochemical properties of layered LiNi_xCo_yMn_zO₂ (x=1/3, 0.5, 0.6, 0.7, 0.8 and 0.85) cathode material for lithium-ion batteries. *Journal of Power Sources* **2013**, *233*, 121-130.
32. Kang, S. H.; Abraham, D. P.; Yoon, W. S.; Nam, K. W.; Yang, X. Q., First-cycle irreversibility of layered Li-Ni-Co-Mn oxide cathode in Li-ion batteries. *Electrochimica Acta* **2008**, *54* (2), 684-689.
33. Buchberger, I.; Seidlmayer, S.; Pokharel, A.; Piana, M.; Hattendorff, J.; Kudejova, P.; Gilles, R.; Gasteiger, H. A., Aging Analysis of Graphite/LiNi_{1/3}Mn_{1/3}Co_{1/3}O₂ Cells Using XRD, PGAA, and AC Impedance. *Journal of the Electrochemical Society* **2015**, *162* (14), A2737-A2746.
34. Zhou, H.; Xin, F. X.; Pei, B.; Whittingham, M. S., What Limits the Capacity of Layered Oxide Cathodes in Lithium Batteries? *Acs Energy Letters* **2019**, *4* (8), 1902-1906.
35. Choi, J.; Manthiram, A., Investigation of the irreversible capacity loss in the layered LiNi_{1/3}Mn_{1/3}Co_{1/3}O₂ cathodes. *Electrochemical and Solid State Letters* **2005**, *8* (8), C102-C105.
36. Li, H. Y.; Zhang, N.; Li, J.; Dahn, J. R., Updating the Structure and Electrochemistry of Li_xNiO₂ for 0 ≤ x ≤ 1. *Journal of the Electrochemical Society* **2018**, *165* (13), A2985-A2993.
37. Zhao, M. C.; Kariuki, S.; Dewald, H. D.; Lemke, F. R.; Staniewicz, R. J.; Plichta, E. J.; Marsh, R. A., Electrochemical stability of copper in lithium-ion battery electrolytes. *Journal of the Electrochemical Society* **2000**, *147* (8), 2874-2879.
38. Jo, J. H.; Jo, C. H.; Yashiro, H.; Kim, S. J.; Myung, S. T., Re-heating effect of Ni-rich cathode material on structure and electrochemical properties. *Journal of Power Sources* **2016**, *313*, 1-8.

39. Mijung, N.; Lee, Y.; Cho, J., Water adsorption and storage characteristics of optimized LiCoO₂ and LiNi_{1/3}Co_{1/3}Mn_{1/3}O₂ composite cathode material for Li-ion cells. *Journal of the Electrochemical Society* **2006**, *153* (5), A935-A940.
40. Park, H.-K.; Shin, S. S.; Park, S. Y.; Shin, H. S.; Paulsen, J. M. Material for lithium secondary battery of high performance. US2011/0117662. 2010.
41. Park, K.; Park, J. H.; Hong, S. G.; Choi, B.; Heo, S.; Seo, S. W.; Min, K., Re-construction layer effect of LiNi_{0.8}Co_{0.15}Mn_{0.05}O₂ with solvent evaporation process. *Scientific Reports* **2017**, *7*.
42. Shim, J. H.; Kim, C. Y.; Cho, S. W.; Missiul, A.; Kim, J. K.; Ahn, Y. J.; Lee, S., Effects of heat-treatment atmosphere on electrochemical performances of Ni-rich mixed-metal oxide (LiNi_{0.80}Co_{0.15}Mn_{0.05}O₂) as a cathode material for lithium ion battery. *Electrochimica Acta* **2014**, *138*, 15-21.
43. Shao-Horn, Y.; Hackney, S. A.; Kahaian, A. J.; Thackeray, M. M., Structural stability of LiCoO₂ at 400 degrees C. *Journal of Solid State Chemistry* **2002**, *168* (1), 60-68.
44. Paulsen, J.; Kim, J. High nickel cathode material having low soluble base content. WO2012/107313. 2012.
45. Kim, D.; Cha, J.; Kim, H. Positive electrode slurry composition for lithium secondary battery, lithium secondary battery comprising the same and method of making the lithium secondary battery. 2012.
46. Xiong, X. H.; Wang, Z. X.; Yue, P.; Guo, H. J.; Wu, F. X.; Wang, J. X.; Li, X. H., Washing effects on electrochemical performance and storage characteristics of LiNi_{0.8}Co_{0.1}Mn_{0.1}O₂ as cathode material for lithium-ion batteries. *Journal of Power Sources* **2013**, *222*, 318-325.
47. Hall, D. S.; Gauthier, R.; Eldesoky, A.; Murray, V. S.; Dahn, J. R., New Chemical Insights into the Beneficial Role of Al₂O₃ Cathode Coatings in Lithium-ion Cells. *Acs Applied Materials & Interfaces* **2019**, *11* (15), 14095-14100.
48. Aad, J. A.; Casale, S.; Michau, M.; Courty, P.; Diehl, F.; Marceau, E.; Carrier, X., Chemical Weathering of Alumina in Aqueous Suspension at Ambient Pressure: A Mechanistic Study. *Chemcatchem* **2017**, *9* (12), 2186-2194.
49. Oh, P.; Song, B. H.; Li, W. D.; Manthiram, A., Overcoming the chemical instability on exposure to air of Ni-rich layered oxide cathodes by coating with spinel LiMn_{1.9}Al_{0.1}O₄. *Journal of Materials Chemistry A* **2016**, *4* (16), 5839-5841.

Chapter IV

Gas evolution upon storage of batteries containing Ni-rich NMC materials

1. Introduction.....	145
1.1. Gas production mechanisms	145
1.1.1. Gas associated with the positive electrode	145
1.1.2. Gas associated with the negative electrode	148
1.2. Gas characterization techniques.....	149
1.3. Conclusion	150
2. Optimization of the instrumentation for gas quantification.....	151
2.1. Comparison of the available gas chromatography instruments.....	151
2.2. Choice of the column.....	152
2.2.1. Use of a capillary column with the GC/MS-IR equipment	153
2.2.2. Use of a capillary column in the GC/BID equipment	154
2.2.3. Use of a micropacked column with the GC/BID equipment	156
2.3. Conclusion	158
3. Gas evolution associated with the storage of Ni-rich NMC materials.....	159
3.1. Gas production from the storage of NMC with electrolyte.....	159
3.1.1. Powder storage.....	159
3.1.2. Film storage.....	163
3.2. Gas production from the storage of NMC/Graphite pouch cells.....	165
3.2.1. Optimization of the pouch cell format	166
3.2.2. Complete storage protocol of pouch cells	168
3.2.3. Gas production of the formation step.....	169
3.2.4. Gas production of NMC 811 with modified surface composition.....	171
3.2.5. Gas production of different NMC compositions.....	174
3.2.5.1. Discussion about gas of the formation step.....	176
3.2.5.2. Discussion about gas of the complete storage protocol	177
3.2.6. Impedance evolution after the complete storage protocol.....	181
3.2.6.1. Adaptation of the complete storage protocol.....	181
3.2.6.2. Impedance from pouch cells NMC 622C/Gr and 811/Gr	184
4. Conclusion of the chapter.....	188
5. References.....	189

1. Introduction

Implementing specific experiments to study the gas production in cells is a of particular interest for the battery community due to the associated safety risks and cycle life deterioration^{1, 2}. This was proved to be especially problematic when Ni-rich NMC materials are used as positive electrode. Indeed, in addition to the gas produced from reduction of carbonate solvents at the surface of the negative electrode to create the solid electrolyte interphase (SEI), gaseous species^{3, 4} may originate from chemical and electrochemical reactions involving NMC surface species and from materials processes that bring about electrolyte degradation.

This section recapitulates and briefly discusses known mechanisms of gas production from each electrode and the main techniques to characterize them.

1.1. Gas production mechanisms

1.1.1. Gas associated with the positive electrode

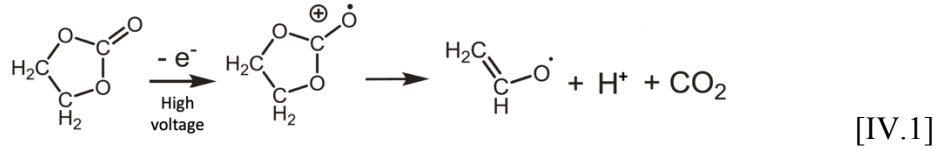
The mechanisms of gas production associated with the positive electrode can be classified into:

- i.** Electrochemical oxidation of alkyl carbonate solvents
- ii.** Chemical oxidation of alkyl carbonate solvents by active oxygen (¹O₂)
- iii.** Chemical and electrochemical reactions with surface species

i. Electrochemical oxidation of alkyl carbonate solvents

In commercial batteries containing Ni-rich NMC materials, no more than 0.6 of lithium is extracted at 4.2 V (referenced vs. Li/Li⁺ throughout this work). To extract the totality of lithium, higher cut-off voltage is needed, which unfortunately provokes the electrochemical oxidation of alkyl carbonate solvents. The alkyl carbonate solvent that is more prone to oxidize electrochemically is EC, due to its tendency to solvate PF₆⁻ most strongly and thus to reach the positive electrode more easily than linear solvents during charge⁵. Based on density functional theory calculations, it is plausible that there is electron withdrawing from EC by PF₅, which weakens the C–O ether bonds of EC and consequently lowers the ring-opening activation energy (Eq. I.10) ⁶. Then, a proton is extracted from EC^{•+} to produce vinyl

alcoholate radical, H^+ and CO_2 (Eq. IV.1). Experimentally, through online electrochemical mass spectrometry (OEMS) analyses, Solchenbach et al.⁷ proposed that the EC oxidation starts at 4.2 V vs. Li/Li^+ on a carbon black electrode. This onset oxidation potential varies as a function of electrolyte concentration.

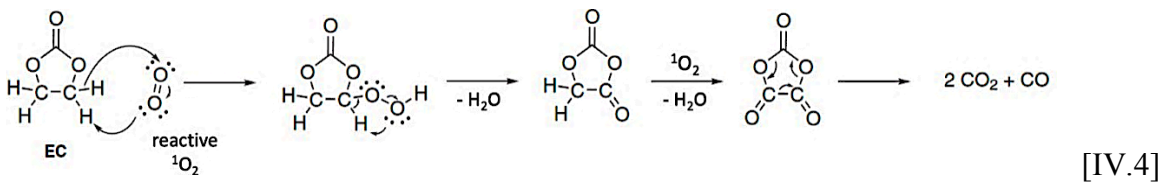


ii. Chemical oxidation of alkyl carbonate solvents by active oxygen

The chemical oxidation of solvents arises from the reaction of EC with active oxygen (1O_2). As explained in [Chapter I](#), at high state of charge (SOC) a large part of the nickel is in Ni^{4+} state, so electron transfer occurs from the $2p$ band of O^{2-} to the Fermi level of Ni^{4+} , reducing it to Ni^{3+} (Eq. IV.2). Meanwhile, due to the lithium deficiency and the presence of Ni^{3+} , the M-O bond covalency increases, decreasing O^{2-} charge density and favoring oxygen release (Eq. IV.3)⁸.

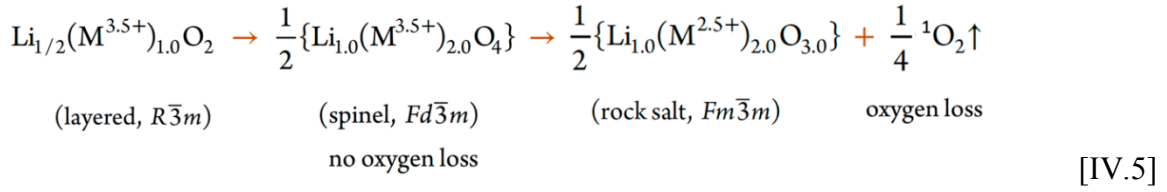


The 1O_2 is considered to be “active” as EC oxidation with ground state O_2 is highly unlikely at ambient temperature⁹. Jung et al.⁹ proposed an 1O_2 nucleophile attack on EC to produce CO_2 , CO and H_2O (Eq. IV.4). Furthermore, they found a relationship between nickel content and the onset potential of gas production. In cells containing NMC 622, it starts at ~ 4.7 V and at ~ 4.3 V for NMC 811. For the authors, the explanation is that at equal cut-off voltage, NMC 811 reaches higher SOC, producing more Ni^{4+} whose reduction releases more 1O_2 .



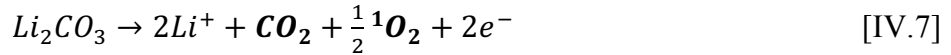
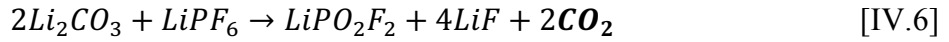
Besides gas production, another consequence of 1O_2 production is the depletion of oxygen, that causes surface phase transformations from layered to spinel and rock salt¹⁰ (Eq. IV.5

exemplary shown for $\text{Li}_{0.5}\text{MO}_2$ ($M = \text{Ni}, \text{Mn}, \text{Co}$). As a result, the cell impedance increases due to the reduction of ionic transport and the loss of active material¹¹.



iii. Chemical and electrochemical reactions with surface species

The storage of Ni-rich NMC with electrolyte, especially at high temperature, chemically produces CO_2 from Li_2CO_3 (Eq. IV.6 also seen as Eq. III.1) and CO_2 and ${}^1\text{O}_2$ from the electrochemical oxidation of Li_2CO_3 (Eq. IV.7 also seen as Eq. III.11).



The latter reaction was demonstrated very recently, through isotope labelling of oxygen¹² or of carbon¹³ in Li_2CO_3 , to be the responsible for most of the CO_2 production in the first charge. Additionally, evidence of the production of ${}^1\text{O}_2$ was given by Mahne et al.¹⁴, through the use of the chemical probe 9,10-dimethylanthracene (DMA) that promptly forms DMA- O_2 in the presence of ${}^1\text{O}_2$, which would not be possible with O_2 .

Note that CO_2 is produced from each of these reactions. Therefore, Fig. IV.1 summarizes the zones in which these reactions are expected to produce CO_2 along the first cycles.

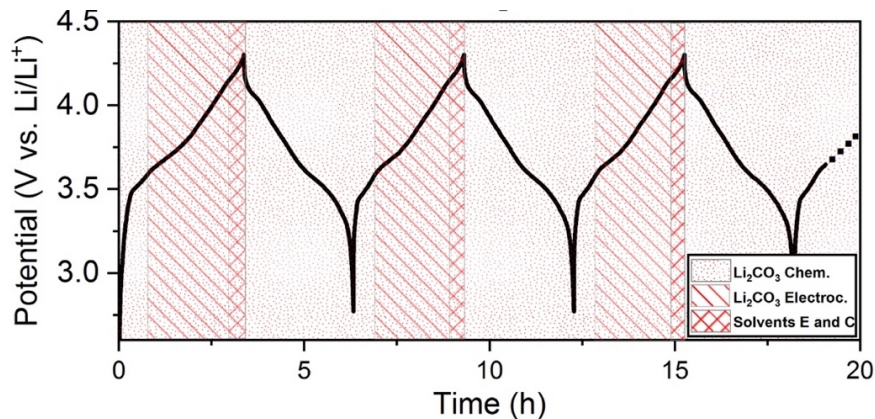
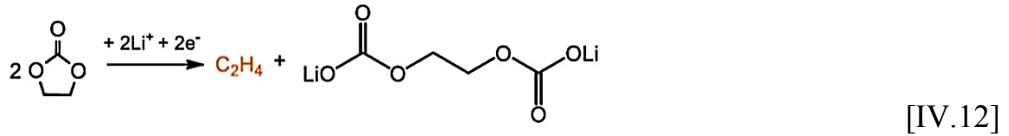
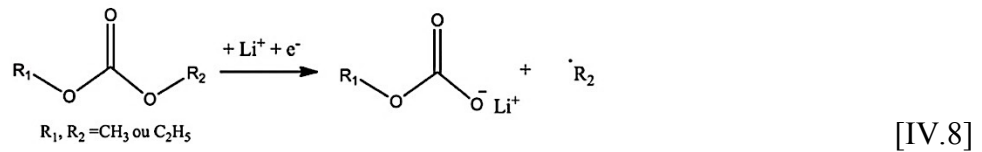


Figure IV.1. Scheme of the stages of CO_2 production associated with NMC materials.

“Chem.” or “C” stands for chemical reaction and “Electroch.” or “E” for electrochemical reaction.

1.1.2. Gas associated with the negative electrode

During the formation procedure, carbon monoxide (CO), methane (CH₄), ethylene (C₂H₄) and ethane (C₂H₆) are produced from one- or two-electron reduction reactions of linear (Eqs. IV.8 – 11) and cyclic carbonates (Eqs. IV.12 – 14)^{1, 3, 15, 16}. These gases are called formation gases and their concentration depends mainly on electrolyte composition and cycling conditions^{16, 17}. In commercial LIBs, the gaseous products are degassed after the formation cycles. Nonetheless, parasitic reactions along the cycle life of the battery are susceptible to continue the production of these gases, especially at temperatures above 40 °C when Lewis acid PF₅ is easily produced.



Another known parasitic reaction is the electrochemical reduction of H₂O, which produces OH⁻ and hydrogen (H₂) (Eq. IV.15)^{18, 19}.



Lastly, it is also possible that gases diffuse from one electrode to the other and perform “crosstalk” reactions. A particular example is the chemical reduction of CO₂ on a lithiated negative electrode that forms lithium oxalate (Eq. IV.16)^{20, 21}. This process evidences the complexity of the gassing reactions inside LIBs.



1.2. Gas characterization techniques

In-situ and ex-situ methods are used to characterize emitted gases from LIBs. In-situ examples are the measure of pressure²² and volume²³ evolution, and OEMS analysis^{15, 24}. Although the first two indicate the extent of swelling, they do not inform about composition. On the contrary, OEMS is able to characterize gas through the use of a mass spectrometer. The OEMS disadvantage is that the constant pumping of gases from the adapted cell to the spectrometer may change the electrolyte composition. Moreover, the cell configuration may be different from the commercial one and may induce different behaviors.

Concerning ex-situ techniques, gas chromatography (GC) is the main used (details about the technique can be found in Annex III). The difference with OEMS is that it offers punctual analysis, often post-mortem, and employs a chromatographic column to separate the gases. Molecular identification and quantification are possible through the use of a variety of chromatographic columns and calibration curve. Among the different options of detectors, MS is the most used, but there are also the barrier ionization discharge (BID), flame ionization (FID) and thermal conductivity (TCD) detectors.

1.3. Conclusion

Table IV.1 summarizes the reaction mechanisms from each electrode described in this section.

Table IV.1. Summary of the mechanisms producing gas in a LIB.

Gas	Source	
	Positive electrode	Negative electrode
${}^1\text{O}_2$	<ul style="list-style-type: none"> - Lattice oxygen at high SOC - Electrochemical oxidation of Li_2CO_3 	<ul style="list-style-type: none"> - ${}^1\text{O}_2$ or O_2 can be reduced at the negative electrode
CO_2	<ul style="list-style-type: none"> - Chem. oxidation of EC by ${}^1\text{O}_2$ - Chem. and electr. oxidation of Li_2CO_3 - Electrochemical oxidation of solvents 	<ul style="list-style-type: none"> - Chemical reduction of CO_2 (consumption of CO_2) from the electrode's crosstalk
CO	<ul style="list-style-type: none"> - Chem. oxidation of EC by ${}^1\text{O}_2$ 	<ul style="list-style-type: none"> - Electr. reduction of cyclic solvents
CH_4	X	<ul style="list-style-type: none"> - Electr. reduction of linear solvents
C_2H_4	X	<ul style="list-style-type: none"> - Electr. reduction of cyclic solvents
C_2H_6	X	<ul style="list-style-type: none"> - Electr. reduction of linear solvents
H_2	X	<ul style="list-style-type: none"> - Electr. reduction of water

The production of CO_2 is in common for almost all of the reactions associated with the positive electrode and most of these processes involve the reactivity of Ni-rich NMC at the delithiated state and at high temperature⁸. This is not the case of the negative electrode, in which mostly hydrocarbons, CO and H_2 are produced. Therefore, in this chapter, we considered the positive electrode to be the main source of CO_2 and intended to understand the role of Ni-rich NMC materials in the gas production upon **storage at a charged state and high temperature (55°C)**, with a preliminary work on the **optimization of the gas quantification**. Discussion and comparisons to the literature of gas production are included along the chapter.

2. Optimization of the instrumentation for gas quantification

2.1. Comparison of the available gas chromatography instruments

A coupled GC/MS-FTIR (described in Reference²⁵, Nicolet 6700) and a GC/BID (Tracera GC/BID-2010 Plus, Shimadzu) are available at the analytical platform (PFA) of Université de Picardie Jules Verne. Some of their characteristics are summarized in Table IV.2.

Table IV.2. Main characteristics of the detection modes available at the analytical platform.

Characteristic	MS	FTIR	BID
Peak area accuracy	Excellent	Good	Excellent
Validity of calibration curves in time	Calibration curves do not last long	Excellent	Excellent
Molecular characterization	With database of ionized fragments	With FTIR database	No
Flow control mode of GC	Pressure		Pressure or linear velocity

MS and FTIR are both capable to **characterize gaseous species**, either through the comparison with a database of ionized fragments or with the NIST database of IR spectra, respectively. However, the ionization source in the MS evolves with time, making the calibration curves quickly unusable, and the accuracy of the quantification by FTIR is compromised by the low peak resolution. On the other hand, the BID detector uses a plasma to ionize the gaseous species, which preserves the validity of calibration curves, but it **does not identify** the detected molecules. To overcome this problem, in our case, the same column is installed in both devices.

In a GC device, the **flow control mode** is intended to direct the flow from the injector to the column and finally to the detector. The coupled system, GC/MS-FTIR, has only the option of **constant pressure mode** (measured in Pa), which means that the pressure of the injection port is fixed and, as the sample travels away into the column, it experiences less pressure. On the other hand, the GC/BID works in **constant pressure mode** or in **constant linear velocity mode** (measured in $\text{cm}\cdot\text{s}^{-1}$). The latter corrects the pressure along the acquisition in order to maintain constant the volume that travels a certain distance down the column.

2.2. Choice of the column

The variety of chromatographic columns suitable for gas analysis are classified in capillary and micropacked types (Fig. IV.2). The capillary type contains a stationary phase coated in the interior walls, whereas in the micropacked type, it fully packs the interior. In general, micropacked columns have wider external diameter (ranging from 0.74 to 1.58 mm vs. 0.25 to 0.53 mm) are shorter in length (ranging from 1 to 2 m vs. 15 to 30 m) and require higher pressure to flow the carrier gas. Consequently, they are more retentive than the capillary type.

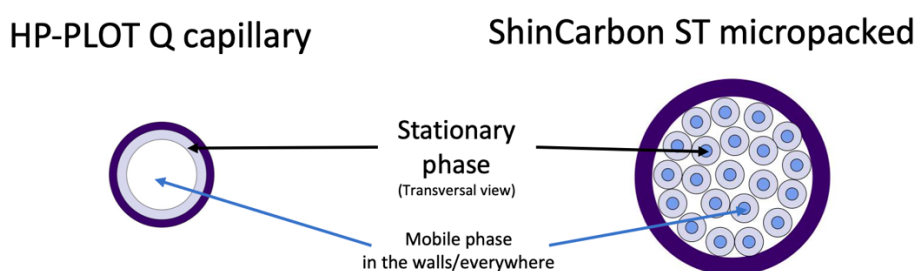


Figure IV.2. Schematic representation of the two types of chromatographic columns.

The separation depends on ²⁶:

- i. the adequate experimental conditions (flow control mode, pressure, temperature...),
- ii. the affinity between the analyte and the stationary phase,
- iii. the boiling points and polarities of the analytes and
- iv. the diameter and length of the column.

The most frequently used are the capillary columns because they are capable to separate most of the permanent gases (gases at room temperature)^{26, 27}. Nonetheless, the classic **HP-PLOT Q capillary column** (used in our study) presents the disadvantage that the gases from air (N₂, O₂, CO), H₂ and CH₄ reach the detector at very similar retention times and thus appear as a single merged peak²⁵. On the other hand, micropacked columns are rarely used, but some of them seem to separate hydrocarbons and inorganic gases including hydrogen²⁸.

Considering this information, a **HP-PLOT Q capillary column** connected to a postcapillary column Rtx-1, and a **ShinCarbon ST micropacked column** were tested in this work with the main objective to improve the separation and quantification of gases within a single acquisition. This was done through the improvement of the GC experimental settings.

2.2.1. Use of a capillary column with the GC/MS-IR equipment

A mixture of 200 μl of gas from a cycled battery (whose cycling conditions are not relevant at this stage) were injected, plus 500 μl of argon were injected with a gas-tight syringe (Hamilton with PTFE plunger tip and 1 ml of volume), into the GC/MS-IR equipped with the capillary column HP-PLOT Q. The injector temperature was set at 100 $^{\circ}\text{C}$, helium was used as carrier gas at a flow rate of 1.3 $\text{ml}\cdot\text{min}^{-1}$ and a split value of 1/10 was used (the analyte was diluted 10 times). The oven program detailed in Annex III was set to obtain the best separation in the shortest amount of time. Fig. IV.3 shows the results.

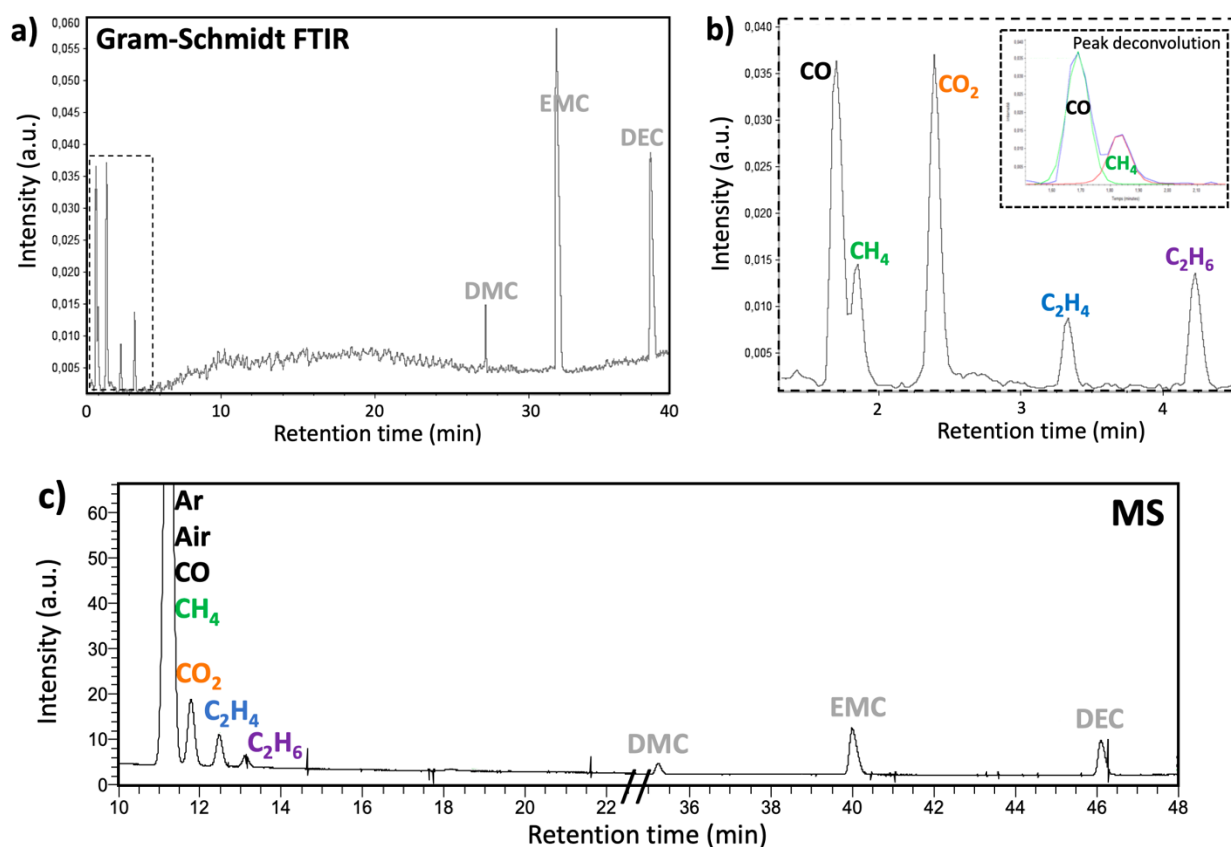


Figure IV.3. GC/MS-IR analysis of a pouch cell, using the HP-PLOT Q column. **a, b)** Gram-Schmidt chromatogram (from FTIR) and **c)** GC/MS chromatogram.

From the FTIR device, a Gram-Schmidt representation is obtained (Fig. IV.3a and b). Within the first five minutes, the Gram-Schmidt exhibits merged CO/CH₄ peaks, that can be deconvoluted with Origin[®] peak analysis, CO₂, C₂H₄ and C₂H₆. The solvents, DMC, DEC and EMC, appear at retention times higher than 30 min. Given the limitations of the number of FTIR spectra acquisitions per minute, the peaks in a Gram-Schmidt are constructed from fewer points, which gives less precision to peak area calculation.

For the same acquisition, an MS chromatogram is obtained as well (Fig. IV.3c). The first gases are detected ten minutes later than in the Gram-Schmidt, this corresponds to the time required for the gases to flow through the coupling system. The first detectable peak corresponds to the merged peak of argon, air (N_2 , O_2), CO and CH_4 ; which appears very visible due to the considerable amount of argon (500 μ l) that was added to the battery to help gas extraction. Immediately after, CO_2 , C_2H_4 and C_2H_6 appear, followed later by the alkyl carbonate solvents. As above-mentioned, main limitation of the GC/MS equipment is the gradual ageing of the ionization source that renders the calibration curves unusable after only one day. Daily construction of calibration curves is time consuming, thus this option was ruled out.

PF_5 , expected gaseous product from the decomposition of $LiPF_6$ (Eq. I.10), is not detected either because it reacts rapidly with the stationary phase of the column or it reacts with water to form gaseous POF_3 (Eq. I.11). In case of POF_3 , it is not detected because the fluorine is easily substituted and the resulting compound stay dissolved in the electrolyte

To conclude, the co-elution of H_2 , O_2 , CO and N_2 with Ar at early retention times seems to be an unavoidable characteristic of GC/MS when working with a HP-PLOT capillary column under these conditions. After deconvolution, the Gram-Schmidt is an adequate option for gases identification and quantification, although it can exist a weak error on the peak area. Alternatively, to improve separation, a more retentive column could be used or the experimental conditions could be modified.

2.2.2. Use of a capillary column in the GC/BID equipment

GC/BID is a valuable alternative to GC/MS-IR, to overcome the problem of the short validity of calibration curves, since the plasma ionization is constant in time²⁹.

First, the same HP-PLOT Q capillary column and experimental conditions were used. A mixture of 200 μ l of the gas sample and 500 μ l of helium were injected. Fig. IV.4 shows the resulting chromatogram. Not surprisingly, the chromatogram is equivalent to what has been previously observed in Fig. IV.3c. Note that even if argon has been changed to helium to avoid argon detection, the co-elution of gases issue has not been eliminated.

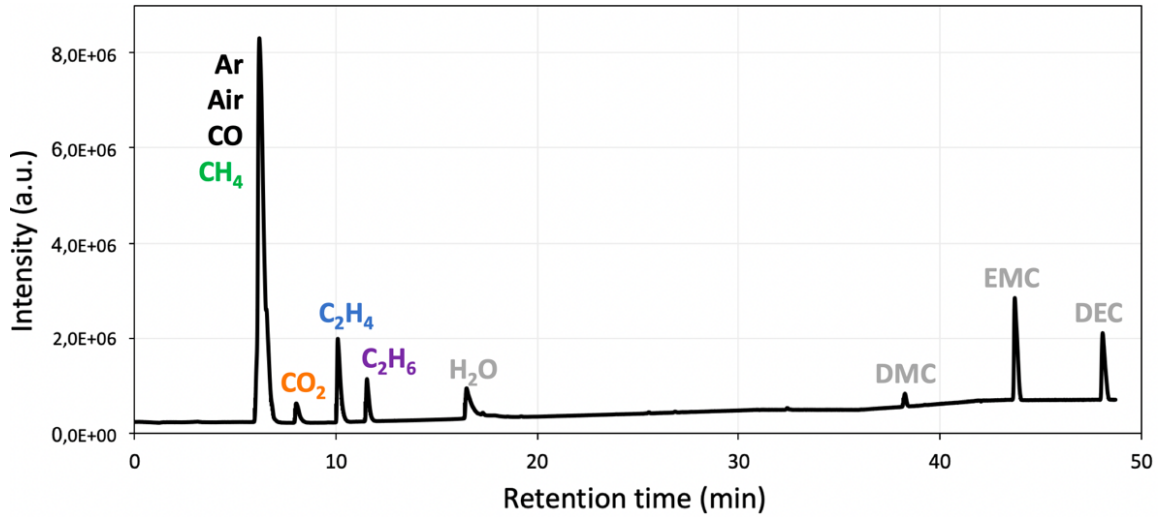


Figure IV.4. GC/BID analysis of a pouch cell, using a HP-PLOT Q column with the constant pressure mode.

In a second instance, the **flow control mode** was changed to **constant linear velocity**, and again gases from an arbitrary battery have been injected. The result is shown in Fig. IV.5.

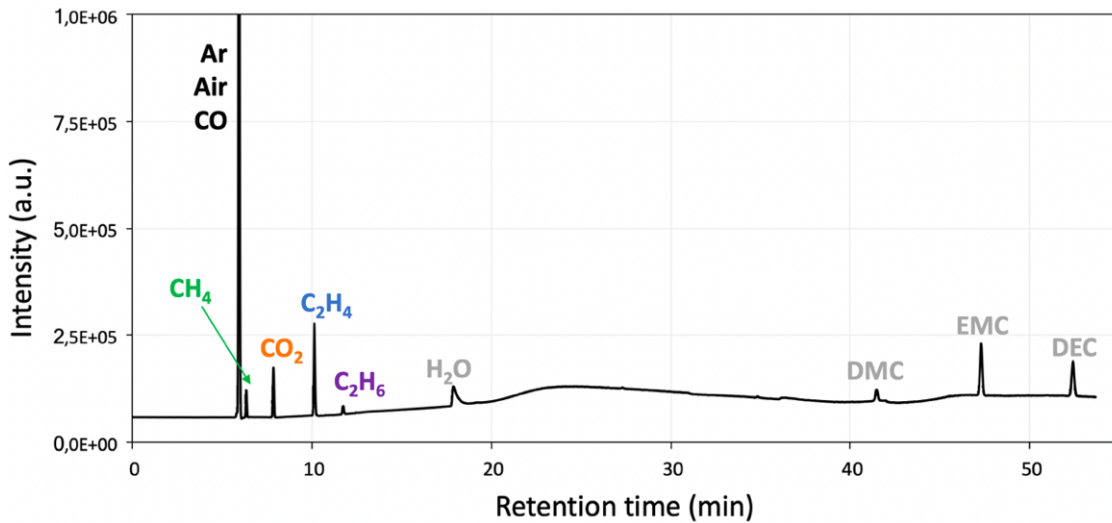


Figure IV.5. GC/BID analysis of a pouch cell, using a HP-PLOT Q column with the constant linear velocity mode.

Favorably, this flow mode decreased the broadening of the peaks and thus separated the CH₄ peak. This is because the constant linear velocity mode compensates for the flow changes that can broaden a peak, caused by the differences in temperature between the injector and the column.

In the course of the thesis, this method improvement was achieved after that several meaningful results were obtained with the previous method. Therefore, in the remainder of this chapter, it is indicated if the “regular” (constant pressure) or the “improved” (constant linear velocity) method is used. For the quantification results, all of the calibration curves from both methods used in the GC/BID equipment are shown in [Annex III](#).

2.2.3. Use of a micropacked column with the GC/BID equipment

The micropacked column was used with the aim of improving gas separation. According to the application note of the manufacturer²⁸, the ShinCarbon ST micropacked column is capable to separate the totality of permanent gases by using a specific oven temperature program (Annex III) and the pressure program starting at 250 kPa and increasing at 15 kPa.min⁻¹ until 400 kPa.

From the injection of gases from a pouch cell under these conditions to the GC/BID, no peaks were detected. We suspected that the initial pressure of 250 kPa was not high enough to push the gases through the dense stationary phase. Therefore, the pressure was set at 400 kPa throughout the acquisition. This pressure increase made the gases detectable (Fig. IV.6).

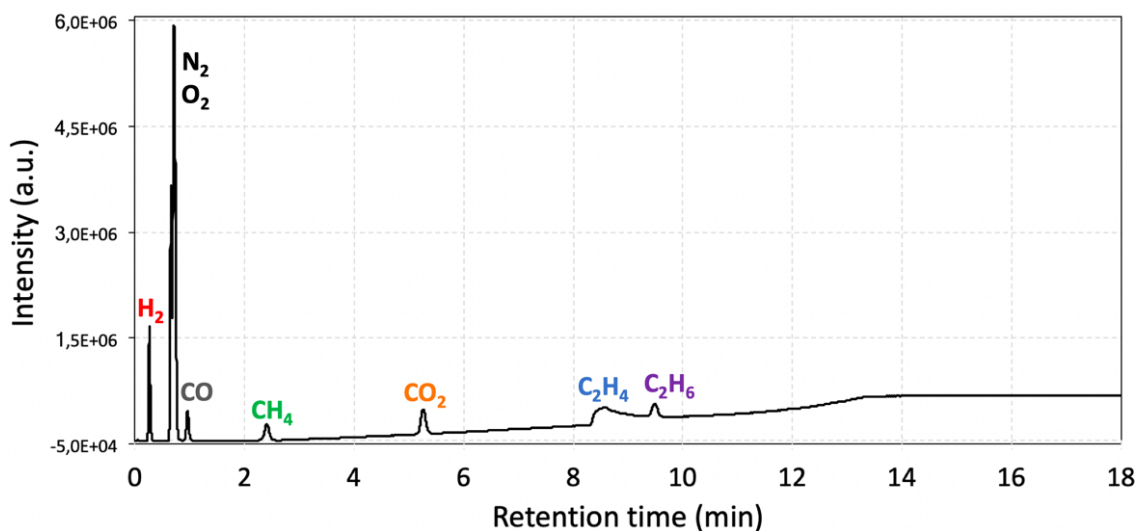


Figure IV.6. GC/BID analysis of a pouch cell, using the ShinCarbon ST micropacked column.

Only within three minutes, the peaks of H₂, the air peak (O₂, N₂), CO and CH₄ appear perfectly separated from each other. Each peak was ascribed thanks to the injection of gaseous

standards. As it can be seen on Fig. IV.6, a gaseous compound was eluted at the same time than C_2H_4 , so its corresponding peak is less well defined than with the previous mode.

Although the GC equipment can reach the pressure of 400 kPa, we observed that the flow of carrier gas to maintain it through this column of ca. $1000 \text{ ml}\cdot\text{min}^{-1}$ is unexpectedly high, as compared to the $70 \text{ ml}\cdot\text{min}^{-1}$ value announced by the manufacturer and to the $1.3 \text{ ml}\cdot\text{min}^{-1}$ value in case of the GC/MS-IR device. Owing to unusual pressure variations, a good reproducibility cannot be obtained (an example is shown in Annex III).

In an attempt to decrease helium consumption and improve reproducibility, the split ratio was changed from 1/10, to splitless. The helium consumption was indeed reduced; however, a massive peak that impacts the detection of CO and CH_4 appears at very early retention time (Fig. IV.7). This is an overloading peak characteristic of unadapted analyte concentration²⁹. The conclusion was drawn from this result that helium saving in splitless mode is not an adequate solution.

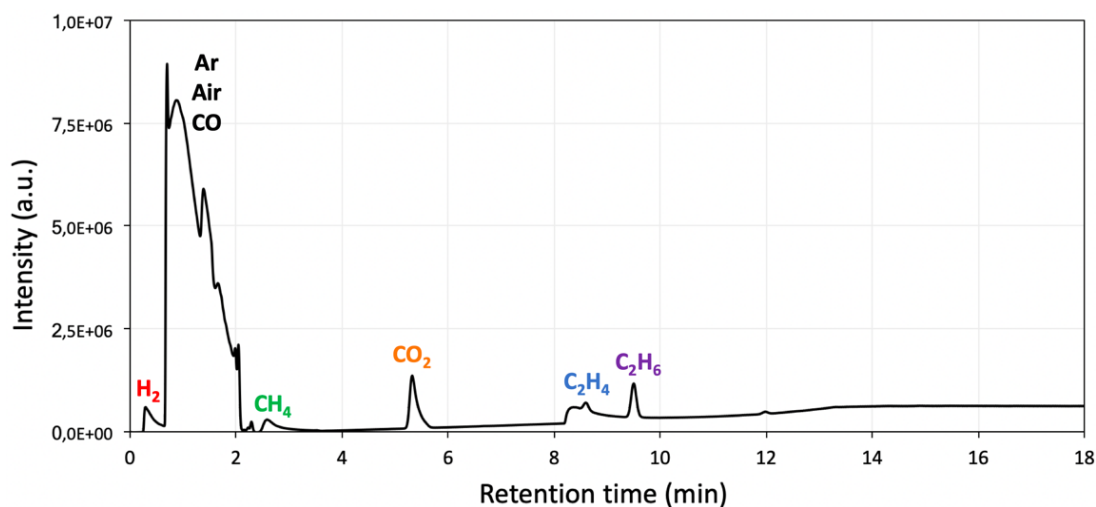


Figure IV.7. GC/BID analysis from a pouch cell, using the ShinCarbon ST micropacked column.

Despite the fact that the separation of permanent gases was successful, unfortunately, the pressure of 400 kPa was too high for sustainable and reproducible measurements. Therefore, we conclude that the implementation of the micropacked column was not achievable at this point.

2.3. Conclusion

Following a brief comparison of the characteristics of both GC techniques available at the PFA, it was decided to use the GC/MS to identify the gaseous compounds and then the GC/BID to quantify them, both using the same capillary column. It was found that some of the permanent gases co-elute at early retention times when using the constant pressure flow mode in both GC/MS-IR and GC/BID. To solve this, first, argon was replaced by helium when extracting the gas from the pouch cell, but unfortunately this did not eliminate the co-elution problem. Then, it was discovered that by changing the flow mode to constant linear velocity in the GC/BID device, it was possible to successfully separate the CH₄ gas from the co-eluted peak.

With a view to detect all the permanent gases with a single equipment and a single acquisition, a micropacked column was installed in the GC/BID equipment. This column presented the main advantage of H₂, CH₄ and CO separation, but the high helium flow needed to maintain the pressure at 400 kPa did not allow the acquisition of reproducible measurements. Profound optimization was left out of the scope of this thesis, although these experiments proved the big potential of this column to be used in future tests.

In the rest of the chapter, only results obtained from the capillary column with “regular” or “improved” method will be presented.

3. Gas evolution associated with the storage of Ni-rich NMC materials

This section focuses on studying the gases produced from the storage i) of the electrolyte in contact with NMC powder or film, with the objective of identifying the thermal degradation that the electrolyte endures in the presence of this material, then, ii) of NMC/Graphite(Gr) cells, by comparing two NMC compositions and modifying the concentration of surface species on NMC 811.

3.1. Gas production from the storage of NMC with electrolyte

This section investigates the thermal electrolyte degradation in the presence of the five Ni-rich NMC powders and of NMC 622C films at different states of charge (SOC).

3.1.1. Powder storage

The storage experiments of **NMC powder + electrolyte** were performed in 18650 stainless steel cans. Inside the argon-filled glovebox, 200 mg of NMC 622C and 0.2 ml of electrolyte were put inside the 18650 can and closed with a septum. The can was placed in an oven at 55°C for four days, and then, cooled to 20°C to extract 1 ml of gas for GC/MS analysis (Fig. IV.8).

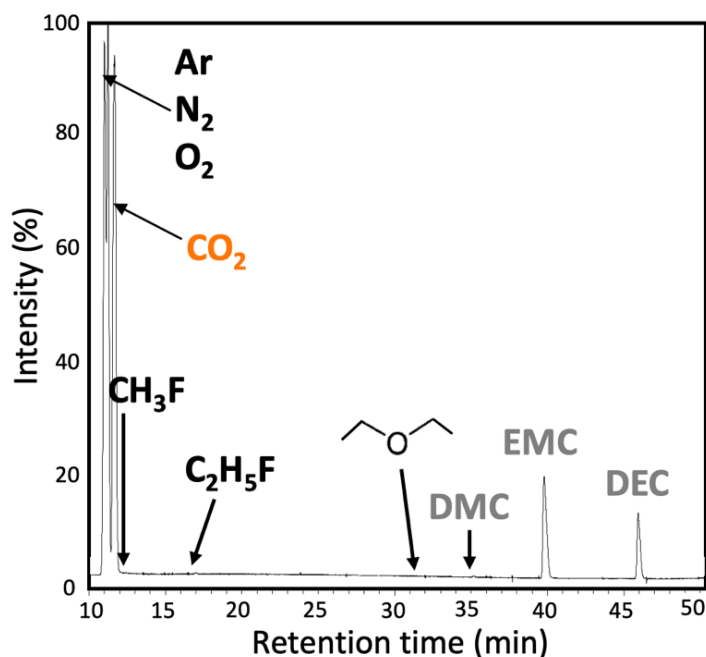
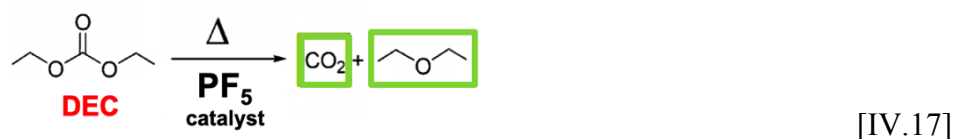


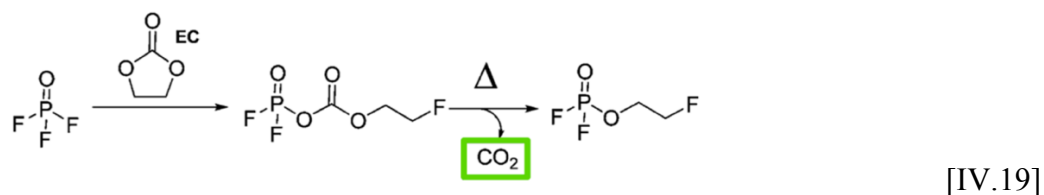
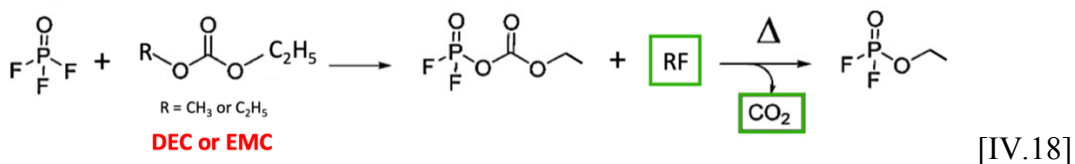
Figure IV.8. GC/MS chromatogram of gases from the storage of 200mg of NMC 622C and 0.2 ml of LiPF₆-based electrolyte in an 18650 can for 4 days at 55°C.

The MS chromatogram (Fig. IV.8) exhibits visible peaks corresponding to Ar-N₂-O₂ and CO₂ between 10 – 12 min of retention time, followed by the solvents DMC, EMC and DEC peaks from 35 min of retention time. Less visible peaks that were detected through background search are fluoromethane (CH₃F), fluoroethane (C₂H₅F) and diethyl ether ((C₂H₅)₂O).

The source of (C₂H₅)₂O is the thermal decomposition of DEC through decarboxylation³⁰ (Eq. IV.17), assisted by PF₅ from the decomposition of LiPF₆ (Eq. I.10). Methyl-ethyl ether and dimethyl ether could be expected from the decomposition of EMC, but they were not detected.



The fluorinated alkanes, CH₃F and C₂H₅F, come from the reaction of alkyl carbonate solvents with POF₃. First, PF₅ reacts with H₂O traces (this electrolyte contains ~18 ppm) to produce POF₃ and HF (Eq. I.11). Then, POF₃ reacts with linear solvents (Eq. IV.18, exemplary shown for DEC) to produce CO₂ and an alkyl fluorophosphate^{30, 31}. In the same way, POF₃ may also react with cyclic solvents to form phosphoro-fluorinated species and CO₂ (Eq. IV.19).



Note that there are two common features in reactions IV.17 – 19:

- CO₂ is always a product. The fact that multiple sources exist confirm why CO₂ appears as an intense peak in the chromatogram.
- PF₅ intervenes directly or indirectly (as POF₃). In fact, the production of PF₅ is facilitated by the available dead volume inside the 18650 can (total volume = 13.64 cm³), as will be evidenced later.

To evaluate the impact of PF_5 in CO_2 production, the quantity of CO_2 coming from a batch of three normal-size 18650 cans stored at 55°C with LiPF_6 -based electrolyte was compared to other three batches: **(i)** normal-size cans with 1M lithium bis(trifluoromethanesulfonyl)imide (LiTFSI)-based electrolyte (to avoid PF_5 presence), **(ii)** normal-size cans with only the solvents mixture and **(iii)** reduced-size 18650 cans (total volume = 6.5 cm^3) with LiPF_6 -based electrolyte.

Since CO_2 is the only gas that exhibits a defined peak, it is the only one that was quantified. The quantification on Fig. IV.9 is represented with respect to the total dead volume (dead volume = total volume of the can – volume occupied by the liquid). The error bars correspond to the standard deviation calculated from three samples.

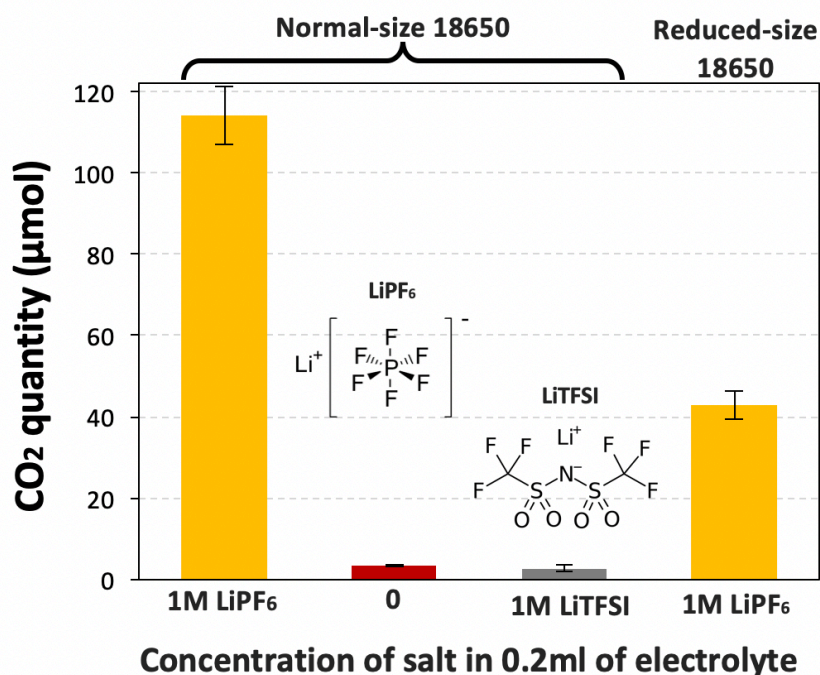


Figure IV.9. CO_2 quantification in GC/BID (regular method and capillary column), from stored 18650 cans containing different electrolytes. **Inset:** molecular structure of salts.

In the presence of 1M LiPF_6 , CO_2 is heavily produced whereas only ca. 5% of this CO_2 quantity is obtained in its absence. Similarly, replacing LiPF_6 by LiTFSI produced around 4% of CO_2 . On the other hand, when the dead volume is decreased almost by half, but with the LiPF_6 -based electrolyte volume kept at 0.2 ml, the CO_2 amount decreases by more than half. In conclusion, CO_2 production is linked to the dead volume and the presence of PF_5 (and POF_3) and it is the main initiator of gassing from the storage of powder NMC.

Afterwards, the five Ni-rich NMC powders were evaluated with the same protocol (Fig. IV.10). Curiously, the CO₂ quantity decreases with the increase of nickel content. This seems contradictory to the general knowledge that higher nickel content equals higher reactivity³². However, in the literature the reactivity has been mostly observed in delithiated states where Ni⁴⁺ can reduce to Ni³⁺. In this case, the materials are fully lithiated and have not experienced electrochemical processes, indicating that the differences come from a physicochemical origin.

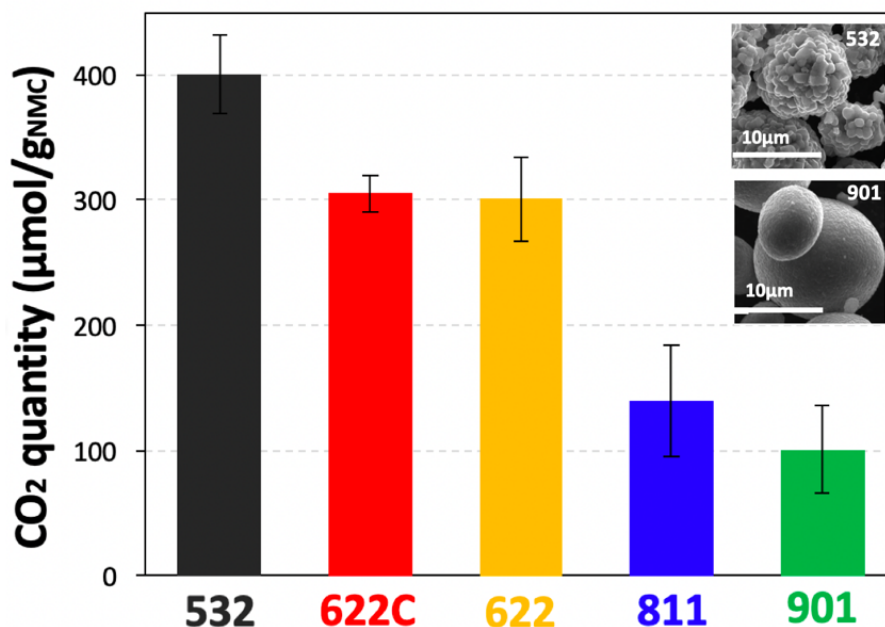


Figure IV.10. CO₂ quantification in GC/BID (regular method and capillary column) from 18650 cans stored 4 days at 55°C. **Insets:** surface morphologies of NMC 532 and 901.

Table IV.3 enlists the transition metals content, BET surface area, water content and expected amount of CO₂ from Li₂CO₃ decomposition; with the aim of finding the origin of the difference in CO₂ experimental quantity (last column).

Table IV.3. Relevant characteristics of Ni-rich NMCs and experimental results (last column).

NMC	Fractional composition				BET (m ² .g ⁻¹)	Water content (ppm)	Expected quantity of CO ₂ from Li ₂ CO ₃ (μmol.g _{NMC} ⁻¹)	Experimental quantity of CO ₂ (μmol.g _{NMC} ⁻¹)
	Ni ³⁺	Ni ²⁺	Mn ⁴⁺	Co ³⁺				
532	0.2	0.3	0.3	0.2	0.27	14	18 ± 0.5	400 ± 30
622C	0.4	0.2	0.2	0.2	0.27	0	37 ± 1	305 ± 15
622	0.4	0.2	0.2	0.2	0.27	114	40 ± 1	300 ± 35
811	0.7	0.1	0.1	0.1	0.24	10	19 ± 0.5	140 ± 45
901	0.9	0	0	0.1	0.20	18	39 ± 1	100 ± 35

The BET surface areas ranging from 0.20 to 0.27 m².g⁻¹ are practically identical, so the CO₂ difference is not related to them. In contrast, the water content varies between 0–114 ppm (measured with a Metrohm Karl-Fisher titrimeter), but this did not show any relationship to CO₂ produced. Again, there is no relation between the expected quantity of CO₂ that would result from the chemical reaction of the total amount of Li₂CO₃ (Eq. IV.6) and experimental CO₂. Note that these experimental amounts are much bigger than the expected.

Moreover, it is worth to look at the fractional composition of transition metals. Indeed, there is a direct relation between the decrease of Ni²⁺, Mn⁴⁺ and Co³⁺, (more evident for Ni²⁺ and Mn⁴⁺) and the decrease of CO₂. The exact reason is unclear, but we hypothesize that the production of PF₅ is linked to the surface energy of each material that varies depending on the transition metals composition and surface species content. Lastly, other characteristic that changes between NMC compositions is the surface texture, the materials become smoother upon nickel content increase (see insets in Fig. IV.10). This observation makes us think that it might exist privileged planes on the multifacet surfaces that have a catalytic effect on the degassing of PF₅. However, this has not been confirmed yet.

To conclude, the storage tests at 55°C of electrolyte allowed us to identify PF₅ as the main cause for gas production, mostly whenever dead volume is available, as a consequence of the thermal decomposition of the electrolyte, producing CO₂. Upon the addition of NMC, surprisingly, the quantity of CO₂ varies depending on the composition of NMC: the more nickel there is, the lower CO₂ is produced. The reason for this behavior remains unexplained.

3.1.2. Film storage

The thermal electrolyte degradation at two different state of charge (SOC) was evaluated through the storage of NMC 622C films and electrolyte in Swagelok-type cells (loading = 11.4 ± 0.5 mg.cm⁻²). **Films** were used as the electrochemical delithiation is more practical. The entire protocol is illustrated in Fig. IV.11 and consists in:

- i. preparation of the Swagelok-type half-cell in the glovebox, as described in Annex II;
- ii. cycling at 30 °C and a rate of C/10 up to a delithiated (4.3V) or lithiated state (2.8 V) (the highest delithiated state is Li_{0.4}Ni_{0.6}Mn_{0.2}Co_{0.2}O₂, which by definition here corresponds to 100% of (achievable) SOC;

- iii. transfer of the cell to the glovebox and relocation of the lithiated or delithiated film in a half Swagelok-type cell with a septum cap and fresh electrolyte;
- iv. storage during 4 days at 55°C, followed by cooling down to 20°C, and
- v. collection of 1 ml of gas for GC/BID analysis.

The advantage of this system is that it does not contain formation gases and reduction products to interfere with the thermal reactions of the electrolyte.

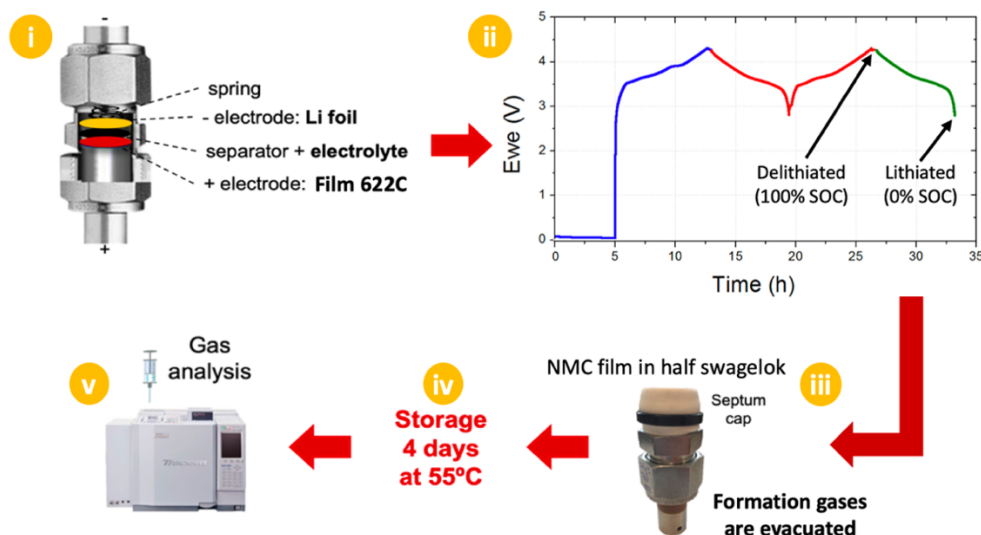


Figure IV.11. Illustration of the steps in the protocol used for the Swagelok-type storage tests at the delithiated or lithiated state (100% or 0% of achievable SOC).

Following the protocol, three batches of three Swagelok-type cells containing NMC 622C were stored in the delithiated, lithiated or pristine state (no cycling). Only CO₂ was quantified as it was the single permanent gas identified (Fig. IV.12a). Fig. IV.12b shows the quantification results.

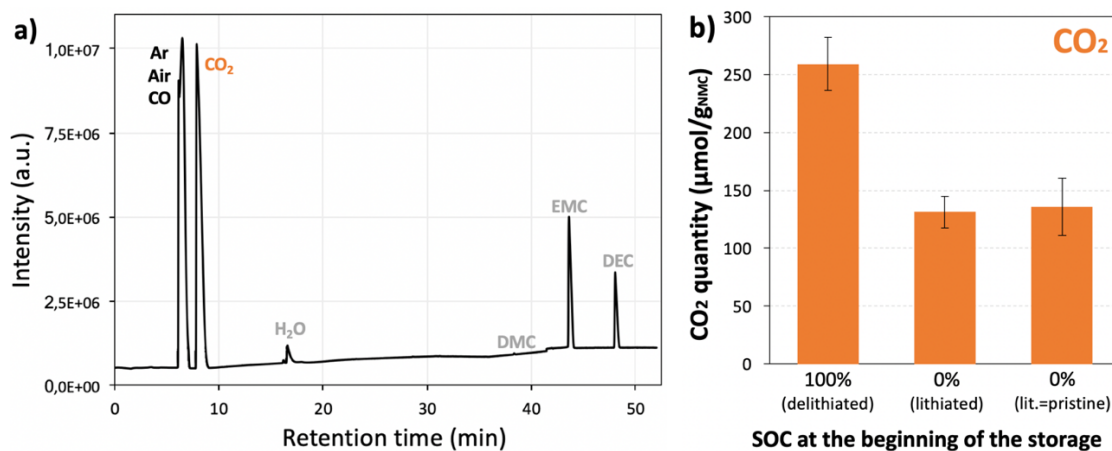


Figure IV.12. a) GC/BID chromatogram (regular method and capillary column) of the gas from the storage of a half Swagelok-type cell containing an NMC 622C film at 100% SOC. **b)** CO₂ quantification from the storage at 100 or 0% SOC.

At least $130 \mu\text{mol.g}_{\text{NMC}}^{-1}$ were produced from the three samples, which corresponds at least to the thermal decomposition of alkyl carbonate solvents. This result is unfortunately not comparable to the previously-shown powder storage due to the several variables: the different dead volume, the NMC-to-electrolyte mass ratio and the carbon and binder contained in the film. However, it is sure that in both cases PF_5 contributed to total CO_2 , due to the existence of dead volume (regardless of the SOC in this case).

Furthermore, the storage of the delithiated film produced two times more CO_2 than the lithiated films, and both lithiated films produced around the same quantity. The difference of $128 \mu\text{mol.g}_{\text{NMC}}^{-1}$ between the delithiated and lithiated film is the evidence of the influence of the SOC in CO_2 production, and also constitutes a proof that the delithiated NMC is more reactive toward the electrolyte. This is possible through the production of active oxygen ($^1\text{O}_2$), that reacts chemically with EC to produce CO and CO_2 (Eq. IV.4)^{33,34}. CO was not identified due to the separation property of the capillary column. According to Eq. IV.4 and the amount of NMC in the film, $128 \mu\text{mol.g}_{\text{NMC}}^{-1}$ of CO_2 corresponds to $1.8 \mu\text{mol}$ of consumed $^1\text{O}_2$, and to **$\sim 0.6 \text{ mol}\%$** of oxygen from NMC. This calculation gives an idea of the reactivity of delithiated NMC 622C and can eventually be compared to other NMC compositions.

The production of $^1\text{O}_2$ at this temperature is supported by the work of Xiong et al.⁸, who showed through TGA/MS that delithiated NMC 442 produces oxygen from 40°C . Kim et al.³⁵ reported that upon storage at 60°C of delithiated NMC 532 (4.45 V), approximately 75% of the gas is produced within the first 10 hours of storage. These results imply for us that the $^1\text{O}_2$ production and the following reactions occur fast at the early stage of the storage at high temperature. Our result complements these works by giving a direct comparison between the lithiated and delithiated state. In upcoming work, it would be interesting to compare the other NMC materials.

3.2. Gas production from the storage of NMC/Graphite pouch cells

The complete cell is a more complex system because, in it, co-exist gases produced from both electrodes and electrolyte. In a first instance, this section deals with the optimization of a 2- and 3-electrode pouch cell format exhibiting reproducible electrochemical performances and making it easy to sample gases. Then, will be described the **special storage protocol** that

consists of **formation cycles** followed by a **storage step at high temperature**. Lastly, the parameters that influence the production of gases from the formation cycles are studied. Gases after the cycling step and the storage step are investigated with two objectives:

- i. Differentiate the contribution of Li_2CO_3 source to total CO_2 .
- ii. Investigate the role of NMC composition.

3.2.1. Optimization of the pouch cell format

For these storage experiments, pouch cells were chosen, since there are customizable. Additionally, the dead volume can be reduced almost to zero.

Graphite was chosen as active material for the negative electrode. Since graphite does not degrade in air, this film was manufactured with an automatized coating machine that controls tightly the parameters of temperature, coating velocity and gap. The electrode composition was 92 wt.% graphite (Timcal TIMREX SLS, $\sim 1.5 \text{ m}^2 \cdot \text{g}^{-1}$), 4 wt.% CMC (ACROS Organics, $M_w = 700000$, degree of substitution = 0.9) and 4 wt.% conductive carbon black C45. The electrodes were calendered to 30% porosity and the electrochemical performance was evaluated through half-cell cycling (Fig. IV.13). At C/10 and C/4, specific capacities of $330 \text{ mAh} \cdot \text{g}^{-1}$ and $220 \text{ mAh} \cdot \text{g}^{-1}$ were obtained, respectively.

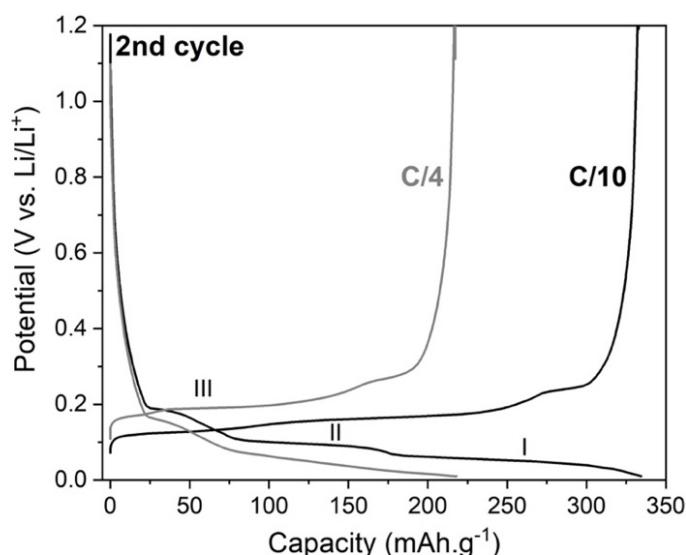


Figure IV.13. Electrochemical performance in half-cell of the graphite film at two different C-rates. The roman numbers correspond to the plateaus mentioned in [Chapter I](#).

The assembly of pouch cells is done inside a dry room (dew point $\leq -60^{\circ}\text{C} \leq 8\text{ppm}$ of H_2O) based on a pre-established pouch cell patron developed by this research group³⁶. Dimensions, sealing areas and sealing conditions were customized (Fig. IV.13), in order to meet the requirements of reproducibility, leak-proof sealing, resistance at 55°C and space to store gas. 3-electrode pouch cells contain a thin lithium foil laminated on a copper grid and placed between the electrodes. Note that the cells are laboratory-made (slurries casting, electrodes and separator cutting and assembling).

After the assembly and three-sides sealing, the pouch cells were kept in a vacuum oven for 12h at 80°C to eliminate adsorbed water. The final sealing was done after electrolyte filling (80 μl of base electrolyte: 1M LiPF_6 in EC/DEC/EMC 1:1:1 vol.), with a vacuum sealer set at 98% vacuum (percentage referred to the vacuum capacity of the oil pump, details in Annex III). The sealing method and conditions were chosen due to its reproducibility, capacity to leave the minimal amount of dry air inside the pouch cell and assurance that the minimum amount of electrolyte is lost during the vacuum procedure (only 3 – 4 wt.% was lost).

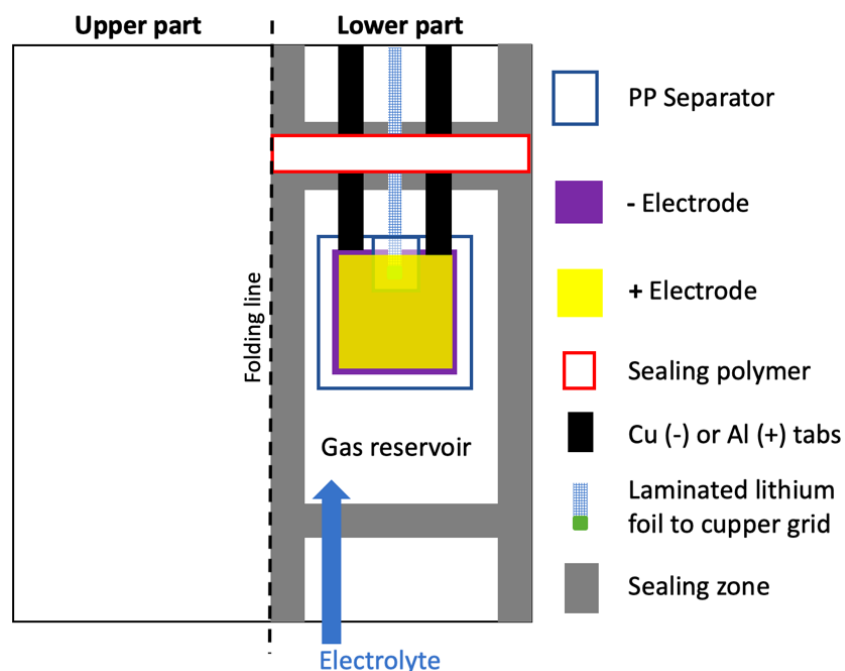


Figure IV.14. Scheme of the interior of a pouch cell after customization for gas storage. The volume of the reservoir is ~ 0.7 ml.

To extract the gas within a single pierce from the reservoir, a protocol was established. It consists in sticking a rubber septum with cyanoacrylate glue to both sides of the gas reservoir to ensure that the needle do not pierce across the pouch cell. Then, to ensure that always

enough gas volume is injected to the GC and that the majority of gas is collected, 500 μl of inert gas are first added to the reservoir, and then the totality of gas is collected. A very recent example of this type of gas recuperation can be found in the literature³⁷.

3.2.2. Complete storage protocol of pouch cells

To study specifically the gas production after the storage of NMC/Gr pouch cells when varying the NMC composition and the concentration of surface species, a complete **storage protocol** was implemented. It includes a **cycling step** followed by a **storage step** at 55°C.

For industrial production of batteries, the formation step varies depending on the materials and the application. Very often, it includes couple of cycles at low C-rate and a resting period at high temperature³⁸. Although battery manufacturers evacuate the gases after the formation step, parasitic reduction reactions as cycling proceeds is likely to occur. In this study, a simpler formation step was used, similar to the one used with Swagelok-type cells in [Section 3.1.2](#). It consists of a five-hour rest (electrolyte impregnation) and one cycle and a half, at 30°C, between 2.8–4.3 V, to reach a delithiated state (Fig. IV.15), which corresponds to $\text{Li}_{0.4}\text{Ni}_{0.6}\text{Mn}_{0.2}\text{Co}_{0.2}\text{O}_2$ in NMC 622C and $\text{Li}_{0.3}\text{Ni}_{0.8}\text{Mn}_{0.1}\text{Co}_{0.1}\text{O}_2$ in NMC 811.

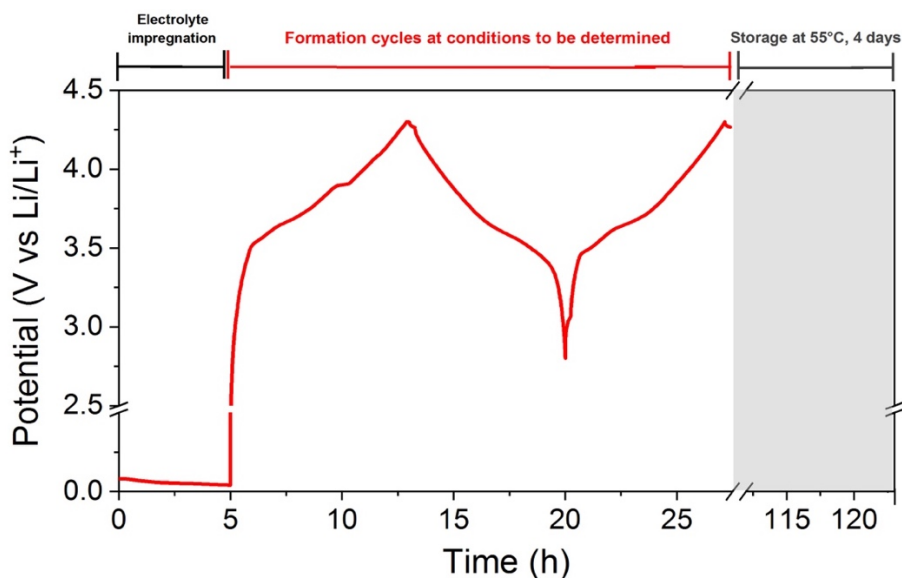


Figure IV.15. Storage protocol established for pouch cells.

3.2.3. Gas production of the formation step

With the aim of identifying which gases are produced during the formation step and the better conditions for the complete storage protocol, this section deals with temperature and the C-rate variations during the formation step.

Four batches of three pouch cells NMC 811/Gr with equivalent loadings, were cycled at 30 or 55°C and at a rate of C/5 or C/10 (Table IV.4). The applied current density was calculated in respect to the mass of NMC. Representative cycling can be found in Annex III and the values in Table IV.4. It was observed that, at equal temperature, there is negligible difference in between the 2nd cycle discharge capacity at a rate of C/5 or C/10; and that pouch cells cycling at 55°C deliver higher capacity than those at 25°C. This may be explained by the improvement of the lithium kinetics during re-lithiation process at temperature above 40°C³⁹.

Table IV.4. Summary of experimental specifications

Specification	C/5		C/10	
	30°C	55°C	30°C	55°C
Negative electrode loading (mg.cm ⁻²)	7.1 ± 0.2			
Positive electrode loading (mg.cm ⁻²)	13.7 ± 0.1			
Current density (with x=1) (mA.cm ⁻²)	0.38 at C/10 and 0.76 at C/5			
2 nd cycle discharge capacity (mAh)	10.7 ± 0.1	11.2 ± 0.1	10.8 ± 0.1	11.4 ± 0.1

The gases were extracted with the protocol previously mentioned and analyzed by GC/BID using the capillary column and the improved method (CH₄ is visible). The gases that were identified from the formation cycling, regardless of the temperature or C-rate, are CH₄, CO₂, C₂H₄, C₂H₆, H₂O, DMC, EMC and DEC. Fig. IV.16a-d reports peak areas of CH₄, CO₂, C₂H₄ and C₂H₆ as function of temperature and C-rate.

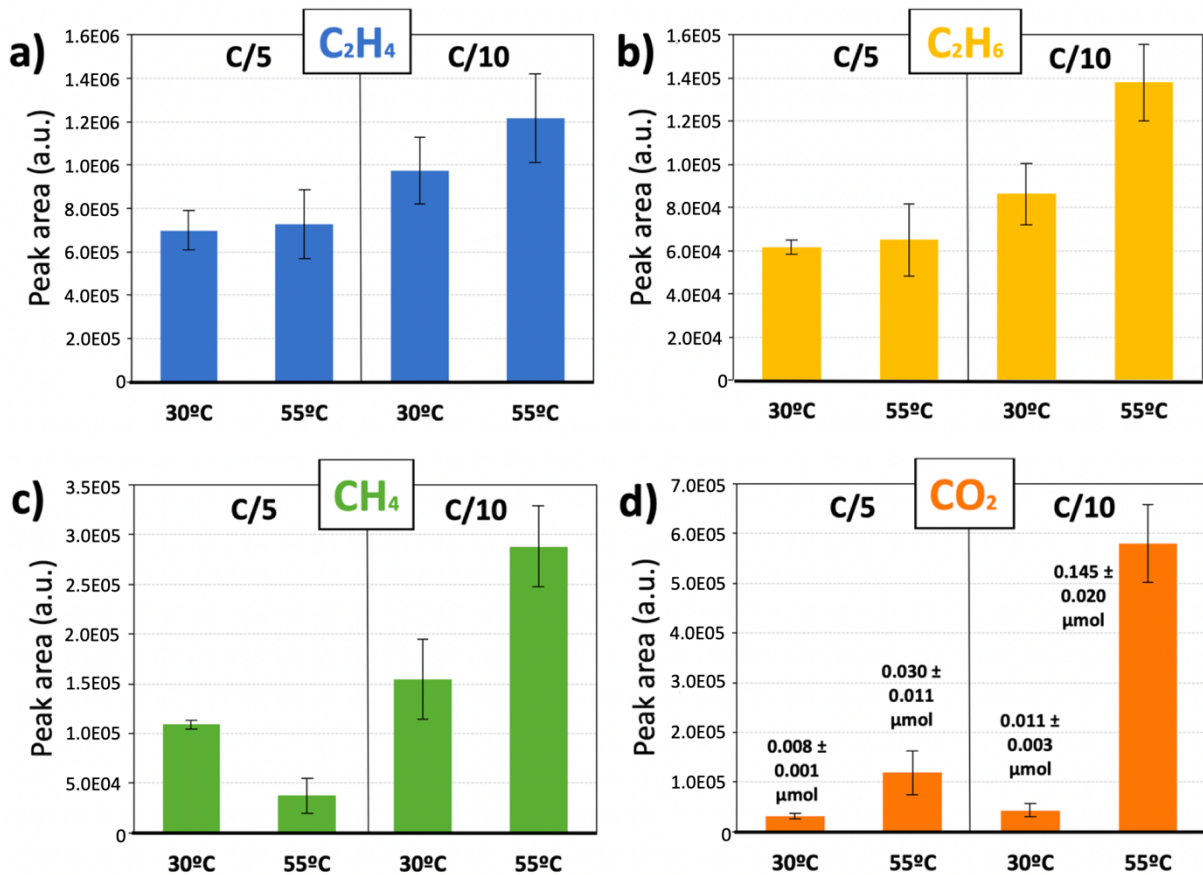


Figure IV.16. Peak areas of a) C₂H₄, b) C₂H₆, c) CH₄ and d) CO₂ detected by GC/BID (improved method and capillary column), from pouch cells NMC 811/Gr after the formation step as function of temperature and current density.

The sources of the formation gases from the reduction of alkyl carbonate solvents have been discussed in the introduction. In short, CH₄ comes from EMC, C₂H₄ from EC and C₂H₆ from EMC and DEC. Regarding their evolution as a function of the cycling conditions, the peak areas (and consequently the quantities) of C₂H₄ and C₂H₆ are not as affected by temperature as they are by C-rate (Fig. IV.16a and b). They increase importantly if the C-rate is decreased from C/5 to C/10, which is explained by a favored reduction process at low current density. In contrast, CH₄ presents a particular behavior, its production is lower at 55°C and a rate of C/5 (Fig. IV.16c), however, no clear explanation can be given and no answer was found in literature.

On the other hand, the peak area of CO₂ is increased with temperature and is almost not affected by C-rate (Fig. IV.16d). For instance, at 55°C and C/10 the peak area of CO₂ is 5 times bigger than at C/5, due to the longer time that the pouch cell stays at 55°C. This means that CO₂ is produced mainly from chemical processes that are PF₅-driven.

As detailed in the introduction, other sources of CO₂ are the chemical and electrochemical reactions of Li₂CO₃. Considering the electrochemical oxidation of the 1.4 μmol of Li₂CO₃ contained in one of the NMC electrodes, 1.4 and 0.7 μmol of CO₂ and ¹O₂ would be produced, respectively. These values are very high compared to the CO₂ values that were found experimentally ranging from 0.008 to 0.145 μmol (inset values in Fig. IV.16d). However, it is not ensured that the totality of Li₂CO₃ is oxidized electrochemically during the formation step. For comparison, in Chapter III through FTIR analyses it was found that in **exposed NMC 622C powder** around 59% of Li₂CO₃ (from which 27% was chemically consumed) could be consumed after one charge at 25°C and a rate of C/10. Due to the use of NMC films in the pouch cell system, it was not possible to quantify the Li₂CO₃ consumption through FTIR (because the reference sulfate band was covered by PVDF bands). Alternatively, in the next section, an experiment was put in place to try to discern the contribution of CO₂ from Li₂CO₃.

From these results, cycling at 30°C and C/10 were the chosen conditions to perform the formation step. Indeed, the lower current density allows to form a SEI with better properties¹⁶, and the lower temperature hinders the thermal degradation of the electrolyte.

3.2.4. Gas production of NMC 811 with modified surface composition

Since the identification of CO₂ production from Li₂CO₃ was not possible from the formation step, the complete storage protocol was performed with an **as-received** and **exposed** NMC 811 material in complete pouch cell.

After the storage at 55°C, the pouch cells were cooled down to 20°C and the gas was collected and analyzed by GC/BID with the improved method (CH₄ is visible). Table 5 shows the main characteristics of the pouch cells. Note that both positive electrodes have equivalent loading, but a very different quantity of Li₂CO₃, the surface of as-received NMC 811 contains only 1.04 μmol, whereas the exposed contains 20.9 μmol.

Table IV.5. Summary of some characteristics of the pouch cells

Characteristic	As-received NMC 811	Exposed NMC 811
Negative electrode loading (mg.cm ⁻²)	7.3 ± 0.3	
Positive electrode loading (mg.cm ⁻²)	13.3 ± 0.1	13.0 ± 0.3
Current density (with x=1) (mA.cm ⁻²)	0.37 ± 0.01	0.36 ± 0.01
Quantity of Li ₂ CO ₃ (μmol.g _{NMC} ⁻¹)	19 ± 1	380 ± 10
Quantity of Li ₂ CO ₃ in the electrode (μmol)	1.04	20.9

As detailed in [Chapter III](#), the electrochemical performance of exposed electrodes is greatly perturbed by the presence of surface species after H₂O/CO₂ exposure. The as-received 811/Gr pouch cells exhibit a 2nd charge capacity of 10.6 mAh, compared to 9.2 mAh of the exposed 811 (Fig. IV.17a). This difference can be explained by the increased polarization of 250 mV (represented for the first charge in Fig. IV.17b), most probably due to the presence of Li₂CO₃, MOOH and MO.

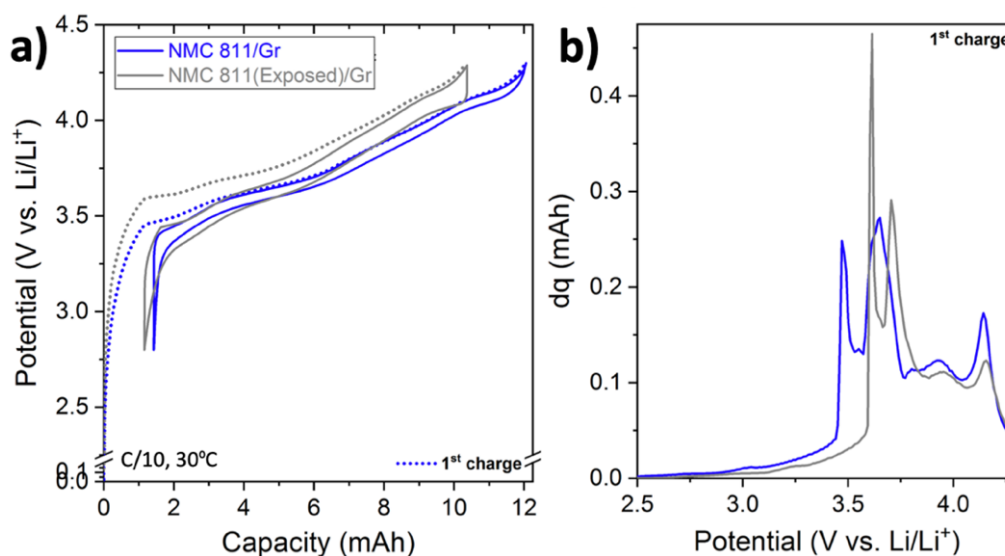


Figure IV.17. a) Capacity vs. potential curves and b) time vs. potential curves of the formation step for pouch cells NMC 811/Gr or NMC 811(exposed)/Gr.

Gases are expected from the electrochemical oxidation of Li₂CO₃ (Eq. IV.7). Fig. IV.18 shows the CO₂, CH₄, C₂H₄ and C₂H₆ peak areas; and the CO₂ quantification values, from the GC/BID gas analysis from pouch cells, as-received or exposed 811, after the complete storage protocol.

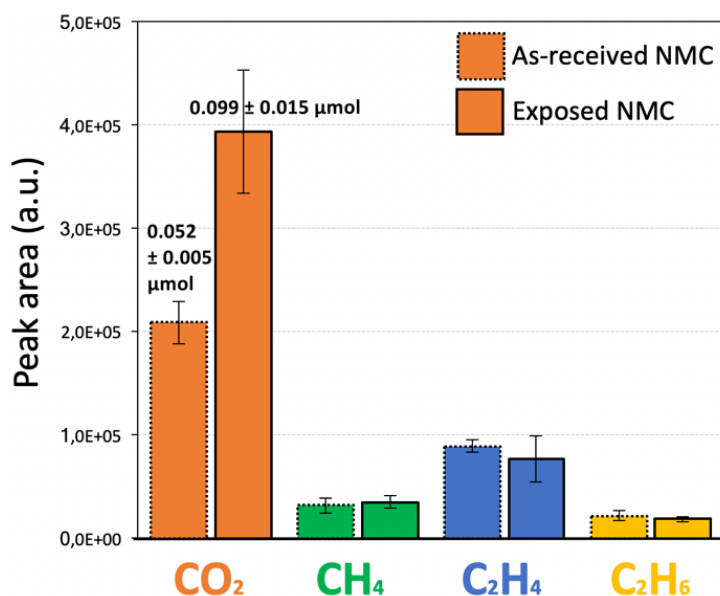


Figure IV.18. Gases detection by GC/BID (improved method and capillary column) after the complete storage protocol of as-received or exposed NMC 811/Gr pouch cells.

It can be observed that the peak areas of formation gases CH₄, C₂H₄ and C₂H₆ remained almost unchanged regardless of surface composition, and that the CO₂ produced from 811(exposed)/Gr ($0.099 \pm 0.015 \mu\text{mol}$) almost doubles compared to the as-received 811/Gr ($0.052 \pm 0.005 \mu\text{mol}$). The most relevant difference between both materials was the concentration of surface species. Therefore, it is safe to assume that the difference of $0.047 \mu\text{mol}$ of CO₂ came exclusively from the chemical (Eq. IV.6) and electrochemical (Eq. IV.7 and IV.4) reactions of Li₂CO₃. This value is far from the theoretical quantity of CO₂ from the complete consumption of Li₂CO₃: $20.9 \mu\text{mol}$. There are two possible explanations for this:

- Incomplete chemical and electrochemical consumption of Li₂CO₃.
- Partial dissolution of CO₂ in the electrolyte^{40, 41}. As an example, the solubility of CO₂ in a solvent mixture 1:1 wt. EC/DMC is $0.568 \text{ mol}_{\text{CO}_2} \cdot \text{L}^{-1}$ at 20°C⁴². This means that in 80 μl of solvents, a maximum of 45 μmol of CO₂ can be solubilized. Because LiPF₆ is contained in the electrolyte, the actual quantity of dissolved CO₂ would be six times lower, as predicted by the Setchenov law (salting-out effect)⁴¹.

In fact, both explanations are likely to occur. The first was proved in [Section 3.2.4](#) of [Chapter III](#), whereas the latter could explain the lesser quantity detected, compared to the expected theoretical one. Deeper study of these phenomena was left out of the scope of this work.

These experiments revealed the contribution of Li₂CO₃ to total CO₂. Unfortunately, it was not possible to differentiate the chemical from the electrochemical contribution. Note that similar

quantities of gas originating from solvents reduction to form SEI are obtained, regardless of the NMC surface state, which show the reliability of the protocol.

3.2.5. Gas production of different NMC compositions

In order to investigate the role of NMC composition on the gases produced in storage, this section studies the gas production at different stages of the complete storage protocol of twelve pouch cells NMC 622C/Gr and twelve pouch cells NMC 811/Gr. Among them, a third of each composition performed the formation step (C/10 and 30°C), a third performed the complete storage protocol (formation + storage) and the last third performed only a storage step (4 days at 55°C just after the electrolyte impregnation 5h-period) to discriminate the amount of gas issuing from the thermal solvents degradation only.

Table IV.6 shows the loadings and current densities of each NMC/Gr system. The applied current density in the formation step was higher in pouch cells containing NMC 622C than 811 (0.48 vs. 0.31 mA.cm⁻²) due to higher positive electrode loading (17.3 vs. 13.7 mg.cm⁻²).

Table IV.6. Summary of some characteristics of the pouch cells

Specification	622C/Gr	811/Gr
Negative electrode loading (mg.cm ⁻²)	7.4 ± 0.2	
Positive electrode loading (mg.cm ⁻²)	17.4 ± 0.3	13.7 ± 0.3
Current density (with x=1) (mA.cm ⁻²)	0.48 ± 0.01	0.31 ± 0.01

Fig. IV.19 shows the formation step of two representative pouch cells. The pouch cells containing NMC 811 took longer time to cycle and deliver higher specific capacity: 186 versus 174 mAh.g⁻¹ from 622C.

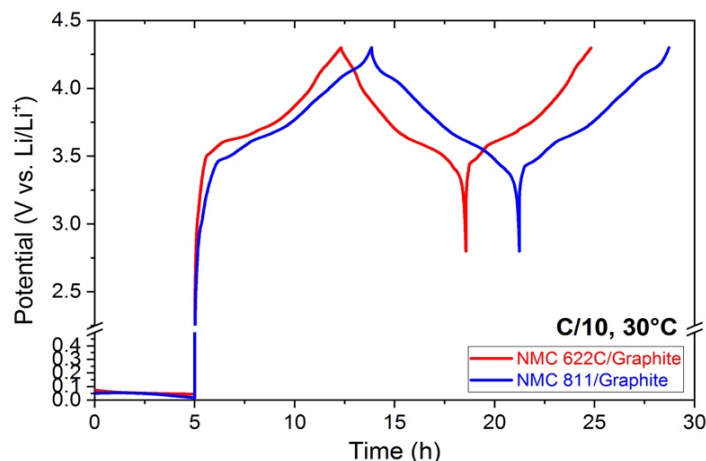


Figure IV.19. Time versus potential curves of the formation cycles of two representative pouch cells NMC 622C/Gr and 811/Gr.

The gas was analyzed by GC/BID using the capillary column with the regular method (CH₄ is not visible) after cooling down the cells to 20°C. The peak area results of the detected gases CO₂, C₂H₄ and C₂H₆ in the different steps (formation (a), formation + storage (b) or storage only (c)) are shown in Fig. IV.19. The quantified values of CO₂ and C₂H₄ are included as insets.

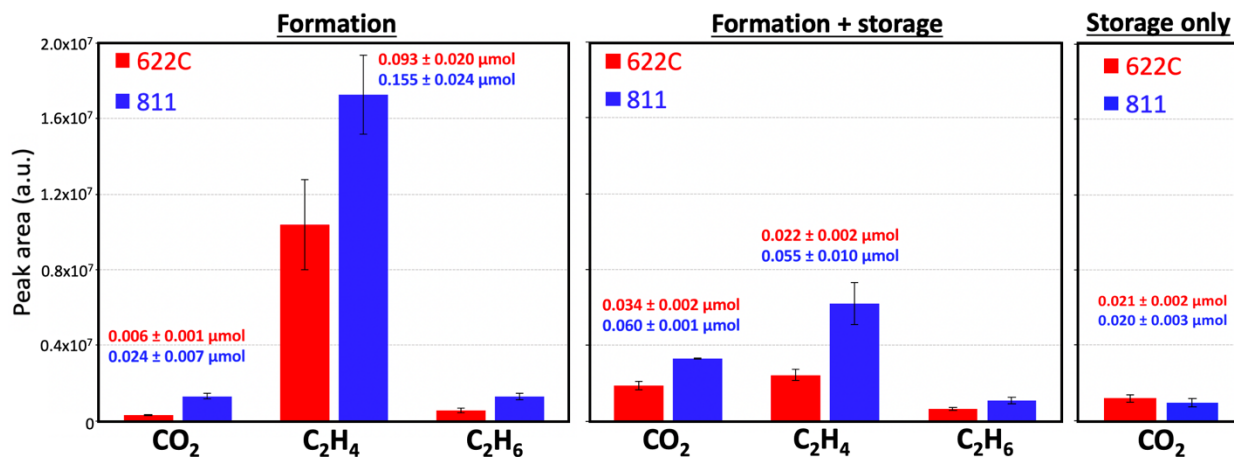


Figure IV.20. a) Gases from the formation step at C/10 and 30°C, b) gases from the complete storage protocol and c) gases only from the storage step. Error bars correspond to the standard deviation from three measurements.

The analysis of the results is separated into two sub-sections: gas from the formation step and gas from the complete storage protocol. The values of “storage only” are used in the discussion.

3.2.5.1. Discussion about gas of the formation step

After the formation step, CO₂, C₂H₄ and C₂H₆ present bigger quantities in pouch cells NMC 811/Gr than in 622C/Gr (Fig. IV.20a). It is normal to find more C₂H₄ and C₂H₆ from 811/Gr because lower current density is applied in this case, which induces more solvents reduction¹⁷ (negative electrodes are equivalent). This can be verified through peak integration (Fig. IV.21), where the integral value of the SEI formation peak in pouch cells 811/Gr is higher than in 622C/Gr (8.0×10^{-4} vs. 5.9×10^{-4} , respectively).

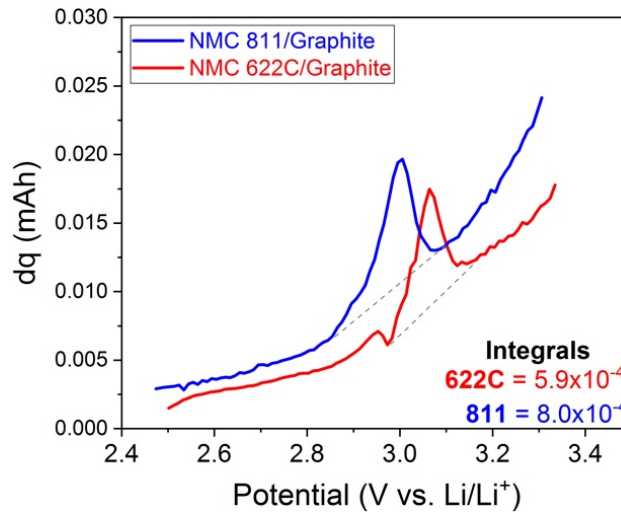


Figure IV.21. Incremental capacity profiles of the first charge of representative pouch cells showing the peak of SEI formation.

On the other hand, higher quantity of CO₂ is detected from 811/Gr than from 622C/Gr. In both systems the CO₂ is originated from several processes:

- i. electrochemical oxidation of EC (Eq. IV.1),
- ii. oxidation of EC by ¹O₂, from NMC at the delithiated state **during cycling** (Eq. IV.4).
- iii. chemical consumption of Li₂CO₃ (Eq. IV.6),
- iv. electrochemical consumption of Li₂CO₃ (Eq. IV.7) and
- v. thermal degradation of alkyl carbonate solvents (at 30°C) (Eqs. IV.17, 18 and 10),

It was not possible to quantitatively assign a value of CO₂ to each process. However, conjectures can be drawn that explain why 811/Gr produces 0.018 μmol of CO₂ more than 622/Gr.

First, the electrochemical oxidation of EC due to cycling above 4.2 V (i) should not vary as much from one system to the other. In contrast, the oxidation of EC due to ¹O₂ (ii) is more

likely to occur in pouch cells NMC 811/Gr than in 622C/Gr. This is supported in the work of Jung et al.⁹, who showed that the production of CO₂ from EC oxidation by ¹O₂ starts at ~4.7 V for NMC 622 and at ~4.3 V for NMC 811.

Concerning the chemical and electrochemical oxidation of Li₂CO₃ (iii and iv), in Chapter III, through NMR experiments, we demonstrated that the chemical consumption of Li₂CO₃ is not efficient at 30°C. Instead, we believe that electrochemical oxidation is predominant over chemical, but we do not know to what extent.

Lastly, regarding the thermal degradation of solvents (v), pouch cells NMC 622C/Gr stayed for 25 h at 30°C, whereas 811/Gr stayed 28.5 h, a difference of only **3.5 h**. Although not discussed, in Section 3.2.3 Fig. IV.16, it was found that in the time of **10h** only 0.003 μmol of CO₂ were produced from 811/Gr at 30°C, therefore, the 0.018 μmol of difference between NMC 622C and 811 pouch cells cannot be mainly attributed to thermal degradation at 30°C.

To summarize, during the formation step of pouch cells NMC 811/Gr, the main CO₂ contributors were assumed to be the electrochemical oxidation of Li₂CO₃ and the EC oxidation.

In conclusion, comparing the gases of the formation step from pouch cells containing NMC 622C and 811, it was found that C₂H₄ and C₂H₆ production stemming from solvents reduction depends on current density. On the other hand, CO₂ depends on cycling time and nickel content.

3.2.5.2. Discussion about gas of the complete storage protocol

The analysis of the gas resulting from the complete storage protocol gets more complex because of the combination of the gases of the formation and the storage steps. As it can be seen in Fig. IV.20b, whatever the NMC composition, more CO₂ was produced and a large part of C₂H₄ was consumed, whereas C₂H₆ remained mostly unchanged.

- Explanation to the consumption of C₂H₄

First, to explain the consumption of C₂H₄, Table IV.7 recapitulates the quantities of C₂H₄ from the formation step, from the complete storage protocol and from the “storage only”. The “difference A” corresponds to the calculated C₂H₄ consumed during the storage step.

Table IV.7. Quantities of C₂H₄ issued from each step and the calculated difference (from Fig. IV.20).

Gases step	C ₂ H ₄ (μmol)	
	622C/Gr	811/Gr
Formation step	0.093 ± 0.020	0.155 ± 0.024
Complete storage protocol (formation + storage)	0.022 ± 0.002	0.055 ± 0.010
Storage only	0	0
Difference A = n_(formation) – n_(formation + storage) (C₂H₄ consumed)	0.071 ± 0.022	0.100 ± 0.034

The explanation of C₂H₄ consumption is rather complicated and to the author’s knowledge, there is very limited information. The most relevant work is the one of Ellis et al.⁴³, who injected C₂H₄ into pouch bags containing lithiated graphite electrodes (without electrolyte and positive electrode) and observed that C₂H₄ was almost completely consumed. They proposed the reduction of C₂H₄ by lithium to form Li(C₂H₄)_n (n = 1,2,3) or Li₂C₂H₄. These species can be synthesized, but are only stable at very low temperature (T ~ -189°C)⁴³, so this hypothesis is highly unlikely.

Instead, we hypothesize that C₂H₄ is oxidized by ¹O₂ (Eq. IV.20), knowing that the storage of delithiated NMC at high temperature facilitates the production of oxygen (Eq. IV.5)⁸. In this case, the 0.071 and 0.100 μmol of C₂H₄ consumed corresponds to ~0.015 and ~0.021 mol% of the oxygen content in NMC 622C and NMC 811, respectively.



Furthermore, if the reaction is complete, 0.14 and 0.20 μmol of CO₂ are expected from 622C/Gr and 811/Gr, respectively. These values do not correspond to the actual increase of CO₂ of only 0.028 and 0.036 μmol of CO₂ in 622C/Gr and 811/Gr, respectively (Table IV.8).

This led us to think that there were other intermediary oxidation reactions, as proposed in Eqs. IV.21 and 22, forming ethylene oxide (C₂H₄O) or CO and H₂O:



C₂H₄O and CO are in fact molecules that may be present in the battery from thermal decomposition²⁵, so if detected, their attribution solely to C₂H₄ oxidation is impossible. Note that C₂H₄ is not the only hydrocarbon that can be oxidized, there are CH₄ and C₂H₆ as well, but it was already observed that the C₂H₆ quantity did not change greatly in Fig. IV.20 and CH₄ was not detected with the used protocol. Likely, EC could also be oxidized (Eq. IV.4). We deduce that gaseous C₂H₄ would be preferentially oxidized over dissolved EC, because most of the EC molecules solvate lithium ions and are thus less prone to oxidation. However, this affirmation requires additional experiments.

- Explanation to the production of CO₂

The processes that contribute to total CO₂ after the complete storage protocol are the same that from the formation step (enlisted hereby as **i** – **iv**). The variant is that processes **ii**, **iii** and **v** are exacerbated by the storage at the delithiated state and at high temperature. Moreover, the possibility that C₂H₄ is oxidized by ¹O₂ (**vi**) is added to the previous five processes:

- i.** electrochemical oxidation of EC (Eq. IV.1),
- ii.** oxidation of EC by ¹O₂, from NMC **during storage** at the delithiated state (Eq. IV.4).
- iii.** consumption of Li₂CO₃ **that was not totally consumed electrochemically** (Eq. IV.6),
- iv.** electrochemical consumption of Li₂CO₃ (Eq. IV.7) and
- v.** **increased** thermal degradation of carbonate solvents (at 55°C) (Eqs. IV.17, 18 and 19),
- vi.** **oxidation of C₂H₄ by ¹O₂ (to an unknown extent, if any),**

Indeed, the quantity of CO₂ increased from 0.006 μmol in the formation step, to 0.034 μmol after the complete storage protocol in pouch cells 622C/Gr. Similarly, CO₂ increased from 0.024 μmol to 0.060 μmol in 811/Gr (recapitulated in Table IV.8). The gap between the CO₂ produced from the complete protocol and the formation step will be called “difference B” in Table IV.8. The results were 0.028 and 0.036 μmol, in pouch cells 622C/Gr and 811/Gr, respectively.

Table IV.8. Quantities of CO₂ issued from each step and the calculated difference, obtained from Fig. IV.20.

Gases step	CO ₂ (μmol)	
	622C/Gr	811/Gr
Formation step (from processes i to v)	0.006 ± 0.001	0.024 ± 0.006
Complete storage protocol (formation + storage)	0.034 ± 0.002	0.060 ± 0.001
Storage only (storage at the lithiated state)	0.021 ± 0.002	0.020 ± 0.004
Difference B = n (formation + storage) – n (formation) (from processes ii and vi and in lesser extent i and iv)	0.028	0.036
Difference C = n (Difference B) – n (storage only) (the CO ₂ result is only due to reactions with ¹ O ₂)	0.007	0.016

The discrepancy among the values of “difference B” is due to the reactivity of each NMC during the storage at high temperature, involving the processes **ii** and **vi** that involve reactions with ¹O₂ (more ¹O₂ is produced from 811 than 622C). In this sense, “difference B” corresponds to the storage step at the **delithiated state**, whereas “storage only” to the **lithiated state**. Thereby, the difference between them (“difference C” in Table IV.8) corresponds to the quantity of CO₂ from the reactions with ¹O₂. The values are 0.007 and 0.016 μmol, from which we deduce that 811/Gr contributes more to total CO₂ than 622C/Gr due to the reactivity of delithiated NMC 811.

Finding more CO₂ after the storage of pouch cells is in fact contradictory to the work of Dahn’s group^{20, 21}, who proposed that CO₂ in the cell NMC 442/Gr diffuses to the negative electrode and reduces to lithium oxalate during storage (Eq. IV.16), based on the sole observation of CO₂ decrease after storage at 40°C. As a supplementary proof, Ellis et al.⁴³ showed XPS analyses where the O=C–O[–] peak was intense for the negative electrodes from stored pouch cells NMC 442/Gr, and through GC analyses showed that CO₂ was the most consumed gas. At the stage of the advancement of this project it is not possible to differentiate if some CO₂ has been consumed in the negative electrode, which can be envisaged to be studied through FTIR analysis of the SEI in future work.

To conclude, these tests gave evidence about the higher reactivity of NMC 811 through the consumption of C₂H₄ and the production of CO₂ after the complete storage protocol. The

higher quantity of C₂H₄ consumed from cells 811/Gr than from 622C/Gr, led us to deduce that the consumption occurs through the reaction with ¹O₂.

3.2.6. Impedance evolution after the complete storage protocol

At the same time that gas is produced from storage at high temperature, increase of the cell impedance has been reported to occur²⁰, due to the formation of a rock salt phase from the structural transformation of layered NMC¹¹. To the author's knowledge, there are not existing comparisons **between different NMC materials** in terms of impedance evolution before and after a storage period at high temperature.

3.2.6.1. Adaptation of the complete storage protocol

The impedance experiments were performed on 3-electrode NMC 622C/Gr and 811/Gr pouch cells. Potentiostatic electrochemical impedance spectroscopy (PEIS) measurements were recorded before and after the storage step of the complete storage protocol, at 30°C, at frequencies ranging from 300 kHz to 0.05 Hz, with 7 points per decade (VMP-3 Biologic). Since self-discharge during the storage step is expected to occur, the protocol includes intermediary PEIS measurements at 90% and 80% after the formation step, in order to have a comparison scale with the PEIS measurements after storage. At the end of the storage, the pouch was allowed to descend to 30°C and a recharge to 100% SOC was done, followed by 15 min. rest period before performing PEIS (Fig. IV.22 summarizes the different steps). Throughout the protocol, the pouch cells were not disconnected or moved to avoid any misinterpretation.

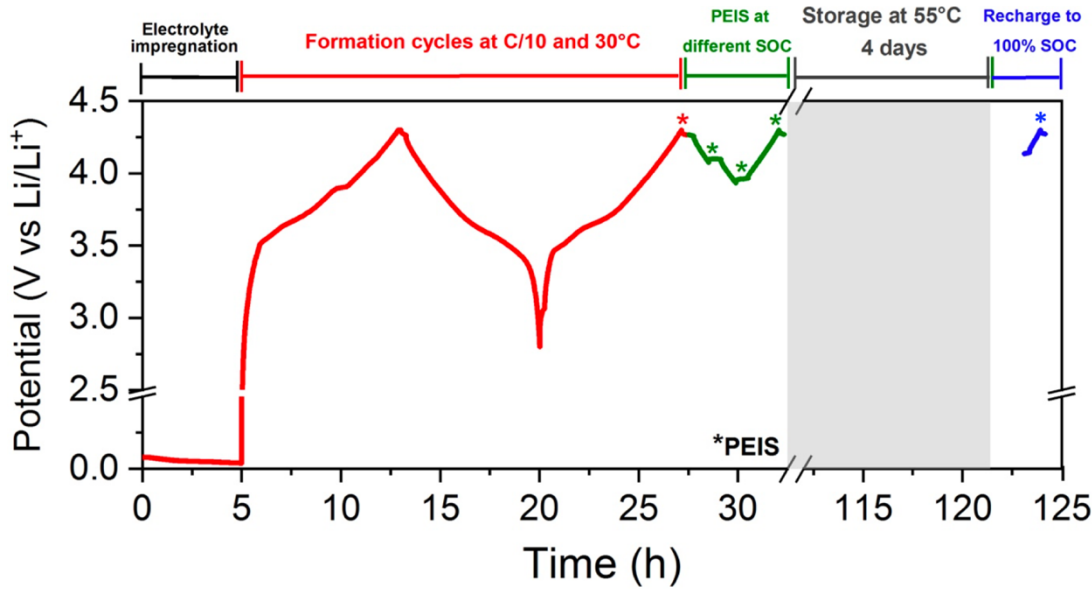


Figure IV.22. Cycling step of the formation protocol established for the testing of 2 and 3-electrode pouch cells NMC 622C/Gr.

Fig. IV.23 shows the impedance spectra of 3-electrode pouch cells 622/Gr that performed only the formation step and the PEIS measurements at 100, 90 and 80% SOC. The Nyquist plots of the full cell (a), positive (b) and negative electrode (c) are shown individually.

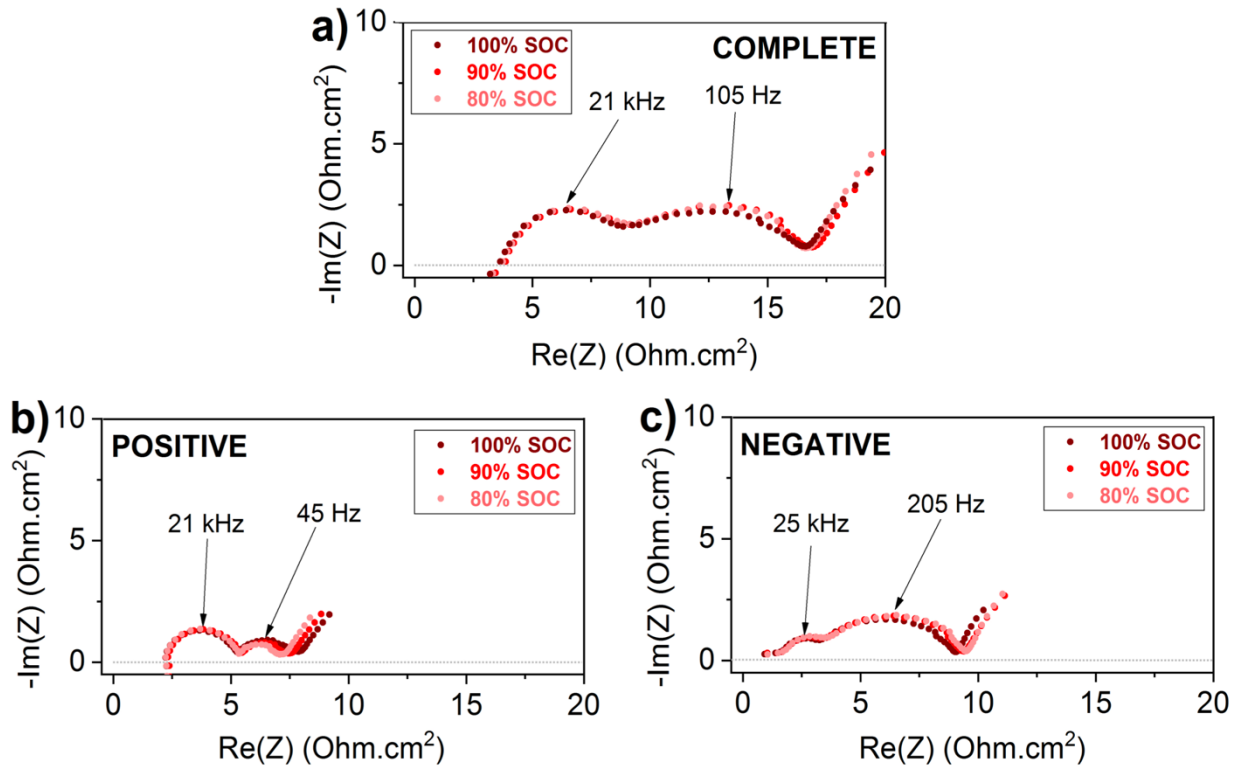


Figure IV.23. Nyquist plots collected at different SOC after the formation step in 3-electrode NMC 622C/Gr pouch cell. a) Complete cell b) positive and c) negative electrode.

Each of these Nyquist plots is composed of three parts, explained by several authors⁴⁴⁻⁴⁷:

- i. a high-frequency semicircle attributed to the contact interface resistance between the current collector and particles (R_{contact}), with frequency values for the positive electrode between 1 – 100 kHz;
- ii. a middle-frequency semicircle attributed to the charge-transfer process (R_{ct}), with frequency values for the positive electrode between 1 – 100 Hz, and
- iii. a low-frequency straight line, corresponding to the Li^+ diffusion.

The resistance value crossing the X axis corresponds to the electrolyte resistance (R_{elect}) and the resistance of the cables.

The full cell spectra are practically identical; however, in the spectra of the individual electrodes there are slight disparities in the process of charge transfer: the shape of the semicircle decreases in the positive electrode and increases in the negative electrode; whereas the shape of the contact interface resistance is unchanged. The variations when measuring at 100, 90 or 80% of SOC are minimal, which means that, up to 20% of discharge, the different interfaces are slightly modified.

To go further in the comprehension, the extraction of the spectra characteristics was undertaken, with the aid of an equivalent circuit model previously used in the literature^{44, 48} (Fig. IV.24). According to this model, R_{ct} and R_{contact} are in parallel with constant phase elements, modeling the imperfect double layer capacitance obtained across the electrolyte interphases, and in series with a Warburg element describing the diffusion tail at low frequency.

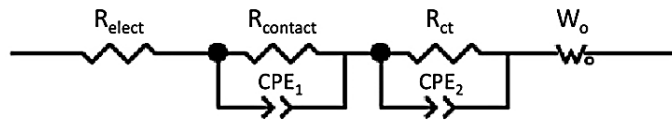


Figure IV.24. Equivalent circuit model used to fit PEIS positive electrode data in Z-view[®].

Landesfeind et al.⁴⁸ consider that the R_{ct} extracted from this model is overestimated because the semicircle includes the contribution of the electrolyte ionic resistance within the pores. In our case, fitting was performed without considering this contribution.

3.2.6.2. Impedance from pouch cells NMC 622C/Gr and 811/Gr

After the storage period, the OCV of pouch cells NMC 622C/Gr and 811/Gr stored in the charged state gradually decreased, until a corresponding calculated self-discharge of 9–12% SOC, which appeared to be totally reversible. In the literature, it has been proposed that the layered materials have a reversible and irreversible part of self-discharge upon high temperature ageing⁴⁹. The self-discharge reversible part has been attributed to lithium ions that re-intercalate from the electrolyte into NMC; whereas the irreversible part has been attributed to surface transformations (hexagonal to spinel in LCO⁴⁹). In our pouch cells, the capacity was totally recovered after recharge to 4.3 V. Maybe the irreversible part was not detected because the amount of produced oxygen ranges *at least* around 0.015–0.021 mol% (Section 3.2.5.2). This implies the creation of a very thin rock salt layer which will not likely affect the capacity, although it may impact the PEIS measurements.

Fig. IV.25 shows the Nyquist plots of 3-electrode pouch cells NMC 622C/Gr and 811/Gr before and after storage from the complete cell (a, b), the positive electrode (c, d) and the negative electrode (e, f). After storage, both electrodes modified their impedance. As self-discharge process is observed in both cases (inferior to 20% of SOC), it implies that surface chemical processes occurred during storage. Note that the main difference between the two is that NMC 811/Gr (b) present bigger semicircles before and after storage than 622C/Gr (a).

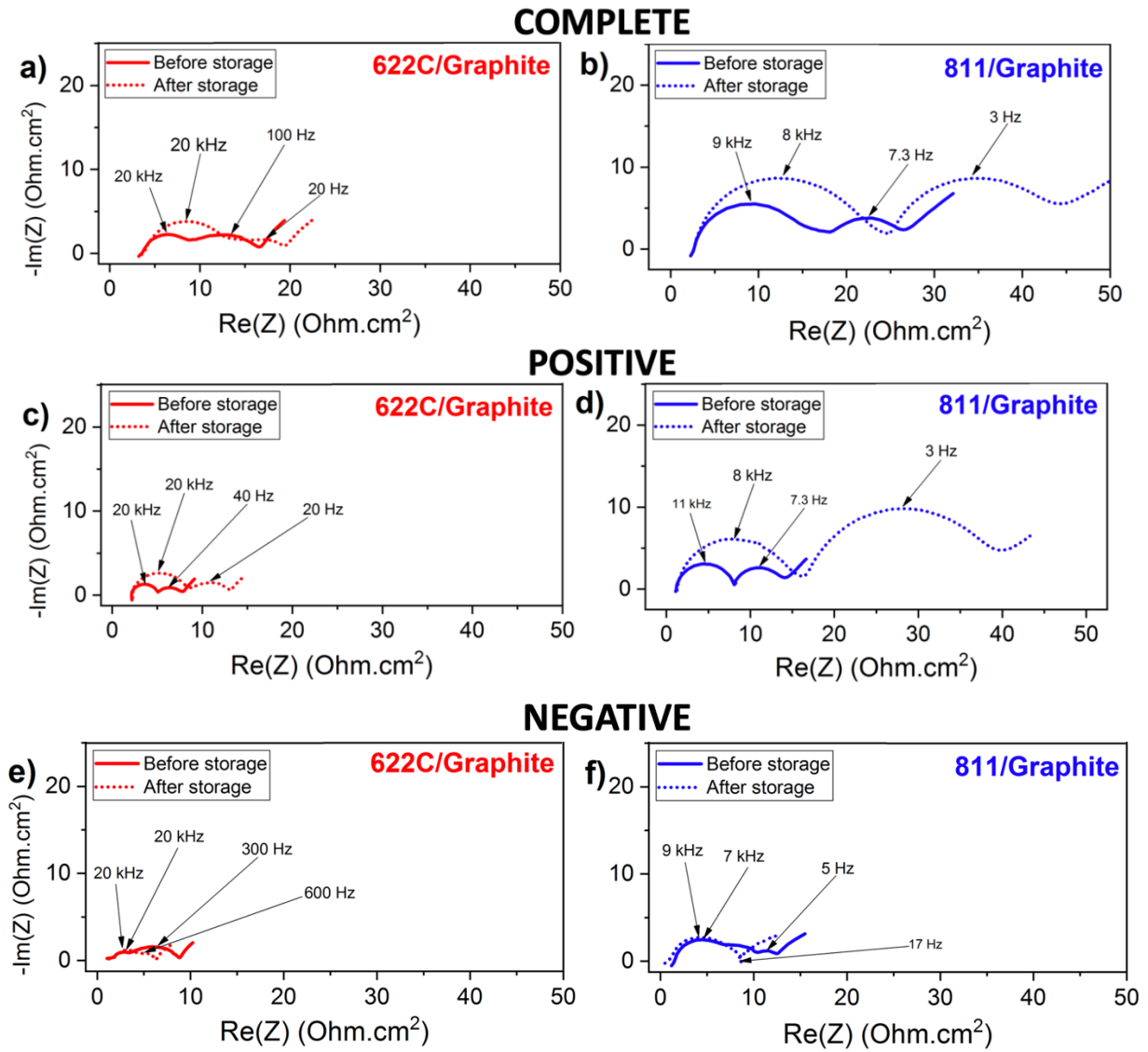


Figure IV.25. Nyquist plots collected before and after 4 days of storage at 55°C, in pouch cells NMC 622C/Gr (a, c, e) and 811/Gr (b, d, f).

The positive electrode is the main contributor to cell in both cases. To compare NMC electrodes, the spectra were fitted with Zview using the equivalent circuit on Fig. IV.24. The fitted values of resistance, capacitances and alpha are reported in Table IV.9.

Table IV.9. Fitted results of resistances from the positive electrode obtained with Z-view.

Fitted values (Ohm.cm ²)	NMC 622C electrode		NMC 811 electrode	
	before	after	before	after
$R_{\text{electrolyte}}$ (Ohm.cm ²)	2.04	2.12	1.20	1.28
R_{contact} (Ohm.cm ²)	2.88	6.24 (+53.8%)	6.84	14.8 (+53.8%)
$\text{CPE}_{\text{contact}}$ (F.s ⁻¹ /cm ²)	7x10 ⁻⁶	6.7x10 ⁻⁶	5x10 ⁻⁶	5x10 ⁻⁶
α_{contact}	0.93	0.87	0.93	0.88
$f_{\text{max}_{\text{contact}}}$ (Hz)	17.8 kHz	17 kHz	10.1 kHz	7.8 kHz
R_{ct} (Ohm.cm ²)	2.76	4.60 (+40%)	5.76	22.4 (+74.3%)
CPE_{ct} (F.s ⁻¹ /cm ²)	0.0062	0.007	0.0057	0.0075
α_{ct}	0.75	0.73	0.89	0.89
$f_{\text{max}_{\text{ct}}}$ (Hz)	35.7 Hz	18.5 Hz	7.3 Hz	1.2 Hz

The frequency values calculated from the contact interface resistance, between 8–18 kHz, match the frequency values reported in the literature⁴⁴⁻⁴⁷. This is also the case of the frequencies calculated from the charge-transfer process, which lie between 1–36 Hz. By looking at the alpha values and the shape of the Nyquist plots, it has been difficult to add a third contribution corresponding to the CEI.

On the Nyquist plot of the positive electrodes before storage, the semicircle attributed to the contact interface resistance is slightly bigger than the one corresponding to the charge transfer process (Fig. IV.25c, d). In terms of values, R_{contact} was found to be 2.88 Ohm.cm² for 622C and 6.84 Ohm.cm² for 811. The higher value of the NMC 811 electrode may be due to the absence of calendaring, compared to 622C electrode.

After storage, the fitted values show that R_{elect} increased very little. This slight increase means that the dissolved species from electrolyte degradation did not change the resistance of the electrolyte significantly. Additionally, R_{contact} doubled in both positive electrodes, and R_{ct} increased by 40% in 622C and 74.3% in 811. The similar increase of R_{contact} means that the contributions of the interfaces between current collector and active particles and the resistance of Li⁺ migration through the CEI (if any) evolve in a proportional way in both NMC electrodes.

In NMC 622C/Gr pouch cell, the R_{contact} increased by 53.8%, compared to +40% of the R_{ct} ; whereas in 811/Gr the contrary is observed: R_{ct} increased by 74.3% compared to +53.8% of R_{contact} . The increase of the resistances in both cases can be attributed to the formation of the

rock salt structure at NMC surface. In this sense, Sallis et al.¹¹ determined that the formation of rock salt phase in layered NCA is reflected as a marked increase of R_{ct} and a lesser increase of $R_{contact}$, which is consistent with the observations in NMC 811 with similar composition. This is also consistent with our analysis of the gas evolution: more CO_2 is produced and more C_2H_4 is consumed as a consequence of the formation of 1O_2 and rock salt phase. In this way, PEIS measurements constitute supplementary evidence to the increased reactivity of Ni-rich NMC and highlight the necessity to avoid surface transformations in Ni-rich NMC materials.

To gain more insight into the impact of rock salt formation on the impedance measured after the storage step, the same protocol was performed in a 3-electrode pouch cell 811/Gr changing the storage temperature to $10^\circ C$. This experiment was undertaken considering that the 1O_2 , and consequently the rock salt production, are less kinetically favored at low temperature. The slight evolution of the middle frequency domain in Fig. IV.26 demonstrates that the rock salt formation was reduced at low temperature. Again, the main difference between the spectra before and after storage is observed for the charge transfer process, but in a lesser way than what was observed at $55^\circ C$.

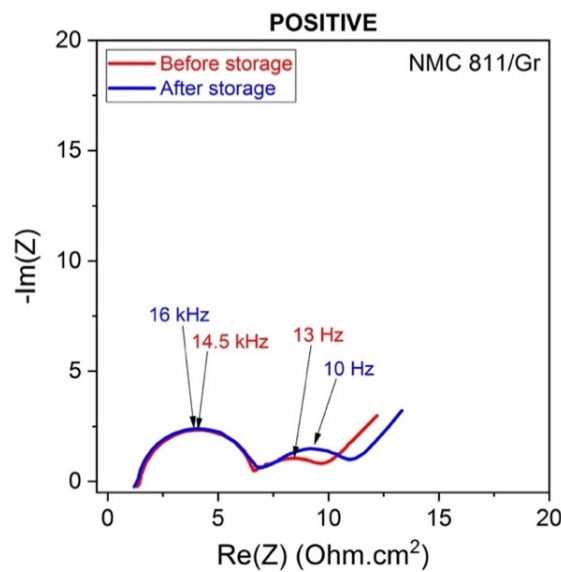


Figure IV.26. Nyquist plots from a pouch cell NMC 811/Gr before and after storage at $10^\circ C$.

4. Conclusion of the chapter

This chapter evidenced the reactivity of Ni-rich NMC materials from the analysis of the gaseous products upon storage with electrolyte at 55°C. First, among the available GC devices, columns and detectors, the best sustainable and reproducible measurements were obtained from the GC/BID device equipped with a capillary column and set in “linear velocity” control mode. A micropacked column with better gas separation properties was also tested, but it was not preferred due to a lack of reproducibility.

The CO₂ quantity produced from pristine NMC and electrolyte storage at 55°C was found to be driven by PF₅ and dependent on dead volume. On the other hand, it was found that the storage at delithiated state increases the CO₂ production, explained by the presence of Ni⁴⁺ that reduces to Ni³⁺ producing ¹O₂, which oxidizes EC.

Gas production from the storage of 2- and 3-electrode pouch cells was then evaluated. For this, their fabrications were optimized and a protocol containing a formation and a storage step was established. After the formation step, it was found that the detectable formation gases (CH₄, C₂H₄, C₂H₆) are dependent on current density. Additionally, several sources of CO₂ were considered: chemical and electrochemical oxidation of solvents and Li₂CO₃, and thermal degradation of solvents. In our case, the NMC composition was found to influence CO₂ production since $n(\text{CO}_2)_{811} > n(\text{CO}_2)_{622\text{C}}$. After storage, two phenomena were observed: C₂H₄ consumption and an increase of CO₂ concentration. Both are issued from the same cause: oxidation of C₂H₄ and EC by ¹O₂, influenced by the composition of NMC. Indeed, in compositions richer in nickel, more Ni⁴⁺ exist, so more ¹O₂ can be produced. At the same time, a restructuration of the surface with the formation of a rock salt phase occurs, causing impedance augmentation. This was evidenced in 3-electrode pouch cell experiments.

Finally, we acknowledge that there are many things left to be investigated, for instance, CO₂ dissolution, crosstalk reactions and long-term gas evolution. The latter is investigated in the next chapter by using the methods here developed.

5. References

1. Park, J.-K., *Principles and Applications of Lithium Secondary Batteries*. WILEY-VCH: 2012.
2. Wen, J. W.; Yu, Y.; Chen, C. H., A Review on Lithium-Ion Batteries Safety Issues: Existing Problems and Possible Solutions. *Materials Express* **2012**, *2* (3), 197-212.
3. Rowden, B.; Garcia-Araez, N., A review of gas evolution in lithium ion batteries. *Energy Reports* **2020**, *6*, 10-18.
4. Schipper, F.; Erickson, E. M.; Erk, C.; Shin, J. Y.; Chesneau, F. F.; Aurbach, D., Review-Recent Advances and Remaining Challenges for Lithium Ion Battery Cathodes. *Journal of the Electrochemical Society* **2017**, *164* (1), A6220-A6228.
5. Xing, L. D.; Li, W. S.; Wang, C. Y.; Gu, F. L.; Xu, M. Q.; Tan, C. L.; Yi, J., Theoretical Investigations on Oxidative Stability of Solvents and Oxidative Decomposition Mechanism of Ethylene Carbonate for Lithium Ion Battery Use. *Journal of Physical Chemistry B* **2009**, *113* (52), 16596-16602.
6. Tebbe, J. L.; Fuerst, T. F.; Musgrave, C. B., Degradation of Ethylene Carbonate Electrolytes of Lithium Ion Batteries via Ring Opening Activated by LiCoO₂ Cathode Surfaces and Electrolyte Species. *Acs Applied Materials & Interfaces* **2016**, *8* (40), 26664-26674.
7. Solchenbach, S.; Metzger, M.; Egawa, M.; Beyer, H.; Gasteiger, H. A., Quantification of PF₅ and POF₃ from Side Reactions of LiPF₆ in Li-Ion Batteries. *Journal of the Electrochemical Society* **2018**, *165* (13), A3022-A3028.
8. Xiong, D. J.; Ellis, L. D.; Li, J.; Li, H. Y.; Hynes, T.; Allen, J. P.; Xia, J.; Hall, D. S.; Hill, I. G.; Dahn, J. R., Measuring Oxygen Release from Delithiated LiNi_xMn_yCo_{1-x-y}O₂ and Its Effects on the Performance of High Voltage Li-Ion Cells. *Journal of the Electrochemical Society* **2017**, *164* (13), A3025-A3037.
9. Jung, R.; Metzger, M.; Maglia, F.; Stinner, C.; Gasteiger, H. A., Oxygen Release and Its Effect on the Cycling Stability of LiNi_xMn_yCo_zO₂ (NMC) Cathode Materials for Li-Ion Batteries. *Journal of the Electrochemical Society* **2017**, *164* (7), A1361-A1377.
10. Lin, F.; Markus, I. M.; Nordlund, D.; Weng, T. C.; Asta, M. D.; Xin, H. L. L.; Doeff, M. M., Surface reconstruction and chemical evolution of stoichiometric layered cathode materials for lithium-ion batteries. *Nature Communications* **2014**, *5*.
11. Sallis, S.; Pereira, N.; Mukherjee, P.; Quackenbush, N. F.; Faenza, N.; Schlueter, C.; Lee, T. L.; Yang, W. L.; Cosandey, F.; Amatucci, G. G.; Piper, L. F. J., Surface degradation of Li_{1-x}Ni_{0.80}Co_{0.15}Al_{0.05}O₂ cathodes: Correlating charge transfer impedance with surface phase transformations. *Applied Physics Letters* **2016**, *108* (26).
12. Renfrew, S. E.; McCloskey, B. D., Residual Lithium Carbonate Predominantly Accounts for First Cycle CO₂ and CO Outgassing of Li-Stoichiometric and Li-Rich Layered Transition-Metal Oxides. *Journal of the American Chemical Society* **2017**, *139* (49), 17853-17860.
13. Hatsukade, T.; Schiele, A.; Hartmann, P.; Brezesinski, T.; Janek, J., Origin of Carbon Dioxide Evolved during Cycling of Nickel-Rich Layered NCM Cathodes. *Acs Applied Materials & Interfaces* **2018**, *10* (45), 38892-38899.
14. Mahne, N.; Renfrew, S. E.; McCloskey, B. D.; Freunberger, S. A., Electrochemical Oxidation of Lithium Carbonate Generates Singlet Oxygen. *Angewandte Chemie-International Edition* **2018**, *57* (19), 5529-5533.
15. Berkes, B. B.; Schiele, A.; Sommer, H.; Brezesinski, T.; Janek, J., On the gassing behavior of lithium-ion batteries with NCM523 cathodes. *Journal of Solid State Electrochemistry* **2016**, *20* (11), 2961-2967.
16. An, S. J.; Li, J. L.; Daniel, C.; Mohanty, D.; Nagpure, S.; Wood, D. L., The state of understanding of the lithium-ion-battery graphite solid electrolyte interphase (SEI) and its relationship to formation cycling. *Carbon* **2016**, *105*, 52-76.
17. Zhang, S. S.; Xu, K.; Jow, T. R., Optimization of the forming conditions of the solid-state interface in the Li-ion batteries. *Journal of Power Sources* **2004**, *130* (1-2), 281-285.
18. Bernhard, R.; Metzger, M.; Gasteiger, H. A., Gas Evolution at Graphite Anodes Depending on Electrolyte Water Content and SEI Quality Studied by On-Line Electrochemical Mass Spectrometry. *Journal of the Electrochemical Society* **2015**, *162* (10), A1984-A1989.

19. Metzger, M.; Strehle, B.; Solchenbach, S.; Gasteiger, H. A., Origin of H₂ Evolution in LIBs: H₂O Reduction vs. Electrolyte Oxidation. *Journal of the Electrochemical Society* **2016**, *163* (5), A798-A809.
20. Xiong, D. J.; Petibon, R.; Nie, M.; Ma, L.; Xia, J.; Dahn, J. R., Interactions between Positive and Negative Electrodes in Li-Ion Cells Operated at High Temperature and High Voltage. *Journal of the Electrochemical Society* **2016**, *163* (3), A546-A551.
21. Xiong, D. J.; Ellis, L. D.; Nelson, K. J.; Hynes, T.; Petibon, R.; Dahn, J. R., Rapid Impedance Growth and Gas Production at the Li-Ion Cell Positive Electrode in the Absence of a Negative Electrode. *Journal of the Electrochemical Society* **2016**, *163* (14), A3069-A3077.
22. Schiele, A.; Hatsukade, T.; Berkes, B. B.; Hartmann, P.; Brezesinski, T.; Janek, J., High-Throughput in Situ Pressure Analysis of Lithium-Ion Batteries. *Analytical Chemistry* **2017**, *89* (15), 8122-8128.
23. Aiken, C. P.; Xia, J.; Wang, D. Y. H.; Stevens, D. A.; Trussler, S.; Dahn, J. R., An Apparatus for the Study of In Situ Gas Evolution in Li-Ion Pouch Cells. *Journal of the Electrochemical Society* **2014**, *161* (10), A1548-A1554.
24. Castel, E.; Berg, E. J.; El Kazzi, M.; Novak, P.; Villevieille, C., Differential Electrochemical Mass Spectrometry Study of the Interface of xLi₂MnO₃·(1-x)LiMO₂ (M = Ni, Co, and Mn) Material as a Positive Electrode in Li-Ion Batteries. *Chemistry of Materials* **2014**, *26* (17), 5051-5057.
25. Gachot, G.; Grugeon, S.; Jimenez-Gordon, I.; Eshetu, G. G.; Boyanov, S.; Lecocq, A.; Marlair, G.; Pilard, S.; Laruelle, S., Gas chromatography/Fourier transform infrared/mass spectrometry coupling: a tool for Li-ion battery safety field investigation. *Analytical Methods* **2014**, *6* (15), 6120-6124.
26. Gachot, G.; Ribiere, P.; Mathiron, D.; Grugeon, S.; Armand, M.; Leriche, J. B.; Pilard, S.; Laruelle, S., Gas Chromatography/Mass Spectrometry As a Suitable Tool for the Li-Ion Battery Electrolyte Degradation Mechanisms Study. *Analytical Chemistry* **2011**, *83* (2), 478-485.
27. Chancelier, L.; Benayad, A.; Gutel, T.; Mailley, S.; Santini, C. C., Characterization of LTO//NMC Batteries Containing Ionic Liquid or Carbonate Electrolytes after Cycling and Overcharge. *Journal of the Electrochemical Society* **2015**, *162* (6), A1008-A1013.
28. *Application data-sheet No. 7: Simultaneous Analysis of Evolved Gas Produced by the Degradation of a Lithium-Ion Battery.*
29. Instruction Manual for GC-2010 Gas Chromatograph. 221-40407F ed.; Shimadzu-Corporation.
30. Champion, C. L.; Li, W. T.; Euler, W. B.; Lucht, B. L.; Ravdel, B.; DiCarlo, J. F.; Gitzendanner, R.; Abraham, K. M., Suppression of toxic compounds produced in the decomposition of lithium-ion battery electrolytes. *Electrochemical and Solid State Letters* **2004**, *7* (7), A194-A197.
31. Champion, C. L.; Li, W. T.; Lucht, B. L., Thermal decomposition of LiPF₆-based electrolytes for lithium-ion batteries. *Journal of the Electrochemical Society* **2005**, *152* (12), A2327-A2334.
32. Manthiram, A., An Outlook on Lithium Ion Battery Technology. *Acs Central Science* **2017**, *3* (10), 1063-1069.
33. Jung, R.; Metzger, M.; Maglia, F.; Stinner, C.; Gasteiger, H. A., Chemical versus Electrochemical Electrolyte Oxidation on NMC111, NMC622, NMC811, LNMO, and Conductive Carbon. *Journal of Physical Chemistry Letters* **2017**, *8* (19), 4820-4825.
34. Renfrew, S. E.; McCloskey, B. D., The Role of Electrolyte in the First-Cycle Transformations of LiNi_{0.6}Mn_{0.2}Co_{0.2}O₂. *Journal of the Electrochemical Society* **2019**, *166* (13), A2762-A2768.
35. Kim, Y., Mechanism of gas evolution from the cathode of lithium-ion batteries at the initial stage of high-temperature storage. *Journal of Materials Science* **2013**, *48* (24), 8547-8551.
36. Jimenez Gordon, I. A. Cycling Performance, Post-Mortem and Impedances Analyses of High-Energy density Li-ion Cells Designed for Fast Charging in BEVs. Université de Picardie Jules Verne, 2014.
37. Leissing, M.; Winter, M.; Wiemers-Meyer, S.; Nowak, S., A method for quantitative analysis of gases evolving during formation applied on LiNi_{0.6}Mn_{0.2}Co_{0.2}O₂ parallel to natural graphite lithium ion battery cells using gas chromatography - barrier discharge ionization detector. *Journal of Chromatography A* **2020**, *1622*.
38. Kim, H. Electrolyte analytical investigation as a suitable approach for studying Li-ion battery formation process. Université de Picardie Jules Verne, 2014.
39. Zhou, H.; Xin, F. X.; Pei, B.; Whittingham, M. S., What Limits the Capacity of Layered Oxide Cathodes in Lithium Batteries? *Acs Energy Letters* **2019**, *4* (8), 1902-1906.

40. Blanchard, F.; Carre, B.; Bonhomme, F.; Biensan, P.; Lemordant, D., Solubility of carbon dioxide in alkyl carbonates and lactones. *Canadian Journal of Chemistry-Revue Canadienne De Chimie* **2003**, *81* (5), 385-391.
41. Dougassa, Y. R.; Jacquemin, J.; El Ouatani, L.; Tessier, C.; Anouti, M., Viscosity and Carbon Dioxide Solubility for LiPF₆, LiTFSI, and LiFAP in Alkyl Carbonates: Lithium Salt Nature and Concentration Effect. *Journal of Physical Chemistry B* **2014**, *118* (14), 3973-3980.
42. Browning, K. L.; Baggetto, L.; Unocic, R. R.; Dudney, N. J.; Veith, G. M., Gas evolution from cathode materials: A pathway to solvent decomposition concomitant to SEI formation. *Journal of Power Sources* **2013**, *239*, 341-346.
43. Ellis, L. D.; Allen, J. P.; Thompson, L. M.; Harlow, J. E.; Stone, W. J.; Hill, I. G.; Dahn, J. R., Quantifying, Understanding and Evaluating the Effects of Gas Consumption in Lithium-Ion Cells. *Journal of the Electrochemical Society* **2017**, *164* (14), A3518-A3528.
44. Keefe, A. S.; Buteau, S.; Hill, I. G.; Dahn, J. R., Temperature Dependent EIS Studies Separating Charge Transfer Impedance from Contact Impedance in Lithium-Ion Symmetric Cells. *Journal of the Electrochemical Society* **2019**, *166* (14), A3272-A3279.
45. Xia, J.; Aiken, C. P.; Ma, L.; Kim, G. Y.; Burns, J. C.; Chen, L. P.; Dahn, J. R., Combinations of Ethylene Sulfite (ES) and Vinylene Carbonate (VC) as Electrolyte Additives in LiNi_{1/3}Mn_{1/3}Co_{1/3}O₂/Graphite Pouch Cells. *Journal of the Electrochemical Society* **2014**, *161* (6), A1149-A1157.
46. Atebamba, J. M.; Moskon, J.; Pejovnik, S.; Gaberscek, M., On the Interpretation of Measured Impedance Spectra of Insertion Cathodes for Lithium-Ion Batteries. *Journal of the Electrochemical Society* **2010**, *157* (11), A1218-A1228.
47. Weber, R.; Louli, A. J.; Plucknett, K. P.; Dahn, J. R., Resistance Growth in Lithium-Ion Pouch Cells with LiNi_{0.80}Co_{0.15}Al_{0.05}O₂ Positive Electrodes and Proposed Mechanism for Voltage Dependent Charge-Transfer Resistance. *Journal of the Electrochemical Society* **2019**, *166* (10), A1779-A1784.
48. Landesfeind, J.; Pritzl, D.; Gasteiger, H. A., An Analysis Protocol for Three-Electrode Li-Ion Battery Impedance Spectra: Part I. Analysis of a High-Voltage Positive Electrode. *Journal of the Electrochemical Society* **2017**, *164* (7), A1773-A1783.
49. Ozawa, Y.; Yazami, R.; Fultz, B., Self-discharge study of LiCoO₂ cathode materials. *Journal of Power Sources* **2003**, *119*, 918-923.
50. Tracera (GC-BID) Solution. Application manual. LAAN-B-GC004 ed.; Shimadzu-Corporation.

Chapter V

Study of LiPO_2F_2 as electrolyte additive in batteries containing Ni-rich NMC materials

1. Introduction.....	195
2. Impact of LiPO_2F_2 on the electrolyte properties.....	198
3. Impact of LiPO_2F_2 on the electrochemical performance of NMC 622C and 811.....	202
3.1. NMC 811 as positive electrode.....	202
3.1.1. Cycling performance of pouch cells NMC 811/Graphite at 25 and 55°C.....	202
3.1.2. Impact of the calendaring process.....	206
3.1.3. Post-mortem analyses.....	208
3.2. NMC 622C as positive electrode.....	211
3.2.1. Cycling performance of pouch cells NMC 622C/Graphite at 55°C.....	211
3.2.2. Post-mortem SEM analysis.....	211
4. Study of the electrolyte degradation products: impact of LiPO_2F_2.....	213
4.1. Study of interphases composition.....	213
4.1.1. Study of SEI composition.....	213
4.1.2. Study of CEI composition.....	216
4.2. Analysis of electrolyte degradation products.....	218
4.2.1. Analysis of electrolytes by “liquid” GC/MS.....	219
4.2.2. Analysis of electrolytes by ESI-HRMS.....	221
4.3. Analysis of gas released.....	224
4.4. Discussion and conclusion.....	228
5. Conclusion of the chapter.....	232
6. References.....	233

1. Introduction

The use of electrolyte additives is one of the most effective and economical ways to improve the electrochemical performance of LIBs. In [Chapter III](#), the salt, lithium difluorophosphate, LiPO_2F_2 (LDFP, Fig. V.1) was proved to be a product of the chemical reaction of NMC surface species (Li_2CO_3 , Li_2O , Li_2SO_4) with LiPF_6 . Attracting much attention as capacity retention improver, the decision was made to evaluate its impact as electrolyte additive in batteries containing Ni-rich NMC materials.

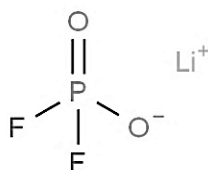


Figure V.1. Structural formula of LDFP molecule

In recent years, interest in LDFP as electrolyte additive has increased due to the suspected ability of fluorophosphate species ($\text{Li}_x\text{PF}_y\text{O}_z$) to build interphases on the positive and negative electrode that improve the electrochemical performances, by hindering parasitic reactions with the electrolyte^{1, 2}. Studies have shown many positive outcomes in a variety of positive and negative electrode chemistries in half or full cell, with NMC materials being among the most common. Under different cycling conditions, temperatures (between -20°C and 55°C) and weight content (usually between 0.5 and 3 wt.%), LDFP is capable to:

- decrease the impedance of the positive electrode³⁻⁵, negative electrode^{2, 6, 7} or full cell⁷⁻¹¹
- prevent lithium plating¹² and decrease cation dissolution⁸
- decrease gas production after storage at high temperature^{9, 12, 13}
- impede surface transformations from layered to rock salt structure in NMC 622¹⁴ and
- improve capacity retention after at least 100 cycles at 1C, C/2, C/3 and 2C; in half cell or pouch cells with upper cut-off voltages as high as 4.5 V vs. Li/Li^+ ^{3, 7-11, 15}.

Usually, the improved electrochemical performances when LDFP is added is ascribed to the formation of a solid electrolyte interphase (SEI) or a cathode electrolyte interphase (CEI). However, there are contradictory opinions about the mechanism. Through theoretical calculations or experiments, some authors⁶ propose that it gets reduced⁶, oxidized^{3, 8} and others, that it simply precipitates onto the electrode material^{2, 6, 11, 15}. Unfortunately, none of these reports present a mechanism and simply assume that the reduction or oxidation would form an

efficient SEI or CEI. Among those who propose that no redox reaction occurs, Yang et al.², explain the precipitation of LDFP into the SEI and CEI through a migration mechanism, where LDFP is the lithium carrier (Fig. V.2). During charge, $\text{Li}_x\text{PO}_2\text{F}_2$ ($x = 3$) would reach the negative electrode by potential difference and deposit, while the supplementary lithium ions would intercalate. Inversely, during discharge, $\text{Li}_x\text{PO}_2\text{F}_2$ ($x = 3$) would migrate to the positive electrode, deposit, and the additional Li^+ intercalate. The fact that PO_2F_2^- and Li^+ ions associate into ion-triplets in the electrolyte, due to the low dissociation of LiPO_2F_2 in alkyl carbonate solvents¹⁶, it is **less likely** that they deposit reversibly on both electrodes.

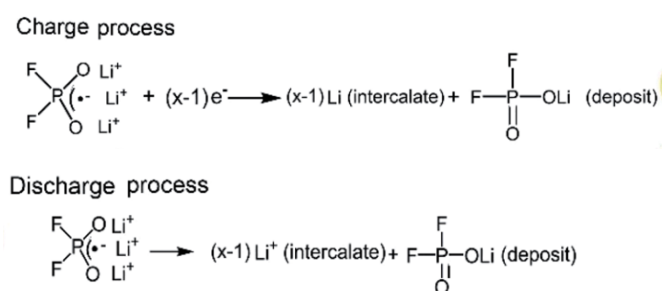
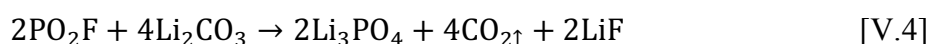
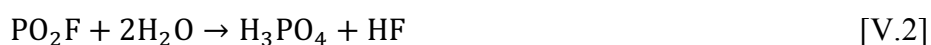


Figure V.2. LDFP precipitation mechanism from Yang et al.².

In 2019, two other hypotheses were postulated. Qian et al.¹⁵, suspected that LDFP prevents electrolyte ageing through the trapping of the initiators of carboxylate species formation, such as 2,5-dioxahexane dicarboxylate (DEDOHC or compound 1₁). Although the GC/MS results are remarkable, no reactions were shown to support this hypothesis, so the mechanism remains unclear. On the other hand, Zhao et al.¹⁶ explained that LDFP forms a CEI that supposedly inhibit to some extent the decomposition of LiPF_6 , prevents cation dissolution, HF formation and contribute to decrease electrolyte oxidation due to the presence of phosphate ions (PO_4^{3-}), as observed by XPS. To explain the presence of PO_4^{3-} , they proposed the formation of Li_3PO_4 through the “self-decomposition” of LDFP into LiF and PO_2F (Eq. V.1), followed by PO_2F reaction with traces of H_2O in the electrolyte then H^+/Li^+ exchange (Eq. V.2, 3) or with Li_2CO_3 from the SEI (Eq. V.4). Additionally, they attributed an oxidation peak around 3.1 V vs. Li/Li^+ to the oxidation of PO_2F into PO_2^+ and F_2 (Eq. V.5). These reactions are highly debatable, since F_2 is not likely to be produced through equation V.5.





None of the three described hypotheses present a concrete and sufficiently grounded explanation to what occurs to the electrolyte or the interfaces when LDFP is used. Even though the last seems very complete, it is based solely on the presumed observation of PO₄³⁻.

In light of the previous information, there is room for better understanding of the LDFP's action mechanism that has not been reported before. In this chapter, in a first instance, the properties of the electrolyte containing LDFP were evaluated. Then, the cycling performance at 25 and 55°C is compared for NMC 811 and at 55°C for 622C, all in full cells. Given the surprising contradictory results, a following section is devoted to the analysis of the solid, liquid and gaseous electrolyte degradation products after prolonged cycling at 55°C in the hope of providing tangible explanations.

2. Impact of LiPO₂F₂ on the electrolyte properties

This section studies the electrochemical stability, viscosity and ionic conductivity changes when LDFP is added. LDFP was used with a concentration of 0.2M (1.92 wt.%) in the base electrolyte (1M LiPF₆ in EC/DEC/EMC 1:1:1 vol.). As the PO₂F₂⁻ ionic volume is lower than that of PF₆⁻ (538.1 and 625.5 Bohr³ ¹⁶, respectively) and the dissolution energy calculated by density functional theory (DFT) is larger (-5.790 eV for LDFP and -6.254 eV for LiPF₆), LDFP is less soluble in the alkyl carbonate solvents, so it can be used as additive not exceeding 2 wt.% ^{11, 16}.

Cyclic voltammetry (CV) at a scan rate of 30 mV.s⁻¹ was performed on the base and base + 0.2M LDFP electrolytes (Fig. V.3) using platinum as working (disc d=3 mm) and counter electrodes, and Li as reference electrode. From the first oxidative scan (anodic scan) from 0 to 6 V, it can be appreciated that the electrolyte's stability was not modified by the presence of LDFP and the absence of additional peaks means that LDFP does not reduce or oxidize up to 6 V. In spite of the very low measured current, normally, signals around ~0.3–0.35 V and ~0.65–0.7 V corresponding to lithium alloy formation are obtained on a platinum electrode upon the anodic scan, whereas upon the cathodic scan, a signal around ~0.55–0.6 V is assigned to bulk lithium dissolution and two peaks around ~0.95-1.0 V and ~1.3 V are related to stripping of lithium from the alloy. The reduction of trace water would take place around ~1.5 V ¹⁷. In reality, in the cathodic scan from 6 to 0 V, a pronounced wave between 3–1.8 V is observed. According to Gnanaraj et al. ¹⁷, it corresponds to the electrochemical reduction of some of the insoluble surface species (such as Pt-X) that passivate the electrode, formed during the anodic scan. The slightly differences around 2.7 V might be due to a different construction of the SEI or an eventual impurity in the electrolyte rather than a process related to the additive. Although not shown here, the second cycle does not show this cathodic wave since the electrode is already passivated.

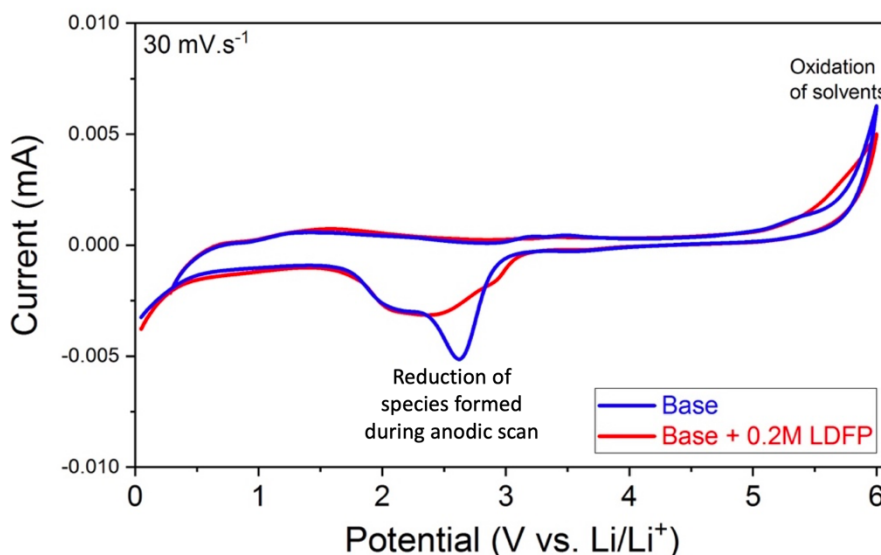


Figure V.3. Cyclic voltammetry of both electrolytes on a Pt working electrode, Pt counter electrode and Li reference at 30 mV.s⁻¹.

In the literature, Kim et al.⁶ reported the reduction of LDFP around 0.6 V vs. Li/Li⁺ through dQ/dV analysis of the first cycle of graphite/Li cells. After careful analysis, we deduced that this peak corresponds only to the solvent's reduction, shifted to higher potentials upon LDFP addition. Regarding the oxidation of LDFP, Chen et al.³ calculated through DFT that the oxidation of LDFP would occur around 5.9 V, before the calculated oxidation of EC at 6.97 V or EMC at 6.78 V⁸. However, experimentally, they explained that LDFP is oxidized below 4.5 V, supported only by the observation of a CEI layer by TEM, formed principally of $\text{Li}_x\text{PF}_y\text{O}_z$ species, as detected by XPS.

To summarize, from these reports, no ground proof of LDFP's reduction or oxidation can be obtained. For the following experiments in this chapter, it is considered that, based on the CV experiments, LDFP is not electrochemically active in the potential window of NMC materials.

Afterwards, the ionic conductivity and viscosity of the electrolyte were investigated (experimental conditions can be found in Annex IV). The ionic conductivity was measured in the liquid form between two platinum electrodes (liquid measurement) and inside a porous polypropylene commercial separator (Celgard 2500 measurement) sandwiched between two copper electrodes. In addition to the base and the base + 0.2M LDFP electrolytes, an electrolyte containing 0.8M LiPF_6 + 0.2M LDFP (in the same solvents mixture) was also tested. This mixture was used with the objective to keep the molar concentration of the salt at

1M, since the maximum ionic conductivity of LiPF_6 in alkyl carbonate solvents is obtained at this concentration¹⁸. The results are shown in Fig. V.4.

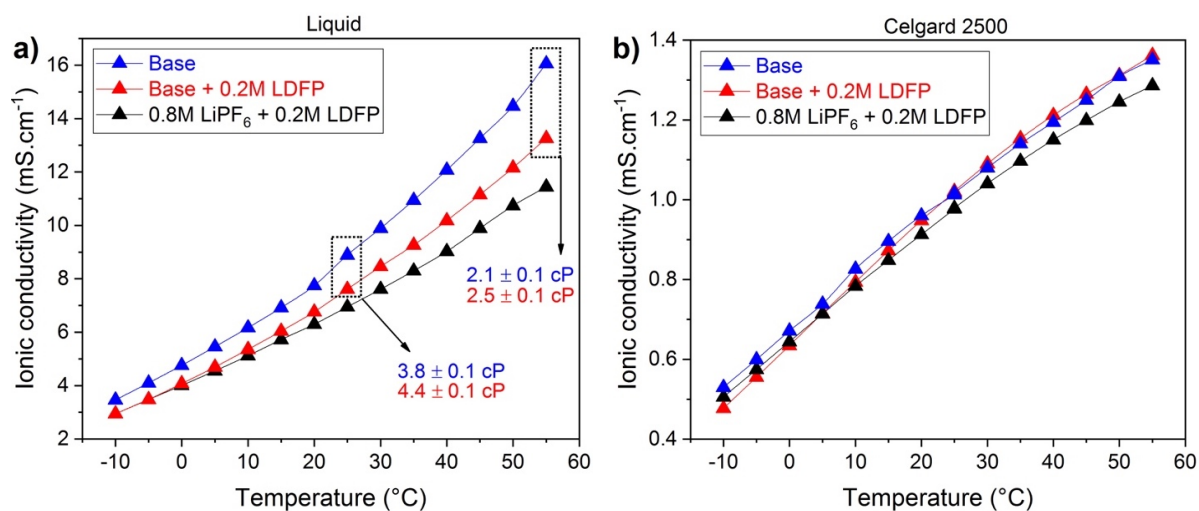


Figure V.4. Ionic conductivity measurements performed in **a)** liquid and **b)** Celgard 2500 separator. Inset values in **a)** correspond to viscosity measurements.

In the liquid measurement, the conductivity of the base electrolyte was found to decrease by ca. 14% and 17% at 25°C and 55°C respectively upon the addition of 0.2M LDFP. In this regard, two similar trends have been recently published with different alkyl carbonate mixtures: Wang et al.¹¹ found that at 25°C, the original ionic conductivity of 6.34 mS.cm⁻¹ decreased by 9.4% with the addition of 2 wt.% of LDFP (base: 1M LiPF_6 in EC/DEC 1:3 wt.%). Meanwhile, Zhao et al.¹⁶ found a decrease from 7.31 to 6.72 mS.cm⁻¹ (-8%) with the addition of 1 wt.% of LDFP (base: 1M LiPF_6 in EC/DMC 1:1 vol.), measured at room temperature.

The decrease in ionic conductivity is in line with the increase of viscosity from 3.8 to 4.4 cP at 25°C and from 2.1 to 2.5 cP at 55°C (insets on Fig. V.4a). At the same time, it is suspected the formation of ion-pairs of LDFP, instead of a complete dissociation like with LiPF_6 . Concerning the 0.8M LiPF_6 + 0.2M LDFP electrolyte, it was projected to be less deleterious to replace part of LiPF_6 than exceed 1M concentration. In reality, among the three electrolytes in the liquid configuration, this electrolyte exhibits the lower ionic conductivity, especially at high temperatures. Contrarily, Liu et al.¹⁹ reported that an electrolyte 1M LiPF_6 in EC/DEC/EMC 1:1:1 wt.% shows ionic conductivity of 10 mS.cm⁻¹, while an electrolyte with 0.8M LiPF_6 and 0.2M LDFP displays a higher conductivity of 11.6 mS.cm⁻¹ (16% more).

Within the Celgard 2500 separator, the ionic conductivity of the three electrolytes is divided almost by 10, due to tortuosity and the restricted ion transport through pores (Fig. V.4b)²⁰, and the differences when LDFP is added are very small. As in liquid configuration, the 0.8M LiPF_6 + 0.2M LDFP presents slightly lower values at temperatures higher than ca. 10°C and thus will be discarded in the following experiments.

The differences in ionic conductivity of electrolyte with and without 0.2M LDFP are so small, that no real impact on the electrochemical performances is expected upon following NMC/Graphite(Gr) pouch cells cycling at C/4.

3. Impact of LiPO₂F₂ on the electrochemical performance of NMC 622C and 811

Previous works that studied the cycling performance of cells containing LDFP have reported the use of 0.5 – 3 wt.% of LDFP in LiPF₆-based electrolytes. The general idea is that LDFP **always** improves the capacity retention. For instance, after 100 cycles at 1C, LDFP addition improved the capacity retention of pouch cells NMC 111/Gr (4.5 V)¹¹, NMC 532/Gr (4.53 and 4.5 V)^{8, 10}, as well as of half-cell NMC 111/Li (4.4 V)³. In the same manner, after 100 cycles at C/2 and C/3 and up to 4.2 V and 4.3 V, pouch cells NMC 111/Gr⁵ and NMC 532(single crystal)/Gr⁹ improved greatly their capacity retention at room temperature. At lower temperature (0°C and -20°C) and C/2, better capacity retention has been reported in NMC 532/Gr⁷. Nonetheless, upon temperature increase, the capacity retention of NMC 532/Gr pouch cell was not improved at 45°C and C/2¹⁵ or was slightly improved in NMC 532(single crystal)/Gr pouch cells at 40°C and C/3⁹, both with cut-off voltages of 4.2 and 4.3 V.

In short, with 0.5 – 3 wt.% of LDFP electrolyte additive, improved performances of relatively low Ni content NMCs-containing cells can be achieved from -20 to 40°C. Note that this additive did not show any improvement at a higher temperature of 45°C in full cells.

With the aim of gaining further insight into the understanding of the impact of this additive in Ni-rich cathode cells, this section compares the electrochemical performance of NMC 622C/Gr and NMC 811/Gr pouch cells cycled at 25 and 55°C, and at C/4 (considering total delithiation, although the maximum for 622C is Li_{0.4}Ni_{0.6}Mn_{0.2}Co_{0.2}O₂ and for 811 is Li_{0.3}Ni_{0.8}Mn_{0.1}Co_{0.1}O₂). Note that due to the nature of the laboratory-made electrodes (little reproducibility given by the absence of calendaring in NMC 811 and loading differences from a film to another), a reference cycling with base electrolyte was performed for each set of cells.

3.1. NMC 811 as positive electrode

3.1.1. Cycling performance of pouch cells NMC 811/Graphite at 25 and 55°C

The preparation of the pouch cells follows the procedure described in [Chapter III](#), using non-calendered NMC 811 electrodes, due to the sensibility to air during the calendaring process.

The electrolytes employed were base and base + 0.2M LDFP and the cycling performance was evaluated at 25°C and 55°C and C/4 between 2.8–4.3 V vs. Li/Li^+ . All cycling tests were reproduced 3 times. The results are shown in Fig. V.5.

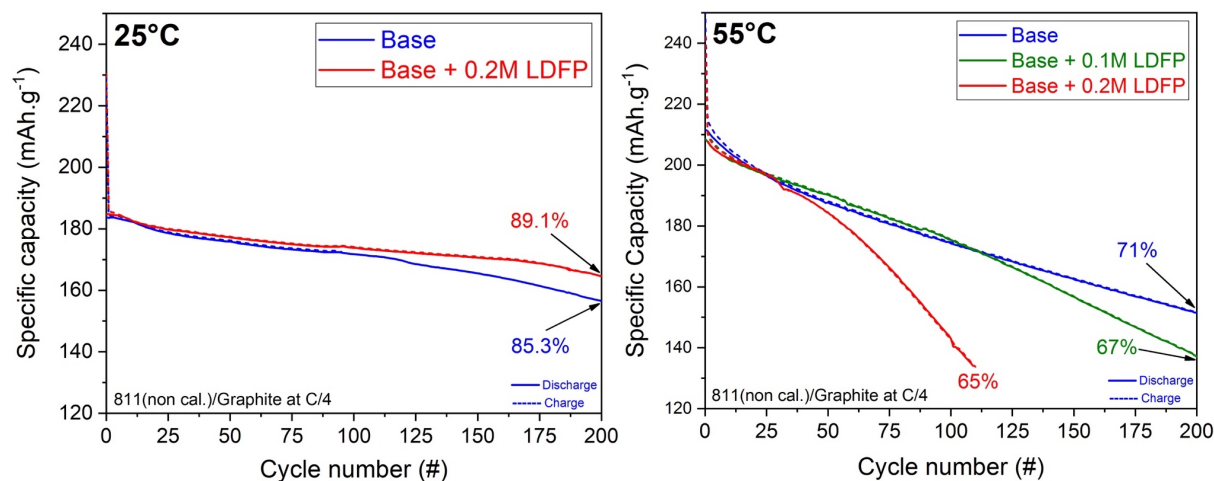


Figure V.5. Electrochemical performances of representative pouch cells of NMC 811(non-calendered)/Gr cycled between 2.8 – 4.3 V at C/4 and at a) 25 and b) 55°C without and with LDFP.

Before comparing the role of the additive, it can be noticed that the initial discharge capacity when cycling at 55°C is 12% bigger than at 25°C: $\sim 210 \text{ mAh.g}^{-1}$ compared to $\sim 185 \text{ mAh.g}^{-1}$. This gain is due to the limited kinetics of lithium intercalation on layered materials at ambient temperature. To compare, Jalkanen et al.²¹ and Zhou et al.²² reported separately ca. 6% of initial capacity gain by only increasing the temperature from RT to 45°C. The first used NMC 111/Gr full cells and the second NMC 811/Li half cells.

However, it is known that the ageing processes on Ni-rich NMC materials, such as structural changes, are accelerated at high temperature as well²³, thus affecting capacity retention. It is especially true for the cells using base electrolyte, since they keep only ca. 70% of the original capacity after 200 cycles, compared to ca. 90% at 25°C.

Surprisingly, the impact of LDFP on cycling performances of NMC 811(non-calendered)/Gr pouch cells is significantly different at 25 and 55°C. At 25°C, the cells containing LDFP display improved capacity retention after 200 cycles (about 85 and 90%, without and with LDFP, respectively). This result is in good agreement with the literature, in regard to the positive contribution of LDFP to capacity retention in full cells containing NMC with “low” nickel content (111^{11, 12} and 532⁸⁻¹⁰).

On the contrary, at 55°C , similar cells containing 0.2M LDFP show a poor capacity retention of ca. 65% after only 110 cycles, although behaving similarly up to 30 cycles. Experiencing a lower concentration of 0.1M LDFP (0.96 wt.%) at this high temperature results in delaying the negative effect. Indeed, performances are even slightly improved up to 110 cycles, and then the capacity falls down, retaining only 67% of the original capacity after 200 cycles.

To investigate the source of the capacity fade when LDFP is used at 55°C , the differential capacity versus voltage profiles were plotted (Fig. V.6). On the first cycle in presence of LDFP, the peak corresponding to the reduction of solvents appears always lower in intensity than the base electrolyte. This possibly means that less solvents were reduced, signifying a differently formed SEI. Further characterizations of electrolyte degradation products are portrayed in the following sections.

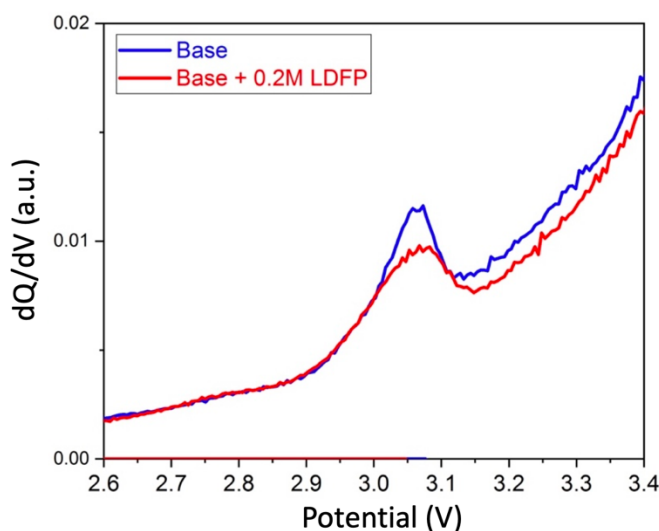


Figure V.6. Representative derivative dQ/dV curves of the first cycle, evidencing SEI formation differences **without** or **with LDFP**.

Moreover, the 2nd, 50th, 100th and 200th cycle for each pouch cell are plotted in Fig. V.7a-d.

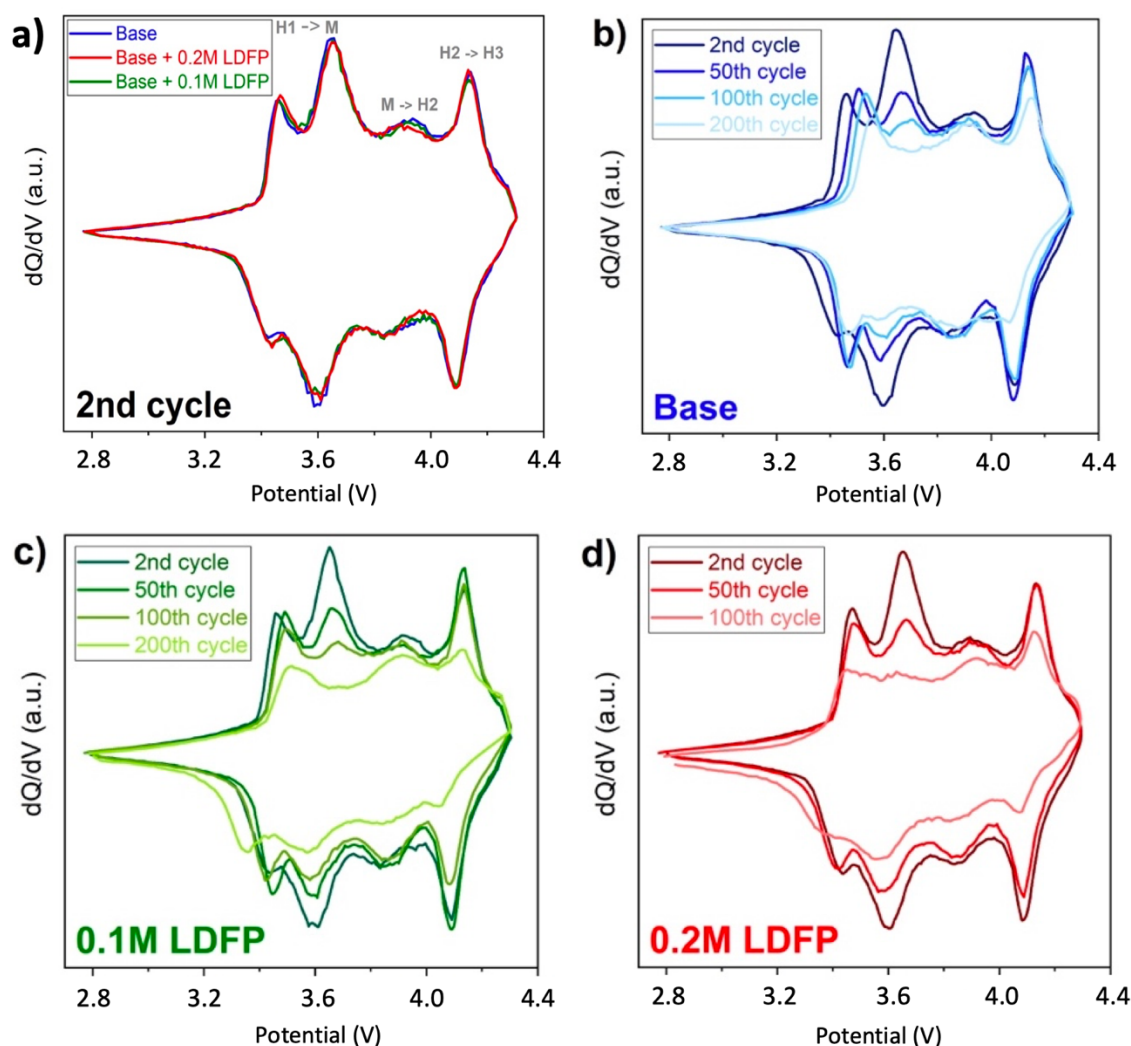


Figure V.7. Differential capacity vs. voltage profiles of pouch cells 811/Gr. **a)** Initial state of the three cells and **b, c, d)** each cell with each electrolyte, separately.

Initially the three cells present the same derivative profile (Fig. V.7a), that represents mostly the derivative NMC profile described in [Chapter III](#), shifted to lower potentials than in half-cell due to the contribution of graphite that does not represent any new peak. As the cycling proceeds, there is a remarkable evolution of the profiles. There are three main observations:

- With the increasing of cycles, all of the peaks decrease in intensity, being the most affected 0.2M LDFP. This means that part of active material is gradually electronically isolated or structurally/chemically damaged. If transition metal dissolution had occurred, metal cations would have migrated, reduced and deposited on the negative electrode. However, through several post-mortem SEM-EDS elemental analyses carried out on the surface of graphite electrodes coming from pouch cells 622C/Gr and 811/Gr cycled with or without LDFP, it was not possible to conclude about a link between the presence of LDFP or the NMC composition and the capacity fade.

- Upon charge of the base electrolyte cell, the first peak centered at 3.45 V shifts continuously to the right, implying that the interfaces are evolving, thus increasing cell polarization. When 0.1M LDFP is added, the shift is less pronounced and it almost disappeared with 0.2M LDFP. This means that LDFP helps reduce the polarization growth either at the positive or the negative electrode. Note that a change in the differential capacity vs. voltage profile (Fig. V.6) pertaining to the SEI formation was observed, suggesting a likely thinner and less resistive SEI.
- Whatever the composition of the electrolyte, the peak centered at 3.65 V (part of H1 → M) decreases its intensity until, at 200 cycles, it has completely disappeared. This has been attributed to the loss of available lithium sites, related to the gradual nickel migration to the lithium layer upon prolonged cycling²⁴.

At this point, the capacity fade of the NMC 811/Gr cells cycled with LDFP at 55°C cannot be unquestionably attributed to one of the electrodes. However, it is supposed that one or both interfaces are modified by the presence of LDFP, limiting cell polarization and that some active materials are isolated.

3.1.2. Impact of the calendaring process

The absence of calendaring can be a source of capacity fade due to increased electrode polarization²², no more percolating particles... Hence, a method to calender air-sensitive films in the dry room was adapted to assess its impact on cells capacity retention. It consists in the implementation of a “portable” laminating machine that uses a gas source to generate pressure between two plates. Then, the film to be calendered is positioned between two brass laminates and introduced between the two plates. After several essays, a compromise was found between the achievable pressure, which was set at 56 psi, and the heating temperature, high enough to calender the material but low enough to avoid polymer melting. This temperature was set at 190°C, although the temperature in contact with the film was obviously lower since PVDF ($160 < T_m < 177^\circ\text{C}$ depending on crystallization state) does not seem to have melted on SEM pictures (Fig. V.8c and d). The calculated initial porosity of the film was 49% and the target porosity 35%. However, the maximum that could be achieved with this dry room setup was 40%. Fig. V.8a–d shows representative SEM pictures of the NMC 811 electrodes before and after calendaring.

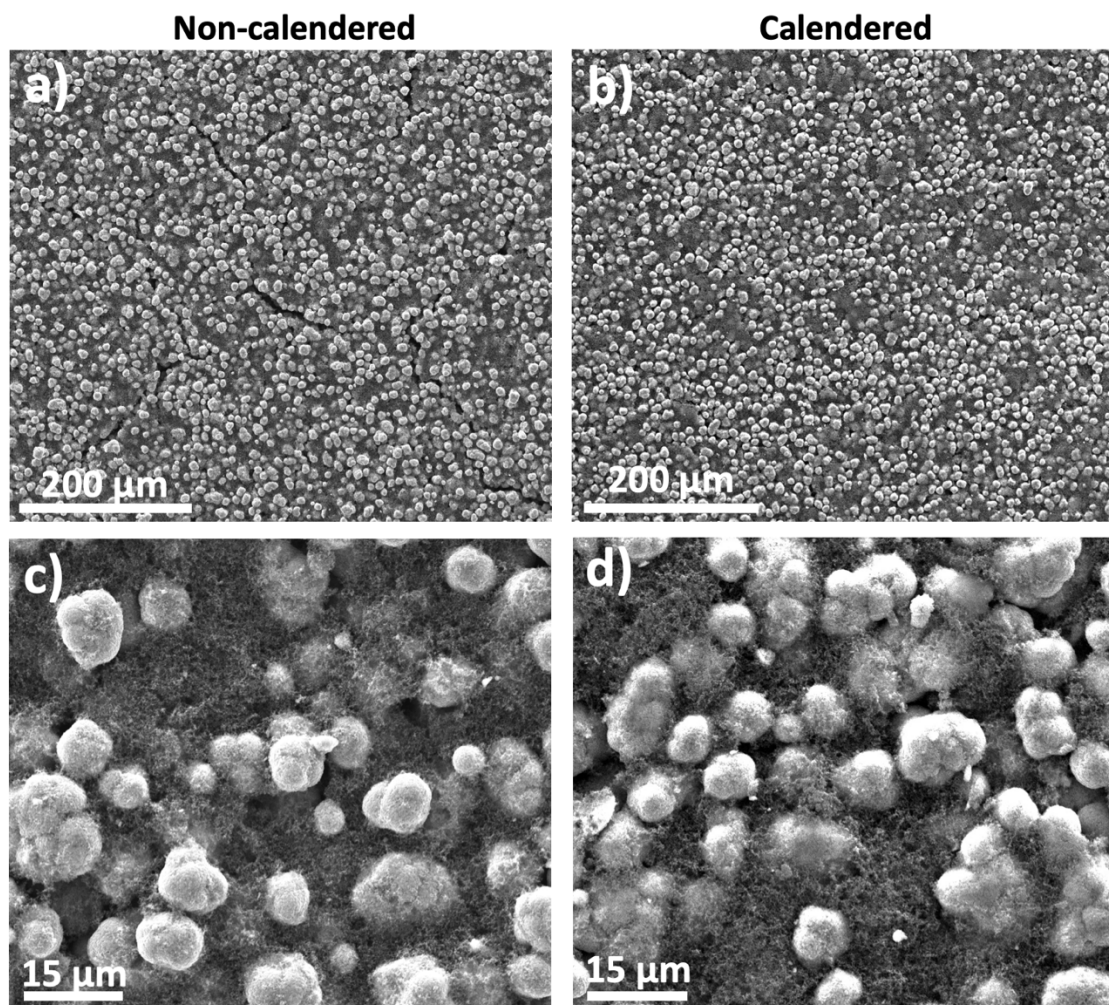


Figure V.8. Representative SEM pictures of the NMC 811 film **a)** before (49% porosity) and **b)** after calendering (40% porosity).

On the initial film, the SEM picture (Fig. V.8a) displays noticeable fissures which are no longer visible after calendering (Fig. V.8b). No other significant change was noticed at higher magnification (Figs. V.8c,d).

The cycling performance of those calendered films was evaluated in pouch cells with and without 0.2M LDFP, at 55°C (Fig. V.9), under similar cycling conditions.

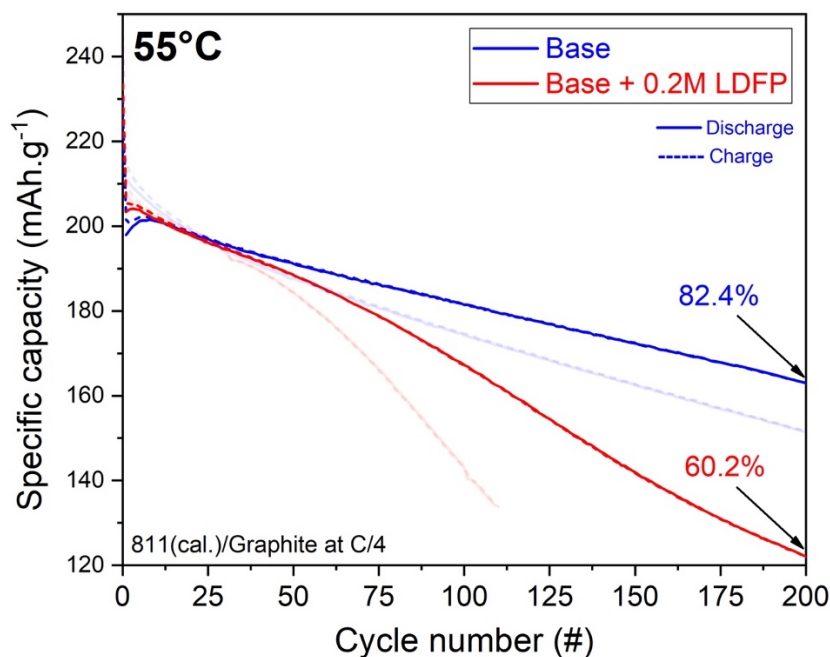


Figure V.9. Representative pouch cells of 811(cal.)/Gr cycled between 2.8–4.3 V at C/4 and at 55°C **without** or **with 0.2M LDFP**. Shown for comparison, watermark curves correspond to the cycling with non-calendered films.

The calendering process improves all the cells' capacity retention; from 71% to 82.4% with base electrolyte after 200 cycles (blue curves) and more significantly, from 65% to 78% after 110 cycles with 0.2M LDFP. The capacity improvement is likely due to enhanced electronic percolation through the electrode thanks to the elimination of the fissures and particles rapprochement. Nevertheless, this mechanical process does not allow for the entire recovery of the capacity; the negative impact of LDFP on the NMC 811/Gr cells capacity retention at 55°C is only stunted.

3.1.3. Post-mortem analyses

The pouch cells NMC 811(cal.)/Gr were disassembled, at the discharged state, after 200 cycles at 55°C. SEM and electrochemical characterizations of each electrode were performed with the aim of determining the origin of the capacity retention fade in presence of LDFP. Prior to use, electrodes were washed three times with dimethyl carbonate and let dry for one hour under vacuum. It is possible that throughout the washing procedure some of the products deposited on the interfaces have been washed away. The electrodes were cut in the form of discs to be cycled in Swagelok-type cell versus lithium, at C/10 and 25°C, with base electrolyte soaking the glass fiber separator.

For comparison, Fig. V.10a and b show the potential vs. specific capacity profiles of the recovered and fresh electrodes. Cycling at 55°C with LDFP provoked capacity loss on both electrodes. In particular, the NMC 811 electrode lost 40% of its original discharge capacity, compared to only 6% of the cell with base electrolyte (Fig. V.10b). Meanwhile, the graphite electrode that cycled with base electrolyte kept almost all of the original capacity, only 2% was lost, and 7% when LDFP was used (Fig. V.10a). This clearly identifies the positive electrode as the main source of the capacity fade at 55°C. However, at this point, it is not possible to know the origin of the capacity fade (structural or chemical).

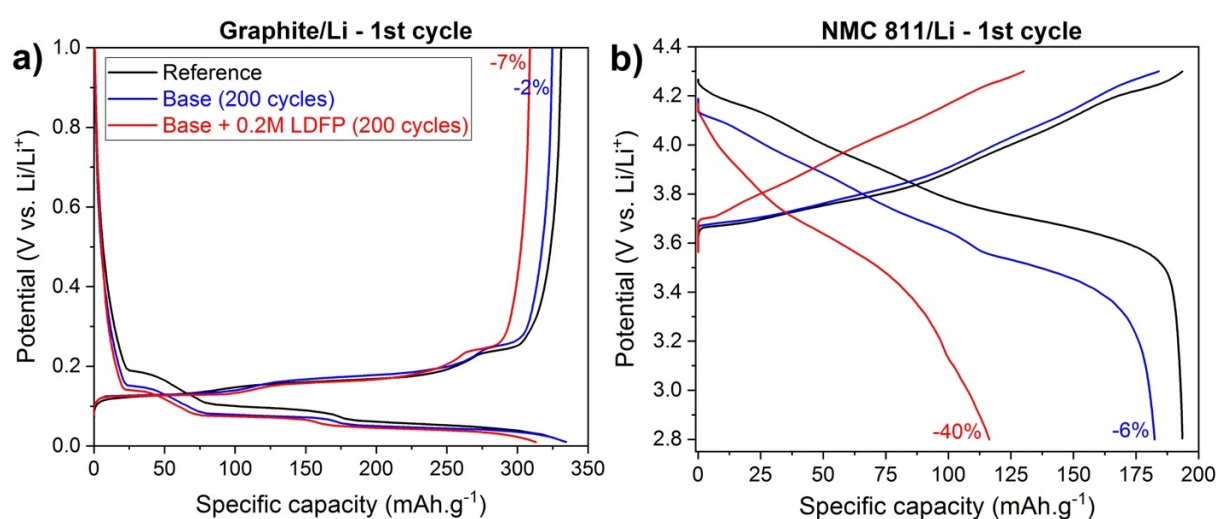


Figure V.10. Re-cycling at 25°C and C/10 of the washed **a)** graphite electrode between 1.5–0.01 V; and **b)** NMC 811(cal.) electrode between 2.8 – 4.3 V vs. Li/Li⁺.

Part of the washed NMC 811 electrode was analyzed by SEM (Fig. V.11a–f), from which several irregularities are evidenced, especially when LDFP is used: some primary particles are broken and agglomerates are detached, highlighting their polycrystalline texture with a ca. 3µm thick shell and a porous core with sometimes less compacted grains inside.

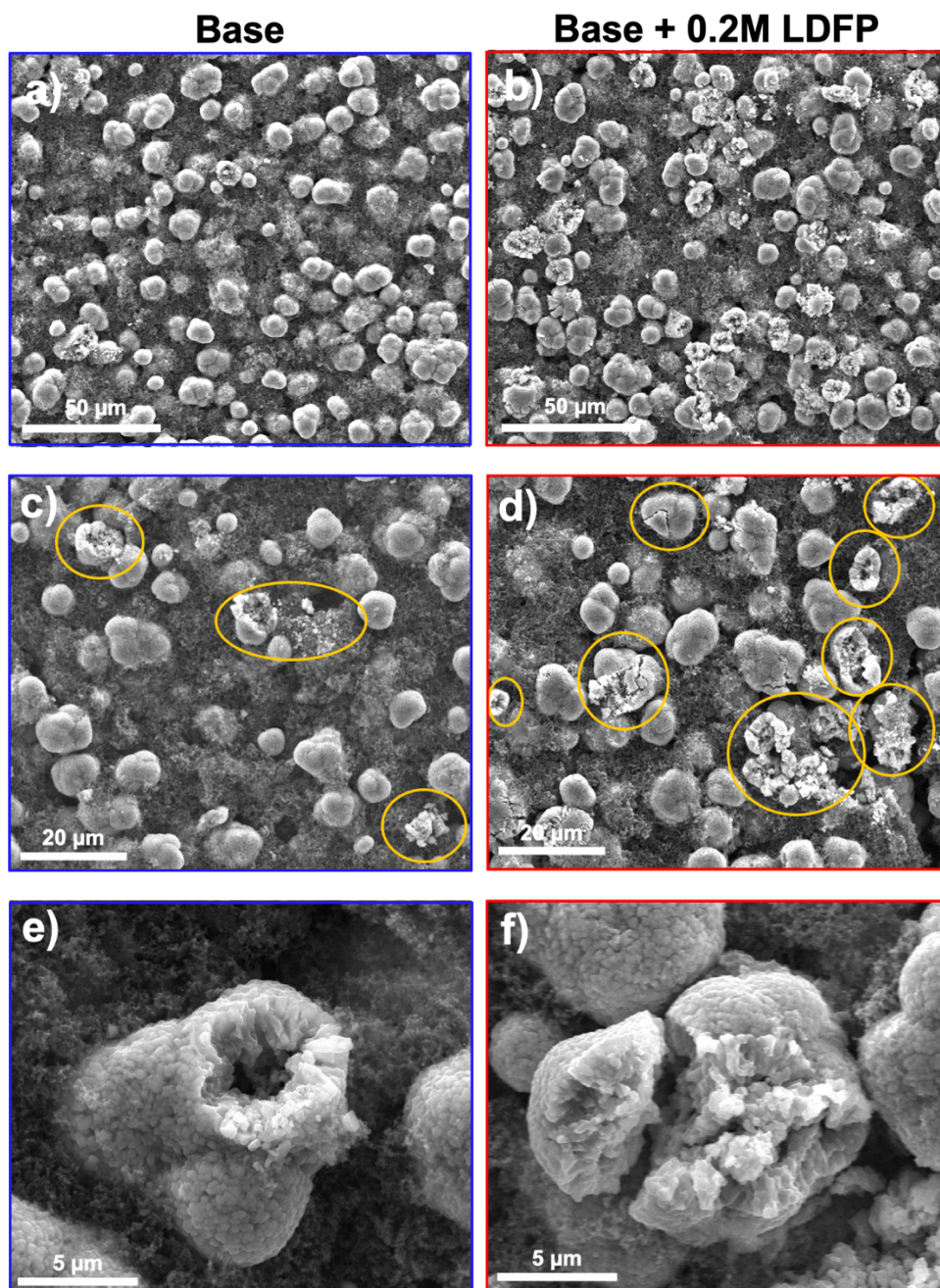


Figure V.11. Representative SEM pictures at different magnifications of the washed NMC 811(cal.) electrodes after cycling with base (blue frame) and base + 0.2M LDFP electrolytes (red frame).

It is known that the stress and strain generated on the particles due to the rapid volume contraction of the c -axis during structural transformation from H2 to H3 during delithiation is one of the origins of particle cracking^{25, 26} and capacity fading²⁷. Since the mechanical failure seems exacerbated in presence of LDFP after cycling at high temperature, in order to understand the role of this additive, the electrochemical performances of NMC 622C films were compared under similar cycling conditions.

3.2. NMC 622C as positive electrode

3.2.1. Cycling performance of pouch cells NMC 622C/Graphite at 55°C

The representative electrochemical performances of 622C(calendered)/Gr pouch cells cycled at C/4 and 55°C, with and without 0.2M LDFP, are shown in Fig. V.12. The NMC 622C films were calendered under air to 35% of porosity.

Unlike the precedent results obtained with NMC 811, the graph clearly shows that NMC 622C-containing pouch cells exhibit, after 200 cycles, enhanced capacity retention: ca. 83% with 0.2M LDFP, compared to ca. 80 % without LDFP.

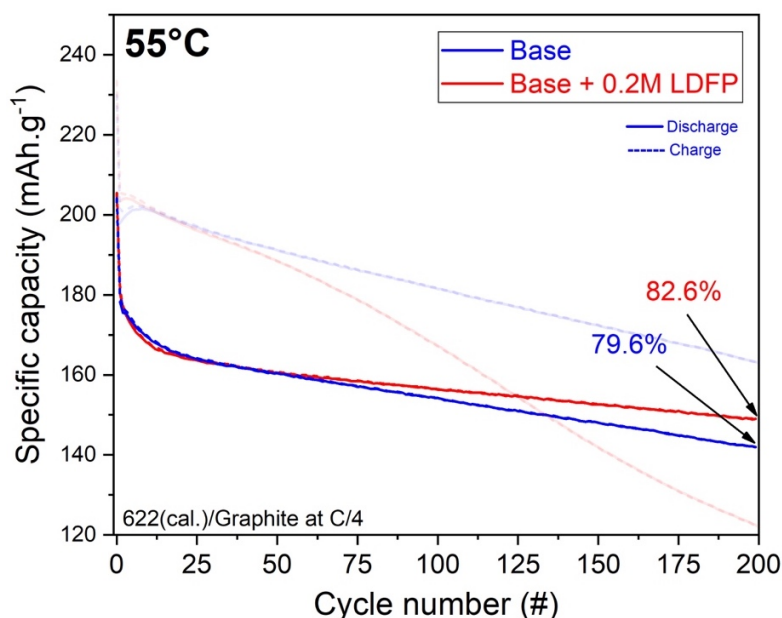


Figure V.12. Representative pouch cells of 622C(cal.)/Gr cycled between 2.8 – 4.3 V at C/4 and at 55°C **without** or **with 0.2M LDFP**. Shown for comparison, watermark curves correspond to the cycling 811(cal.)/Gr.

3.2.2. Post-mortem SEM analysis

After 200 cycles at 55°C, almost all the NMC 622C particles remains intact at the surface of the electrodes whatever the electrolyte composition, with or without LDFP (Fig. V.13). Noh et al.²⁸ demonstrated lower lattice parameters (a and c) and less volume change for NMC 622 after 100 cycles at 25°C, up to 4.3V than for NMC 811, which may explain why the particles did not crack. The presence of LDFP additive does not lead to particles cracking either, thus leaving us with a mystery surrounding its harmful impact regarding NMC 811 cycled at 55°C.

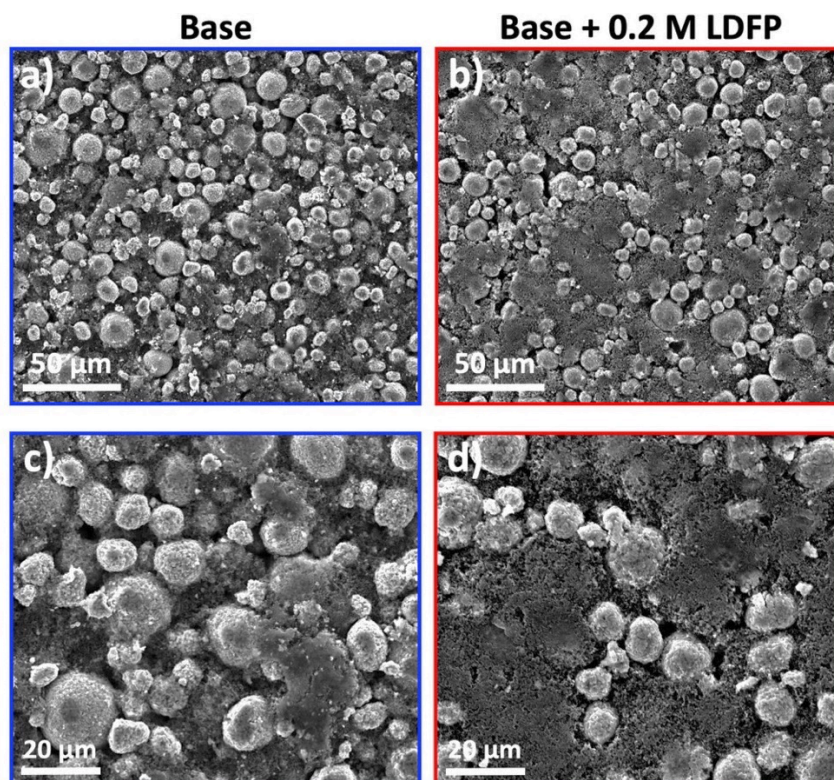


Figure V.13. Representative SEM pictures at different magnifications of the washed NMC 622C(cal.) electrodes after cycling with **base electrolyte** and **base + 0.2M LDFP**.

Similar trends have been revealed in a very recent work²⁹ comparing the electrochemical performances of NMC 622 and 811 of polycrystalline structure, in presence of a VC-containing base electrolyte with or without trimethylsilyl(TMS)-based additives known as HF scavengers. They found that upon cycling at 1C and 25°C, the capacity retention of full cell 811/Gr decreases faster when TMS-based additive is used, compared to NMC 622/Gr. In this study, the harmful effect of the additive on the retention capacity of NMC 811-containing cells was supposed to be the result of chemical reactions of additives with surface species LiOH and PF_5 , leaving aggressive HF and resistive byproducts between micro grains. This was more pronounced in NMC 811 as it contained 2.5 times more LiOH than NMC 622 (quantified through titration and TOF-SIMS techniques). It is worth noting here the indirect role of surface species on cells performances by countering the effect of an additive.

The beneficial impact of electrolyte additives on cycling performances is generally due to specific chemical or electrochemical attributes. Hence, similarly to the here-above reported chemical study ([Chapter III](#)), we proceeded with the study of electrolyte degradation products that could trace back to the origin of the intriguing electrochemical behavior of NMC 811-containing cells cycled with 0.2M LDFP at 55°C.

4. Study of the electrolyte degradation products: impact of LiPO₂F₂

A wide array of techniques was deployed to analyze a majority of degradation components in solid, liquid and gaseous state. Firstly, the study of the SEI and CEI composition at the surface of the graphite and NMC 811 materials, respectively, was undertaken by means of the FTIR technique. Secondly, the electrolyte degradation products were investigated through mass spectrometry techniques (GC/MS and ESI-HRMS) and finally, the gases were studied through GC/BID or GC/MS techniques.

4.1. Study of interphases composition

4.1.1. Study of SEI composition

The SEI layers formed at the surface of graphite composite powders (graphite and C45 9:1 mass ratio) after one cycle in a Swagelok-type half-cell, between 1.5 - 0.01 V, at C/20, were characterized by means of FTIR in transmission mode (experimental details can be found in **Annex IV**).

As shown on the incremental capacity curves (Fig. V.14), the electrochemical reduction of the alkyl carbonate solvents (mostly EC³⁰) takes place around 0.7–0.9 V vs. Li/Li⁺ at 25 and 55°C respectively. Note that, at 25°C, this potential is slightly shifted toward a higher value (ca. +50 mV) in presence of 0.2M LDFP. Strangely, the lower intensity depicted in the derivative curves obtained from NMC 811/Gr full cells cycled in presence of LDFP at 55°C (Fig. V.6 in Section 3.1.1.) is not observed. It can be hypothesized a contribution of CMC, acting as a passivation layer, and which could react with LDFP through a nucleophilic substitution reaction according to Eq. V.6, and thus, endow the SEI with enhanced passivation properties. Such assumption would deserve further detailed investigation. It is noteworthy that similar bonding between CMC and Si already proved efficient in achieving improved capacity retention upon lithiation/delithiation of silicon-based negative electrodes³¹.



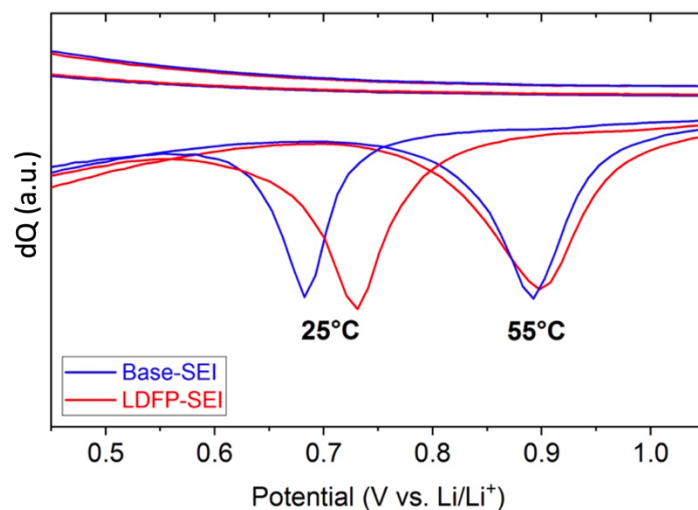


Figure V.14. Incremental capacity curves of the SEI formation during the first lithiation of graphite composite powder, in half-cell configuration.

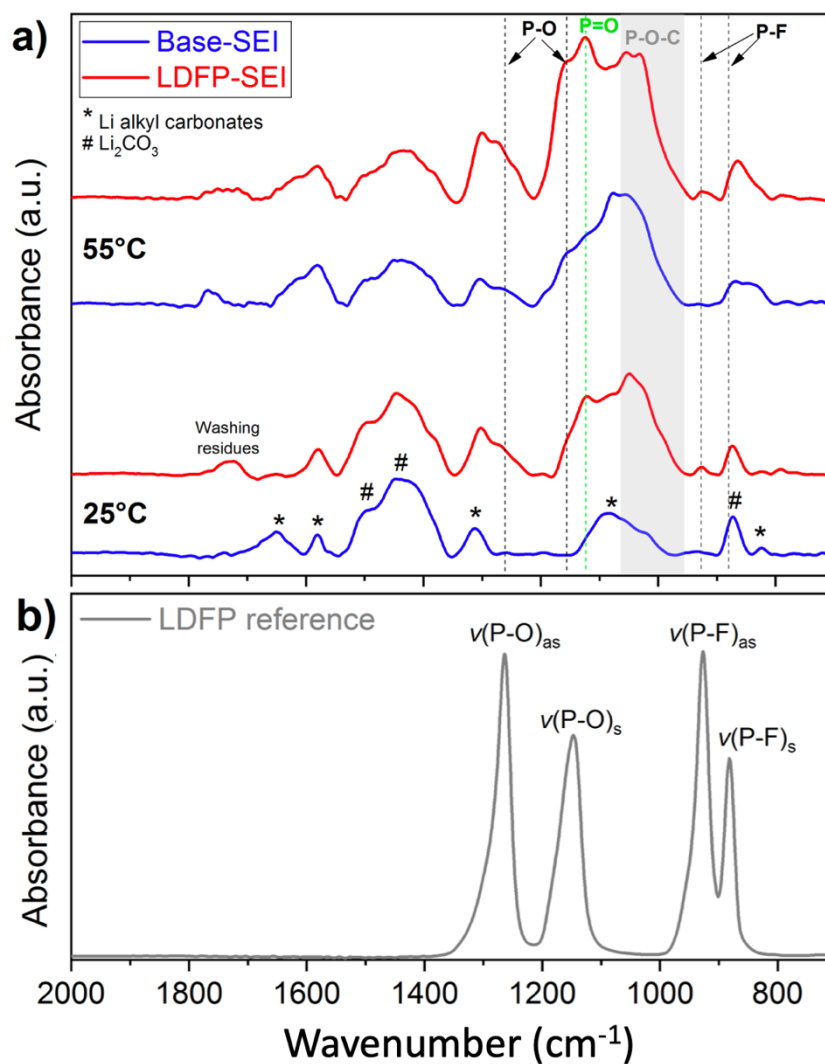
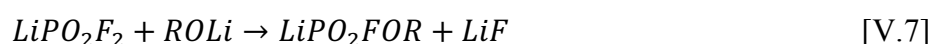


Figure V.15. FTIR analyses of a) the SEI formed on graphite composite powders at 25°C and 55°C without/with LDFP and b) LDFP reference.

From FTIR spectra (Fig. V.15a), it is noticeable that the composition of the SEI is not so much influenced by the presence of LDFP electrolyte additive. Indeed, at 25 and 55°C, the bands observed in the SEI formed from the base electrolyte (called base-SEI) are also present in the SEI formed from the LDFP-containing electrolyte (called LDFP-SEI). Marked with stars and hash characters in the figure, they are assigned to the reduction products of alkyl carbonates solvents, ROCO₂Li and Li₂CO₃³², respectively. This result is in good agreement with the SEI-related incremental capacity curves, from which conclusion can be drawn that LDFP does not hinder solvents reduction at the surface of a graphite composite powder. As hereabove discussed, this would be a little bit different with graphite composite surrounded with CMC binder.

However, supplementary bands or more pronounced shoulders appear in the LDFP-SEIs, at both temperatures, in the 900-1300 cm⁻¹ range, typical of the absorption range of phosphate- or fluorophosphate-type compounds with P–O, P–O–C and P–F bonds. The reference LDFP powder displays four bands in this region (Fig. V.15b)^{33,34}; the two bands at 885 and 930 cm⁻¹ correspond to P–F symmetric and asymmetric stretching vibrations, whereas the two other bands at 1150 and 1270 cm⁻¹ originate from P–O asymmetric and symmetric stretching vibrations. As a peak at 930 cm⁻¹ of low intensity is depicted in all the LDFP-SEI spectra, it could be suggested that a small amount of LDFP is precipitated and trapped in the SEI, or that other species phosphate-containing exist, such as Li₂PO₃F, less soluble than LiPO₂P₂.

The set of at least two broad peaks between 960 – 1070 cm⁻¹ that, according to Becker et al.³⁵, corresponds to P–O–C stretching vibration, implies that when 0.2M LDFP is used, the SEI contains (or contains more) phosphate species with alkyl groups attached. These molecules are supposed to originate from a nucleophilic substitution of LDFP's fluorine with alkoxide ion RO⁻ formed during solvent reduction (Eq. V.7), as further detailed later in [Section 4.2.1](#). These species can also be present in base-SEI as LDFP can be formed from the reaction between lithium carbonate or alkyl carbonates with LiPF₆ (Chapter III).



Along with phosphate-based compounds, this reaction also yields the passivating compound, LiF, hence preventing from further degradation of electrolyte. Even more, LiF can be

produced from the thermal degradation of LiPF₆ producing PF₅ and from the reaction between LDFP and the CMC binder (Eq. V.6). In literature, XPS results agreed that the amount of LiF increases with addition of LDFP in electrolyte. However, they also highlight some contradictions with respect to Li_xPF_yO_z species content; Kim et al.⁶, reported that upon addition of 1 wt.% of LDFP, the quantity of LiF in the SEI increases, whereas Li_xPF_yO_z changes very little. Shi et al.⁵, reported that the content of LiF increases at the expenses of Li_xPF_yO_z when 1.4 wt.% of LDFP is added. Yang et al.⁷ found that both amounts of LiF and Li_xPF_yO_z increase drastically with 1wt.% of LDFP. Furthermore, Ma et al.⁹ reported that the SEI formed with 0.5 wt.% of LDFP contains fewer carbonate species and more fluorophosphate species, after the formation cycles. It is worth noting here that P, O, F-based compounds (LiPO₂F₂, organofluorophosphates...) are not directly formed from electrochemical reduction processes, hence, they can be present in electrolyte and not necessarily inside the SEI layers. This could explain the different results obtained by XPS technique regarding the amount of Li_xPF_yO_z.

To sum up, the investigation of the SEI composition making use of the FTIR spectroscopy technique provides fruitful information about the role of LDFP on the graphite composite powder upon cycling: it does not inhibit the reduction of solvents and the SEIs are richer in LiF and phosphate or fluorophosphate species. On electrodes, it may react with CMC binder and as a consequence, marginally limit the solvents reduction.

4.1.2. Study of CEI composition

Upon cycling, a cathode electrolyte interphase (CEI) may form. It is similar to the SEI in a sense that it contains organic and inorganic compounds, which may form depending on the temperature and cycling conditions^{36, 37}. In the case of cycling with LDFP, some authors proposed that the CEI layer (referred as LDFP-CEI) is passivating toward electrolyte oxidation thanks to the deposition of LiPF₆-derived decomposition products³ or LDFP itself^{2, 6}. Regarding LiF, Lei et al.⁸ showed that it is almost absent in the LDFP-CEI and Zhao et al.¹⁶ did not observe any difference in content. Finally, Qian et al.¹⁵ asserted that, based on XPS analyses, the LDFP-CEI is richer in fluorine.

In order to characterize the CEI formed upon cycling, FTIR analyses were performed on washed NMC 811 composite powders (93.7 wt.% lithiated NMC and 6.3 wt.% C45) after 3

cycles vs. lithium at 55°C and a rate of C/20. The experiments were done in FTIR in transmission mode (Annex IV), to provide a greater chance of obtaining an exploitable signal.

In the original spectra, no additional peak other than those of the active material are visible, indicating a very thin CEI layer, if any. After highly magnifying the spectra (Fig. V.16), almost identical peaks appear but could not be objectively assigned to a CEI component or impurity.

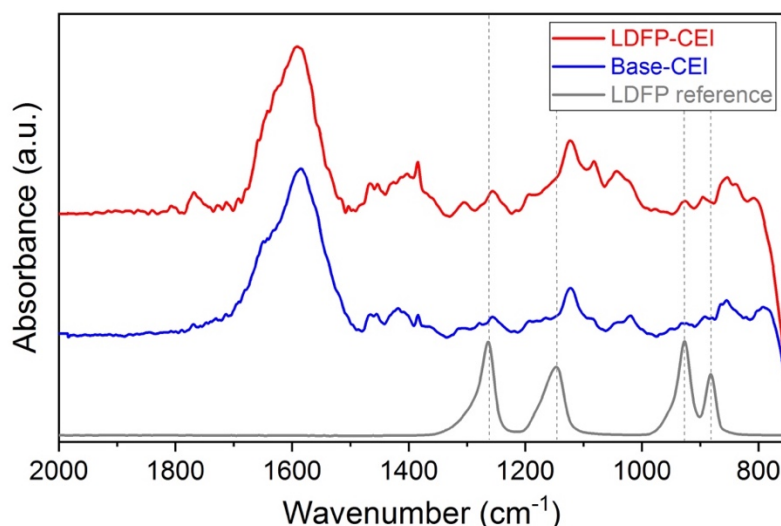
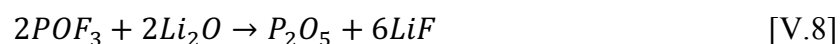


Figure V.16. FTIR analysis of LDFP and the CEI formed on washed NMC 811 composite powder after 3 cycles at 55°C without or with LDFP.

Willing to go further with the characterization of the CEI, FTIR in ATR mode analyses were performed at the surface of NMC 811 electrodes after 200 cycles (such high cycle number could not have been achieved with NMC composite powder at 55°C under safe conditions).

The spectrum of the reference film shows mainly PVDF bands (Fig. 17a). After long cycling, remarkably, spectra are quite similar. Their bands can be assigned to phosphate and/or organo-fluorophosphate and/or fluorophosphates such as LDFP (Fig. 17b). The presence of LDFP and possible derivatives in base-CEI would not come as a surprise as this product was found to be produced along with LiF, through the reaction between Li_2CO_3 or Li_2O surface species and LiPF_6 . In literature, the band centered at 1280 cm^{-1} was suggested to correspond to the P–O stretching vibration of the phosphorous pentoxide (P_2O_5), formed by the reaction of POF_3 with Li_2O ³⁶ (Eq. V.8).



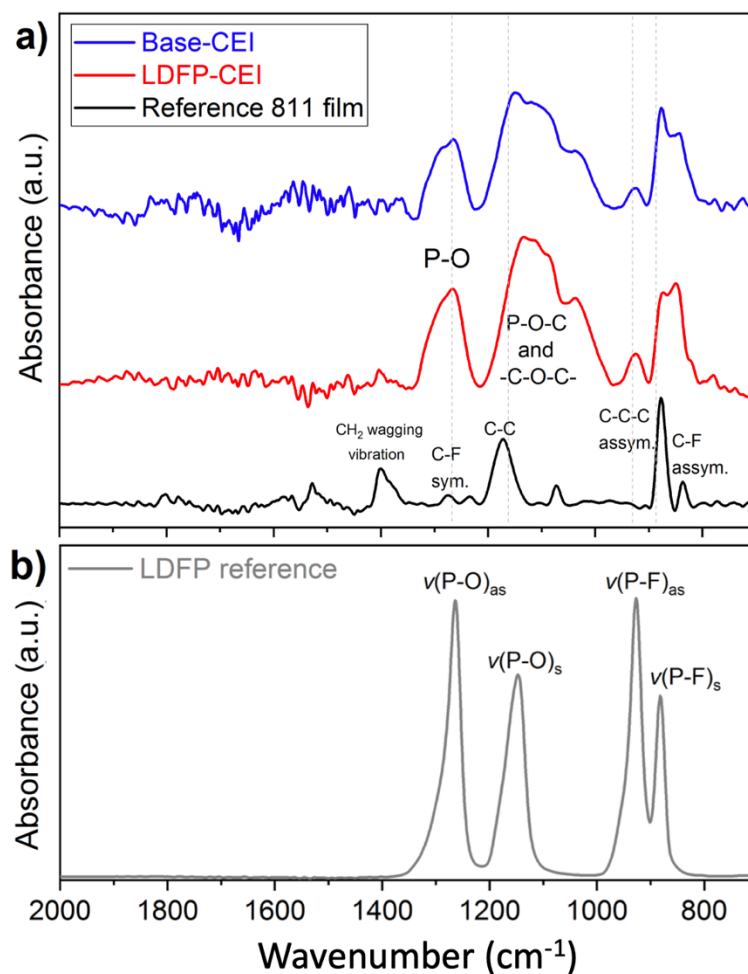


Figure V.17. FTIR analysis of **a)** the surface of non-cycled and washed NMC 811 electrodes after 200 cycles at 55°C in pouch cell, **without** or **with LDFFP** and **b)** pure LDFFP.

In summary, both FTIR spectra obtained at the surface of NMC 811 electrodes recovered after long cycling at 55°C , with and without 0.2M LDFFP, reveal phosphate-based compounds (fluoro, organo), that can be part of CEIs or come from the electrolyte-in-separator side. Unfortunately, these results do not provide any clue for explaining the different electrochemical behaviors.

4.2. Analysis of electrolyte degradation products

The analysis of SEI suggested the presence of organo-fluorophosphate compounds stemming from chemical reaction, which could have changed the nature of the degradation products accumulated in the electrolyte. In literature, only Qian et al.¹⁵ have been interested in the electrolyte composition very recently. They analyzed the electrolyte 1M LiPF_6 with 1 wt.% of LDFFP in EC/DEC (3:7 in weight ratio) from cells NMC 532/Gr after cycling (4 cycles at RT

between 3 – 4.2V) through gas chromatography/mass spectrometry (GC/MS). The analysis of the electrolyte showed that the degradation product, diethyl 2,5-dioxahexane dicarboxylate (DEDOHC) stemming from the trans-esterification reaction between EC and DEC, via an electrochemical reduction-initiated process has disappeared. No mechanism was given but they hypothesized that LDFP inhibits this trans-esterification reaction. Therefore, a stepwise investigation of the cycled electrolyte was undertaken with the aim of clarifying the impact of LDFP on electrolyte degradation reactions.

The electrolyte was extracted from the pouch cells NMC 811(cal.)/Gr after 200 cycles with and without 0.2M LDFP, and the resulting liquid was analyzed by “liquid” GC/MS and by mass spectrometry/electrospray ionization (ESI-HRMS), in collaboration with the analytical platform of the University of Picardie Jules Verne (experimental conditions in Annex IV).

4.2.1. Analysis of electrolytes by “liquid” GC/MS

Fig. V.18 shows the chromatograms obtained from both base and base + LDFP electrolytes. In addition to the peaks corresponding to the alkyl carbonate solvents EMC, DEC and EC, three defined peaks marked as 1_n , $1_n''$ and $1_n'$ (Fig. V.18) are clearly visible in case of the base electrolyte, but are completely absent when 0.2M LDFP is used, even in the background. These results are in good agreement with those of Qian et al.¹⁵

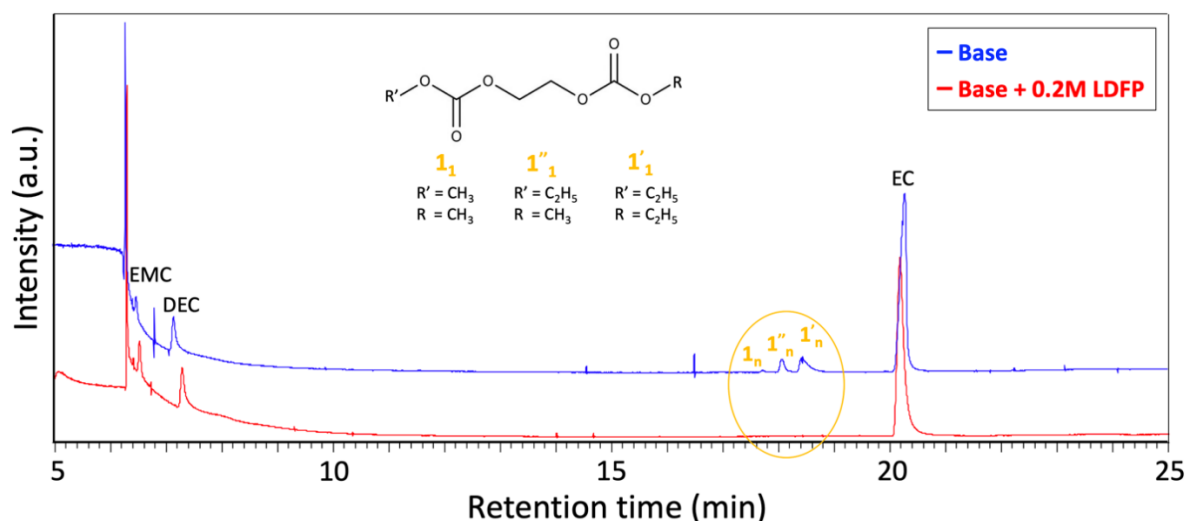
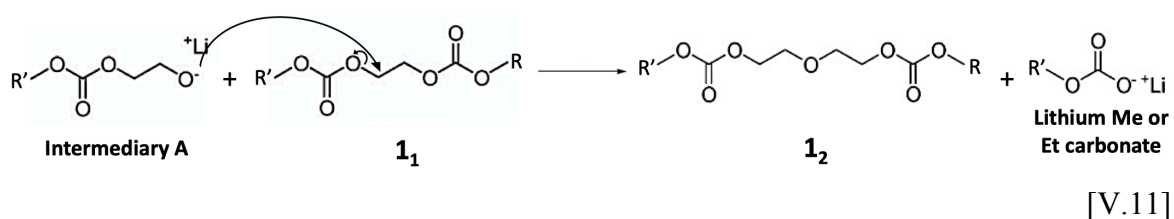
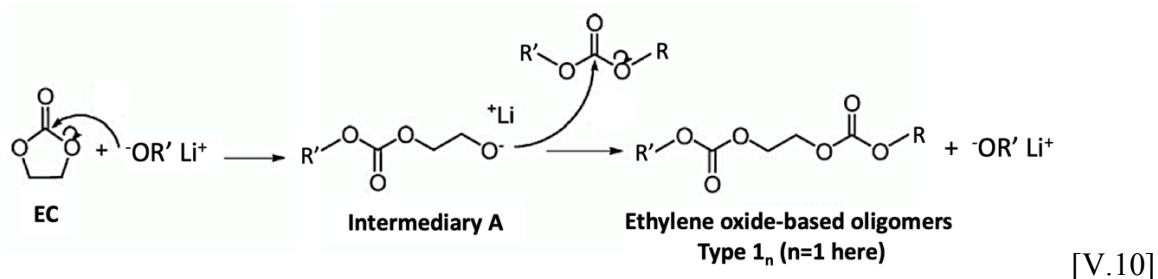
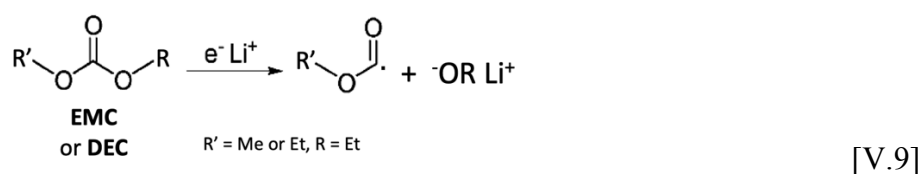


Figure V.18. “Liquid” GC/MS of the electrolyte in pouch cells NMC 811/Gr that performed 200 cycles **without** and **with LDFP**.

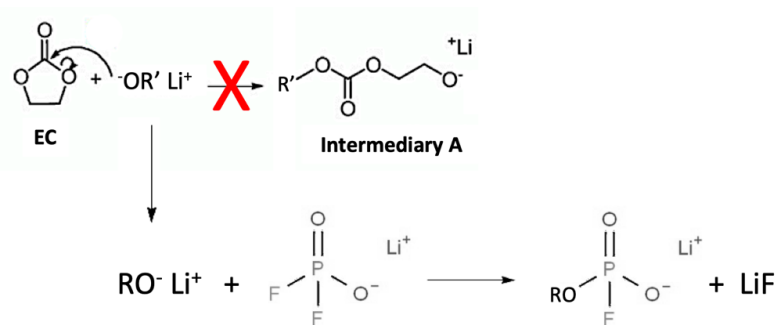
According to previous studies of electrolyte degradation by ESI-HRMS and GC/MS³⁸, these three peaks correspond to the first member of a family of ethylene oxide oligomers terminated with alkyl (methyl or ethyl) carbonate groups (also called 1_n , $1'_n$ and $1''_n$, whose structural formula appears as inset). The more concentrated peak corresponds to $1'_1$ with ethyl, ethyl terminations, which matches well with the statistical presence of this group in the electrolyte containing the EC/EMC/DEC (1:1:1 vol.) carbonate mixture.

According to Sasaki et al.³⁹, the reaction mechanisms to form the 1_1 family consist in two steps that start with the single electron electrochemical reduction of linear solvents (Eq. V.9). Then, the produced alkoxide anions (RO^-) attack the carbonate function of EC to form the so-called intermediary A, followed by a reaction with a linear carbonate. Note that these reactions (Eq. V.10) regenerate ROLi . Consecutive reactions of the intermediary A with 1_1 compounds can lead to the elongation of the chain to form oligomers (Eq. V.11) as shown in the following section.



The FTIR results seem to indicate that LDFP does not inhibit the solvents reduction and as a consequence the formation of alkoxides. Hence, the absence of 1_1 -type compounds suggests that the alkoxides are rapidly scavenged before reacting with EC. They are supposed to substitute fluorine of LDFP, yielding a lithium organo-fluorophosphate salt. The latter may correspond to a phosphate-based compound detected in SEI, through FTIR analysis (Eq.

V.12). It is noticeable that all of the substitution reactions result in increasing the LiF amount in interfacial layers.



[V.12]

4.2.2. Analysis of electrolytes by ESI-HRMS

ESI-HRMS experiments were performed in the positive ion mode on a Q-TOF Ultima Global instrument (Waters-Micromass, Manchester, UK). Data acquisition and processing were performed with TargetLynx software and a listing method to distinguish the main compounds was employed (details in Annex IV).

The results from the base and base + LDFP electrolytes recovered after cycling, shown in Fig. V.19, are organized in two families: none phosphate- and phosphate-containing compounds. The structural formulae are shown in Table V.1 and V.2. Strikingly, the base electrolyte contains both families, whereas the base + 0.2M LDFP electrolyte contains mostly the phosphate-containing compounds in a slightly lower amount.

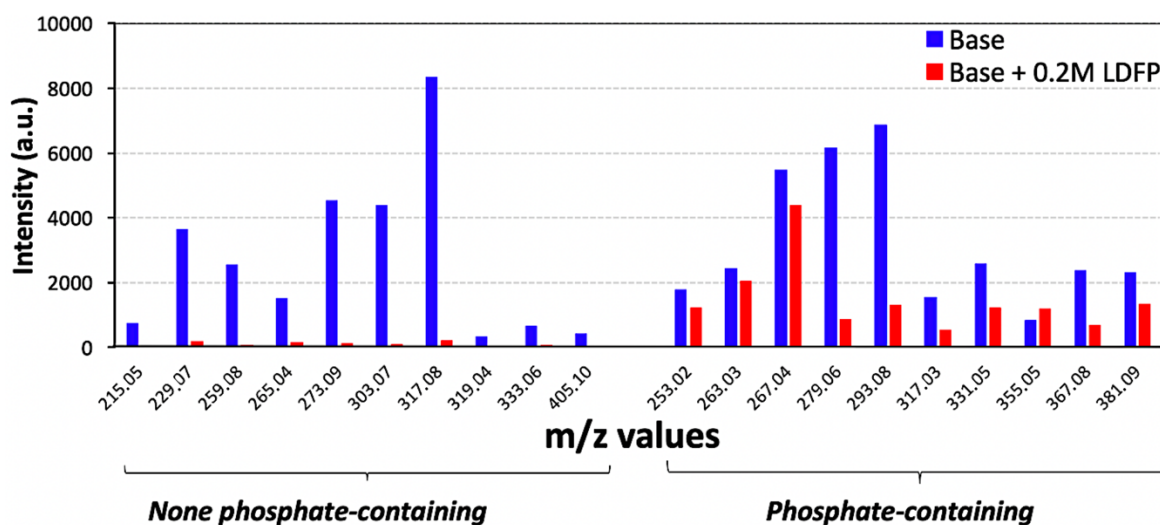


Figure V.19. Phosphate- and non-phosphate-containing compounds analyzed by ESI-HRMS in electrolyte after cycling **without** or **with** LDFP.

Table V.1. List of m/z values, retention time (RT) and formulae of compounds without phosphates, observed in ESI-HRMS.

m/z	RT (min)	Brute formula	Structural formula
215.053	6.86	$\text{C}_7\text{H}_{12}\text{NaO}_6$	
229.068	7.62	$\text{C}_8\text{H}_{14}\text{NaO}_6$	
259.079	7.05	$\text{C}_9\text{H}_{16}\text{O}_7\text{Na}$	
273.094	7.73	$\text{C}_{10}\text{H}_{18}\text{O}_7\text{Na}$	
303.068	7.51	$\text{C}_{10}\text{H}_{16}\text{NaO}_9$	
317.084	8.09	$\text{C}_{11}\text{H}_{18}\text{NaO}_9$	
319.041	7.63	$\text{C}_{10}\text{H}_{16}\text{KO}_9$	
405.100	8.39	$\text{C}_{14}\text{H}_{22}\text{NaO}_{12}$	

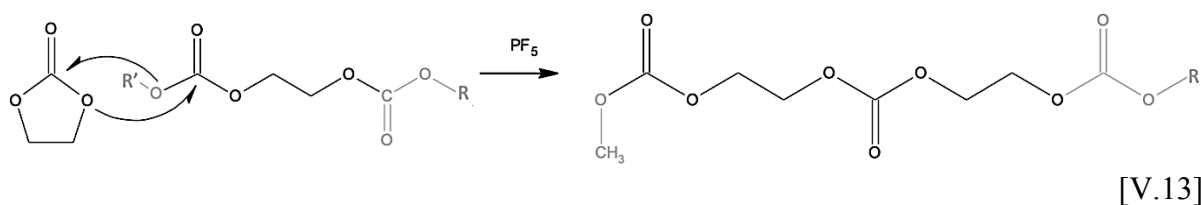
Table V.2. List of m/z values, retention time (RT) and formulae of compounds containing phosphates, observed in ESI-HRMS.

m/z	RT (min)	Brute formula	Structural formula
253.025	6.48	$\text{C}_6\text{H}_{12}\text{O}_6\text{FNaP}$	
263.028	5.74	$\text{C}_7\text{H}_{13}\text{O}_7\text{NaP}$	
265.044	6.14	$\text{C}_7\text{H}_{15}\text{O}_7\text{NaP}$	
267.040	7.15	$\text{C}_7\text{H}_{14}\text{O}_6\text{FNaP}$	
279.060	6.67	$\text{C}_8\text{H}_{17}\text{O}_7\text{NaP}$	

293.076	7.24	$\text{C}_9\text{H}_{19}\text{O}_7\text{NaP}$	
317.032	6.45	$\text{C}_7\text{H}_{17}\text{O}_7\text{FNaP}_2$	
331.048	6.89	$\text{C}_8\text{H}_{19}\text{O}_7\text{FNaP}_2$	
355.055	7.64	$\text{C}_{10}\text{H}_{18}\text{FNaO}_9\text{P}$	
367.076	7.18	$\text{C}_{11}\text{H}_{21}\text{O}_{10}\text{NaP}$	
381.092	7.66	$\text{C}_{12}\text{H}_{23}\text{O}_{10}\text{Na P}$	

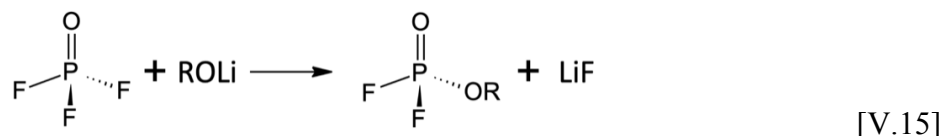
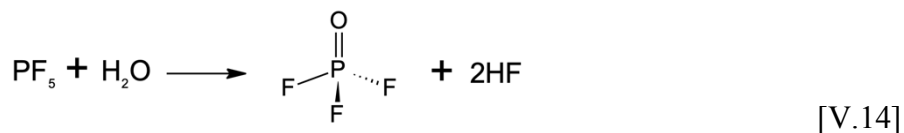
The none-phosphate-containing compounds are low-mass oligomers ($n \leq 2$) with ethylene oxide and ethylene carbonate units:

- The ethylene oxide-based compounds correspond to the 1_n family produced through Eqs. V.10 and 11 presented in Section 4.2.1. It comprises the molecules detected by GC/MS (m/z 215.053 and 229.068) and those with $n=2$ (m/z 259.079 and 273.094).
- The carbonate-based molecules are produced through a transesterification reaction involving EC and a carbonate oligomer in presence of PF_5 ⁴⁰ (Eq. V.13):



All of these compounds are produced from the hereabove described reactions initiated by alkoxides. Their quasi absence in case of LDFP electrolyte underpins the assumption that most alkoxides are scavenged by LDFP (as precipitated salt or dissociated salt in electrolyte, not detected here) or other fluorophosphates before reacting with EC.

The phosphate-containing compounds present in both electrolytes are the product of fluorine substitution reactions between anions (alkoxides, intermediary A.) and fluorophosphates (Eq. V.15). The latter is originating from the degradation of LiPF_6 into PF_5 and LiF (Eq. I.10), followed by the reaction with water to yield POF_3 (Eq. V.14, also I.11).



To sum up, in base electrolyte, anions originating from the reduction of solvents bring about the formation of ethylene oxide and ethylene carbonates oligomers as well as phosphate ending oligomers due to the reaction of PF_5 with water.

In presence of LDFP electrolyte additive, the reaction of alkoxides RO^- with LDFP must be kinetically favored, thus preventing the formation of the above-mentioned ethylene oxide and ethylene carbonates oligomers. The generated lithium organo-fluorophosphate salt must be precipitated in SEI, as suggested by FTIR analysis, or dissociated in electrolyte. Part of the alkoxides can also start attacking EC but all the resulting anions react with POF_3 formed from the reaction of LiPF_6 (PF_5) with water, as in base electrolyte. Note that, with LDFP or not, the amount of phosphates detected through ESI-HRMS stems from water traces.

4.3. Analysis of gas released

The limited literature on the effect of LDFP on gas production includes the work by Song et al.¹³, who claimed that the combination of 0.5 wt.% of LDFP with 15 vol. of FEC (fluoroethylene carbonate) in a LiPF_6 -based electrolyte reduced the swelling ratio of a charged (4.25 V) pouch cell NMC 811/SiOx@C to 1.96% after 7 days storage at 55°C, in comparison to 5.91% when only using 15% FEC. Liu et al.¹² reported a decrease of ~78% and ~88% in the volume of pouch cells NMC 532/Gr containing 1-2% of LDFP after 500h storage at 60°C, both at the charged (4.4 V) and discharged state (2.5 V), respectively. From the same group, Ma et al.⁹ reported a decrease of ~83% of the volume of pouch cells NMC 532/Gr containing 0.5 wt.% of LDFP stored in the charged state. According to Dahn's group^{9, 12}, the decreased gas production is due to "the suppression of parasitic reactions", caused by the passivation of

the SEI by LDFP deposition, but the mechanisms are not detailed. The aforementioned works studied the volume change of stored pouch cells upon the formation cycles, but neither of them studied the elemental composition of the gases, nor their evolution after prolonged cycling. Therefore, this section reports on the gas content and composition analysis from cycled pouch cells NMC 811/Gr, in the hope of obtaining further information about the role of LDFP.

Two batches of four 811/Gr whose cycling results were previously shown (Section 3.1), were taken for gas analysis after 200 cycles at 55°C by means of GC/BID, following the preparation, gas recuperation and quantification protocols described in Chapter IV. Fig. V.20 presents the results expressed in peak areas to be able to compare CH_4 and C_2H_6 for which calibration curves are not available. The inset values are the results of the quantification of CO_2 and C_2H_4 and the error bars correspond to standard deviation of the analyzed samples in each batch.

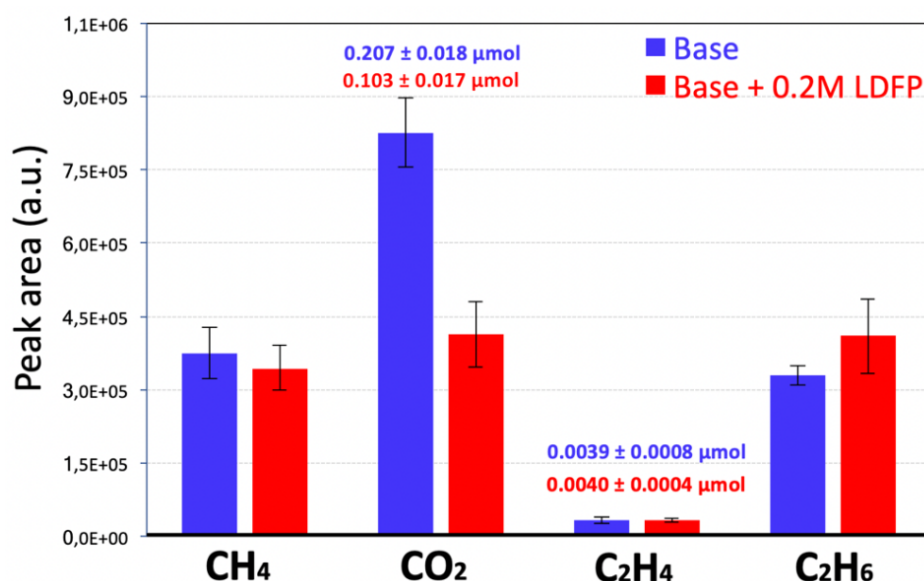


Figure V.20. GC/BID analysis of gas from pouch cells 811/Gr after 200 cycles at 55°C , without or with LDFP.

As shown in Fig. V.20, the peak area of gases released upon the SEI formation (CH_4 , C_2H_4 and C_2H_6) present around the same values, in presence or absence of LDFP. This result corroborates the assumption deduced from the previous electrochemical analysis that LDFP hardly inhibits the reduction of solvents during SEI formation in CMC-based electrode.

Interestingly, C_2H_4 peak areas are smaller than CH_4 and C_2H_6 , which is opposite to the results shown in Chapter IV obtained after the formation step, where the peak area of C_2H_4 was always superior to CH_4 and C_2H_6 . Furthermore, the same observation was pointed out while analyzing the gases released from two batches of cycled NMC 622C/Gr pouch cells, by GC/MS technique (Fig. V.21).

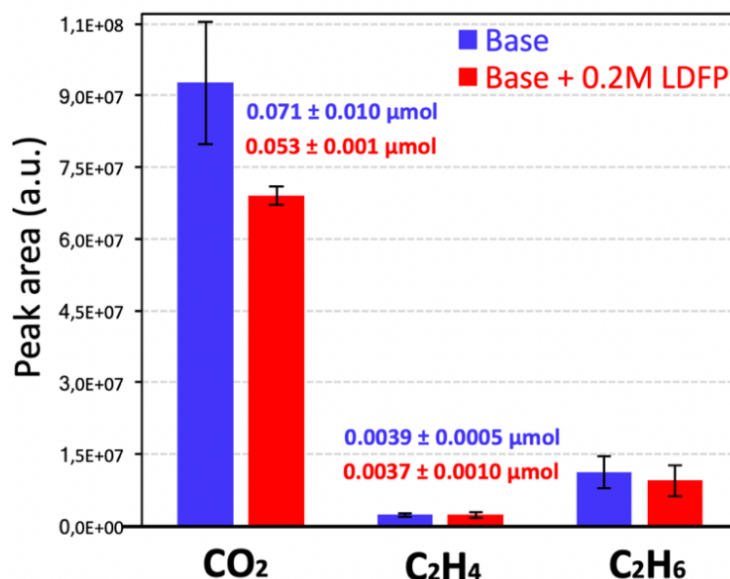


Figure V.21. GC/MS analysis of gas from pouch cells 622C/Gr, after 200 cycles at 55°C without/with LDFP.

Three possible explanations stand out:

- i. The sources of CH_4 and C_2H_6 are the linear carbonates EMC and DEC; whereas the source of C_2H_4 is the cyclic EC. Hence, linear carbonates would be continuously reduced along the cycling and not EC. This is not likely to occur since, according to the calculations made by Tasaki et al.⁴¹, EC is the carbonate solvent more prone to undergo the first electron reduction ahead of the other linear solvents.
- ii. According to some works^{42, 43}, C_2H_4 is electrochemically reduced along cycling producing $\text{Li}_2\text{C}_2\text{H}_4$. However, this reaction has been reported to occur only on solid argon^{44, 45} and thus, it cannot be envisaged in battery conditions.
- iii. C_2H_4 may be oxidized by $^1\text{O}_2$. For comparison, in the last chapter, pouch cells NMC 811(non-cal.)/Gr at C/5 and 55°C produced 0.087 ± 0.019 μmol of C_2H_4 after the formation cycles, an almost 23 times bigger value than that found here, after the long cycling at C/4 and 55°C . It can be presumed that C_2H_4 has been oxidized by $^1\text{O}_2$ to ethylene oxide or CO_2 , as discussed in the previous chapter.

With respect to the quantification of CO₂ released from pouch cells containing base electrolyte, it is remarkable that the quantity is almost three times bigger when NMC 811 is used compared to 622C. The thermal degradation of solvents cannot be at the origin of this difference as pouch cells spent an almost equivalent time span in the oven at 55°C (40 days for 622C/Gr and 41.5 days for 811/Gr).

Other CO₂ sources are the oxidative processes of C₂H₄ and alkyl carbonate solvents with ¹O₂. As already discussed, the latter is supposed to be produced from layered NMC phase transformations (to spinel and rock salt) upon aging and the consumption of Li₂CO₃ through electrochemical oxidation or chemical reaction with LiPF₆ ([Chapter III](#)); both processes being exacerbated in case of NMC 811 compared to 622.

On the other hand, the impact of LDFP is very clear: there is less CO₂ produced in the order of ~50 and ~25% less in pouch cells containing NMC 811 and 622C, respectively, whenever LDFP is contained in the electrolyte. This huge decrease in case of NMC 811/Gr cells must be interpreted with caution as the cells displayed a premature capacity loss (PCL) in presence of LDFP and thus, might not have spent the same accumulated time at oxidative high voltages.

However, the cells with and without LDFP, for each NMC, spent exactly the same time span in the oven at 55°C, hence discarding the thermal degradation at the origin of the difference. It is interesting to note that the PCL seen with NMC 811 is not accompanied with an important CO₂ gas release related to electrolyte oxidation. Therefore, it can be assumed that the usual NMC aging process that brings about oxygen releasing-structural transformations is not at the origin of this PCL phenomenon.

NMC 622C/Gr cells that were found to depict improved performances when cycled with LDFP at 55°C also release a less amount of CO₂, which thus proves the efficiency of this additive to mitigate solvents degradation. In literature, the creation of a CEI at the surface of NMCs was suggested to explain the less reactivity of these interfaces toward electrolyte, what we were not able to confirm from FTIR analysis. Further investigations are required to determine the origin of such CO₂ decrease in presence of this additive, through chemical simulation tests.

To conclude about the gas study, the similar amount of gases, C₂H₄, CH₄ and C₂H₆, with and without LDFP, whatever the NMC composition, 811 or 622C, is in compliance with the previous suggestion that the additive does not hinder the solvent reduction processes. The

decreased amount of C₂H₄ between the formation step and the 200th cycles may be due to its oxidation with reactive singlet oxygen released from NMC transformation phases, or the oxidation of Li₂CO₃ from the SEI or the surface species at the surface of the raw NMC materials.

The presence of LDFP was found to inhibit the production of CO₂ and maybe more importantly in case of NMC 811 than 622C, nonetheless, further investigations are required to explain this effect. Last but not least, a conclusion can be drawn that the PCL observed with NMC 811 pouch cycled at 55°C with LDFP does not involve or is not due to supplementary production of the gases hereabove studied.

4.4. Discussion and conclusion

The study of degradation products in the electrolyte was conducted with the aim of better grasping the contradictory role of the LDFP additive upon complete cells cycling at 55°C, which is beneficial in case of NMC 622C and deleterious in case of NMC 811. To this end, a stepwise investigation of interfacial layers, electrolytes and gases has been achieved through FTIR, mass spectrometry and GC/BID or MS analysis, respectively.

It was determined that LDFP does not act as classical additives (VC, FEC...) since it does not reduce before alkyl carbonate solvents and thus, does not prevent the formation of lithium carbonate and lithium alkyl carbonate in the SEI of graphite powder. Only a marginal decrease in the reduction of solvents has been revealed by analyzing the electrochemical curves from pouch cells, but this phenomenon may result from a reaction between CMC binder and LDFP.

On the other hand, the additive is prone to scavenge alkoxides (RO⁻) formed from linear carbonate reduction, before they react with EC to yield ether/carbonate-based oligomers. The “scavenging” substitution reaction leads to the formation of lithium organo-fluorophosphates and LiF as potential additional salts in the SEI layer. This new SEI composition may confer higher passivating properties and thus contribute to the capacity retention improvement in presence of LDFP. This additive also decreases the CO₂ gas release, which still needs conclusive explanations. Overall, all these analyses help clarify the beneficial role of LDFP. However, they do not allow to conclude about the premature capacity loss of NMC 811/Gr pouch cells cycled at 55°C. Only few observations can be stated:

- i. the positive electrode is the culprit,

- ii. the cells do not generate a higher amount of gases upon cycling and thus, the classical aging processes inducing structural transformations at the surface of NMC might not be involved,
- iii. the highest the LDFP concentration, the less pronounced the capacity fade and
- iv. the electrode calendaring has a beneficial impact.

In light of all these results, the structural collapse of the NMC 811 particles evidenced by SEM at the surface of the electrode after the separator is taken off, was considered as the main issue that causes the capacity fade. It has to be recalled the different global morphologies. As shown in SEM images (Fig. V.22a and b), both NMC 622C and 811 particles are polycrystalline, however, only the NMC 811 particles present an inner porosity.

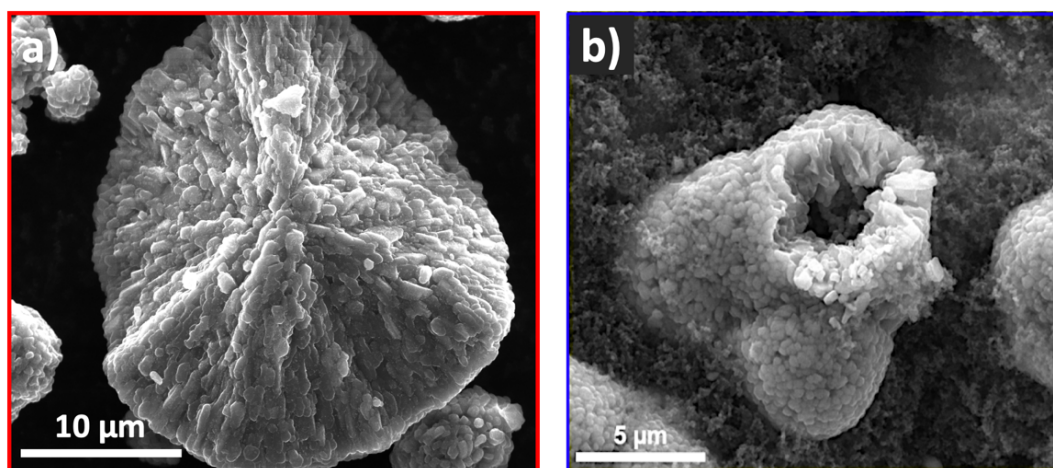


Figure V.22. Illustrative SEM pictures of broken particles of NMC **a) 622C** and **b) 811** showing their polycrystalline structure and the porous texture of NMC 811.

This porous structure is further portrayed on transmission electron microscopy (TEM) images of NMC 811 electrode cycled in base electrolyte at 55°C. For the sample preparation, the cycled electrode was taken out of the pouch cell, rinsed with DMC, dried in vacuum and prepared for focused-ion beam (FIB) cut (experimental details in Annex IV).

Fig. V.23a of the cycled electrode exhibits a large inner void with detached agglomerates of primary particles as well as a shell made of cohesive primary particles. Magnified images of this shell (Fig. V.23b) and of a particle before cycling (Fig. V.23c) show, systematically, amorphous grain boundaries of ~10 nm around the primary particles, probably made of light elements due to the color contrast. From results of [Chapter II](#), we can hypothesize that this

interface is made of residual synthesis products, such as Li_2CO_3 or Li_2O , depending on the annealing temperature, *i.e.* if it was elevated enough to decompose Li_2CO_3 ($> 700^\circ\text{C}$). After cycling, this layer displays crystalline parts in the region closer to the grains.

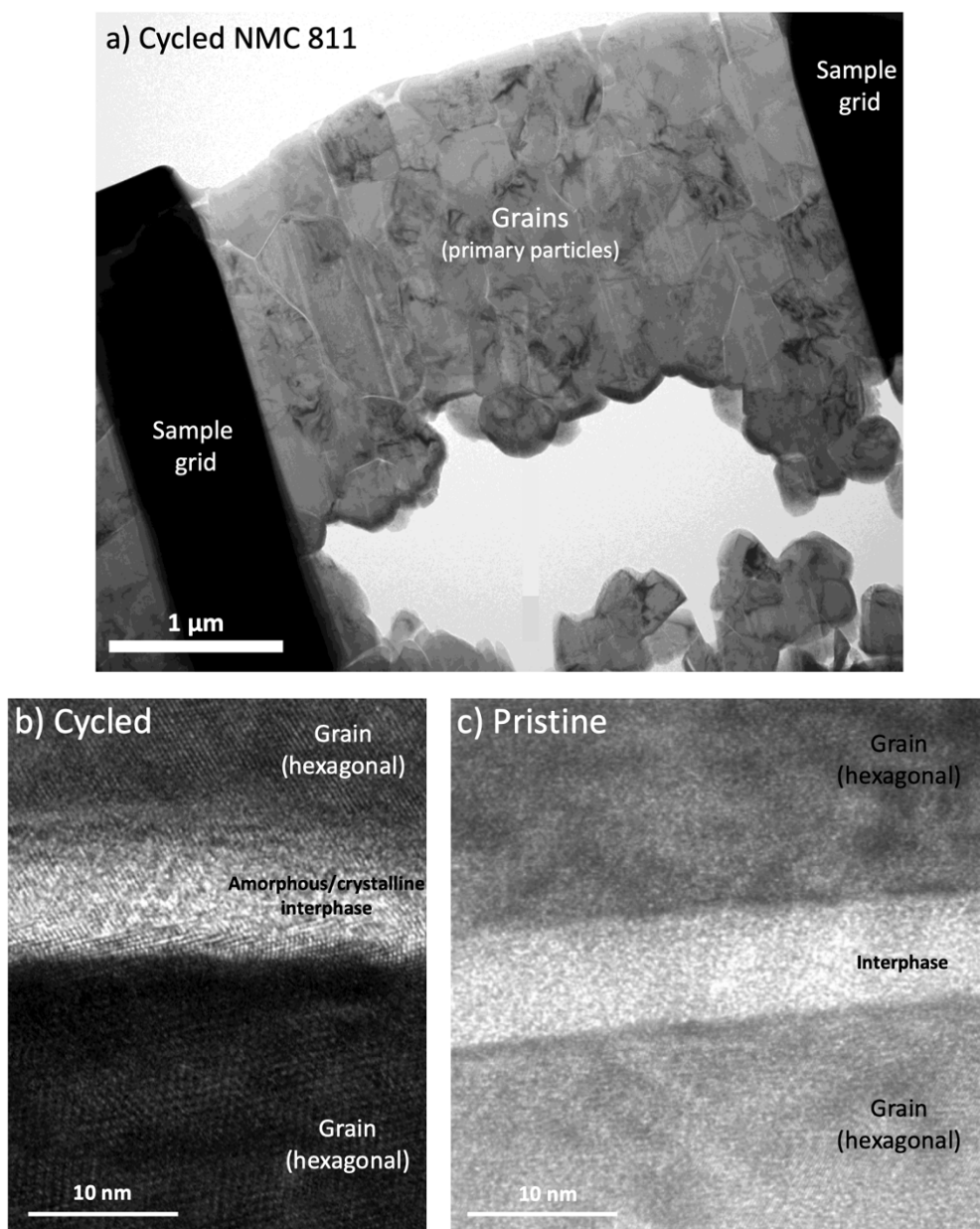


Figure V.23. **a)** TEM picture NMC 811 particles cycled with base electrolyte (100 cycles at 55°C), cut transversally by FIB. Magnified images **b)** after and **c)** before cycling.

TEM image of the NMC 622C particle (Fig. V.24a) confirms the absence of inner porosity; the darker part, at the bottom, only denotes a higher thickness of the slice. Some grain boundaries are also visible but not systematically all around the grains (Fig. V.24b). It is worth

noting that the CEI, if any, is not visible whatever the NMC; the outermost layer is made of platinum that is deposited to protect the sample during FIB preparation.

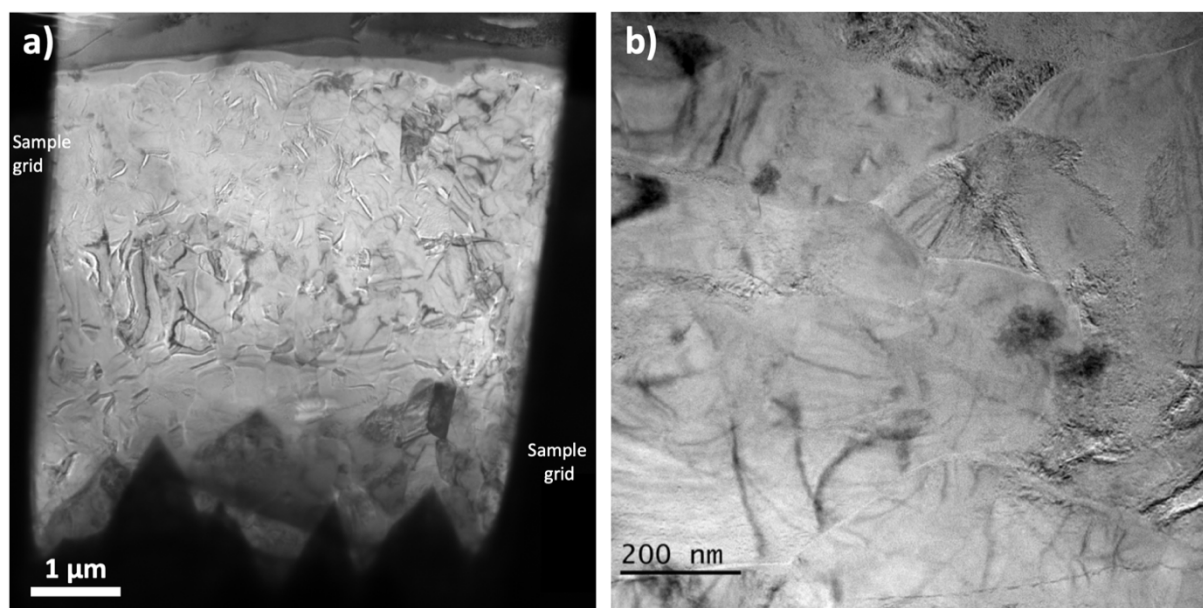


Figure V.24. a, b) Two different TEM magnifications of the particles in NMC 622C cycled with base electrolyte (100 cycles at 55°C), cut transversally by FIB.

These TEM analyses bring about valuable information regarding the inner structure and composition of NMCs that may help decipher the PCL phenomenon of NMC 811. They suggest the idea that the grain boundaries form a more percolating network within the NMC 811 particle's shell than within the NMC 622C particles. If composed of soluble bases (Li_2CO_3 or Li_2O), these interfacial layers would more highly react with LiPF_6 (through Lewis acid PF_5 generation) when cycling at high temperature ([Chapter III](#)). This would result in grains decohesion and an easier access of the electrolyte to primary grain interfaces, thus favoring deleterious reactions known in Ni-rich NMC ⁴⁶. This would explain the lower capacity retention of NMC 811 compared to NMC 622C.

This phenomenon is exacerbated with the increasing amount of LDFP additive. It is suspected that the reaction of soluble bases with LiPF_6 releases an additional amount of LDFP which cannot solubilize in LDFP-rich electrolyte and thus precipitates at the interfaces, amplifying the grains decohesion. Besides, after the electrolyte has penetrated the inner porous part of the particles, it may favor their disintegration through the mechanical force induced by the displacement of anions while subjected to the electric field upon cycling; this phenomenon being enhanced owing to the highest concentration of salts in LDFP-rich electrolyte.

5. Conclusion of the chapter

There are two main motivations to study LDFP as electrolyte additive in LIBs containing Ni-rich NMC materials. First, to take advantage of the in-situ reactions between surface species and LiPF₆ that produce LDFP ([Chapter III](#)). Second, to test if LDFP improves the electrochemical performance and reduces gas production, as agreed in the literature.

In a first instance, it was found that LDFP does not behave as a typical additive that reduces/oxidizes to generate a SEI/CEI. In fact, virtually no difference in the CEI formed with/without LDFP was found and the only difference in the SEI is the enrichment with fluorine- and phosphor-based species when LDFP is used. The evaluation of the cycling performance revealed that LDFP improves the capacity retention after 200 cycles of cells NMC 622C/Gr cycled at 55°C and NMC 811/Gr cycled at 25°C, but intriguingly, PCL is observed at 55°C. A possible explanation was given by TEM analyses that revealed the presence of an interphase in-between the primary grains of NMC 811, possibly made of soluble bases. In agreement with the study reported in [Chapter III](#), we hypothesized that LiPF₆ reacts with this interphase to produce LDFP, inducing grain decohesion and contact loss. The presence of LDFP additive in electrolyte favors its deposition and thus exacerbates this phenomenon, which ultimately causes the particle disintegration observed when the 811/Gr pouch cells were opened.

Regarding the controversy around the action mechanism of LDFP, it was found that it scavenges RO⁻, thus preventing electrolyte ageing. In addition, it inhibits some CO₂ production in 622C or 811-containing cells, although this part merits further clarification. These two characteristics are very interesting for the application of this additive in LIBs for the automotive industry, nonetheless, its implementation in cells containing polycrystal NMC 811 cycled at high temperature appears to be restricted by its surface chemistry. The use of monocrystal NMC can be envisaged so that the reactivity of NMC 811 is minimized.

6. References

1. Wagner, R.; Korth, M.; Streipert, B.; Kasnatscheew, J.; Gallus, D. R.; Brox, S.; Arnereller, M.; Cekic-Laskovic, I.; Winter, M., Impact of Selected LiPF_6 Hydrolysis Products on the High Voltage Stability of Lithium-Ion Battery Cells. *Acs Applied Materials & Interfaces* **2016**, *8* (45), 30871-30878.
2. Yang, G. H.; Shi, J. L.; Shen, C.; Wang, S. W.; Xia, L.; Hu, H. S.; Luo, H.; Xia, Y. G.; Liu, Z. P., Improving the cyclability performance of lithium-ion batteries by introducing lithium difluorophosphate (LiPO_2F_2) additive. *Rsc Advances* **2017**, *7* (42), 26052-26059.
3. Chen, J. W.; Xing, L. D.; Yang, X. R.; Liu, X.; Li, T. J.; Li, W. S., Outstanding electrochemical performance of high-voltage $\text{LiNi}_{1/3}\text{Co}_{1/3}\text{Mn}_{1/3}\text{O}_2$ cathode achieved by application of LiPO_2F_2 electrolyte additive. *Electrochimica Acta* **2018**, *290*, 568-576.
4. Zhao, W. M.; Zheng, G. R.; Lin, M.; Zhao, W. G.; Li, D. J.; Guan, X. Y.; Ji, Y. J.; Ortiz, G. F.; Yang, Y., Toward a stable solid-electrolyte-interfaces on nickel-rich cathodes: LiPO_2F_2 salt-type additive and its working mechanism for $\text{LiNi}_{0.5}\text{Mn}_{0.25}\text{Co}_{0.25}\text{O}_2$ cathodes. *Journal of Power Sources* **2018**, *380*, 149-157.
5. Shi, P. C.; Zhang, L. C.; Xiang, H. F.; Liang, X.; Sun, Y.; Xu, W., Lithium Difluorophosphate as a Dendrite-Suppressing Additive for Lithium Metal Batteries. *Acs Applied Materials & Interfaces* **2018**, *10* (26), 22201-22209.
6. Kim, K. E.; Jang, J. Y.; Park, I.; Woo, M. H.; Jeong, M. H.; Shin, W. C.; Ue, M.; Choi, N. S., A combination of lithium difluorophosphate and vinylene carbonate as reducible additives to improve cycling performance of graphite electrodes at high rates. *Electrochemistry Communications* **2015**, *61*, 121-124.
7. Yang, B. W.; Zhang, H.; Yu, L.; Fan, W. Z.; Huang, D. H., Lithium difluorophosphate as an additive to improve the low temperature performance of $\text{LiNi}_{0.5}\text{Co}_{0.2}\text{Mn}_{0.3}\text{O}_2$ /graphite cells. *Electrochimica Acta* **2016**, *221*, 107-114.
8. Lei, Q. F.; Yang, T. X.; Zhao, X. Y.; Fan, W. Z.; Wang, W. L.; Yu, L.; Guo, S. B.; Zuo, X. X.; Zeng, R. H.; Nan, J. M., Lithium difluorophosphate as a multi-functional electrolyte additive for 4.4 V $\text{LiNi}_{0.5}\text{Co}_{0.2}\text{Mn}_{0.3}\text{O}_2$ /graphite lithium ion batteries. *Journal of Electroanalytical Chemistry* **2019**, *846*.
9. Ma, L.; Ellis, L.; Glazier, S. L.; Ma, X. W.; Liu, Q. Q.; Li, J.; Dahn, J. R., LiPO_2F_2 as an Electrolyte Additive in $\text{Li Ni}_{0.5}\text{Mn}_{0.3}\text{Co}_{0.2}\text{O}_2$ /Graphite Pouch Cells. *Journal of the Electrochemical Society* **2018**, *165* (5), A891-A899.
10. Wang, C. Y.; Yu, L.; Fan, W. Z.; Liu, R.; Liu, J. W.; Ouyang, L. Z.; Yang, L. C.; Zhu, M., Enhanced high-voltage cyclability of $\text{LiNi}_{0.5}\text{Co}_{0.2}\text{Mn}_{0.3}\text{O}_2$ -based pouch cells via lithium difluorophosphate introducing as electrolyte additive. *Journal of Alloys and Compounds* **2018**, *755*, 1-9.
11. Wang, C. Y.; Yu, L.; Fan, W. Z.; Liu, J. W.; Ouyang, L. Z.; Yang, L. C.; Zhu, M., Lithium Difluorophosphate As a Promising Electrolyte Lithium Additive for High-Voltage Lithium-Ion Batteries. *Acs Applied Energy Materials* **2018**, *1* (6), 2647-2656.
12. Liu, Q. Q.; Ma, L.; Du, C. Y.; Dahn, J. R., Effects of the LiPO_2F_2 additive on unwanted lithium plating in lithiumion cells. *Electrochimica Acta* **2018**, *263*, 237-248.
13. Song, W. F.; Qin, Z. M.; Duan, B. Y.; Hong, B.; Liu, Y. X.; Hong, S., LiPO_2F_2 as a LiPF_6 Stabilizer Additive to Improve the high-temperature Performance of the NCM811/SiOx@C Battery. *International Journal of Electrochemical Science* **2019**, *14* (9), 9069-9079.
14. Seok, J. W.; Lee, J.; Rodgers, T.; Ko, D. H.; Shim, J. H., Effect of LiPO_2F_2 Electrolyte Additive on Surface Electrical Properties of $\text{LiNi}_{0.6}\text{Co}_{0.2}\text{Mn}_{0.2}\text{O}_2$ Cathode. *Transactions on Electrical and Electronic Materials* **2019**, *20* (6), 548-553.
15. Qian, Y. X.; Hu, S. G.; Zou, X. S.; Deng, Z. H.; Xu, Y. Q.; Cao, Z. Z.; Kang, Y. Y.; Deng, Y. F.; Shi, Q.; Xu, K.; Deng, Y. H., How electrolyte additives work in Li-ion batteries. *Energy Storage Materials* **2019**, *20*, 208-215.
16. Zhao, D. N.; Song, S. N.; Ye, X. S.; Wang, P.; Wang, J.; Wei, Y.; Li, C. L.; Mao, L. P.; Zhang, H. M.; Li, S. Y., New insight into the mechanism of LiPO_2F_2 on the interface of high-voltage cathode $\text{LiNi}_{0.5}\text{Mn}_{1.5}\text{O}_4$ with truncated octahedral structure. *Applied Surface Science* **2019**, *491*, 595-606.
17. Gnanaraj, J. S.; Levi, M. D.; Gofer, Y.; Aurbach, D.; Schmidt, M., $\text{LiPF}_3(\text{CF}_2\text{CF}_3)_3$: A salt for rechargeable lithium ion batteries. *Journal of the Electrochemical Society* **2003**, *150* (4), A445-A454.

18. Ding, M. S.; Xu, K.; Zhang, S. S.; Amine, K.; Henriksen, G. L.; Jow, T. R., Change of conductivity with salt content, solvent composition, and temperature for electrolytes of LiPF_6 in ethylene carbonate-ethyl methyl carbonate. *Journal of the Electrochemical Society* **2001**, *148* (10), A1196-A1204.
19. Liu, L. L.; Gu, S. J.; Wang, S. L.; Zhang, X. Y.; Chen, S. M., A $\text{LiPO}_2\text{F}_2/\text{LiPF}_6$ dual-salt electrolyte enabled stable cycling performance of nickel-rich lithium ion batteries. *Rsc Advances* **2020**, *10* (3), 1704-1710.
20. Landesfeind, J.; Hattendorff, J.; Ehrl, A.; Wall, W. A.; Gasteiger, H. A., Tortuosity Determination of Battery Electrodes and Separators by Impedance Spectroscopy. *Journal of the Electrochemical Society* **2016**, *163* (7), A1373-A1387.
21. Jalkanen, K.; Karppinen, J.; Skogstrom, L.; Laurila, T.; Nisula, M.; Vuorilehto, K., Cycle aging of commercial NMC/graphite pouch cells at different temperatures. *Applied Energy* **2015**, *154*, 160-172.
22. Zhou, H.; Xin, F. X.; Pei, B.; Whittingham, M. S., What Limits the Capacity of Layered Oxide Cathodes in Lithium Batteries? *Acs Energy Letters* **2019**, *4* (8), 1902-1906.
23. Vetter, J.; Novak, P.; Wagner, M. R.; Veit, C.; Moller, K. C.; Besenhard, J. O.; Winter, M.; Wohlfahrt-Mehrens, M.; Vogler, C.; Hammouche, A., Ageing mechanisms in lithium-ion batteries. *Journal of Power Sources* **2005**, *147* (1-2), 269-281.
24. Li, H. Y.; Zhang, N.; Li, J.; Dahn, J. R., Updating the Structure and Electrochemistry of Li_xNiO_2 for $0 \leq x \leq 1$. *Journal of the Electrochemical Society* **2018**, *165* (13), A2985-A2993.
25. Li, J.; Downie, L. E.; Ma, L.; Qiu, W. D.; Dahn, J. R., Study of the Failure Mechanisms of $\text{LiNi}_{0.8}\text{Mn}_{0.1}\text{Co}_{0.1}\text{O}_2$ Cathode Material for Lithium Ion Batteries. *Journal of the Electrochemical Society* **2015**, *162* (7), A1401-A1408.
26. Schipper, F.; Erickson, E. M.; Erk, C.; Shin, J. Y.; Chesneau, F. F.; Aurbach, D., Review-Recent Advances and Remaining Challenges for Lithium Ion Battery Cathodes. *Journal of the Electrochemical Society* **2017**, *164* (1), A6220-A6228.
27. Li, W.; Reimers, J. N.; Dahn, J. R., In-situ X-Ray Diffraction and Electrochemical Studies of $\text{Li}_{1-x}\text{NiO}_2$. *Solid State Ionics* **1993**, *67* (1-2), 123-130.
28. Noh, H. J.; Youn, S.; Yoon, C. S.; Sun, Y. K., Comparison of the structural and electrochemical properties of layered $\text{Li Ni}_x\text{Co}_y\text{Mn}_z\text{O}_2$ ($x=1/3, 0.5, 0.6, 0.7, 0.8$ and 0.85) cathode material for lithium-ion batteries. *Journal of Power Sources* **2013**, *233*, 121-130.
29. Park, M. W.; Park, S.; Choi, N.-S., Unanticipated Mechanism of the Trimethylsilyl Motif in Electrolyte Additives on Nickel-Rich Cathodes in Lithium-Ion Batteries. *ACS Applied Materials & Interfaces* **2020**, *12* (39), 43694-43704.
30. Kim, H.; Grugeon, S.; Gachot, G.; Armand, M.; Sannier, L.; Laruelle, S., Ethylene bis-carbonates as telltales of SEI and electrolyte health, role of carbonate type and new additives. *Electrochimica Acta* **2014**, *136*, 157-165.
31. Vogl, U. S.; Das, P. K.; Weber, A. Z.; Winter, M.; Kostecki, R.; Lux, S. F., Mechanism of Interactions between CMC Binder and Si Single Crystal Facets. *Langmuir* **2014**, *30* (34), 10299-10307.
32. Gireaud, L.; Grugeon, S.; Laruelle, S.; Pilard, S.; Tarascon, J. M., Identification of Li battery electrolyte degradation products through direct synthesis and characterization of alkyl carbonate salts. *Journal of the Electrochemical Society* **2005**, *152* (5), A850-A857.
33. Han, G. P.; Wang, Y.; Li, H.; Yang, Z. H.; Pan, S. L., The first lithium difluorophosphate LiPO_2F_2 with a neutral polytetrahedral microporous architecture. *Chemical Communications* **2019**, *55* (12), 1817-1820.
34. Reed, W. Studies of difluorophosphoric acid and its alkali metal salts. The University of British Columbia, 1963.
35. Becker, G.; Ackermann, L. M.; Schechtel, E.; Klapper, M.; Tremel, W.; Wurm, F. R., Joining Two Natural Motifs: catechol-Containing Poly(phosphoester)s. *Biomacromolecules* **2017**, *18* (3), 767-777.
36. Edstrom, K.; Gustafsson, T.; Thomas, J. O., The cathode-electrolyte interface in the Li-ion battery. *Electrochimica Acta* **2004**, *50* (2-3), 397-403.
37. Xu, K., Electrolytes and Interphases in Li-Ion Batteries and Beyond. *Chemical Reviews* **2014**, *114* (23), 11503-11618.

38. Gachot, G.; Grugeon, S.; Armand, M.; Pilard, S.; Guenot, P.; Tarascon, J. M.; Laruelle, S., Deciphering the multi-step degradation mechanisms of carbonate-based electrolyte in Li batteries. *Journal of Power Sources* **2008**, *178* (1), 409-421.
39. Sasaki, T.; Abe, T.; Iriyama, Y.; Inaba, M.; Ogumi, Z., Formation mechanism of alkyl dicarbonates in Li-ion cells. *Journal of Power Sources* **2005**, *150*, 208-215.
40. Yoshida, H.; Fukunaga, T.; Hazama, T.; Terasaki, M.; Mizutani, M.; Yamachi, M., Degradation mechanism of alkyl carbonate solvents used in lithium-ion cells during initial charging. *Journal of Power Sources* **1997**, *68* (2), 311-315.
41. Tasaki, K., Solvent decompositions and physical properties of decomposition compounds in Li-ion battery electrolytes studied by DFT calculations and molecular dynamics simulations. *Journal of Physical Chemistry B* **2005**, *109* (7), 2920-2933.
42. Ellis, L. D.; Allen, J. P.; Thompson, L. M.; Harlow, J. E.; Stone, W. J.; Hill, I. G.; Dahn, J. R., Quantifying, Understanding and Evaluating the Effects of Gas Consumption in Lithium-Ion Cells. *Journal of the Electrochemical Society* **2017**, *164* (14), A3518-A3528.
43. Camacho-Forero, L. E.; Balbuena, P. B., Elucidating electrolyte decomposition under electron-rich environments at the lithium-metal anode. *Physical Chemistry Chemical Physics* **2017**, *19* (45), 30861-30873.
44. Manceron, L.; Andrews, L., Evidence for Alkali Metal Induced Intermolecular Acetylenic Hydrogen Atom Transfer between Hydrogen-Bonded Alkyne Complexes in Solid Argon. *Journal of Physical Chemistry* **1985**, *89* (19), 4094-4098.
45. Manceron, L.; Andrews, L., Infrared Spectra and Structures of Li(C₂H₄)_n (n = 1, 2, 3) and Li₂C₂H₄ in Solid Argon. *The Journal of Physical Chemistry* **1986**, (90), 4514-4528.
46. Kim, J.; Cha, H.; Lee, H.; Oh, P.; Cho, J., Surface and Interfacial Chemistry in the Nickel-Rich Cathode Materials. *Batteries & Supercaps* **2020**, *3* (4), 309-322.

General conclusions and perspectives of the work

This work has been dedicated to the surface reactivity of Ni-rich NMC materials and the understanding of the related degradation mechanisms. A focus was given to the reactions that lead to gas production upon high-temperature storage and to the study of the impact an electrolyte additive.

To begin with, this work introduced the main limitations of Ni-rich NMC materials associated with their reactivity: non-stoichiometric synthesis that leaves unreacted precursors in the form of soluble bases, the degradation in air that produces surface species and the electrolyte degradation upon battery functioning.

Concerning the soluble bases left from synthesis, we identified and accurately quantified, Li_2CO_3 , Li_2O and M_2SO_4 ($\text{M} = \text{Li}$ or Na), on five commercial Ni-rich NMC materials (532, 622, 622C, 811 and 901), by means of acid-base titration, ICP and AAS analyses after fine-tuning of water-solubilization parameters as duration, atmosphere and powder-to-water mass ratio. Attention must be paid to hydrolysis reaction, as it was proved to be at the origin of the LiOH soluble base. Commonly reported in the literature as being part of NMC surface species, this salt affects the electrode processing through NMP slurries gelation¹. Its absence in our materials was confirmed through FTIR, TGA/MS and NMR analyses. Beyond the scope of this work, establishing the stability limits of NMC materials in water is important for the development of water-based electrode processing, to replace the conventional NMP-based slurries, that so far has been attempted for NMC 111² and 532³.

Regarding the degradation of layered materials in air, for years, only lithium-based surface species were assumed to be produced. In this work, the degradation as function of NMC composition was studied through an accelerated exposure process in specific atmospheres. As a result, a novel degradation mechanism upon exposure to $\text{H}_2\text{O}/\text{CO}_2$, that does not involve any reduction process, was proposed. We suggest that, in addition to Li_2CO_3 , insoluble oxyhydroxide and oxide surface species of transition metals, are produced. Furthermore, the heaviest degradation was detected in the material with the highest nickel content, meaning that fresh Ni-rich NMC materials require more careful storage conditions than a typical NMC 111.

After the surface composition of our materials was exhaustively examined, their reactivity upon battery functioning was investigated. It was found that the presence of certain surface species, namely of Li_2CO_3 , Li_2O and M_2SO_4 ; could be advantageous for the electrochemical performances of the battery, since they produce LiPO_2F_2 (a known electrolyte additive) and LiF (a known stable passivating compound), by chemically reacting at high temperature with the electrolyte. As a perspective, these findings could be used to improve the industrial formation process of LIBs, in which by adjusting the storage temperature and time, an electrolyte additive would be generated in-situ. If not reacted, the risk is that Li_2CO_3 gets electrochemically oxidized into harming CO_2 and $^1\text{O}_2$, at a potential dependent on the particle size of Li_2CO_3 .

It is known that NMC materials that contain surface species often suffer from low electrochemical performances. In an effort to improve them, and comforted by the in-situ reactions evidenced by TG/MS analyses, a heat treatment at 500°C under argon atmosphere was carried out on as-received, washed and exposed NMC 622C. First, it was found that the capacity retention of the NMC material was not improved by the elimination of most of the soluble bases through washing; this result could have been expected from the literature as the quantity falls below a puzzling experimentally determined equilibrium value⁴. Similarly, annealing the as-received and the washed materials did not improve them either. On the other hand, annealing helped recover some capacity of the exposed material. We suggest that this is due to the in-situ reaction between Li_2CO_3 , oxygen and metal oxides, that decreased polarization and reformed an electrochemically-active layered phase. This would explain the literature about the improvement of the electrochemical performances after an annealing treatment at relatively low temperature.

Other consequence of the presence of surface species is slurry gelation. In our case, it was found that at a defined shear rate value, the viscosity of an as-received or of an exposed NMC remained the same, but at low shear rates it differed. With the knowledge of surface composition, a study devoted to slurries stabilities would be interesting to be undertaken.

Having found that many of the reactions of surface species produce gas, and knowing the safety risks and cycle life deterioration associated with gas production, the next step was to study the reactivity of Ni-rich NMC materials, from the analysis of gaseous products.

One of the goals of the thesis was to quantify permanent gases produced from batteries during storage and/or cycling. The GC-BID has demonstrated to be the best technique to achieve it. The key point of the gases quantification is their separation which operates through the use a column. Unfortunately, in our case, the appropriated conditions (column, GC mode...) to separate all the permanent gases were not found, H₂ and CO were missing. Although interesting results were obtained, this left an incomplete view of the total reaction mechanisms of the solvents degradation leading to gas formation, and did not allowed to estimate the total volume of produced gases. So, it seems important to pursue the work on separation optimization in the future.

As a preliminary stage to quantifying gas from pouch cells, storage tests of materials with electrolyte in specific containers were performed with the aim of assessing the impact of the NMC materials, the state of charge, the electrolyte salt and the dead volume on CO₂ production. Beforehand, it was found that the CO₂ produced from the electrolyte storage at 55 °C, was driven by PF₅ and thus was dependent on the dead volume of the container. Upon storage of pristine NMC powders with electrolyte, surprisingly, lower-nickel materials produced larger amount of CO₂, suggesting different electrolyte absorption properties. Afterwards, it was proven that the storage of delithiated NMC films increases CO₂ production, and was dependent of the nickel content. We inferred that this occurs through the oxidation of EC by ¹O₂.

The analyses in optimized 2- and 3-electrode pouch cells showed that the inside of the battery is a complex and dynamic system, with reactions of gas generation, and surprisingly, also of gas consumption. Through the use of a simplified storage protocol, it was possible to evidence that CH₄, C₂H₄, C₂H₆, from the formation step, are dependent mainly on current density. Additionally, several sources of CO₂ were evidenced (but not differentiated): chemical and electrochemical oxidation of solvents and Li₂CO₃, and thermal degradation of solvents. After storage, two phenomena were observed: C₂H₄ consumption and an increase of CO₂ concentration. Both are issued from the same cause: oxidation of C₂H₄ and EC by ¹O₂, influenced by the composition of NMC, due to more ¹O₂ being produced from higher nickel compositions. At the same time, the layered phase becomes rock salt phase, triggering impedance augmentation. This was evidenced in 3-electrode pouch cell experiments, but a meticulous TEM study to link the surface reactions to the suspected structural transformations would be ideal to confirm it.

These conclusions convey the key message that there is still room for understanding the crosstalk reactions and the mechanism through which $^1\text{O}_2$ oxidizes C_2H_4 and EC. The work on gas evolution constitute the bases for following research.

As stated at the beginning of this work, the use of electrolyte additives is one of the most effective and economical ways to improve the electrochemical performances of LIBs containing Ni-rich NMC materials. LiPO_2F_2 (LDFP) was chosen as electrolyte additive after we found that it is produced from the in-situ chemical reactions of certain surface species. Moreover, the literature agrees that it improves the cycling performances and decreases the gas production; although its action mechanism remains a controversial point.

It was found that LDFP does not behave as a typical additive that reduces or oxidizes in the first cycles and also does not hinder the solvent reduction processes. In fact, virtually no differences in the CEI formed with/without LDFP were found and the only difference in the SEI, is the enrichment with fluorine- and phosphor-based species, when LDFP is used. Regarding the action mechanism, electrolyte analyses revealed that LDFP scavenges RO^\cdot , thus preventing electrolyte ageing. However, determining its exact role on CO_2 production in NMC 622C- and 811-containing cells, needs further investigation.

Moreover, it was shown that LDFP exhibits a contradictory role upon complete cells cycling at 55°C : beneficial in case of NMC 622C and deleterious in case of NMC 811. Upon opening of the 811/Gr cells, broken particles are observed, mostly when LDFP is used. TEM analyses helped us to hypothesize that chemical reactions occurred on the interphase in-between the primary grains of NMC 811, possibly made of soluble bases, inducing grain decohesion and contact loss. This phenomenon is exacerbated due to the increased LDFP concentration and eventually causes particle cracking. Therefore, we conclude, that the use of LDFP in cell containing NMC 811 is restricted by its surface chemistry. In this regard, the use of monocrystal NMC can be envisaged to minimize these reactions. Xiong et al.⁵ have already reported reduced reactivity from NMC 532 toward the electrolyte, although NMC with higher nickel content has not been tested yet.

Lastly, the results in this thesis not only open up lines of research that might be pursued in this research group, but also helped to enrich the understanding of Ni-rich NMC materials for its implementation in the automotive industry.

References

1. Kim, D.; Cha, J.; Kim, H. Positive electrode slurry composition for lithium secondary battery, lithium secondary battery comprising the same and method of making the lithium secondary battery. 2012.
2. Cetinel, F. A.; Bauer, W., Processing of water-based $\text{LiNi}_{1/3}\text{Mn}_{1/3}\text{Co}_{1/3}\text{O}_2$ pastes for manufacturing lithium ion battery cathodes. *Bulletin of Materials Science* **2014**, *37* (7), 1685-1690.
3. Bichon, M.; Sotta, D.; Dupre, N.; De Vito, E.; Boulineau, A.; Porcher, W.; Lestriez, B., Study of Immersion of $\text{LiNi}_{0.5}\text{Mn}_{0.3}\text{Co}_{0.2}\text{O}_2$ Material in Water for Aqueous Processing of Positive Electrode for Li-Ion Batteries. *Acs Applied Materials & Interfaces* **2019**, *11* (20), 18331-18341.
4. Paulsen, J.; Kim, J. High nickel cathode material having low soluble base content. 2012.
5. Xiong, D. J.; Ellis, L. D.; Li, J.; Li, H. Y.; Hynes, T.; Allen, J. P.; Xia, J.; Hall, D. S.; Hill, I. G.; Dahn, J. R., Measuring Oxygen Release from Delithiated $\text{LiNi}_x\text{Mn}_y\text{Co}_{1-x-y}\text{O}_2$ and Its Effects on the Performance of High Voltage Li-Ion Cells. *Journal of the Electrochemical Society* **2017**, *164* (13), A3025-A3037.

Annex I (Chapter II)

- **Scanning electron microscopy (SEM)**

SEM images of each NMC powder were carried out by means of a field emission gun scanning electron microscope fitted with an energy dispersive X-ray spectrometer (SEM-EDX, Oxford Instrument), operating at 15 kV and in secondary electrons (SE) or backscattered electrons (BSE) mode.

- **Powder X-ray diffraction (XRD)**

An XRD (Bruker) using Cu K α radiation, accelerating voltage of 40 kV and current of 100 mA was used to identify the crystalline structure of each powder. The data were obtained in the 2θ range of 10–80° with a step size of 0.02° and scan rate of 2°·min⁻¹.

- **Atomic absorption spectroscopy (AAS)**

The AAS equipment (Perkin Elmer, Analyst 300) is composed of a hollow cathode lamp specific for each element, a 3200 °C blue flame produced from the combustion of air/acetylene with flow rate 7:16; a monochromator to isolate the specific wavelength to be measured and a detector to measure the light accurately (Fig. A.1a). For the element analysis, the filtrate solution was diluted 25 and 50 times in bi-distilled water and standards solutions of Li, Na, K, Mg, Ca, Al, Ni, Co and Mn were prepared with concentrations between 0.2 – 5 ppm. Each diluted solution was sprayed into the flame and the adsorbed light was measured.

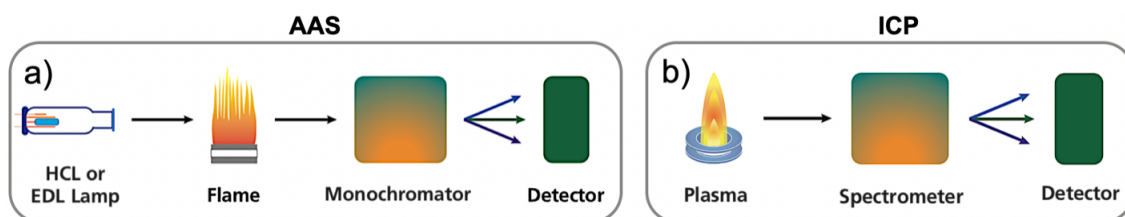


Figure A.1. Simplified representations of the main components in **a)** AAS and **b)** ICP-AES spectroscopies. Taken from Perkin Elmer resources⁶³.

- **Inductively coupled plasma atomic emission spectroscopy (ICP-AES) (analyses performed at Technocentre - Renault)**

The ICP-AES equipment (Varian 720 ES) consists in an argon plasma that can reach temperatures as high as 10000 °C, allowing the complete atomization of a wide range of elements. Then, the spectrometer separates and focuses the desired emitted wavelengths onto

the detector (Fig. A.1b). Since this technique does not require lamps specific for each element, a wide range of elements was sought: Al, Si, P, S, Na, Mg, K, Ca, Ti, Cr, Mn, Fe, Co, Ni, Cu, Zn and Mo. Only those with significant concentrations were quantified through comparison of their emission intensities to the calibration curve constructed with standards of known concentration.

For the element analysis in the filtrate solution, the filtrate solution was diluted to a factor of 2 and acidified to 2% with 1M HNO₃. Calibration curves were constructed from the elements that were found in significant concentration in the analyte solution. For the powders, 250 mg of each NMC powder were dissolved separately in 30 ml of *aqua regia* (HCl/HNO₃ 2:1, vol.), during four hours in a sand bath at 140 ± 10 °C. The transition metals and aluminum were dosed from the solution diluted by a factor of 1000 and 100 in ultra-pure water, respectively. In both ICP and AAS, every analysis was performed at least three times to ensure reproducibility and the error bars were constructed from the standard deviation of the repetitions, in addition to the error inherent to water dilutions. The amount of every element, in ppm, in each filtrate solution was converted into concentration mol.g_{NMC}⁻¹, given that the amount of water and powder is known.

- **Fourier transform infrared (FTIR)**

FTIR was carried out in ATR mode (FTIR-ATR, Nicolet iS20) using a Ge crystal, in a dry room with dew point between -58 and -63 °C (~5-10 ppm of H₂O). Anhydrous lithium sulfate was obtained from the vacuum-drying at 130 °C overnight of Li₂SO₄.1H₂O (Sigma-Aldrich, 99%).

- **Thermogravimetric analysis–mass spectrometry (TGA-MS)**

The TGA-MS instrument (STA 449F3, NETZSCH, Germany) is placed inside an argon-filled glovebox (< 0.1 ppm O₂ and H₂O, Jacomex). The experiments were performed from 25 to 900 °C at a rate of 5 K.min⁻¹ under argon atmosphere at a flow rate of 40 ml.min⁻¹.

- **Raman Spectroscopy**

The exposed NMC powder was measured without further treatments, on a Raman DXR microscope (Thermo Fisher Scientific) with a He-Ne laser ($\lambda = 532$ nm, 4mW), an objective with 10X magnification and 50 μ m pinhole aperture. The Raman spectra were measured under air within no more than five minutes to avoid heavy decomposition and on different areas to ensure reproducibility.

Annex II (Chapter III)

- **Preparation of reference materials and electrolyte**

The reference materials Li_2CO_3 (> 99%) and Li_2O (97%) were purchased from Sigma-Aldrich. Li_2SO_4 was obtained by vacuum-drying at 130 °C of $\text{Li}_2\text{SO}_4 \cdot \text{H}_2\text{O}$ (Sigma-Aldrich, 99%). LiOH was synthesized by Li reaction with methanol, then vacuum-dried. The electrolyte consists in 1M LiPF_6 in a mixture of EC/DEC/EMC 1:1:1 vol. (99.9%, H_2O < 20 ppm; Solvionics).

- **Nuclear magnetic resonance (NMR)**

The NMR analyses were performed in a Bruker Ultrashield 400 MHz and the fluorine (376.5 MHz) spectra were acquired with a 5-mm nitrogen cryoprobe and recorded with a relaxation delay of 5s prior to one 90° pulse excitation (13.5 μs) and an acquisition time of 0.8 s (total relaxation for relative quantification).

- **Preparation for ball milling**

Inside the argon-filled glovebox (< 0.1 ppm O_2 and H_2O , MBraun), to avoid air exposure, 5 g of Li_2CO_3 powder were weighed and introduced to the SPEX cell to be mechanically milled by means of a ball miller (SPEX 800) during 35 minutes, in order to reduce the particle size.

- **Preparation for electrochemical analysis with powder in half-cells**

The Li_2CO_3 (pristine or milled) and Li_2SO_4 powders, and the 20-days exposed NMC 622C, were grounded separately with conductive carbon black C45 (and $\text{BET} = 45\text{m}^2 \cdot \text{g}^{-1}$, 20 nm particle size Sigma Aldrich) in a 9:1 mass ratio to form conductive composites. Half-cells Swagelok-type (Fig. A.2) with a lithium foil (battery grade, >99%, Alfa Aesar) as negative electrode, were assembled inside the argon-filled glovebox, with a dried glassy fiber (Whatman GF/D) and a dried monolayer porous polypropylene (PP, Celgard 2500, 25 μm thick and 55% of porosity) as separators, impregnated with 150 μL of LiPF_6 -based electrolyte. The PP separator faces the positive electrode side, so the powder can be recovered easily for FTIR analysis, if needed. On the positive electrode side, 12 ± 0.2 mg of the powder composites made of Li_2CO_3 or Li_2SO_4 were used or 16.8 ± 0.1 mg. Potential limitation charge-discharge cycling was performed on the assembled Swagelok-type cells using a VMP-3 potentiostat/galvanostat (Biologic SA). The potential window was 2.8–4.5V at C/40 and 25 °C. Prior cycling, the cells rested 5h to allow complete electrolyte impregnation.

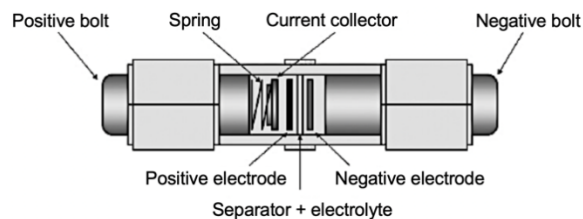


Figure A.2. Scheme of the Swagelok-type cell with an inside view of the components.

- **Fabrication of positive electrodes**

The positive electrodes were fabricated in the dry room with dew point between -58 and -63 °C (~ 5 - 10 ppm of H_2O), from a slurry with 90 wt.% active material, 6 wt.% conductive carbon black C45 and 4 wt.% of PVDF binder (Sigma-Aldrich); using N-Methyl-2-Pyrrolidone (NMP, Sigma-Aldrich) as solvent. The ratio between dry and wet mass was 55:45 wt.%. Then, the slurry was spread onto an aluminum foil 21.5 ± 0.5 μm thick by means of a doctor blade with gap of 250 μm on an automatic film applicator (Elcometer 4340), and left to dry at 60 °C overnight in the dry room. The porosity of the electrodes (only the compositions NMC 532, 622 and 622C) was fixed to 35% with a calendaring machine of double rolls maintained at 60 °C (People and Technology INC. BPN-250); the process was finished within 15 minutes. Prior to utilization, the positive electrode films were dried again under vacuum in a Büchi oven at 110 °C overnight.

- **Powder preparation for FTIR analysis**

Immediately after the electrochemical evaluation, the Swagelok-type cells containing NMC powder were transferred to the glovebox and the powders were rinsed with dimethyl carbonate (DMC) and centrifuged three times to remove the electrolyte salts. Then, they were left to vacuum dry at ambient temperature overnight. The FTIR experiments were carried out in ATR mode, using a Ge crystal, in the dry room.

- **Annealing of powder materials**

The annealing consisted in putting 10g of the material in an alumina boat inside a tubular furnace under constant argon flow (0.5 ml.min $^{-1}$). The temperature program was defined to heat at 5 K.min $^{-1}$ up to 500 °C, then 7 hours fixed at this temperature and finally cool at 5 K.min $^{-1}$ until 40 °C. At the end of the temperature program, the tube was isolated from both sides while keeping argon atmosphere inside, and the annealed powders were transferred from the tube to the glovebox with limited air exposure.

- **Calculation of shear rate (γ)**

Shear rate is defined as the rate at which a shearing deformation is applied to the slurry (Fig. A.3) by a moving plate. The formula to calculate the shear is the following:

$$\gamma = \frac{\Delta x / \Delta t}{Gap}$$

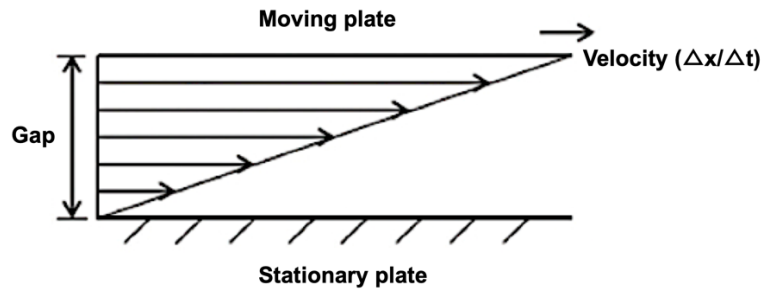


Figure A.3. Scheme representing the origin of the shear rate.

In the case of the shear rate during the coating of a film onto the aluminum film, the velocity used is $0.85 \text{ cm}\cdot\text{s}^{-1}$ and the gap 0.025 cm , which gives a shear rate of 34 s^{-1} .

Annex III (Chapter IV)

- **Description of the gas chromatography (GC) device**

GC is composed of an inert gaseous mobile phase that flows through the separation column toward the detector, and a stationary phase, which is a solid or liquid coated or packed onto the column located inside a temperature-controlled oven (Fig. A.4). Gaseous and liquid samples are injected with gas-tight syringes. After the injection, the analyte sample gets vaporized in the heated injector (3) and then enters to the column (5) contained inside a temperature-controlled oven (4), where each component is retained differently depending on the interaction of the stationary phase and the analytes. Finally, the quality of the chromatogram (7) depends on the conditions defined in the method (2), the type of gas in the mobile phase (1) and the sensibility of the detector (6).

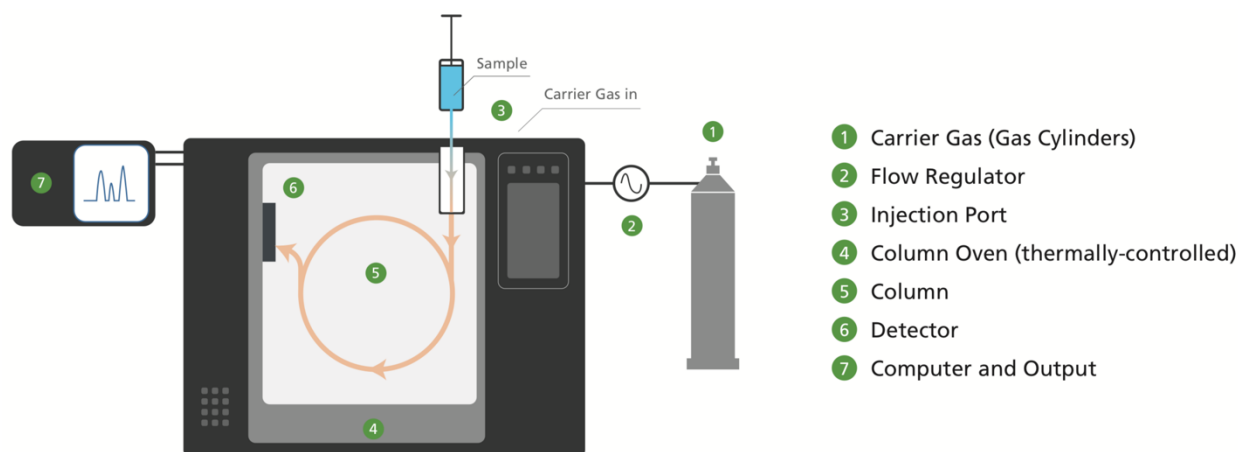


Figure A.4. Scheme of the gas chromatography technique⁵¹.

- **Irreproducibility of the micropacked column in a GC/BID device**

To illustrate the irreproducibility, three different concentrations of standard gaseous mix CO-CH₄-CO₂-C₂H₄-Ar in 1:1:1:1:96 mol% were analyzed three times each. It can be appreciated that the values do not cross zero and most of them present very high standard deviation.

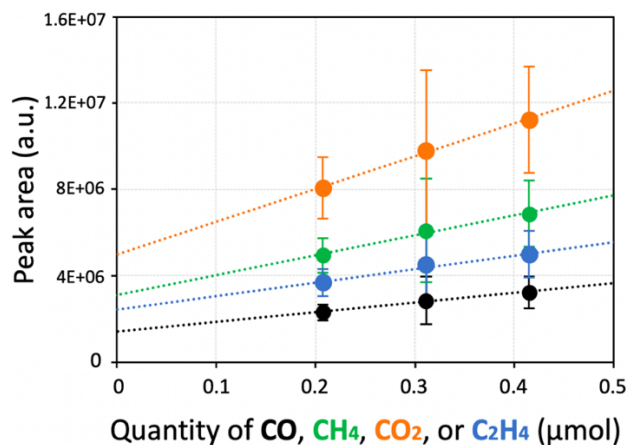


Figure A.5. Reproducibility tests with standard gaseous mix of CO-CH₄-CO₂-C₂H₄-Ar, evidencing the irreproducibility. The tests were performed in with a micropacked column installed in a GC/BID.

- **Pouch cell sealing conditions**

All of the pouch cells were prepared in the dry room, where three sides were sealed prior electrolyte filling with a Joke Registron machine at 115 °C during 3.5 s, followed by 3 s of cooling. Then, the pouch cells were vacuum-dried overnight at 80 °C. The pouch cell was degassed for 8 seconds and the last side was sealed after electrolyte filling (80 μl) with a vacuum sealer (Henkelman Boxer 42 XL) until 98% of the oil pump capacity. The electrolyte was 1M LiPF₆ in a 1:1:1 vol. mixture of EC/DEC/EMC (99.9%, H₂O < 20 ppm; Solvionics). The separator is the Celgard 2500.

- **GC/MS-IR experimental conditions**

GC/MS-IR analyses were performed using a trace GC ultra-gas chromatograph (Thermo Scientific) connected to an ISQ 1100 mass spectrometer (Thermo Scientific) and to a FTIR system Nicolet 6700 with a mid-infrared source and a medium band, liquid nitrogen cooled mercury cadmium telluride detector. The GC was interfaced with a light-pipe GC/FTIR (Thermo Scientific), according to the procedure described by Gachot et al.²⁶. The Aldrich vapour phase FTIR library and the National Institutes of Standards (NIST) library of ionized compounds were used.

- **Capillary column for GC/MS-IR and GC/BID**

The capillary column used is a HP-PLOT Q capillary column from Agilent J & W Technologies (30m, d=0.32mm, 0.020 mm ID, polystyrene-codivinybenzene-based) connected to a postcapillary column Rtx-1 from Restek (15 m, 0.25 mm ID, 0.25 μm, 100%

poly(dimethylsiloxane)). Helium was used as carrier gas and was maintained at a constant flow rate of $1.3 \text{ ml}\cdot\text{min}^{-1}$. The oven program starts at $40 \text{ }^\circ\text{C}$ for 6min, then ramps at $10 \text{ }^\circ\text{C}\cdot\text{min}^{-1}$ up to $90 \text{ }^\circ\text{C}$, increased at $5 \text{ }^\circ\text{C}\cdot\text{min}^{-1}$ up to $190 \text{ }^\circ\text{C}$, held for 5 min, increased at $10 \text{ }^\circ\text{C}\cdot\text{min}^{-1}$ up to $250 \text{ }^\circ\text{C}$, where it was held for 10 min (Fig. A.6). The total duration of GC analysis was 52 min. The transfer line was maintained at $250 \text{ }^\circ\text{C}$ in the GC/MS-IR and the ion source was set at $200 \text{ }^\circ\text{C}$. In the GC/BID the plasma temperature was set at $280 \text{ }^\circ\text{C}$ and the injector port at $150 \text{ }^\circ\text{C}$.

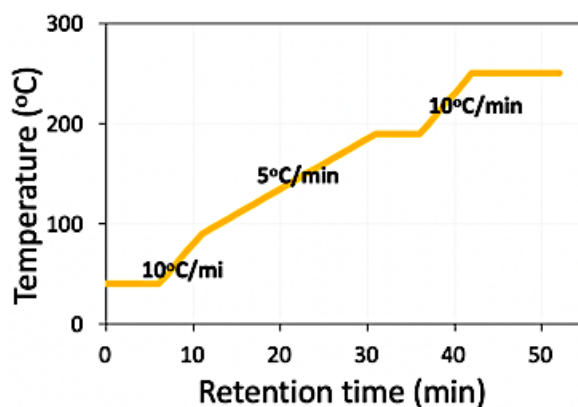


Figure A.6. Oven temperature program for the capillary column.

- **Micropacked column for GC/BID**

The micropacked column used is a ShinCarbon ST micropacked column from Restek (100/120 mesh, 2m, $d=1.587 \text{ mm}$, 1mm ID, cat.# 19808, carbon molecular sieve-based of $\sim 1500 \text{ m}^2\cdot\text{g}^{-1}$). Helium was used as carrier gas and the flow rate started at $1.3 \text{ ml}\cdot\text{min}^{-1}$ but varied in function of the pressure necessities. The oven temperature program starts at $40 \text{ }^\circ\text{C}$ for 3 min, then ramps at $8 \text{ }^\circ\text{C}\cdot\text{min}^{-1}$ up to $250 \text{ }^\circ\text{C}$ where it is held for 12 minutes (Fig. A.7). The total duration of GC analysis was 38 min. The plasma temperature was set at $280 \text{ }^\circ\text{C}$ and the injector port at $150 \text{ }^\circ\text{C}$.

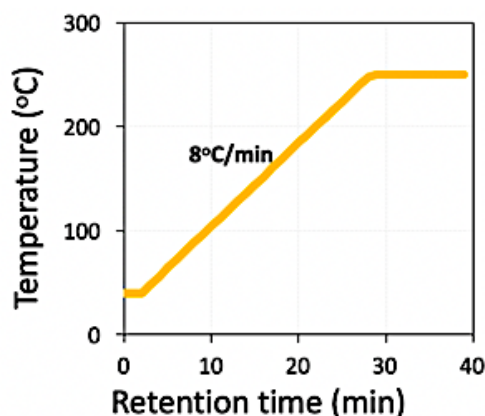


Figure A.7. Oven temperature program for the micropacked column.

- **Calibration curves in GC/BID**

Calibration curves were performed with a standard gaseous mix of CO-CH₄-CO₂-C₂H₄-Ar in 1:1:1:1:96 mol%. Known volumes of the mixture were injected and the peak areas were measured to construct the calibration curves of CO₂ and C₂H₄ using the “regular” method (Fig. A.8); and of CH₄, CO₂ and C₂H₄ using the “improved” method (Fig. A.9); both used a capillary column in GC/BID.

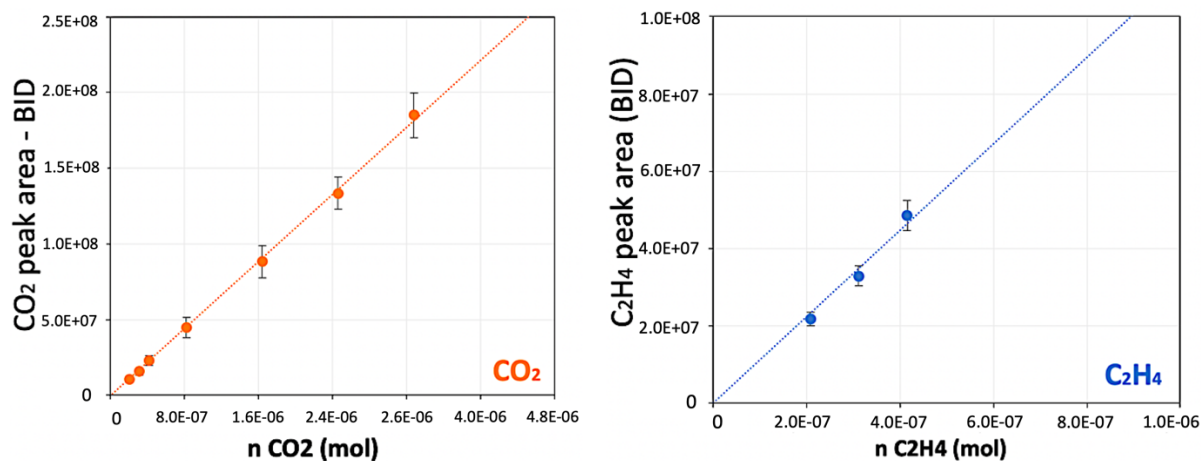
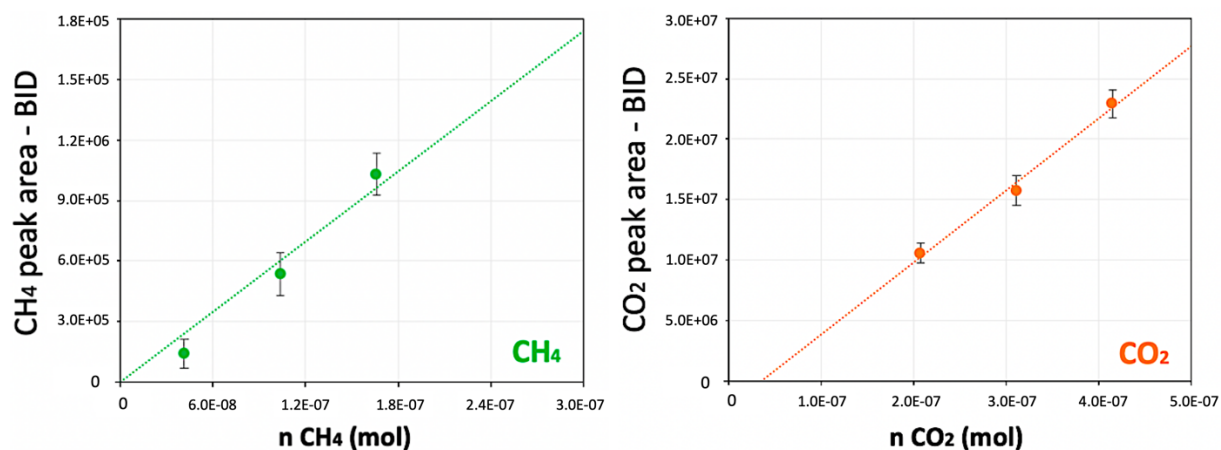


Figure A.8. Calibration curves obtained from the analysis of multiple acquisitions in GC/BID with a capillary column and the “regular” method.



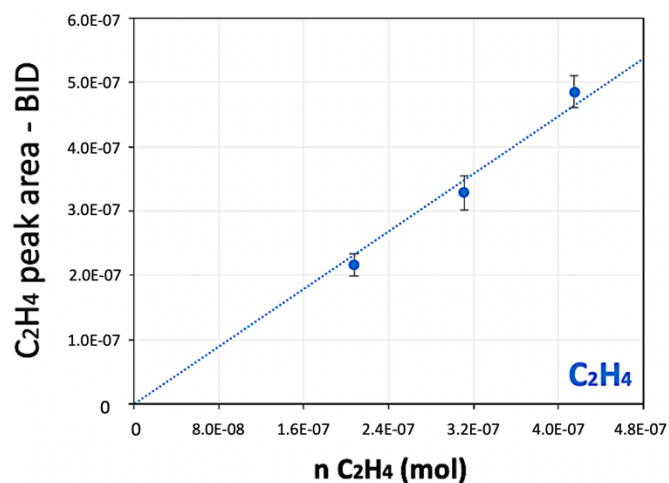


Figure A.9. Calibration curves obtained from the analysis of multiple acquisitions in GC/BID with the “improved” method and a capillary column.

- **Representative cycling of pouch cells NMC 811/Gr**

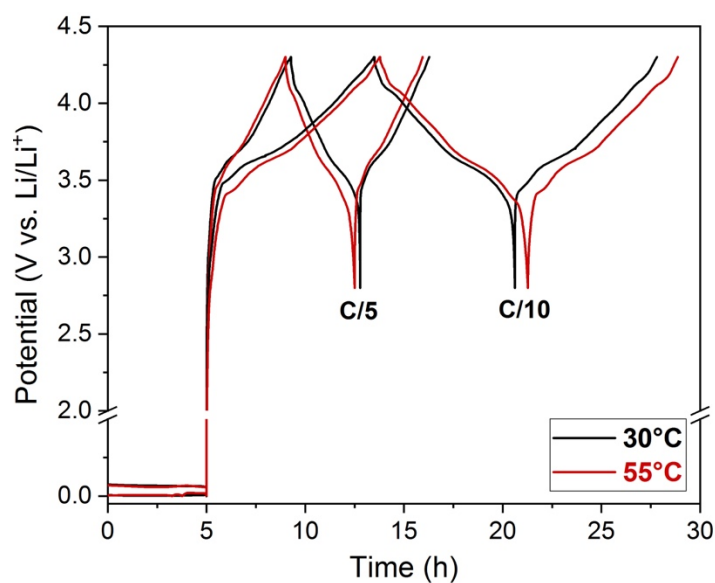


Figure A.10. Time vs. potential representative curves of the formation cycles at different temperatures and C-rates.

Annex IV (Chapter V)

- **Ionic conductivity measurements**

An MTZ-35 frequency response analyzer was used to perform the ionic conductivity measurements. The starting and ending frequencies were 3×10^7 Hz and 30 Hz, with 20 points per decade and the temperature on the cells was controlled by introducing them in a H₂O/EtOH bath inside a cryostat that was manually changed between -10 to 55 °C. The starting temperature of 25 °C was first decreased to -10 °C measuring every 5 °C and with 15 minutes of resting time in between measurements. Then, the temperature was increased to 25 °C, with a space of 30 minutes in between, to check that the electrolyte has not changed its properties; and then the measurements were taken every 5 °C.

For the measurements in separator, pouch cells with a Celgard 2500 separator sandwiched between two symmetrical electrodes of copper of 4cm² were constructed. 1 h of impregnation was allowed after adding the electrolyte and sealing under vacuum.

- **Graphite composite preparation and cycling**

The graphite powder (Timcal TIMREX SLS, ~ 1.5 m².g⁻¹) was grounded with conductive carbon black C45 (20nm and BET = 45m².g⁻¹, Sigma Aldrich) in a 9:1 mass ratio to form conductive composites. Half-cells Swagelok-type were assembled following procedure in Annex II. Around 11mg of the composite were used. One cycle with potential limitation was performed using a VMP-3 potentiostat/galvanostat (Biologic SA). The potential window was 1.5 – 0.01 V at C/20 and 25 °C or 55 °C.

- **FTIR analyses in transmission mode**

The composite powders were recovered following the protocol of Annex II. Then, KBr pellets were prepared inside the glovebox by grounding in a mortar the dry composite and the dry KBr, followed by analysis in a FTIR device (Nicolet iS20) with minimal air exposure.

- **Focused-ion beam (FIB) cut and transmission electron microscopy (TEM)**

Samples of NMC 622C and 811 in film were shipped for TEM sample preparation by FIB cut to the Institut d'Electronique, de Microélectronique et de Nanotechnologie (IEMN) through the RENATECH platform. Each sample was first positioned in a sample holder and taken inside of a FIB dual Beam FEI Strata DB 235 equipped with both a gallium ion source and an electron source. Then, a platinum thin layer was deposited on top of an area of interest to

protect it from the ion irradiation. In the selected area, gallium ions were used to pulverize the matter to create a section of a hundred of nanometers thick over 3-4 μm in depth. The created section is cut on the edges and attached using platinum to a micromanipulator to be afterwards positioned at the edge of a grid holder. It is then separated from the micromanipulator and attached to the TEM grid using platinum. Finally, the sample was thinned by consequent gallium ion irradiation with lower beam energy until the desired thickness was achieved. The samples were then shipped back and analyzed by (TEM) (FEI Tecnai G2 electron microscope operating at 200 kV) without further treatments and with minimal air exposure.

- **Electrolyte recovery from pouch cells and “liquid” GC/MS conditions**

The electrolyte was extracted from pouch cells by vortexing each separator in 1mL of acetonitrile for 1 minute. The resulting liquid was diluted with dry acetonitrile (HPLC grade) by a factor of 200 and then 2 μL were analyzed by “liquid” GC/MS and by a factor of 2000 for ESI-HRMS analysis.

“Liquid” GC/MS analyses were performed using a trace 1300 series GC Ultra gas chromatograph interfaced with an ISQ mass spectrometer (both Thermo Scientific). The chromatographic separation was performed on a “BPX70” cyanopropyl polysilene–siloxane based capillary column (30 m x 0.25 mm i.d., 0.25 mm) from SGE.

- **High resolution mass spectrometry – electrospray ionization (ESI-HRMS)**

Experimental conditions

ESI-HRMS experiments were performed in the positive ion mode on a Q-TOF Ultima Global instrument (Waters- Micromass, Manchester, UK) equipped with a pneumatically assisted electrospray ion source (Z-spray) and an additional sprayer for the reference compound (LockSpray). The prepared solutions were directly introduced (5 L.min⁻¹) via an integrated syringe pump in the electrospray source. The source and desolvation temperatures were kept at 120 and 450 °C, respectively. Nitrogen was used as a drying and nebulizing gas. The cone gas flow and desolvation gas flow rates are 50 and 800 L.h⁻¹, respectively; and the capillary voltage was 3.0 kV (POS).

Method for ion listing

- Record the maximum chromatographed ions associated with a retention time in each sample and delete duplicates.

- Create a method for integrating peaks by TargetLynx by specifying the mass measured at the appropriate retention time.
- Use TargetLynx on all mode samples (positive or negative), including at least one blank per sample.

Method for cleaning TargetLynx results

- Replace with 0 all values less than $Moyenne_{blancs} + (10 \times Ecarttype_{blanc})$.
- If variables are equal to 0 in all samples (blanks excluded), then delete the variables.
- Application of a threshold for the positive mode in order to keep only the strongly expressed variables: if the integration of a variable is greater than 1000 in at least one of the samples, this variable is kept, otherwise it is deleted.
- Format data as a matrix (column = ions; row = samples).

Table of abbreviations

Abbreviation	Definition
AAS	Atomic absorption spectroscopy
BET	Brunauer–Emmett–Teller
C45	Carbon black Timcal Super 45
Cal.	Calendered
CE	Coulombic efficiency
CEI	Cathode electrolyte interphase
CMC	Carboxymethyl cellulose
CV	Cyclic voltammetry
DEC	Diethyl carbonate
DMA	9,10-dimethylantracene
DMC	Dimethyl carbonate
E + A	Exposed + annealed material
EC	Ethylene carbonate
EIS	Electrochemical impedance spectroscopy
ESI	Electrospray ionization
EMC	Ethyl methyl carbonate
E _{ox}	Oxidation potential
EV	Electric vehicle
Exp.	Exposed
FIB	Focused-ion beam
FID	Flame ionization detector
FTIR	Fourier Transform Infrared spectroscopy
GC/MS	Gas chromatography coupled with mass spectrometry
Gr	Graphite
HEV	Hybrid electric vehicle
HRMS	High-resolution mass spectrometry
HRTEM	High-resolution transmission electron microscopy
ICE	Internal combustion engine
ICP-AES	Inductively coupled plasma atomic emission spectroscopy
IEA	International Energy Agency
LCO	Lithium cobalt oxide or LiCoO ₂
LDFP	Lithium difluorophosphate or LiPO ₂ F ₂
LIB	Lithium-ion battery
LFP	Lithium iron phosphate or LiFePO ₄
LiTFSI	Lithium bis(trifluoromethanesulfonyl)imide
LNO	Lithium nickel oxide or LiNiO ₂
LTO	Lithium titanate or Li ₄ Ti ₅ O ₁₂
<i>n</i>	Quantity of moles
NCA	Lithium nickel cobalt aluminum oxide or LiNi _{0.8} Co _{0.15} Al _{0.05} O ₂
Ni-Cd	Nickel cadmium battery
Ni-MH	Nickel metal-hydride battery
NMC	Lithium nickel manganese cobalt oxide or LiNi _{1-x-y} Mn _x Co _y O ₂
NMP	N-methyl-2-pyrrolidone
NMR	Nuclear magnetic resonance spectroscopy
OCV	Open circuit voltage
OEMS	On-line electrochemical mass spectrometry

Table of abbreviations

PC	Propylene carbonate
PCL	Premature capacity loss
PE	Polyethylene
PEIS	Potentiostatic electrochemical impedance spectroscopy
PET	Polyethylene terephthalate
PHEV	Plug-in hybrid electric vehicles
PP	Polypropylene
PSD	Particle size distribution
PVDF	Polyvinyl difluoride
Q	Capacity
R	As-received materials
R-A	As-received + annealed materials
Refs	References
RT	Retention time
SEI	Solid electrolyte interphase
SEM	Scanning electron microscopy
SEM/EDX	SEM with electron dispersive X-ray
SOC	State of charge
SoH	State of health
T _b	Boiling temperature
TCD	Thermal conductivity detector
TEM	Transmission electron microscopy
TG-MS	Thermogravimetric/mass spectrometry
T _m	Melting temperature
ToF-SIMS	Time-of-flight secondary ion mass spectroscopy
UPD	Under-potential deposition
VC	Vinylene carbonate
vs.	versus
W	Washed material
W-A	Washed + annealed material
XRD	X-Ray diffraction
XPS	X-Ray photon spectroscopy
ε	Dielectric constant

Résumé développé de la thèse en Français

Au cours de la dernière décennie, le marché des batteries s'est rapidement développé avec l'adoption croissante des véhicules électriques. Pour répondre aux besoins en termes de densité d'énergie, les matériaux lamellaires $\text{LiNi}_{1-x-y}\text{Mn}_x\text{Co}_y\text{O}_2$ (NMC) de composition 111, 442 et 532 ont fait leurs preuves comme matériaux actifs pour l'électrode positive. Néanmoins, la tendance actuelle s'oriente désormais vers l'utilisation de matériaux NMC riches en nickel ($\text{Ni} > 0,5$), tels que NMC 811, en raison de l'augmentation de la densité d'énergie donnée par la teneur en nickel (Fig. 1a). Cependant, les performances électrochimiques et son utilisation étendue sont grandement limitées par la réactivité de surface vis-à-vis de l'air et de l'électrolyte à base de LiPF_6 (Fig. 1b).

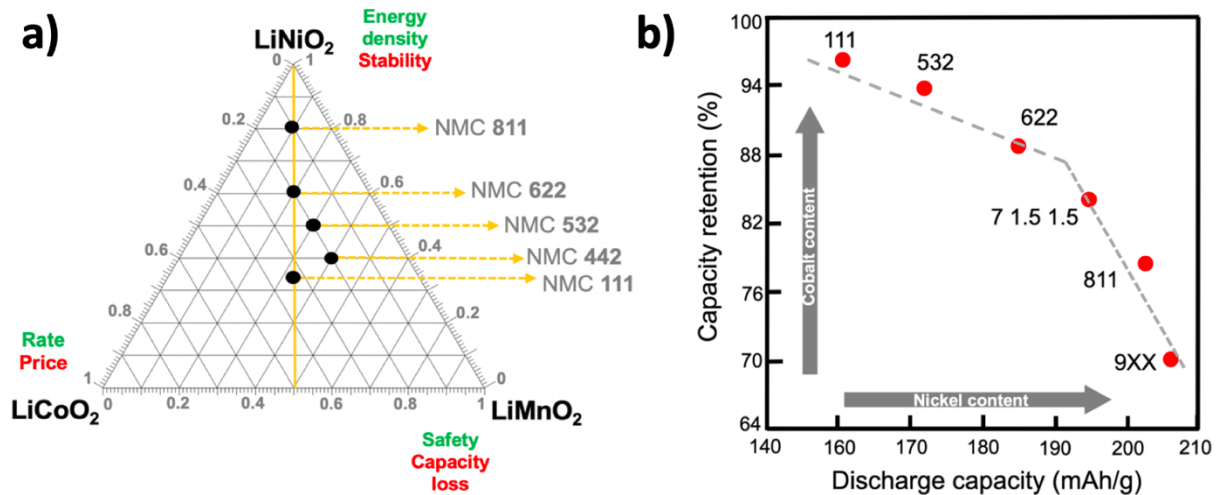


Figure 1. a) Diagramme de phase ternaire LiCoO_2 - LiMnO_2 - LiNiO_2 avec les principaux avantages en vert et inconvénients en rouge. Adapté de Schipper et al.¹ **b)** Comparaison de la performance électrochimique des matériaux NMC. Adapté de Noh et al.²

Dans ce contexte, divisé en cinq chapitres, ce travail prétend à contribuer à la compréhension des réactions de dégradation et à la réactivité de surface des matériaux NMC riches en nickel, en mettant l'accent sur les réactions qui génèrent du gaz. Dans un premier temps, une étude de la composition et de la quantification des espèces de surface en fonction de la teneur en nickel est réalisée. Ceci est suivi d'une étude de leurs mécanismes respectifs de formation et de leur réactivité dans des conditions de batterie. Ensuite, les produits gazeux issus de la dégradation de l'électrolyte sont étudiés en fonction de la teneur en espèces de surface et de la composition en métaux de transition. Enfin, un additif d'électrolyte est testé avec des matériaux NMC

riches en nickel, dans l'espoir de contrecarrer la réactivité et ainsi de diminuer la production de gaz.

Chapitre I : État de l'art et contexte de l'étude.

Ce chapitre est une revue de la littérature sur les batteries rechargeables pour les applications automobiles. Les avantages et les limitations des matériaux NMC riches en nickel y sont présentés. Les limitations discutées sont (i) la difficulté de synthétiser des matériaux stœchiométriques, qui laisse souvent des bases hydrosolubles sur la surface, (ii) la dégradation structurelle de surface due à l'exposition à l'environnement, et (iii) la dégradation structurelle des matériaux NMC lors du fonctionnement de la batterie. Sa relation avec la perte des performances électrochimiques est expliquée. De plus, les revêtements de surface et les additifs d'électrolyte sont décrits comme des stratégies pratiques pour l'industrie pour contrer les limitations de ces matériaux. En effet, lorsque les matériaux NMC contiennent plus de nickel, ils ont tendance à être plus réactifs vis-à-vis de l'air, entraînant la formation d'espèces de surface³; et vers l'électrolyte, en raison de l'état délithié hautement réactif¹. Les deux ont un impact négatif sur les performances électrochimiques et doivent donc être traités.

Chapitre II : Identification, quantification et mécanisme de formation des espèces de surface dans les matériaux NMC riches en nickel.

Dans un premier temps, la caractérisation de cinq matériaux commerciaux NMC riches en nickel (Fig. 2), avec $0,5 \leq \text{Ni} \leq 0,9$, a été réalisée.

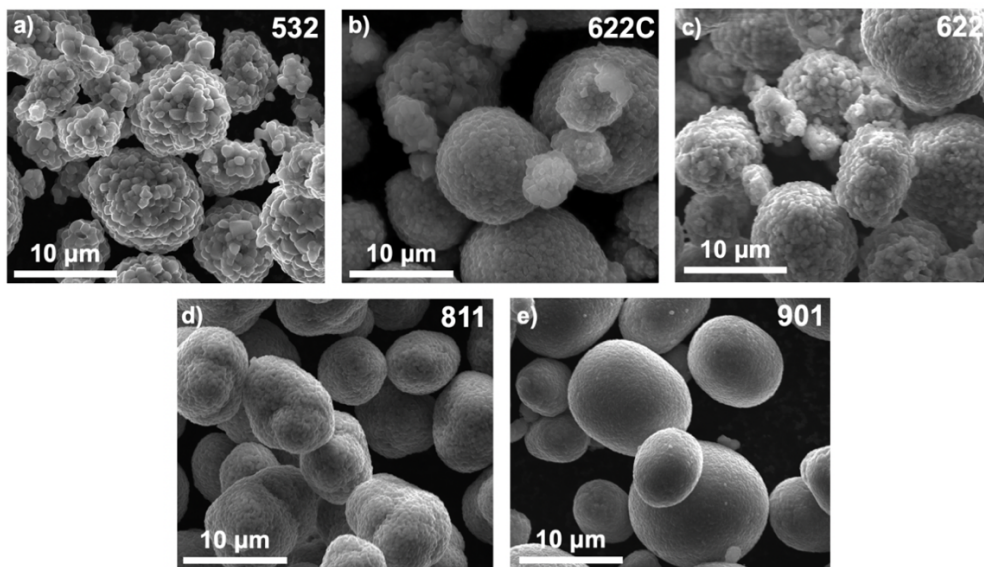


Figure 2. Images SEM représentatives de matériaux NMC riches en nickel : **a) 532**, **b) 622C**, **c) 622**, **d) 811** et **e) 901**.

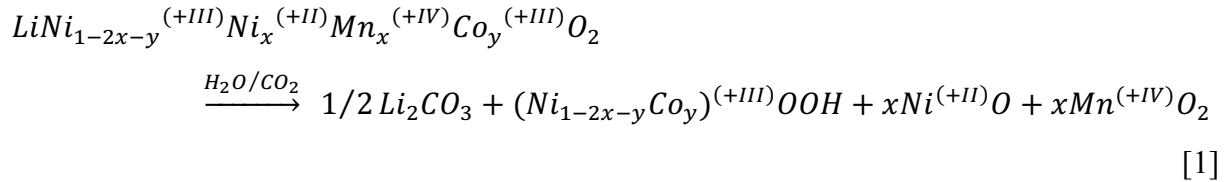
Afin d'assurer la quantification précise de la totalité des espèces de surface, l'optimisation des protocoles et méthodes a été réalisée (Fig. 3). Par exemple, pour éviter les erreurs causées par le CO_2 dans l'air, le temps de solubilisation, l'atmosphère et le rapport massique poudre/eau ont été optimisés. Nous avons identifié et quantifié, Li_2CO_3 , Li_2O et M_2SO_4 ($\text{M} = \text{Li}$ ou Na), sur les cinq matériaux, au moyen de titrage acido-basique, et d'analyses ICP et AAS. Contrairement à ce qui est communément rapporté sur le LiOH , à savoir qu'il est d'ordinaire systématiquement trouvé sous forme de base soluble, son absence dans nos matériaux a été démontré par des analyses FTIR, TGA/MS et RMN.



Figure 3. Diagramme schématique du protocole de solubilisation et d'analyse des bases solubles.

Pendant des années, il était connu que seules les espèces de surface à base de lithium étaient produites à partir de la dégradation à l'air de matériaux lamellaire. Dans ce travail, la dégradation en fonction de la composition des NMC a été étudiée par un processus d'exposition accéléré en atmosphères contrôlées (Fig. 4a, b).

Les analyses TG/MS de ces matériaux ont permis de proposer un nouveau mécanisme qui explique la dégradation des matériaux NMC riches en nickel au contact de l'air, produisant des espèces de surface solubles et insolubles (Eq. 1, exemplifié pour NMC 811), et n'impliquant aucun processus de réduction. Nous suggérons que, en plus du Li_2CO_3 , des espèces insolubles de surface, de type oxyhydroxyde et oxyde de métaux de transition, soient produites. En outre, la dégradation la plus importante a été détectée dans le matériau avec la teneur en nickel la plus élevée, ce qui signifie que les matériaux NMC « as-received » à haute teneur en nickel nécessitent une méthode de stockage plus méticuleuse qu'un NMC 111 classique.



Chapitre III : Réactivité chimique et électrochimique des espèces de surface dans les matériaux NMC riches en nickel.

L'objectif de ce chapitre est d'évaluer l'impact des espèces de surface dans des conditions de batterie. Pour ce faire, leurs produits de dégradation d'électrolyte provenant du stockage à haute température (réactivité chimique), ou des tests de cyclage (réactivité électrochimique), sont analysés.

Il a été constaté que la présence de certaines espèces de surface, à savoir de Li_2CO_3 , Li_2O et M_2SO_4 ; pouvait être avantageuse pour les performances électrochimiques de la batterie, puisque ces dernières produisent du $LiPO_2F_2$ (un additif d'électrolyte bien connu) et du LiF (un composé passivant stable connu), par réaction chimique à haute température avec l'électrolyte (Fig. 4 exemplifie le stockage du Li_2CO_3 à 55 °C).

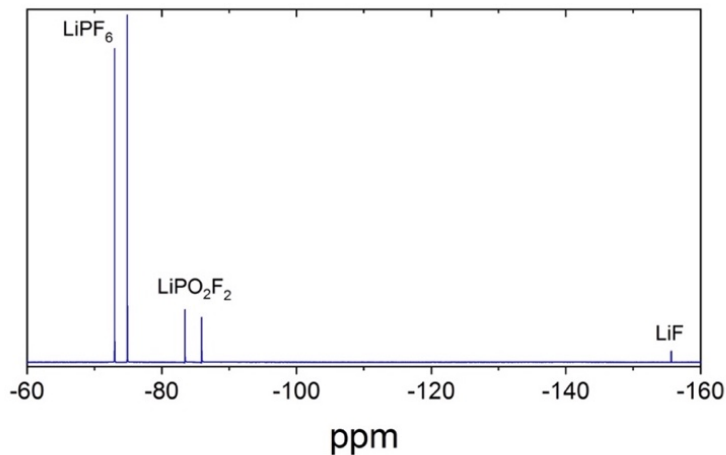


Figure 4. Spectre RMN liquide ^{19}F de l'électrolyte récupéré après stockage de Li_2CO_3 et de l'électrolyte frais pendant 4 jours à 55 °C.

Si toutes ces espèces de surface n'ont pas réagi, le risque est que Li_2CO_3 s'oxyde électrochimiquement en CO_2 et 1O_2 , à un potentiel dépendant de la taille des particules de Li_2CO_3 . Bien que Li_2O , M_2SO_4 et les espèces oxyhydroxyde et oxyde soient électrochimiquement inactifs dans la fenêtre de potentiel utilisée pour les matériaux NMC, leur présence provoquera une augmentation de l'impédance.

Il est connu que les matériaux NMC contenant des espèces de surface souffrent de faibles performances électrochimiques. En vue de les améliorer, et conforté par les réactions in-situ mises en évidence par des analyses TG/MS, un traitement thermique (« annealing ») à 500 °C sous atmosphère d'argon a été réalisé sur le NMC 622C « as-received », lavé (« washed ») et « exposed ». Premièrement, il a été constaté que la capacité de rétention du matériau NMC n'était pas améliorée par l'élimination de la plupart des espèces de surface par lavage; probablement parce que la quantité est inférieure à une valeur d'équilibre décrite dans la littérature⁴. De même, le traitement thermique des matériaux « as-received » et « washed » ne les améliorerait pas non plus. D'un autre côté, le traitement thermique a grandement amélioré la rétention de capacité du matériau exposé (Fig. 5a). Nous suggérons que cela est dû à la réaction in-situ entre Li_2CO_3 , l'oxygène et les oxydes métalliques, qui a diminué la polarisation (Fig. 5b) et rétabli une phase lamellaire électrochimiquement active (Eq. 2).

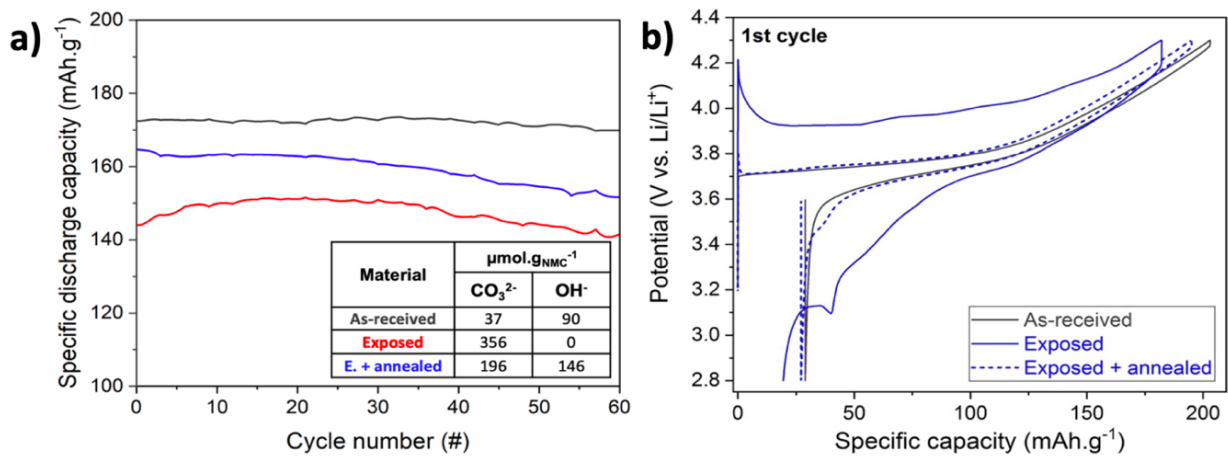
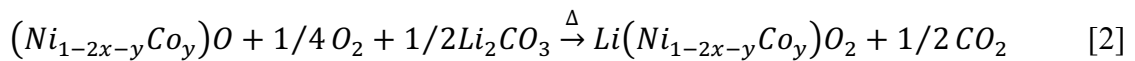


Figure 5. a) Courbes de rétention de capacité de décharge en demi-pile NMC 622C/Li « as-received », « exposed », et « exposed + annealed » à C/10 entre 2,8 et 4,3 V vs. Li/Li^+ . Encart : résultat de la quantification des bases solubles. **b)** Profils de tension vs. capacité.



Chapitre IV : Dégagement de gaz lors du stockage de batteries contenant des matériaux NMC riches en nickel.

Ayant constaté que de nombreuses réactions des espèces de surface produisent du gaz, et connaissant les risques pour la sécurité et la détérioration de la durée de vie associés à la production de gaz, l'étape suivante a consisté à étudier la réactivité des matériaux NMC riches en Ni, à partir de l'analyse des produits gazeux.

Au moyen d'un appareil GC/MS-IR et d'une colonne capillaire, les principaux gaz identifiés à partir de nos batteries étaient CH_4 , CO , C_2H_4 , C_2H_6 et CO_2 . Étant donné que la quantification est limitée dans le cas de l'appareil MS par la co-élution de certains gaz et que la précision des pics obtenus avec l'appareil IR n'est pas optimale, un appareil GC/BID a été utilisé. Cela a conduit à deux résultats principaux : (i) avec la colonne capillaire, un constituant du pic co-élué a été séparé par l'amélioration des conditions expérimentales (Fig. 6a). (ii) avec la colonne « micropacked », le H_2 a été détecté et le pic co-élué a été complètement séparé (Fig. 6b). Malgré l'excellente séparation, celle-ci nécessite encore une amélioration avant d'être utilisable dans des conditions acceptables.

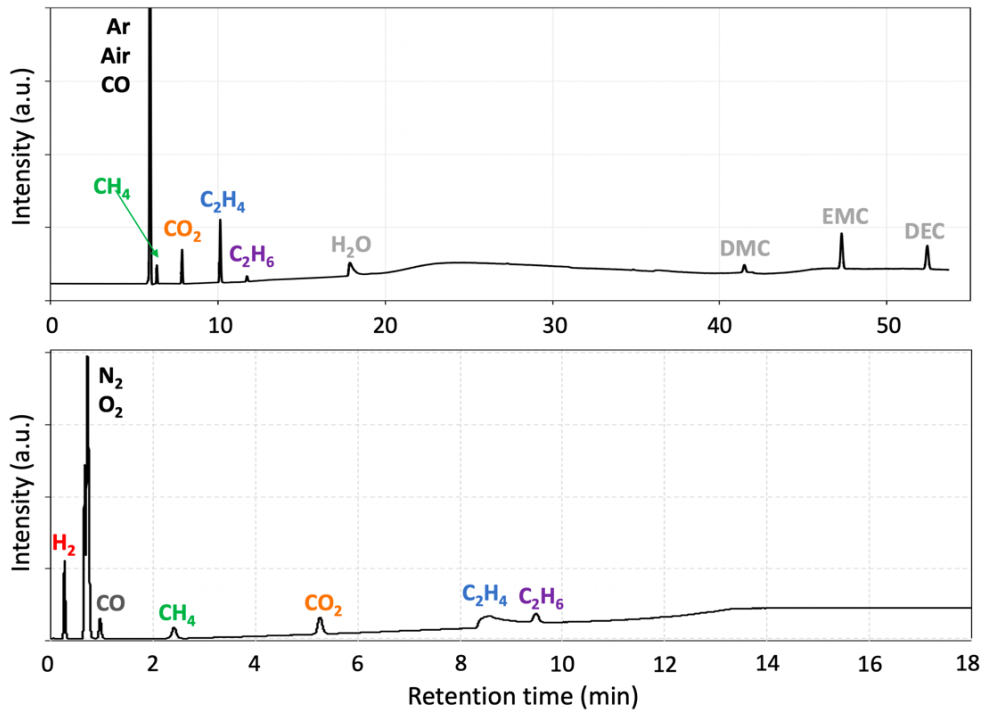


Figure 6. Analyses GC/BID des « pouch cells », **a)** en utilisant une colonne capillaire avec les conditions expérimentales améliorés et **b)** en utilisant la colonne « micropacked ».

Comme étape préliminaire à la quantification des gaz issus de « pouch cells », des tests de stockage avec électrolyte dans des conteneurs spécifiques ont été réalisés dans le but d'évaluer l'impact des matériaux NMC, de l'état de charge, du sel d'électrolyte et du volume mort sur la production de CO_2 . Il a été constaté que le CO_2 produit par le stockage d'électrolyte à $55\text{ }^\circ\text{C}$ était catalysé par PF_5 et dépendait donc du volume mort du conteneur. Lors du stockage de poudres NMC « as-received » avec un électrolyte, de manière surprenante, les matériaux à plus faible teneur en nickel ont produit une plus grande quantité de CO_2 , suggérant différentes

propriétés d'absorption de l'électrolyte. Par la suite, il a été prouvé que le stockage des films NMC délithiés augmente la production de CO₂ (Fig. 7) avec la teneur en nickel. Nous avons déduit que cela se produisait par l'oxydation de l'EC par ¹O₂.

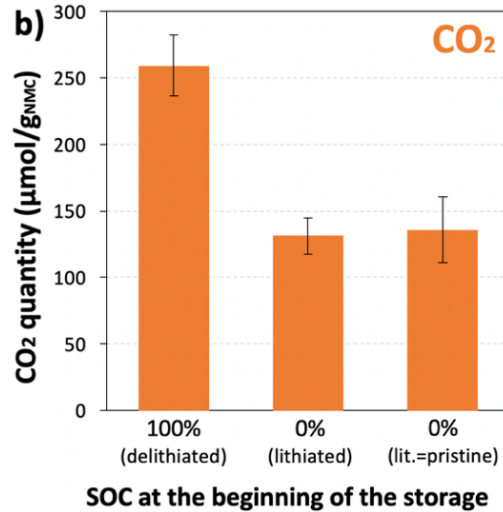


Figure 7. Résultats de la quantification du CO₂ en utilisant l'appareil GC/BID et une colonne capillaire, à partir des films NMC 622C à 100 ou 0% d'état de charge (« SOC »).

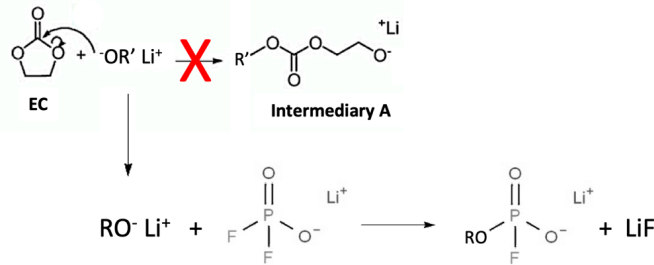
Les analyses dans des « pouch cells » optimisées à 2 et 3 électrodes ont montré que l'intérieur de la batterie est un système complexe et dynamique, avec des réactions générant des gaz et, étonnamment, consommant certains d'entre eux. Grâce à l'utilisation d'un protocole de stockage simplifié, il a été possible de mettre en évidence que la formation de CH₄, C₂H₄ et C₂H₆, dépend principalement de la densité de courant appliqué. De plus, plusieurs sources de CO₂ ont été mises en évidence (mais non différenciées): l'oxydation chimique et électrochimique des solvants et du Li₂CO₃, et la dégradation thermique des solvants. Après stockage, une consommation de C₂H₄ et une augmentation de la concentration de CO₂ ont été observés. Ces deux phénomènes sont engendrés par la production de ¹O₂ par les compositions les plus riches en nickel et à l'état delithié. Dans le même temps, la phase lamellaire se transforme en une phase « rock salt », augmentant l'impédance de l'électrode positive après stockage. Cela a été mis en évidence par des expériences sur des « pouch cells » à 3 électrodes.

Chapitre V : Étude du LiPO₂F₂ comme additif d'électrolyte dans les batteries contenant des matériaux NMC riches en nickel.

Le difluorophosphate de lithium, LiPO₂F₂ (LDFP), a été choisi comme additif d'électrolyte après avoir observé qu'il était produit à partir des réactions chimiques in-situ de certaines

espèces de surface. De plus, la littérature convient que ce dernier améliore le cyclage⁵⁻⁷ et diminue la production de gaz⁷; bien que son mécanisme d'action reste un point controversé.

Il a été constaté que le LDFP ne se comporte pas comme un additif classique qui se réduit ou s'oxyde lors du premier cycle. En effet, pratiquement aucune différence dans la CEI (électrode positive) formée avec et sans LDFP n'a été trouvée. La seule différence se trouve dans le SEI (électrode négative), constatée par l'enrichissement d'espèces à base de fluor et de phosphore, lorsque LDFP est utilisé. En ce qui concerne le mécanisme d'action, les analyses de l'électrolyte ont révélé que le LDFP piège les espèces RO⁻, empêchant ainsi le vieillissement de l'électrolyte (Eq. 3). Cependant, la détermination de son rôle exact sur la production de CO₂ dans les batteries contenant NMC 622C et 811, nécessite des investigations plus approfondies.



[3]

De plus, il a été montré que le LDFP présente un rôle contradictoire lors du cyclage complet des cellules à 55 °C : bénéfique en cas du NMC 622C et délétère en cas du NMC 811 (Fig. 8).

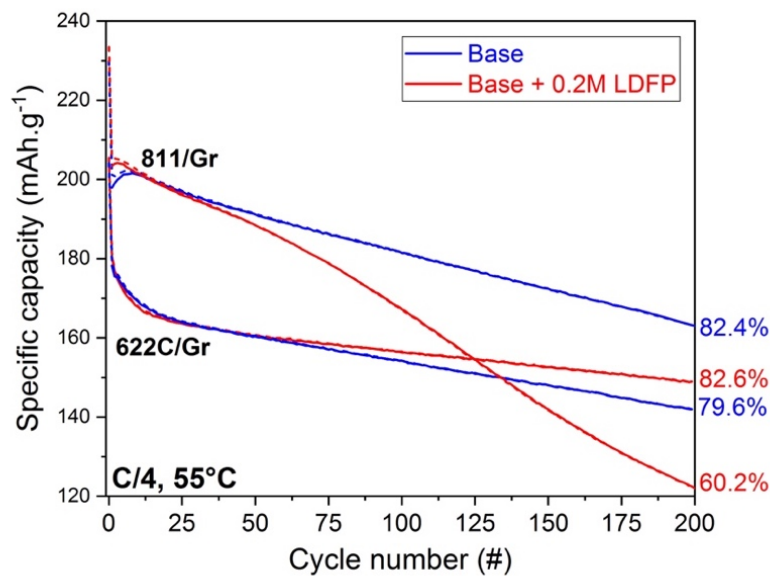


Figure 8. Performances de cyclage des « pouch cells » représentatives 622C/Gr et 811/Gr cyclées entre 2,8 - 4,3 V vs. Li/Li⁺ à C/4 et à 55 °C; **sans** ou **avec 0,2M de LDFP**.

Lors de l'ouverture des cellules 811/Gr, des particules NMC 811 fracturées sont observées, principalement lorsque LDFP est utilisé, ce qui n'est pas observé dans le cas du NMC 622C (Fig. 9).

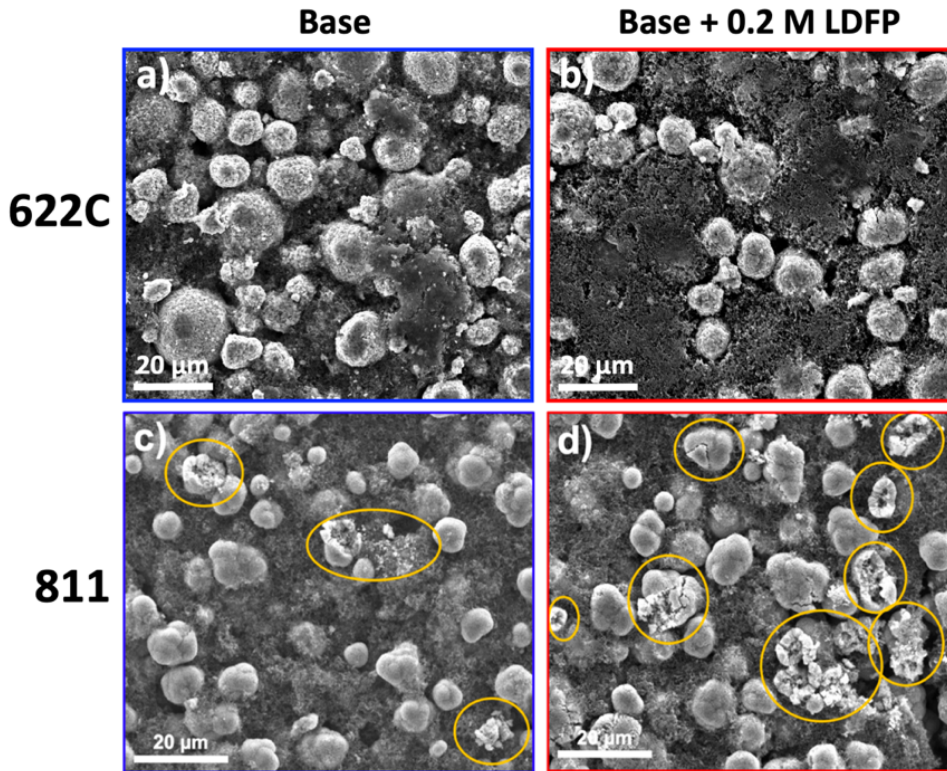


Figure 9. Images représentatives de microscope électronique à balayage, des électrodes NMC 622C (a, b) et 811 (c, d) après le un long cyclage sans ou avec 0,2M de LDFP.

Une étude par microscopie électronique à transmission a permis d'émettre l'hypothèse que des réactions chimiques se produisaient à l'interface des grains primaires du NMC 811, constitué possiblement de bases solubles, induisant une décohésion des grains et une perte de contact. Ce phénomène est exacerbé par la présence du sel LDFP et provoque finalement le « cracking » des particules.

Les résultats de cette thèse ouvrent non seulement des pistes de recherche qui pourraient être poursuivies, mais également contribue à enrichir la compréhension des matériaux NMC riches en Nickel en vue de leur utilisation dans l'industrie automobile.

Références

1. Schipper, F.; Erickson, E. M.; Erk, C.; Shin, J. Y.; Chesneau, F. F.; Aurbach, D., Review-Recent Advances and Remaining Challenges for Lithium Ion Battery Cathodes. *Journal of the Electrochemical Society* **2017**, *164* (1), A6220-A6228.
2. Noh, H. J.; Youn, S.; Yoon, C. S.; Sun, Y. K., Comparison of the structural and electrochemical properties of layered $\text{LiNi}_x\text{Co}_y\text{Mn}_z\text{O}_2$ ($x=1/3, 0.5, 0.6, 0.7, 0.8$ and 0.85) cathode material for lithium-ion batteries. *Journal of Power Sources* **2013**, *233*, 121-130.
3. Liu, H. S.; Zhang, Z. R.; Gong, Z. L.; Yang, Y., Origin of deterioration for LiNiO_2 cathode material during storage in air. *Electrochemical and Solid State Letters* **2004**, *7* (7), A190-A193.
4. Paulsen, J.; Kim, J. High nickel cathode material having low soluble base content. 2012.
5. Wang, C. Y.; Yu, L.; Fan, W. Z.; Liu, R.; Liu, J. W.; Ouyang, L. Z.; Yang, L. C.; Zhu, M., Enhanced high-voltage cyclability of $\text{LiNi}_{0.5}\text{Co}_{0.2}\text{Mn}_{0.3}\text{O}_2$ -based pouch cells via lithium difluorophosphate introducing as electrolyte additive. *Journal of Alloys and Compounds* **2018**, *755*, 1-9.
6. Lei, Q. F.; Yang, T. X.; Zhao, X. Y.; Fan, W. Z.; Wang, W. L.; Yu, L.; Guo, S. B.; Zuo, X. X.; Zeng, R. H.; Nan, J. M., Lithium difluorophosphate as a multi-functional electrolyte additive for 4.4 V $\text{LiNi}_{0.5}\text{Co}_{0.2}\text{Mn}_{0.3}\text{O}_2$ /graphite lithium ion batteries. *Journal of Electroanalytical Chemistry* **2019**, *846*.
7. Ma, L.; Ellis, L.; Glazier, S. L.; Ma, X. W.; Liu, Q. Q.; Li, J.; Dahn, J. R., LiPO_2F_2 as an Electrolyte Additive in $\text{Li Ni}_{0.5}\text{Mn}_{0.3}\text{Co}_{0.2}\text{O}_2$ /Graphite Pouch Cells. *Journal of the Electrochemical Society* **2018**, *165* (5), A891-A899.

Résumé

Ce travail de thèse a porté sur la compréhension des mécanismes de dégradation de surface ainsi que sur l'étude de la réactivité des matériaux NMC riches en nickel, en mettant l'accent notamment sur la compréhension des phénomènes générant des gaz.

Dans un premier temps, la quantification des espèces solubles, laissées lors la synthèse ou produites par l'exposition à une atmosphère spécifique, a été réalisée par titrage mais également par des techniques complémentaires telles que l'AAS, l'ICP-OES et la spectroscopie infrarouge. Cette étude comparative révèle la réactivité de cinq matériaux NMC commerciaux. Les analyses TG/MS de ces matériaux ont permis de proposer un nouveau mécanisme qui explique (i) la dégradation des matériaux NMC riches en nickel au contact de l'air, produisant des espèces de surface solubles et insolubles; et (ii) la récupération partielle des performances électrochimiques des matériaux exposés, après un processus de recuit. Il a été prouvé que certaines de ces espèces présentent à la surface de NMC réagissaient chimiquement avec les composants de l'électrolyte pour produire le sel LiPO_2F_2 .

Dans le but de quantifier les produits gazeux, préalablement, la mise au point d'un protocole de séparation a été réalisé à l'aide d'un appareil GC/BID. L'analyse des gaz produits issus d'un protocole de stockage défini, a mis en évidence la consommation de C_2H_4 et les multiples sources de CO_2 ; les deux ayant en commun, la réactivité du matériau NMC délithié. Enfin, étant produit à partir de réactions chimiques in situ et décrit dans la littérature comme un additif d'électrolyte efficace, le sel LiPO_2F_2 a été évalué comme solution pour améliorer les performances électrochimiques des cellules à base des matériaux NMC riches en nickel. L'analyse des produits de dégradation solides, liquides et gazeux après le cyclage a permis de clarifier le mécanisme d'action par lequel cet additif peut améliorer la rétention de capacité et réduire le gazage. De manière surprenante, une perte de capacité prématurée a été observée lors du cyclage des cellules contenant du NMC 811, à 55 °C. Grâce à des analyses en microscopie électronique, l'hypothèse d'une désintégration des particules, causée par les réactions entre l'électrolyte et l'interphase des joints de grains a été émise.

Mots-clés : NMC riches en nickel, bases solubles, stockage de batteries, génération de gaz, LiPO_2F_2

Abstract

This work was dedicated to the understanding of the surface degradation mechanisms and reactivity of Ni-rich NMC materials, with a focus on the reactions that generate gas.

In a first approach, the exact nature and accurate quantification of the water-soluble species left from synthesis or produced from specific atmosphere-exposure were investigated through complementary techniques as titration, AAS, ICP-OES and FTIR. This comparative study unveils the reactivity of five commercial NMC materials, as function of the increasing nickel content. TG/MS analyses of these materials allowed the proposition of a novel mechanism that explains (i) the degradation of Ni-rich NMC materials toward air, producing soluble and insoluble surface species; and (ii) the partial recovery of the electrochemical performances of exposed materials, after annealing at relatively low temperature. Some of those NMC surface species were proved to chemically react with the electrolyte components into LiPO_2F_2 .

With the aim of quantifying gaseous products, first, different separation conditions were studied by making use of a GC-BID apparatus. The analysis of gases produced from a defined storage protocol, evidenced the consumption of C_2H_4 and the multiple sources of CO_2 ; both having in common, the reactivity of delithiated NMC. Lastly, being produced from in-situ chemical reactions and described in the literature as an efficient electrolyte additive, LiPO_2F_2 was evaluated as a solution for enhancing electrochemical performances of Ni-rich NMC materials-based cells. The analysis of solid, liquid and gaseous degradation products after cycling helps clarify the action mechanism through which it can improve the capacity retention and seemingly reduces gassing. Surprisingly, a premature capacity loss was observed when cycling NMC 811-containing cells, at 55 °C. Through electron microscopy analyses, it was hypothesized that it was due to the particle disintegration, caused by the reactions between the electrolyte and grains boundaries interphase.

Key-words: Ni-rich NMC, soluble bases, battery storage, gas generation, LiPO_2F_2